MECHANICS OF STRAIN-INDUCED TRANSFORMATION TOUGHENING IN METASTABLE AUSTENITIC STEELS

by

RICHARD GRAHAM STRINGFELLOW

B.S.E., Civil Engineering, Princeton University
(1982)
M.Sc., Mechanical Engineering, MIT
(1988)

Submitted to the Department of
Mechanical Engineering
In Partial Fulfillment of
the Requirements for the Degree of

Doctor of Philosophy in Mechanical Engineering

at the

MASSACHUSETTS INSTITUTE OF TECHNOLOGY

November, 1990

Signature of Author_____
Department of Mechanical Engineering
November 2, 1990

Certified by_____
David M. Parks
Associate Professor of Mechanical Engineering
Thesis Supervisor

Accepted by_____
Ain A. Sonin, Chairman
Departmental Committee on Graduate Studies

Mechanics of Strain-Induced Transformation Toughening in Metastable Austenitic steels

by

Richard G. Stringfellow

Submitted to the Department of Mechanical Engineering
on November 2, 1990 in partial fulfillment of the
requirements for the Degree of Doctor of Philosophy in
Mechanical Engineering

Abstract

The phenomenon in which metastable austenitic steels gradually transform into a much harder, fine-scale martensite phase under the driving force of plastic deformation is termed "strain-induced transformation plasticity" (SITP). Certain high strength (σ_y = 1380 MPa) alloys of this type have displayed remarkably high fracture toughness (K_{Jc} = 380 MPa$\sqrt{\text{m}}$) [1]. These high toughness values can be attributed to the transformation process and its effect on the fracture event. We propose a constitutive model which describes the transformation plasticity accompanying *strain-induced* martensitic transformation in nonthermoelastic alloys. The model consists of two parts: a transformation kinetics law describing the evolution of the volume fraction of martensite and a constitutive law defining the flow strength of the evolving two-phase composite. The Olson-Cohen model for martensite volume fraction evolution is recast in a generalized rate form so that the extent of martensite nucleation is not only a function of plastic strain and temperature, but also of the *stress state*. A self-consistent method is then used for predicting the resultant stress-strain behavior. The model describes both the *hardening* influence of the transformation product, and the *softening* influence of the transformation itself, as represented by a spontaneous *transformation strain*. The model is then implemented in a finite element program suitable for analysis of boundary value problems. Model predictions are shown to be reasonably consistent with existing experimental data for austenitic steels. We then examine the effect of the transformation on the state of stress and strain at three critical length scales: in the neck of a tensile specimen; near the tip of a stationary crack; and at the interface of an included particle. The predominant mechanism of fracture in high strength steels involves the nucleation, growth and coalescence of voids in highly localized bands of intense deformation. We therefore focus attention on the influence of the transformation on these critical fracture processes. We find that transformation-softening can lead to suppression of void nucleation while subsequent transformation-hardening significantly increases the stability of plastic flow in highly triaxial regions. Finally, in order to *directly* assess the interaction of transformation with the fracture processes, we incorporate a model accounting for the continuum effects of porosity evolution into our constitutive framework. Finite element calculations using this model clearly indicate that the transformation hardening accompanying SITP directly combats the deleterious strain-softening effects of void nucleation and growth

and therefore leads to suppression of plastic flow localization. We conclude that, fundamentally, the sources of transformation toughening in these materials can be traced to the observation that the mechanical features which promote void nucleation and growth, namely high strain and triaxiality, are precisely the same features that promote nucleation of martensite. Moreover, our calculations indicate that the beneficial consequences of this localized formation of martensite are twofold: (1) retardation of void nucleation through early transformation-softening; and (2) counteraction of the strain-softening effects of void growth by means of transformation-hardening.

Thesis Supervisor: Dr. David M. Parks

Title: Associate Professor of Mechanical Engineering

Acknowledgments

I wish to express my sincere thanks to Professor David Parks for his guidance during the last five years. Professor Parks' warm friendship, enthusiastic support and undying patience helped me through many difficult times. He has in every way filled the complex roles of teacher, advisor, counselor and friend (as well as soccer coach!).

I would also like to thank the other members of my committee: Professors Olson, Argon and Abeyaratne, for the considerable time and effort that they spent attending meetings and reading this thesis, and for many helpful discussions. Special thanks to Rohan for sharing many enjoyable "snax" (not to mention the use of his car).

Thanks to the Department of Energy, who provided support for this research under grant DE-FG01-84ER45154.

Much thanks to all the *many* office mates that have shared with me good and difficult experiences of MIT. Thanks Greg, Mary, Ed, Michelle K., Allen, Peter, Jimmy, Yong-yi, Li, Albert, Hyungyil, Michelle H., Boon, Ellen, Hang-sheng, Debbie, Apostolous, Vijay and Simmy. To the one in this list that managed to fall asleep at my defense, I thank you for sharing these often difficult times and making every minute a great pleasure. I look forward to sharing the years to come with you.

Thanks also to my teammates on the MIT graduate soccer team, and the players on the MIT varsity teams who have provided the diversions that allowed me to keep the proper perspective (and my sanity). Special thanks to coach Walter Alessi, for giving me the opportunity to work with him, and for 5 years of friendship.

Finally, I must thank my parents for instilling in me the importance of an education, for the sacrifices they made giving me the opportunities I have had, and for the love and support they have shown along the way. Mom, wherever you are, I know you would have been proud!

Table of Contents

Appendices

List of Figures

List of Tables

List of Symbols

a, a_0	width of ligament, deformed/undeformed configurations
A	effective martensite nucleation shear strain rate
A_f	martensite nucleation strain coefficient
A_0	effective martensite nucleation shear strain rate constant
A_1	effective martensite nucleation shear strain rate constant
A_N	void nucleation strain rate coefficient
B_f	martensite nucleation triaxiality coefficient
B_N	void nucleation shear stress rate coefficient
C	geometric intersection constant
C_i	material hardening law constant
C_N	void nucleation pressure rate coefficient
d, d_0	width of tensile specimen, deformed/undeformed configurations
D_0	diameter or width, undeformed configuration
$\dot{e}_V^T$	total dilatation rate
$\dot{e}_V^p$	plastic dilatation rate
f	martensite volume fraction
f_I	volume fraction of shear band intersections
f_{sb}	volume fraction of shear bands
f_i	phase volume fraction
h	hardening rate
H	Heaviside step function
h_i	phase hardening rate
$\mathbf{D}$	stretching tensor
$\mathbf{D}^e$	elastic stretching tensor
$\mathbf{D}_i$	phase stretching tensor
$\overline{\mathbf{D}}$	volume average stretching tensor
$\mathbf{D}^p$	plastic stretching tensor
$\mathbf{D}^{slip}$	slip stretching tensor
$\mathbf{D}^{nucl}$	martensite nucleation stretching tensor
g	dimensionless driving force for martensite nucleation
g_0	constant
g_1	temperature dependence coefficient, $\partial g/\partial \Theta$
g_2	linear triaxiality dependence coefficient
g_3	quadratic triaxiality dependence coefficient
$\bar{g}$	mean value of dimensionless probability function
G	shear modulus
G_M	matrix shear modulus
J_{Ic}	fracture toughness parameter

K	bulk modulus
K_M	matrix bulk modulus
K_ρ	$(\rho_U^* - \rho)/(\rho_F - \rho_c)$
L	number of terms in material hardening law
L_0	undeformed length
$\mathbf{L}$	velocity gradient tensor
M	rate sensitivity exponent
M_d	extinction temperature for transformation
M_s	temperature for spontaneous transformation
M_s^σ	temperature at which yield stress equals transformation stress
$\mathbf{M}$	deviatoric total deformation normal tensor
n_i	phase strain-hardening exponent, one term
n_{ij}	phase strain-hardening exponent, general form
N	number of phases
N_I	number of shear band intersections per unit volume
N_m	number of martensitic embryos per unit volume
$\mathbf{N}$	normal of stress state
P	probability of martensite nucleation
P_{max}	maximum probability seen by each ΔN_I
P_{app}	applied load
P_{max}^{nt}	maximum load, nontransforming case
p	hydrostatic pressure
r	radial position
r_∞	radial extent of self-similar region
R, R_0	specimen radius, deformed/undeformed configurations
R_d	distance along crack plane, deformed configuration
r_I	exponent in shear band intersection relation
s	hardness
s_i	phase hardness
s_i^*	phase reference hardness
$\bar{s}$	average hardness
$\mathbf{S}$	deviatoric stress tensor
$\mathbf{S_i}$	phase deviatoric stress tensor
$\bar{\mathbf{S}}$	volume average deviatoric stress tensor
s_g	standard deviation of dimensionless probability distribution function
s_γ	standard deviation of strain-based void nucleation distribution function
s_σ	standard deviation of stress-based void nucleation distribution function

t	time
T	temperature
$\mathbf{T}$	Kirchhoff stress
T_H	homologous temperature
$\overset{\nabla}{\mathbf{T}}$	Jaumann rate of Kirchhoff stress
V	volume
V_a	relative volume occupied by austenite phase
V_i	relative volume occupied by ith phase
V_m	relative volume occupied by martensite phase
$\bar{v}_I$	average volume per shear band intersection
$\bar{v}_m$	average volume per martensitic unit
$\mathbf{W}$	spin tensor
x	transverse position
z	longitudinal position
Z_i	void nucleation function
$\mathbf{1}$	identity tensor
α	temperature-dependent rate of shear band production
β	$\mathbf{M} \cdot \mathbf{N}$
β_0	$C\bar{v}_m/\bar{v}_I$
$\Delta\boldsymbol{\epsilon}$	strain increment tensor
Δ_V	transformation volume change
ϵ	one-dimensional strain
$\bar{\epsilon}$	equivalent tensile strain
ϵ_d	diametral strain
ϵ^∞	remote axial strain
ϵ_L	strain at recovery of stability (Luder's strain)
ϵ_u	first uniform strain limit
ϵ'_u	second uniform strain limit
γ	equivalent plastic shear strain
μ_i	phase viscosity
μ_i^*	phase average viscosity
$\overline{\gamma}^p$	average equivalent plastic strain
$\overline{\gamma}^p_N$	mean nucleation strain
$\dot{\gamma}_a$	equivalent austenite shear strain rate
$\dot{\gamma}_m$	equivalent martensite shear strain rate
γ_i^*	reference phase strain
$\dot{\gamma}_i^0$	reference phase strain rate

$\dot{\gamma}^0$	reference strain rate
$\bar{\dot{\gamma}}^p$	average equivalent plastic strain rate $= \sqrt{2\mathbf{D}^{p'} \cdot \mathbf{D}^{p'}}$
$\bar{\dot{\gamma}}^p_M$	matrix average equivalent plastic strain rate
$\dot{\gamma}^T$	total equivalent shear strain rate
$\dot{\lambda}$	work hardening parameter
μ	effective viscosity
μ_i	phase viscosity
$\bar{\mu}$	average viscosity
ν	Poisson's ratio
Φ	plastic potential function
Π_i	normalized phase hardness $= s_i/\bar{s}$
ρ	void volume fraction
ρ^*	void volume fraction function
ρ_c	critical void volume fraction
ρ_F	void volume fraction at fracture
ρ_N	volume fraction of void nucleating particles
ρ^*_U	void volume fraction corresponding to zero strength
$\dot{\rho}_{nucleation}$	void volume fraction nucleation rate
$\dot{\rho}_{growth}$	void volume fraction growth rate
σ	one-dimensional stress
$\boldsymbol{\sigma}$	Cauchy stress tensor
Σ	triaxiality parameter $= -p/(\sqrt{(3)}\bar{\tau})$
$\bar{\sigma}$	Mises equivalent stress
σ_N	mean nucleation stress
Σ_M	matrix triaxiality parameter $= -p/(\sqrt{3}\bar{\tau}_M)$
τ	equivalent shear stress
$\bar{\tau}$	average equivalent shear stress
$\bar{\tau}_M$	matrix average equivalent shear stress
τ_i	phase average equivalent shear stress
Θ	dimensionless temperature
χ_i	normalized phase strain rate
χ_f	normalized martensite nucleation rate
$\mathcal{I}$	fourth order identity tensor
$\mathcal{L}^e$	elastic modulus tensor (4^{th} order)
$\mathcal{L}^e_a$	austenite elastic modulus tensor (4^{th} order)
$\mathcal{L}^e_m$	martensite elastic modulus tensor (4^{th} order)

Chapter 1

Introduction

The search for alloys which exhibit both high strength and high fracture toughness is an area of continual interest. Unfortunately, it is rare for one material to possess both of these desirable properties. In fact, there is typically an inverse relationship between the two, because the same microstructural processes which strengthen an alloy, particularly the precipitation of hard particles that interfere with slip mechanisms, generally lower the toughness of the metal by inhibiting plastic flow, and ultimately serve as the "seeds" of fracture by a process of nucleation, growth, and coalescence of voids which form around these particles. It is nevertheless desirable for a structural material to be both strong and tough, and a material demonstrating both of these qualities would certainly have many practical applications.

One means of achieving this desirable but rare combination of properties is through *transformation toughening*, whereby toughness is achieved through a martensitic transformation which occurs *during* plastic deformation, a process which has been named *transformation plasticity.* Transformation plasticity accompanying martensitic transformations under applied stress has provided several examples of extraordinary mechanical behavior, ranging from substantial enhancements of ductility and toughness in metallic and ceramic alloys exhibiting nonthermoelastic transformations [2–4], to the reversible plasticity phenomena in thermoelastic shape memory alloys

[5].

Within a specific range of temperatures, martensitic transformations occur subsequent to, and as a result of, plastic slip in the austenite matrix. We refer to this temperature range as the *strain-induced transformation regime.* Experiments on metastable austenite steels, precipitation-strengthened to 1300 MPa tensile yield stress, have demonstrated remarkable transformation toughening in the strain-induced transformation regime when ductile fracture is controlled by plastic shear localization [1,2,6–7]. Recent results show J_{Ic} toughness in excess of 500 kJ/m^2 [1]. Fig. 1.1 compares fracture toughness measured in [1] and [6] with those of other high strength materials [8]. It is clear from this figure that the fracture toughness/strength combinations of the transforming steels are significantly greater than those of the other listed high strength steels, where toughness is achieved by more standard means. These high toughnesses can be attributed to the transformation process and its effects on the fracture event. The complex nature of this process, however, makes it difficult to pinpoint the sources of the beneficial effects of the transformation. It is generally argued that the toughness increase results from one or both of the following features of the transformation: the gradual hardening of the two-phase austenite/martensite composite due to evolution of the much harder martensite phase, and the volume expansion (as high as 5 percent) that accompanies the transformation. With regard to the first of these features, the predominant mechanism of failure in high strength steels involves nucleation, growth and coalescence of voids which form around hard particles embedded in the ductile matrix [9-11]. It is argued here that local transformation hardening toughens the region near the crack tip by countering the softening effects of void nucleation and growth, and retarding the closely associated process of localization of plastic deformation into shear bands. Controlled experiments further indicate that the transformation toughening effect is greatly enhanced with increased

transformation dilatation [6,7,12]

The macroscopic mechanical behavior of high strength austenitic steels which exhibit strain-induced martensitic transformations is a result of three primary processes at the microscale: crystallographic slip of both phases, nucleation of martensite, and the fracture process. The driving forces that control the evolution of a single process depend upon the applied boundary conditions as well as the current state of each process. The broad scope of this research has been to quantify the complex interactions of these processes and their macroscopic consequences through continuum mechanics modelling.

In preliminary research conducted as part of a Master's thesis project [13], we examined some of the more basic aspects of strain-induced transformation plasticity using existing models for martensite evolution and stress-strain relationships. This work focussed primarily on the effects of the transformation on the shape of the stress-strain curve, as illustrated in Fig. 1.2, and its consequences on the mechanical behavior of the material studied through numerical analyses of boundary value problems. Although this work suggested possible explanations for the increased toughness, the relative simplicity of the constitutive model implemented for numerical analyses limited the usefulness of the results. An important parameter which was not considered in this previous model is the stress-state sensitivity of the transformation. Recent results have shown that *the state of stress has a pronounced effect on the extent of transformation*, as demonstrated by the great differences between the amount of martensite formed in tension versus that formed in compression for an overaged 0.5Mn-phosphocarbide-strengthened alloy studied by Young [7] (Fig. 1.3). Stress-state dependence is viewed as a critical feature of the transformation because the regions of interest in the study of fracture resistance, *i.e.*, the area ahead of the tip of a crack or along the interface of a hard particle, are also regions of high *triaxiality*,

where triaxiality is a measure of the size of the hydrostatic component of stress relative to its deviatoric component. Moreover, several investigations have shown that the triaxial nature of the stress state is a critical factor controlling the rate of growth of voids ultimately leading to fracture [15–19].

The research discussed in this thesis consists of two major parts. The first, and perhaps most critical portion of the research, described in chapter 3, has been devoted to improvement of existing constitutive models, implementing new features that allow for quantification of the interactions of slip-based plasticity, stress, temperature and transformation. Analysis of the interactions of transformation plasticity with crack-tip shear localization processes and investigation of the role of transformation dilatation require reliable constitutive models which take proper account of transformation strain hardening, transformation dilatation, and the associated pressure sensitivity of transformation kinetics.

In the temperature regime of enhanced toughness, the transformation is dominated by *strain-induced* nucleation on potent sites created by plastic strain, and as a result, transformation kinetics and plastic flow behavior involve a complex interaction of slip and transformation; constitutive models for this regime [20–21] are not as well developed as models for transformation at stress levels which preclude slip in the austenite — *stress-assisted* transformation. Here, we re-examine and improve upon existing kinetics models and develop techniques for averaging the stress-strain properties of the evolving two phase composite in a manner that directly accounts for the sizable transformation shape strain. A relatively straightforward but critical third step in this first portion of the research is the correlation of model predictions with existing tensile and compressive test data at various temperatures [7,21]. Finally, an extended form of the model is proposed, accounting for the continuum effects of porosity evolution, in order to evaluate directly the interaction of transformation with

the failure process. Here we have adapted methods for evaluating void volume fraction nucleation and evolution as proposed by Needleman and Tvergaard [22], based on the models of Needleman and Rice [23] and Gurson [24,25].

With a relatively general formulation accounting for these phenomena in hand, in the second portion of the research (chapters 4 and 5) we analyze several boundary value problems in order to evaluate the effects of the transformation, especially in regard to its interactions with the fracture process. We believe that a better grasp of the mechanical aspects of this interaction is essential to an understanding of the toughening mechanism. We have therefore applied these models to simulations of various problems of inhomogeneous deformation, each designed to identify critical aspects of the transformation.

At the smallest continuum length scale over which our models can be reasonably applied, we have considered the stress and strain fields surrounding an included particle, in order to directly assess the effects of the transformation on the void nucleation process. At a larger continuum length scale, we have embedded the effects of void nucleation and growth into a continuum model appropriate for numerical study of the interactions of transformation and nucleation and growth, and their combined effect on the state of stress and strain at blunt notches and blunting crack tips.

Finally, we correlate the results of these analyses with experimental observations concerning ductility and fracture. Young [7], for example, found strong correlations between the increment in fracture toughness due to transformation and the transformation volume change. This sort of correspondence, as well as other empirical findings, are investigated in order to assess the relative importances of various features of the transformation.

Our hope is that, with a better understanding of this phenomenon, future alloys can be designed to maximize the benefits of the transformation *for particular ap-*

plications. In recent experiments on phosphocarbide-strengthened steels, Young has demonstrated that alteration of the critical transformation parameters, *i.e.*, the phase hardness difference and the extent of volume change, can be accomplished simply by changing the ageing process. Thus, once the nature of the transformation/fracture interaction is clarified, it may be relatively easy to process alloys for which the beneficial mechanical effects of the transformation are maximized for the environment and loading conditions to which they will be subjected.

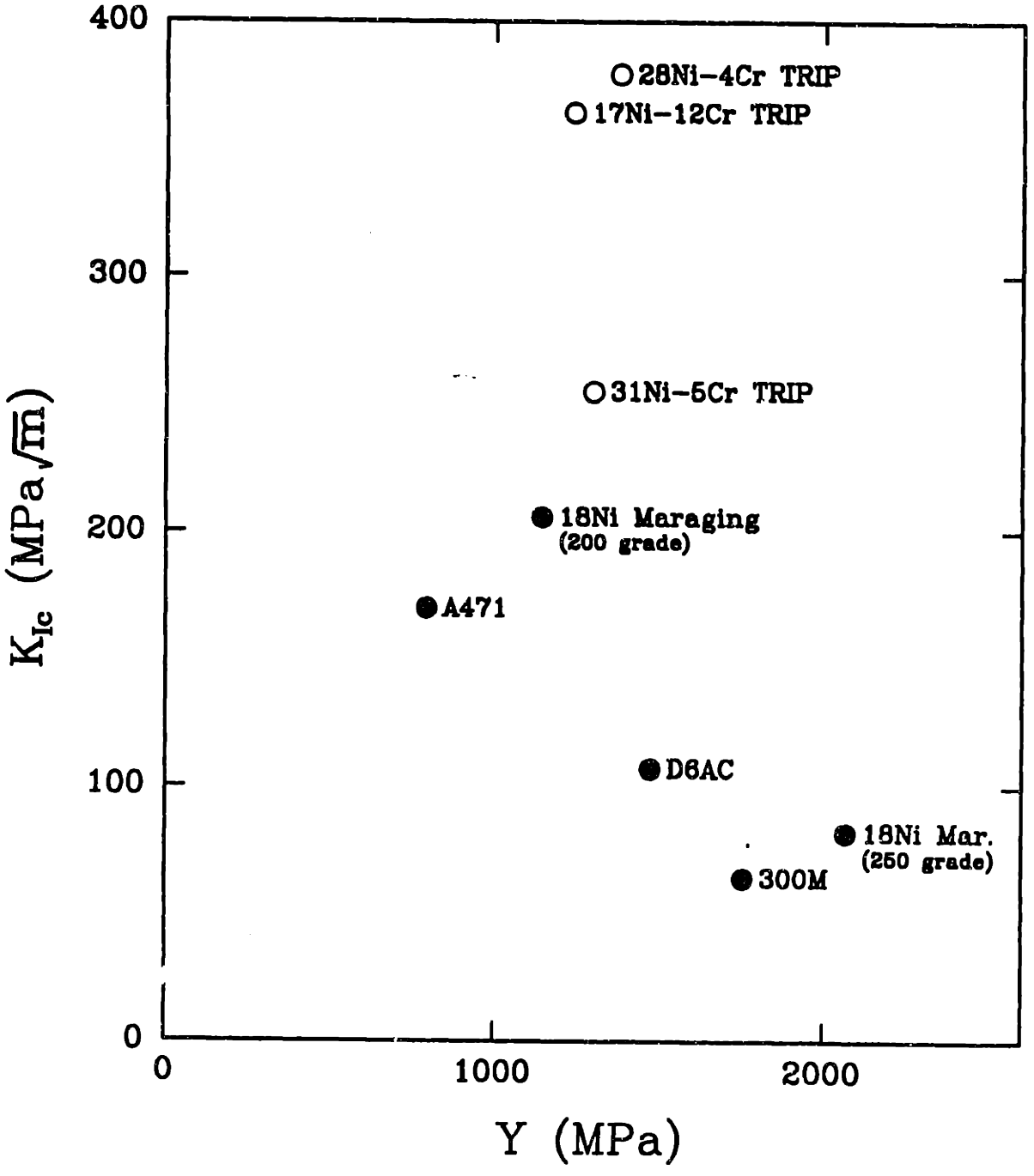

Figure 1.1 Comparison of fracture toughness (K_{Ic}) versus yield strength (Y) for several high strength and/or high fracture toughness alloys. Data for the "TRIP" alloys were obtained from [1] and [6]. Data for the remaining alloys were taken from [8].

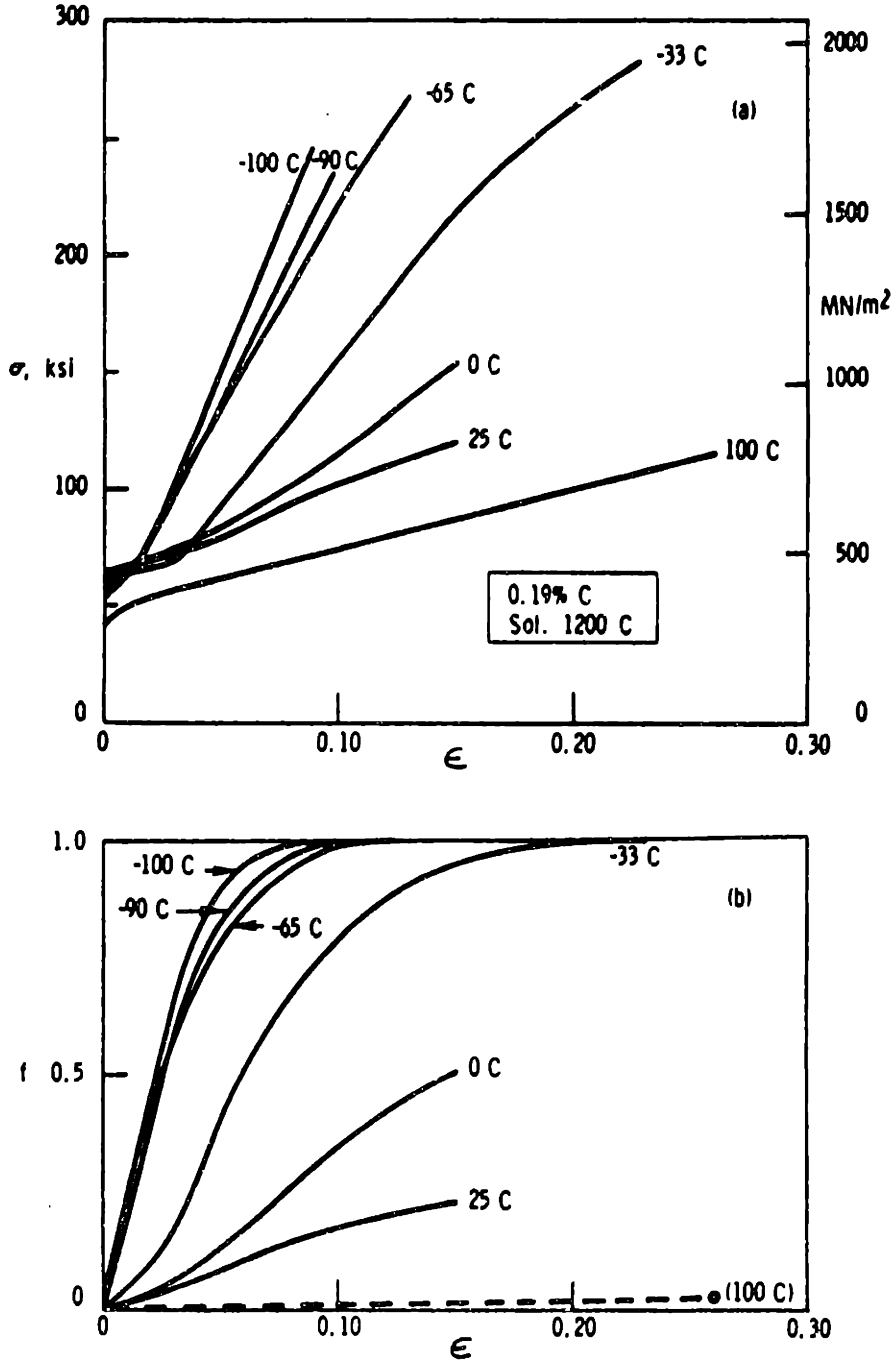

Figure 1.2 Tensile properties and transformation curves for a 0.19C TRIP steel solution treated at 1200°*C*. (a) true stress versus true strain. (b) volume fraction martensite versus true strain (taken from [14]).

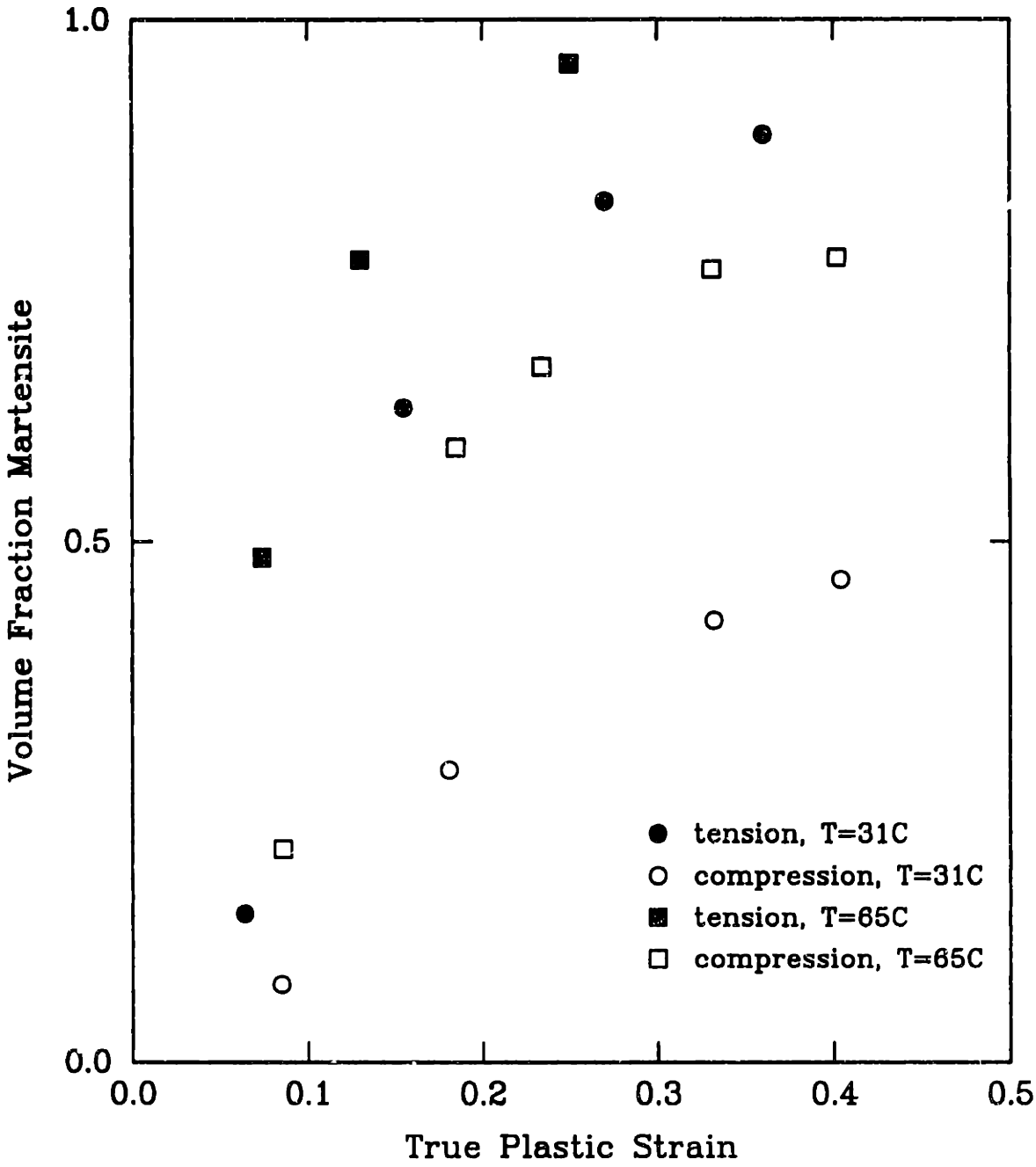

Figure 1.3 Comparison of data for volume fraction martensite versus true plastic strain measured at 31°C and 65°C during simple tension and compression tests for a overaged 0.5Mn-phosphocarbide-strengthened alloy [6].

Chapter 2

Historical Perspective

In this chapter, we review some of the relevant research that has been performed leading up to this thesis project. We first present a short description of martensitic transformations, followed by a more specific discussion of the mechanically-induced martensitic transformations which produce transformation plasticity. We then review the pertinent experimental work on transformation toughening that has motivated this research, and discuss the possible sources of transformation toughening that we will later explore through analysis. Finally, we review the processes of fracture in high strength steels and discuss a few basic mechanical issues related to these experimental observations.

2.1 Martensitic Transformations

The strengthening of steel through quenching is a process that has been used for thousands of years. It has been only in relatively recent years, however, that this strengthening has been shown to be the result of a structural change called a *martensitic transformation.* The martensitic transformation is a widely observed phenomenon which has been observed in many metallic as well as ceramic systems.

The phenomenological features which distinguish martensitic transformations have been reviewed by Cohen, Olson and Clapp [26]. Martensitic transformations repre-

sent a subset of a more general classification of *displacive* (diffusionless) phase transformations which are characterized by high speeds of transformation during which atoms move over distances less than the atomic spacing. The transformation is characterized by lattice-distortive displacements rather than shuffle displacements (see Fig. 2.1). Moreover, the deviatoric component of the displacement dominates, rather than the dilatational component, with the result that there are lines within the crystal structure that remain undistorted during transformation. Within the group of transformations which exhibit the above characteristics, a martensitic transformation is defined to be one in which strain energy dominates the kinetics and morphology of the transformation.

In iron-based alloys, martensitic transformation alters the fcc crystal structure of the parent austenite to the bcc or bct structure of martensite, as depicted in Fig. 2.2. (Transformations from fcc to hcp are also observed.) Parent and product structures of several systems are summarized in Table 2.1. The transformation produces a *shear strain* of about 20 percent [28] as well as a volume expansion or positive *hydrostatic strain* which can vary from 0 to 5 percent, depending upon the chemical composition of the alloy [6,28,29].

Alloy	Structural Change
Co, Fe-Mn, Fe-Cr-Ni	fcc → hcp
Fe-Ni	fcc → bcc
Fe-C, Fe-Ni-C, Fe-Cr-C, Fe-Mn-C	fcc → bct
In-Tl, Mn-Cu	fcc → fct
Li, Zr, Ti, Ti-Mo, Ti-Mn	bcc → hcp
Cu-Zn, Cu-Sn	bcc → fct
Cu-Al	bcc → distorted hcp
Au-Cd	bcc → orthorhombic

Table 2.1 Systems in which martensitic or quasimartensitic (martensitic-like) transformations occur (adapted from [27]).

2.2 Temperature/Stress-Dependence of Martensitic Transformations

At any given temperature, there exists one preferential crystallographic structure corresponding to the lowest energy level. The martensite phase has the thermodynamically preferred crystal structure at relatively low temperatures, so that when the steel is quenched, the original austenite structure — stable at high temperatures — tends to transform into martensite. For the transformation to occur, an energy barrier must be overcome, since, during transformation, crystal atoms will temporarily assume configurations corresponding to higher energy levels. If the driving force for transformation is not high enough, the energy barrier cannot be overcome: the parent state (austenite) cannot transform into the the thermodynamically favorable product phase (martensite), and it is said to be *metastable.* As the temperature decreases, the difference between the energy levels of the two structures, *i.e.*, the driving force for transformation, increases so that, when austenite is rapidly cooled below a sufficiently low temperature, M_s, a spontaneous transformation to martensite occurs. Another means of altering the driving force for transformation is by supplying mechanical work in the form of an applied stress. In this manner, the austenite/martensite transformation can occur at temperatures higher than that for spontaneous transformation. Transformation at temperatures above M_s is said to be *mechanically-induced.* Fig. 2.3 gives a schematic representation of the conditions for transformation under applied macroscopic loading. Nucleation of martensite at temperatures just above M_s is termed *stress-assisted*, since it relies on applied stress to provide the additional driving force required for transformation. As the temperature increases above M_s, the amount of stress required to produce the transformation increases linearly until it finally reaches the yield stress of the austenitic phase at that temperature, Y_0. This occurs at M_s^σ, the temperature at which the observed linear relationship between the nucleation stress and temperature abruptly ends [31]. Subsequently, the stress for transformation follows a curve which lies slightly above the yield stress versus temperature line of the austenite, and well below the extrapolated stress-assisted

transformation line.

At temperatures below M_s^σ, martensite particles form at pre-existing sites in the parent austenite. Above M_s^σ, however, new nucleation sites are created by plastic strain in the austenite (e.g., [14]). This *strain-induced* form of the transformation is observed at temperatures between M_s^σ and M_d, the temperature at which fracture occurs prior to transformation [32]. At temperatures near M_s^σ, both stress-assisted and strain-induced modes of nucleation are observed [33].

The morphology of the two-phase product of the transformation is dependent upon the general conditions of plastic flow in the parent austenite [14]. As shown in Fig. 2.4a for a 0.27C (0.27 weight percent carbon) metastable austenitic steel, solution treated at $1200C$, martensite forms spontaneously during isothermal holding at $-196C$. The wide, jagged bands observed here are indicative of an autocatalytic nucleation process [34]. A similar morphology is depicted in Fig. 2.4b for stress-assisted transformation at $-196C$, however, the bands here have become more randomly oriented, most likely due to interference in the growth process caused by slip in the austenite [14]. The similarities between the stress-assisted and spontaneous morphologies are consistent with the notion that the essential mechanism of nucleation is the same in both cases, the only difference being the thermodynamic assistance given by the applied stresses [14]. At temperatures well into the strain-induced regime, however, the morphology is quite different, indicating that the nucleation process is different at these higher temperatures ($-28C$ and $25C$), as shown in Figs. 2.4e and 2.4f. Although there has been much debate over the exact nature of the nucleation process for strain-induced martensite, most investigators agree that, in austenitic steels, the martensite forms at the intersections of microscopic shear-bands, which typically consist of one of the following: intermediately formed ϵ'-martensite (hcp), mechanical twins, or stacking fault bundles [35–39]. Recent experimental work by Young [7] on phosphocarbide precipitate-strengthened alloys suggests that the nucleation process can also involve interactions between shear bands and the precipitate particles. At intermediate temperatures ($-128C$ and $-75C$), both types of morphologies are present, as shown in Figs. 2.4c and 2.4d, which suggests that the boundary

between stress-assisted and strain-induced transformation regimes is not sharp.

Kulin, *et al.* [40] demonstrated in the early 1950's that M_s^σ changed under different states of stress. Shortly thereafter, Patel and Cohen [29] quantified the effect of stress on the driving force for transformation. It is now well established (*e.g.*, [41]) that the M_s^σ and M_d temperatures are strong functions of stress state. In the next section, we review the mechanisms of transformations that occur in conjunction with, and as a result of, an applied stress. One should keep in mind when reading this section and the remainder of this thesis that, when we speak of temperatures in the "stress-assisted" or "strain-induced" temperature regimes, we are referring to temperatures relative to the M_s, M_s^σ and M_d temperatures for a *particular stress state*, *e.g.*, $M_{s,ut}^\sigma$ (the M_s^σ temperature in uniaxial tension) or $M_{d,ct}$ (the M_d temperature in the triaxial stress field ahead of the tip of a crack).

2.3 Mechanically-Induced Transformations

The macroscopic deformation associated with phase transformations under applied stress has been termed *transformation plasticity.* Transformation plasticity occurs not only during martensitic transformations, but has also been observed in diffusional allotropic transformations and precipitation reactions, such as the carbide precipitation during the tempering of steels [42–47]. Even biological structures with crystalline arrays of molecules have been observed to display transformation plasticity [48].

The transformation plasticity that accompanies martensitic transformations in the presence of an applied stress provides substantial alteration of the mechanical properties of the material. This unique process allows for the design of materials which take advantage of the transformation *itself*, not simply the properties of the transformation product. The notion of exploiting the properties of such a structural change is quite novel with respect to the classical view of the relationships between a material's structure and its properties.

When transformation plasticity is accompanied by an accommodating slip, as it is in the strain-induced regime, the transformation is irreversible or *non-thermoelastic.* If there is no slip, then the transformation is reversible, or *thermoelastic.* The unique

properties of thermoelastic martensitic transformations have been utilized to produce the so-called *shape memory effect*, where a reversal of transformation plasticity occurs upon heating, allowing martensite to transform back into austenite at the new temperature. The remarkable consequence of this reversibility, first discovered by Kurdjamov [49], is that, after being deformed by means of transformation plasticity at one temperature, the *original shape* of the material is recovered upon being heated to a second temperature. The two temperatures can be controlled by the alloy composition. In recent years, a wide body of research has been devoted to taking practical advantage of this phenomenon. At least one such family of alloys, Nitinol (Nickel-Titanium), has found several technical applications, ranging from pipe fittings that are installed at low temperature, and shrink to fit when heated to the working temperature, to space antennas that unfold when deployed [50].

The focus in this thesis, however, will be on non-thermoelastic transformations leading to transformation toughening. In the following section, we review certain aspects of the kinetic models that have been developed for non-thermoelastic transformations.

2.3.1 Kinetic Models

Stress-assisted Nucleation

The kinetics of stress-assisted transformations have been modeled by simply adapting existing models for spontaneous transformation kinetics to take into account the thermodynamic effects of an applied stress [32]. Patel and Cohen [20] estimated the contribution of an applied stress by considering the work done by this stress acting during the transformation strain. Let ΔG represent the driving force for transformation. Patel and Cohen suggested that the kinetics of stress-assisted transformation could be treated by adding the mechanical contribution to the transformation driving force, ΔG^{σ}, to the chemical contribution to the driving force, ΔG^{ch}:

$$\Delta G = \Delta G^{ch} + \Delta G^{\sigma}. \tag{2.1}$$

For an invariant-plane shape strain with shear and normal components γ_s and ϵ_n and corresponding resolved stresses τ_s and σ_n, the work done per unit volume during the transformation (the mechanical contribution to the driving force) is given by:

$$W \equiv \Delta G^{\sigma} = \tau_s \gamma_s + \sigma_n \epsilon_n. \tag{2.2}$$

Fig. 2.5 shows, in terms of Mohr's circle diagrams, how this extra contribution to the driving force varies for a few different stress states. Expressions (2.1) and (2.2) are in reasonable agreement with the linear portion of the curve given in Fig. 2.3 [32, 51]: as the chemical driving force, ΔG^{ch}, decreases with temperature (roughly linearly, due to the entropy term), a correspondent (linear) increase in ΔG^{σ}, and thus in stress, is required in order to maintain the same level of driving force for transformation.

At temperatures in the stress-assisted regime (well below M_s^{σ}), where kinetics are not affected by slip in the parent phase, experimental data for volume fraction martensite formed, f, versus uniaxial tensile plastic strain, ϵ, also show linear behavior:

$$f = k\epsilon\,, \tag{2.3}$$

where k is a proportionality factor, and $k^{-1} = d\epsilon/df$ can be regarded as a measure of the average transformation strain per unit transformed volume. Stress-strain data measured in the stress-assisted temperature regime suggest that k is a stress-dependent quantity [14]. The linear relationship between f and ϵ implied by eq. (2.3) is consistent with the suggested work contribution term given by eq. (2.2).

Strain-induced Nucleation

In the strain-induced temperature regime, transformation kinetics are more complex due to the interaction of slip in the parent austenite phase with the transformation process. A one-dimensional quantitative model for transformation kinetics in this regime was developed by Olson and Cohen [20], based on the assumption that intersections of shear-bands created by slip constitute the primary strain-induced nucleation sites (see Fig. 2.6). Their model was designed to predict martensite evolution in one-dimensional stress states (namely uniaxial tension), and as such, does

not explicitly account for the effect of stress state on the nucleation process. It yields sigmoidal $f - \epsilon$ curves which are in excellent agreement with existing experimental data, including the uniaxial tensile data of Angel [53], obtained over a wide range of test temperatures for an annealed type 304 stainless steel (Fig. 2.7). We utilize the Olson-Cohen model in this thesis as the foundation of our more complex kinetics model, which does account for stress-state effects; a complete description of the detailed model is given in section 3.3.

2.3.2 Constitutive Flow Relations

Stress-assisted Nucleation

Models for flow behavior in the stress-assisted temperature regime, where plastic flow is controlled by transformation kinetics, are based on accounting for the operation of the transformation as a deformation mechanism. Olson and Cohen [51] developed one-dimensional constitutive relations predicting flow stress, σ as a function of temperature, strain, strain rate and stress state, given by

$$\begin{aligned} \sigma &= \hat{\sigma}(\sigma, f, \dot{f}) \\ &= \left(\frac{-B}{\partial \Delta G^{\sigma}/\partial \sigma}\right)\left\{\left(A + B\Delta G^{ch} + RT\right) ln\left[\frac{\dot{f}}{(n_i + p_a f - N_v)(1-f)v_\nu}\right]\right\}, \end{aligned} \tag{2.4}$$

which, using (2.2), yields $\sigma = \hat{\sigma}(\sigma, \epsilon, \dot{\epsilon})$. Here A and B are constants, R is the gas factor, n_i is the initial density of nucleation sites, p_a is an autocatalytic factor accounting for new nucleation sites created during transformation, N_v is the number of martensitic plates per unit volume, V is the instantaneous mean plate volume and ν is the nucleation attempt frequency. This expression produces the fit to experimental stress-strain data for a high strength metastable austenitic steel shown in Fig. 2.8. As indicated in the figure, the model flow curve shown here fits the transformation softening behavior well, but produces a much sharper upturn than the experimental curve. Olson [29] attributed the error between model and experimental curves at high strain levels to the assumption of a single activated nucleation process involving *the most favorably oriented* martensite nucleus as assumed in the Patel-Cohen model (see eq. 2.2). More recently, Olson, *et al.* [39], have produced better fits to experimental

data using constitutive equations based on statistical models of martensite nucleation accounting for the *distribution* of plate orientations.

Strain-induced Nucleation

Models for flow behavior in the strain-induced regime are not as well defined, again because of the complicated nature of the interactions between stress, strain, and transformation kinetics. A simple model was proposed by Narutani, *et al.* [20], which, along with the Olson-Cohen model for transformation kinetics, formed the basis for the preliminary Master's thesis work. Its principal feature is the use of a Voigt upper bound approach in which the incremental and total strain in both phases are assumed equal. Due to the typically large difference in strength between martensite and austenite, this model, unaugmented, significantly overestimates the plastic stiffness, and does not correctly predict the strain levels in the individual phases. This upper bound estimate is then scaled to match experimental data by subtracting a "dynamic softening" factor proportional to the rate of martensite formation. In addition, in calculating the respective phase contributions to the total flow stress, a "shape strain" contribution to the total strain is subtracted because it does not directly contribute to the strain-hardening of either phase. The functional form used in this model yields reasonable agreement with experimental data from uniaxial tension tests, as shown in Fig. 2.9, but, in our experience, leads to numerical problems when introduced into computer codes for study of boundary value problems. With pressure sensitivity of transformation incorporated into the model, triaxiality gradients can lead to tremendous local changes in the rate of martensite formation — and thus to large changes in flow stress as a result of this dynamic softening term.

2.4 Transformation Toughening

2.4.1 Stress-assisted Temperature Range

At temperatures below M_s^σ, the two-phase transformation product material is inclined to be brittle, as coarse martensitic plates tend to fail by cleavage. For this

reason, stress-assisted transformations in metallic systems typically do not produce particularly tough materials. On the other hand, in ceramic systems, deformation-induced transformation of dispersed metastable zirconia (ZrO_2) particles have lead to significant increases in fracture toughness at temperatures where stress-assisted nucleation is observed [54]. The process of toughening in ceramics now seems to be well understood. The volume change accompanying the transformation relaxes local stresses, acting to shield the crack tip from the applied far-field stress, thereby reducing the stress-intensity factor [55]. As the crack advances, a transformation "wake" forms above and below the crack, which, in effect, acts to clamp the crack shut [3, 56] (see Fig. 2.10). Ductile second-phase particles, such as aluminum, have been added in other instances to further increase toughness.

2.4.2 Strain-induced Temperature Range

Returning our attention to steels, the enhancement of ductility and toughness by means of transformation plasticity in the strain-induced regime is well established. In the late 1960's, Zackay, *et al.* [57] found that transformation plasticity in the strain-induced temperature regime suppressed tensile necking in low-carbon metastable austenitic steels by means of the strain-hardening accompanying the gradual transformation to the much harder martensite phase. This process resulted in high ultimate tensile strength (UTS) and uniform ductility (187 ksi [1290 MPa] UTS with 75% elongation and 312 ksi [2150 MPa] UTS with 22% elongation) for this class of metastable austenitic steels exhibiting strain-induced transformation, which were termed TRIP (TRansformation-Induced Plasticity) steels. These results generated a wide body of research in the late 1960's and early 1970's concerning ductility and toughness of TRIP steels.

The more interesting aspects of toughening lies in the ability to retard fracture. The same alloys that showed such promise in the early tensile tests did not behave as well in fracture toughness tests. Significant toughness enhancements were measured in lower strength alloys [58]. Results for higher strength alloys were not quite as impressive. Antolovich and Singh [59] did report K_{Ic} fracture toughness increments

(with respect to nontransforming values) ranging from 37 to 57 ksi $\sqrt{\text{in}}$ (41 to 63 MPa$\sqrt{\text{m}}$) for a high strength (UTS = 250 ksi [1700 MPa]) alloy. Antolovich and Singh proposed a model accounting for the toughness increment due to transformation based which was based on the energy dissipated by the transformation shape strain. They found that their model predictions correlated well with their experimental data, despite the fact that transformation volume change, to which the toughness increment in ceramic systems has since been attributed, was not considered in their analysis.

These relatively small increases in toughness were not great enough to compensate for several problems inherent to these steels that severely limited their practical application. They required a significant amount of difficult processing and used large amounts of expensive alloying metals such as chromium [60]. In addition, the transformation process during uniform tensile deformation was found to be quite sensitive to the rate of deformation — high strain rates retard transformation [31,61]. This unfortunate consequence can be attributed, in part, to local adiabatic heating produced by the high strain rates which raise the local temperature. Finally, the strain-induced temperature range ($M_d - M_s^\sigma$) was generally quite small for these alloys, greatly affected by the alloying process, and often too low relative to room temperature. Consequently, research on transformation toughening in metals slowed, and much of the attention gradually shifted toward transformation toughening in ceramics.

One reason why these early fracture toughness tests were not successful is that they were likely conducted at temperatures much too low relative to M_s^σ and M_d. In fact, they seem to have been carried out at the *same* temperatures for which the remarkable tensile properties were measured. However, because of the previously noted stress-state dependence of transformation kinetics, M_s^σ and M_d are much different in the crack tip stress field than in uniaxial tension. More specifically, because of the triaxial state of stress ahead of the crack tip, local M_s^σ and M_d temperatures increase, and the kinetics and morphology of stress-assisted nucleation often take over, resulting in brittle modes of fracture. Antolovich and Singh [59], for example, reported that the fracture modes in their experiments were indeed brittle, and plate martensite was clearly evident in their micrographs. Thus, the crack tip region was clearly governed

by the kinetics and morphology of stress-assisted transformation, despite the fact that they were investigating strain-induced transformation toughening.

A renewed interest in TRIP steels as a means of achieving toughness in high strength materials was generated in 1984 by the work of Leal [6], who measured extremely high fracture toughness values for certain high strength ($Y \approx 1300$ MPa) Ni-Cr alloys in tests *where ductile fracture modes were observed.* His measured fracture toughness results are summarized in Fig. 2.11. The toughness increments measured by Leal are much higher than those reported by Antolovich and Singh for equivalent strength TRIP steels. Moreover, the toughnesses shown in Fig. 2.11 are significantly higher than any steel of equivalent strength (recall Fig. 1.1). For each of the alloys Leal studied, maximum toughness was measured at test temperatures at or above the estimated M_d temperature for uniaxial tension. Unfortunately, the stability of these alloys was such that both the M_s^σ and M_d temperatures were quite low relative to room temperature, and thus were difficult to pinpoint experimentally, so that a quantitative experimental assessment of the optimal temperature for peak toughness could not be made.

The next comprehensive data set regarding transformation toughening of high strength austenitic steels was produced by Young [7], who conducted tests on a 0.5Mn-overaged alloy, phosphocarbide-strengthened to 1300 MPa tensile yield strength. Precipitate strengthening was chosen here as a means of achieving high strength, because warm-working, the other predominant strengthening mechanism, limits the commercial application of the material. The emphasis of Young's work was toward a better characterization of the parameters which affect toughness in high strength steels, for which available data is sparse compared with that for lower strength alloys. Young studied the effects of aging on the stability of the austenite, conducted tests in both tension and compression to better characterize the stress-state dependence of transformation kinetics, and varied the alloy content in order to correlate fracture toughness with transformation volume change and with the hardness difference between martensite and austenite. He found that there is indeed a strong correlation between toughness and volume change, as indicated in Fig. 2.12. Young also found that in-

creased martensite/austenite hardness difference enhanced toughness (also shown in Fig. 2.12), but to a lesser degree. An important question which must be answered is whether the beneficial effects of positive transformation volume change are due directly to the mechanical effects of plastic dilatation on the failure process, or indirectly related through the positive correlation of volume change with the pressure-sensitivity of transformation kinetics. Since dilatation is normally a destabilizing effect, the latter notion seems more plausible. Previous investigators (*e.g.*, [59]) have speculated that transformation dilatation leads to relaxed stresses in much the same manner that it does during stress-assisted transformations in ceramics, by dissipating energy that would otherwise be available for crack advance. Closer scrutiny of this notion reveals that the volume change is likely easily elastically accommodated; preliminary results obtained in [13] in fact showed little, if any, direct effects from transformation volume change.

Taking advantage of the improved knowledge of the stress-state dependence of transformation plasticity and improved alloying techniques, Stavehaug [1] recently completed a fracture toughness study where the goal was to produce a high strength, high fracture toughness alloy that exhibits peak toughness *at room temperature*. Using a γ'-strengthened A286 steel with tensile yield strength of 1300 MPa as a baseline, he then added chromium to increase the width of the $M_d - M_s^\sigma$ temperature band. He developed two series of alloys: a 4% chromium series with 24%, 25% and 28% Ni, and a 12% chromium series with 17%, 19%, 21% and 23% nickel. The 12% chromium series was chosen for the practical reasons that the resultant alloy is not only stainless, but requires a smaller amount of nickel, a costly alloying element. Stavehaug performed tensile tests and three-point bending fracture toughness tests, all at room temperature, as summarized in Fig. 2.13. The fracture specimens were all fatigue-pre-cracked at high temperature so as to avoid premature formation of martensite, as Leal [6] observed. Pre-cracking was also conducted in a vacuum, in order to avoid crack-branching. He chose the several weight percents of nickel hoping to bracket peak toughness. He found, however, that peak toughness values were reached at the ends of each series, as evident in the figure, so that higher toughness

values are possible for this combination of alloys. Stavehaug's experimental results relating to fracture are discussed in more detail later in the thesis.

Strain-induced transformation toughening has also been demonstrated in titanium alloys [62]. Here a retained metastable β-phase transforms into an orthorhombic martensite α''-phase. Fig. 2.14 shows data taken from both static and dynamic fracture toughness tests conducted on a Ti-6Al-4V alloy [62]. The high toughnesses reported here for the dynamic tests are especially encouraging in light of the noted difficulties caused by high strain rates.

2.5 Mechanical Features of Transformation Toughening

In this final section of background information, we review some of the mechanical issues which must be considered in assessing the mechanisms of transformation toughening. In particular, we review the processes of fracture in high strength steels, and then discuss a simple, but nevertheless critical, consequence of the unique stress-strain behavior of transforming steels, which we believe lends insight into the effects of transformation with regard to ductility on a macroscopic scale and with regard to fracture toughness on a microscopic scale.

2.5.1 Fracture Mechanisms in High Strength Steels

The term *toughness* is used to describe the ability of a material to absorb energy prior to and during fracture. The terms *brittle* and *ductile* are further used to distinguish between materials and fracture modes which, on a macroscopic scale, exhibit low toughness and high toughness, respectively. On a microscopic scale, the most brittle fracture mechanism is *cleavage*, wherein fracture occurs by separation along crystallographic planes across which atomic bonds have been broken. Fracture surfaces are flat and shiny, indicating smooth planar separation. In contrast with the fine, "needle" martensite produced through strain-induced transformation, plate martensite tends to behave in a brittle fashion; in the stress-assisted temperature range, as noted, fracture occurs by cleavage within the thick martensite plates. The mechanism of ductile

fracture involves nucleation, growth, and coalescence of voids which form around particles or inclusions present in the matrix material. Smaller particles are generally in the form of a second phase, purposefully put into the matrix to refine grain size (*e.g.*, as in the precipitation-strengthened materials of Leal [6], Young [7] and Stavehaug [1]). Larger particles are usually in the form of impurities which remain in the matrix after processing. Fracture by void nucleation, growth and coalescence is regarded as the predominant mechanism of fracture in ductile metals. The transforming steels which demonstrate high fracture toughness in the strain-induced temperature range exhibit this latter mode of fracture.

Although it is generally agreed that nucleation of voids around particles is an important part of the fracture process, the critical conditions for nucleation are not yet entirely clear. Nucleation occurs in one of two ways: cracking of the particle or decohesion of the particle/matrix interface. Nucleation of voids around equiaxed particles such as Fe_3C (iron carbide) is generally observed to occur by decohesion of the particle-matrix interface [63]. The necessary conditions for debonding include reaching a critical energy level for formation of a new surface, and reaching a critical value of either the interfacial tractions or the matrix strain at the interface. For particles greater than 250Å in diameter, such as the $0.1\mu m$ to $0.3\mu m$ alloy carbides often found in TRIP steels, the energy criterion is always satisfied [64]. There is still debate over the second necessary condition for nucleation of voids at large equiaxed particles. Although a majority of investigators (*e.g*, [65]), agree that nucleation occurs when a critical level of the interfacial normal traction is reached, others [66] argue that reaching a critical matrix strain at the interface induces nucleation or that some combination of interfacial traction and strain might be the key parameter [67].

Experimental data from tension tests suggest that the nucleation event starts near the pole axis of the particle, *i.e.*, the axis of applied stress (*e.g.*, [68]). This evidence would seem to preclude the possibility of a strictly strain-controlled event, because peak interfacial strains are generally found at 45^o away from the pole. Peak interfacial normal tractions, on the other hand, occur near the pole, and thus a stress-controlled nucleation event seems much more likely. A critical combination of traction and strain

remains possible given this nucleation scenario, since a parameter of this sort would peak somewhere between the pole and the 45^0 line. The precise location of the initial debond is still unclear and may, in fact, be different for different materials.

Voids generally nucleate around larger particles first (*e.g.*, [69]). In relatively low strength, low purity materials containing a large volume percentage (2–4%) of large particles (mean particle radius between about 0.1 μm and 10 μm), a significant amount of porosity develops prior to localization and fracture. Fracture is governed by growth and coalescence of the voids. At the tip of a crack, rupture occurs by eventual interaction of the coalescence process with the surface of the crack (see Fig. 2.15). In clean, high strength steels with a low volume percentage (0.01 – 0.1%) of small particles (mean particle radius less than 0.1 μm) fracture occurs by a process of "zig-zagging", or ridge formation on a fine scale above and below the fracture surface [71] (see Fig. 2.16). Here fracture may be predicated on a nucleation criterion rather than a growth criterion. Rogers [10] first noted periodic ridge markings in tensile specimens of OFHC copper. Van den Avyle [71] showed that the zig-zags follow paths of highly localized local shear strain at directions $\pm 45°$ to the macroscopic fracture surface. Within the highly localized region (void sheets) microvoids form around the smaller particles. Van den Ayvle attributed the zig-zag pattern to be a result of the combined effect of strain and triaxiality. The localized path of deformation follows the direction of highest combined strain and triaxiality. At a certain point, the combination of strain and triaxiality in the path direction becomes too small, and the optimal direction, in terms of these two parameters, becomes the path at right angles to the original path following the macroscopic propagation direction. This process has been observed in a wide variety of high strength, high purity materials, including OFHC copper, 200 grade maraging steels, 4340 steels, titanium, aluminum and cobalt series alloys [72]. In the absence of transformation, the metastable austenitic steels considered in our studies also exhibit this fracture mode [1]. With transformation, the fracture mode can be much different, as evidenced by the micrograph shown in Fig. 2.17, taken from the crack-tip region of Stavehaug's 12Cr-17Ni three point bend specimen just after crack advance. This micrograph shows a much more diffuse

fracture process, with a tremendous amount of crack tip blunting as well as crack branching.

Void nucleation not only leads to failure, but it also reduces the macroscopic strain-hardening capacity of the steel. The shedding of the load carried by nucleated particles results in a redistribution of stress and strain within the matrix, altering its stress-strain response in a deleterious fashion. There is evidence [23] that shear localization can occur almost simultaneously with the onset of void nucleation. An obvious and, we believe, critical consequence of martensitic transformation is that the extra strain-hardening brought about by martensite formation can counteract the strain-softening of void nucleation and growth, resulting in retardation of localization to higher levels of strain and altering the onset and the subsequent direction of localized flow. This notion is discussed in further detail in section 3.6.2.

Mechanical analysis reveals that the triaxiality of the state of stress has a strong effect on void nucleation, because negative pressure adds directly to the peak normal tractions at the matrix-particle interface (see section 4.3). The observed pressure-dependence of shear localization supports this mechanical evidence. On the other hand, the experimental findings of Cox and Low [68] show little or no evidence of triaxiality dependence. This lack of *direct* experimental evidence of the triaxiality-dependence of nucleation may be the result of the difficulty of capturing the nucleation phenomenon experimentally. Furthermore, MnS inclusions of the sort present in the 4340 alloy studied in [68] are generally poorly bonded, thus the alloy likely behaved as if cavities were present to begin with.

Numerous investigations, *e.g.* [15–19], have further shown that triaxiality plays a critical role in determining the rate of growth of voids. Within this context, it is both interesting and important to note that *the mechanical features which promote void growth, namely high strain and triaxiality, are precisely the same features that promote nucleation of martensite.*

In assessing the toughening effect of strain-induced transformations, one must consider how the transformation interacts with these fracture processes, *i.e.*, how the transformation alters the stress and strain fields which interact with the microstruc-

ture of the material. Within this context, the critical question that must be addressed, from the viewpoint of continuum mechanics modeling, is whether the transformation does indeed retard the nucleation and associated localization that leads to failure in these steels.

With these microscopic features of fracture in mind, we end this chapter with a short discussion demonstrating how the unique stress-strain behavior of these steels is close to ideal with respect to retarding flow localization from a continuum, macroscopic viewpoint and offering qualitative insight into the microscopic behavior of these materials.

2.5.2 The Stability of Plastic Flow

The enhancement of ductility observed in the early experiments on TRIP steels can be attributed to the curve-shaping of strain-induced transformation. As is evident in Fig. 1.2, the tremendous strain-hardening which accompanies formation of the much harder martensite phase leads to stress-strain curves which have an unusual "S"-shape. This unique shape turns out to be beneficial for producing large uniform ductility and represents perhaps the most potentially beneficial effect of martensitic transformations in the strain-induced regime. As reviewed by Olson in [31], and discussed at length in [13], this S-shape leads to prolonged stabilization of plastic flow. Here, we review a few aspects of the aforementioned discussion, which we feel lend critical insight into the nature of the toughening mechanism.

Consider a one-dimensional (uniaxial) tension test in which a load P is applied to a bar of length l and cross-sectional area A, resulting in a uniform axial stress σ. Backofen [72], consistent with the ideas of Considère, suggested that in a one-dimensional framework, loss of stability during tensile plastic loading occurs when the point of maximum tensile load is reached. Assuming that the load increases until it reaches some peak and then drops off, as is generally observed, then at the point of maximum load, $dP = d(\sigma A) = 0$, so that:

$$\sigma dA + A d\sigma = 0, \tag{2.5}$$

or

$$\sigma = \frac{d\sigma}{\frac{-dA}{A}}. \tag{2.6}$$

If elastic and plastic volume changes are neglected, then $A \cdot l$ is constant during plastic flow, so that:

$$ldA + Adl = 0 \implies \frac{-dA}{A} = \frac{dl}{l} = d\epsilon. \tag{2.7}$$

Restricting attention to rate-independent materials, let the hardening rate, h, be defined as the slope of the stress-strain curve; *i.e.*, $h = d\sigma/d\epsilon$. Then substituting for $-dA/A$ in (2.6) yields a relationship for the minimum strain hardening rate necessary to maintain "stable" plastic flow:

$$h \equiv \frac{d\sigma}{d\epsilon} = \sigma. \tag{2.8}$$

Use of the term stability is restricted here to the one-dimensional meaning of the term, as implied by Considère and defined in (2.6), which suggests that stability is lost at the maximum tensile load. Other, more sophisticated measures of stability, such as those suggested by Needleman and Rice [23], exist and are briefly discussed later in this section. Careful studies of bifurcation in tensile tests, however, suggest that the point of bifurcation, or loss of stability, is generally just a little beyond the point of maximum load [73].

One consequence of strain hardening is that, as the material hardens, the strain-hardening rate must increase in order for plastic flow to remain stable. Thus, stability becomes more and more difficult to maintain with increasing strain. For a typical power-law material, which assumes the following stress-strain relationship:

$$\sigma = \sigma_0 \left(\frac{\epsilon}{\epsilon_0}\right)^N, \tag{2.9}$$

where σ_0 and ϵ_0 are reference stress and strain, stable flow cannot be maintained past a few percent, as demonstrated in Fig. 2.17 for a power-law material with a strain hardening exponent $N = 0.1$. In fact, for power-law-hardening materials, it can easily be shown that ϵ_u, the true strain at which h decreases below σ, is equal to N. Thus, in this example, as this figure illustrates, the intersection of the flow stress and strain-hardening curves is reached at a strain $\epsilon_u = 0.1$.

For steels which undergo strain-induced transformations, however, the dramatic strain-hardening resulting from transformation delays the final loss of stability to much higher strain levels, as illustrated in Fig. 2.18. In this figure, the hardening curve dips below the flow stress curve at a relatively low strain, ϵ_u, but as martensite continues to form, there is a recovery of stability which brings the level of hardening back above the flow stress at a higher strain, ϵ_L. A second instability point is not reached until a strain $\epsilon_{u'} \approx 0.32$.

In fact, for strains less than about 40%, the shape of the flow curves for transforming materials at certain temperatures within the strain-induced regime is very close to the "ideal" stress-strain curve for maintaining stability, given by the integration of (2.8):

$$\sigma = \sigma_0 exp(\epsilon) \; . \tag{2.10}$$

Fig. 2.19, which depicts the flow curve for this ideal case as well as for a transforming and a non-transforming, power-law material, demonstrates how the curve for the transforming material follows the ideal curve much more closely than the curve for the non-transforming material.

In order to provide a better picture of how the degree of tensile stability changes with strain, the parameter h/σ has been plotted for several values of Θ in Fig. 2.20. (The parameter Θ represents a normalized temperature in the strain-induced regime — $\Theta = 0$ at $M^{\sigma}_{s,ut}$; $\Theta = 1$ at $M_{d,ut}$ [see section 3.2].) Within our one-dimensional framework, stability of plastic flow is lost when h/σ decreases below unity. A non-transforming material ($\Theta = 1.0$) with a power-law exponent $N = 0.045$, behaves in the manner shown by the solid line. At low strains, its flow behavior is quite stable, but at a strain of $\epsilon_u = 0.045$, the $h/\sigma = 1$ line is crossed, indicating that stability is lost. At higher strains this material becomes increasingly unstable. TRIP steels exhibit markedly different behavior at certain temperatures within the strain-induced regime. Due to the unique shape of their stress-strain curves, these materials undergo a loss of stability at relatively low strains (even lower than for the power-law material). However, due to the hardening action of the transformation, a "restabilization" of flow occurs at ϵ_L and subsequent flow proceeds in a stable manner. Finally, these

materials undergo a second and final loss of stability at $\epsilon_{u'}$ as the saturation level of the transformation is reached, but not until the strains are much higher than when transformation does not take place. At higher temperatures in the strain-induced range ($\Theta > 0.6$), the effect of the transformation is not great enough to result in a recovery of stability. Experimental evidence, however, suggests that the increase in h/σ delays the onset of fracture even though restabilization never occurs [7,31]. This feature of the transformation is explored in some detail in chapter 4.

As previously noted, other, more sophisticated measures of stability, such as those suggested by Needleman and Rice in [23], account for the destabilizing effects of triaxiality and porosity evolution. Needleman and Rice, for example, offer the following formula for determining the critical hardening rate/stress ratio necessary for localization when porosity evolution is accounted for using a stress-controlled nucleation model:

$$\left(\frac{h}{\sigma}\right)_{crit} \approx \frac{1}{1 - K^{nucl}\cosh\left(\frac{3}{2}\Sigma\right)}\left\{\frac{3}{2}\rho\cosh\left(\frac{3}{2}\Sigma\right)\sinh\left(\frac{3}{2}\Sigma\right) + \frac{(1+\nu)\,K^{nucl}\sigma}{6\,(1-\nu)}\cosh\left(\frac{3}{2}\Sigma\right)\left[1+\frac{1}{6}EK^{nucl}\cosh\left(\frac{3}{2}\Sigma\right)\right]\right\}, \quad (2.11)$$

where ρ is the void volume fraction, $\Sigma = -p/\sigma$ (see section 3.2) is triaxiality, E is Young's modulus, ν is Poisson's ratio, and K^{nucl} is a parameter related to the void nucleation rate, which can be varied to fit this criterion to tensile fracture data. This equation yields critical hardening/stress ratios which are generally on the order of ρ, but increase with increasing triaxiality.

We do not wish to suggest here that localization of plastic flow occurs simply when $(h/\sigma)/(h/\sigma)_{crit} \leq 1$. Nevertheless, the simple notion that stability is lost at some critical value of $h/\bar{\sigma}$ can lead to a qualitative understanding of the tendencies for plastic flow to localize, and as such, is useful for interpreting results from finite element simulation of boundary value problems, in which there is an artificial numerical stability resisting localization, due to the discrete nature of the elements.

It is evident that the hardening which accompanies the transformation has a pronounced effect on the stability of the plastic flow process in this material. This could be significant in explaining the increase in fracture toughness of these materials,

especially since the onset of fracture in these relatively impurity-free low carbon materials is thought to be closely associated with the localization of plastic flow in the fracture area [31]. Moreover, localization conditions, such as those proposed by Needleman and Rice, are qualitatively similar to a local loss of Considère stability, since they also depend on the hardening rate reaching some criticallly small fraction of flow strength.

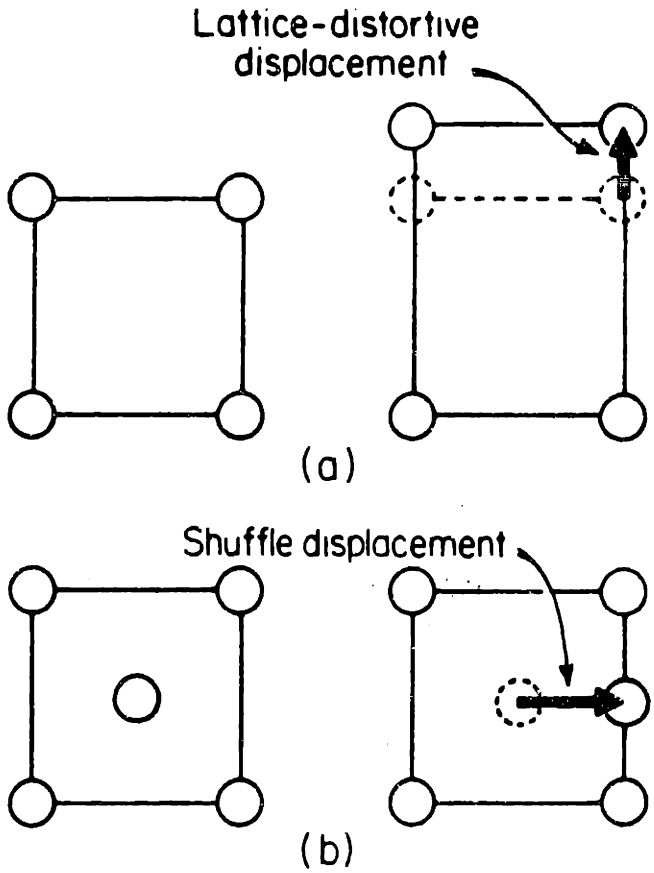

Figure 2.1 Schematic illustration of simple lattice distortive and shuffle displacements [26].

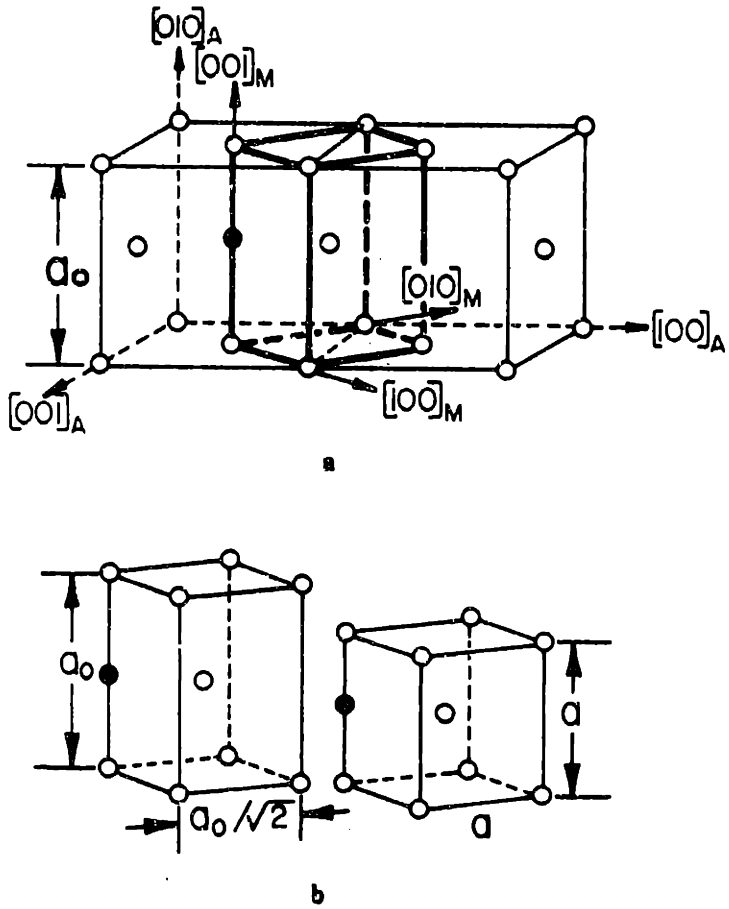

Figure 2.2 Lattice correpondence for the formation of martensite in steels: (a) bct cell of axial ratio 2 outlined in austenite structure of cell size a_0; (b) deformation carrying this structure into a martensite cell with parameter a (taken from [27]).

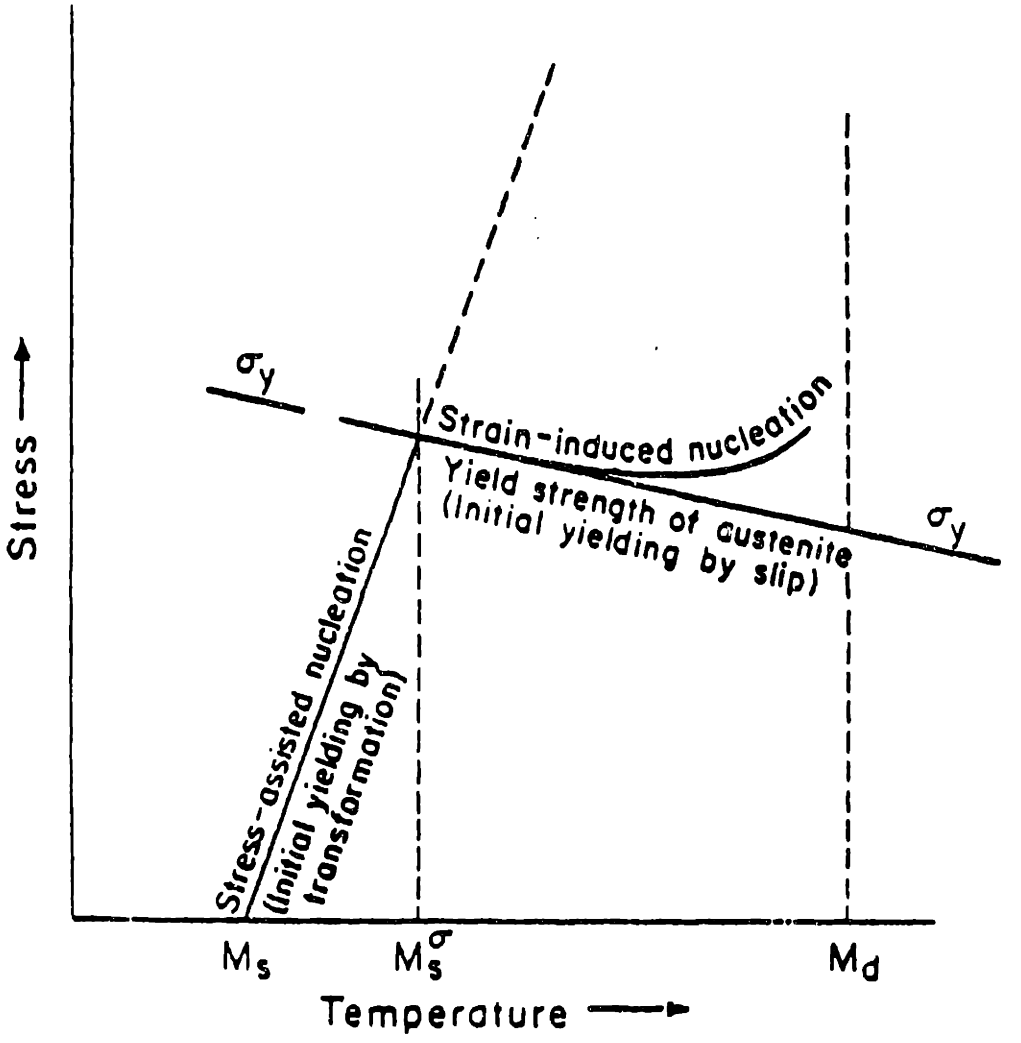

Figure 2.3 Schematic representation of the interrelationships between stress-assisted (below M_s^σ) and strain-induced (above M_s^σ) martensitic transformation [30].

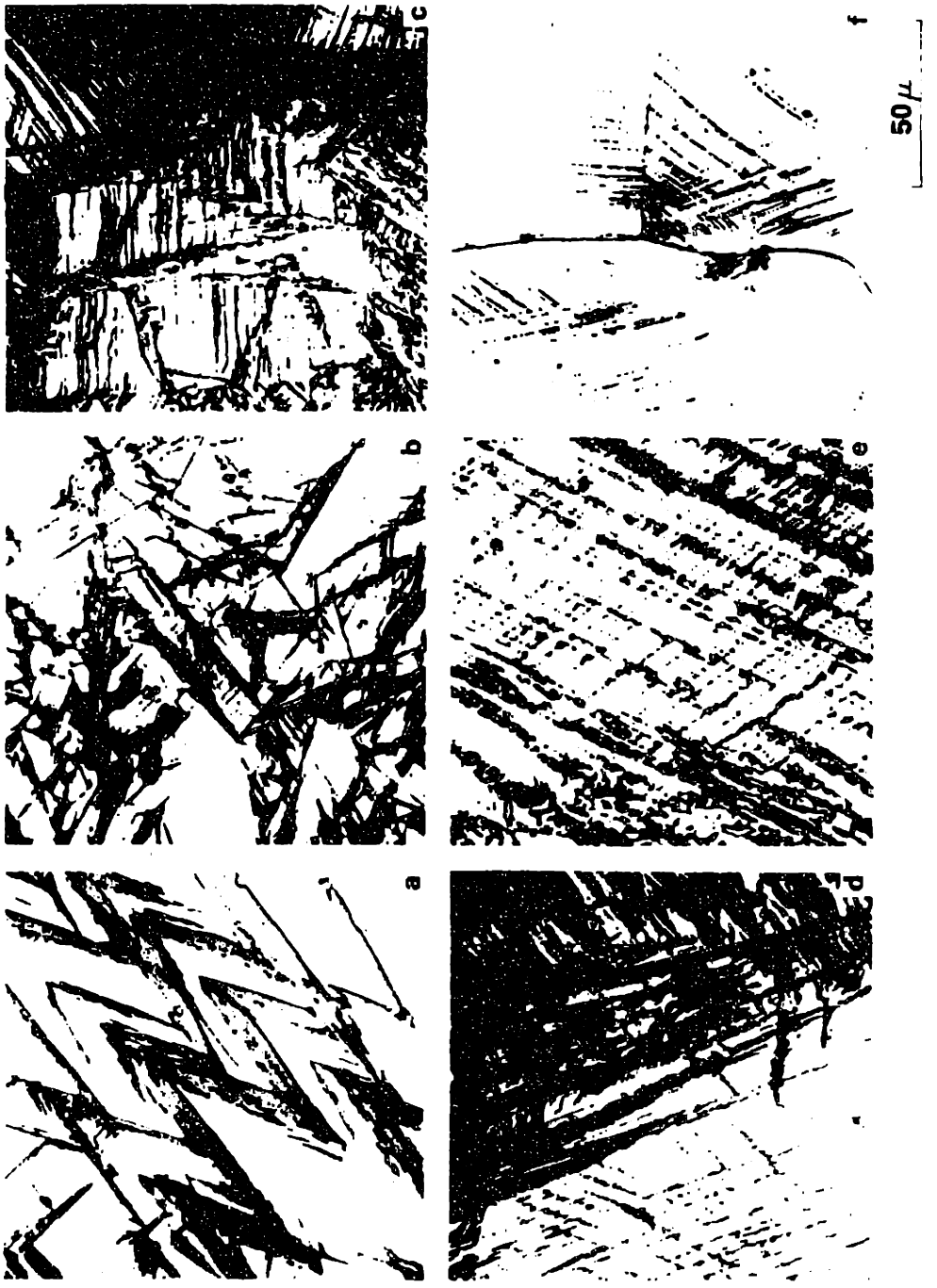

Figure 2.4 Morphology of martensites formed in 0.27C TRIP steel solution treated at 1200 °C. (a) Spontaneously formed martensite ($-196C$); (b) Stress-assisted martensite formed near M_s ($-196C$) (c) Stress-assisted martensite ($-128C$); (d) Stress-assisted martensite formed just below M_s^σ ($-75C$); (e) Stress-assisted and strain-induced martensite formed just above M_s^σ; ($-28C$); (f) Strain-induced martensite formed well above M_s^σ but well below M_d ($-175C$) [14].

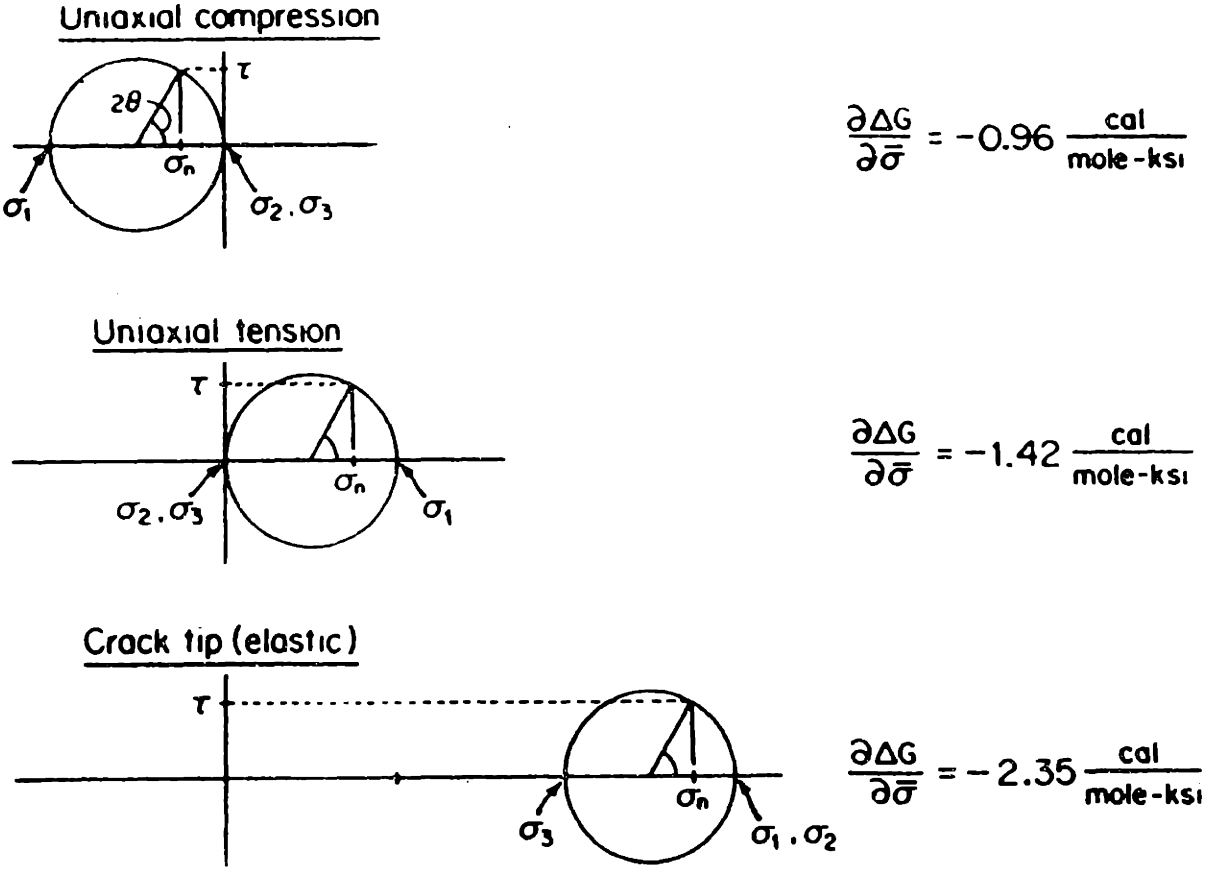

Figure 2.5 Mohr's circle diagrams and thermodynamic assist of applied stress for stress states corresponding to uniaxial compression, uniaxial tension and an elastic crack tip [31].

a

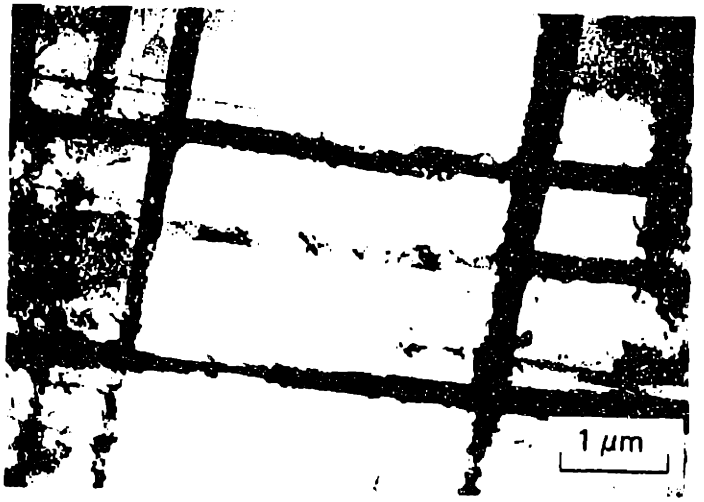

b

Figure 2.6 Nucleation of martensite in AISI 304. The intersections of needles with the plane of polish in (a) are seen as dark spots due to heavy etching. Transmission electron micrograph in (b) shows dark bands with martensite forming at the intersections. (taken from [52]).

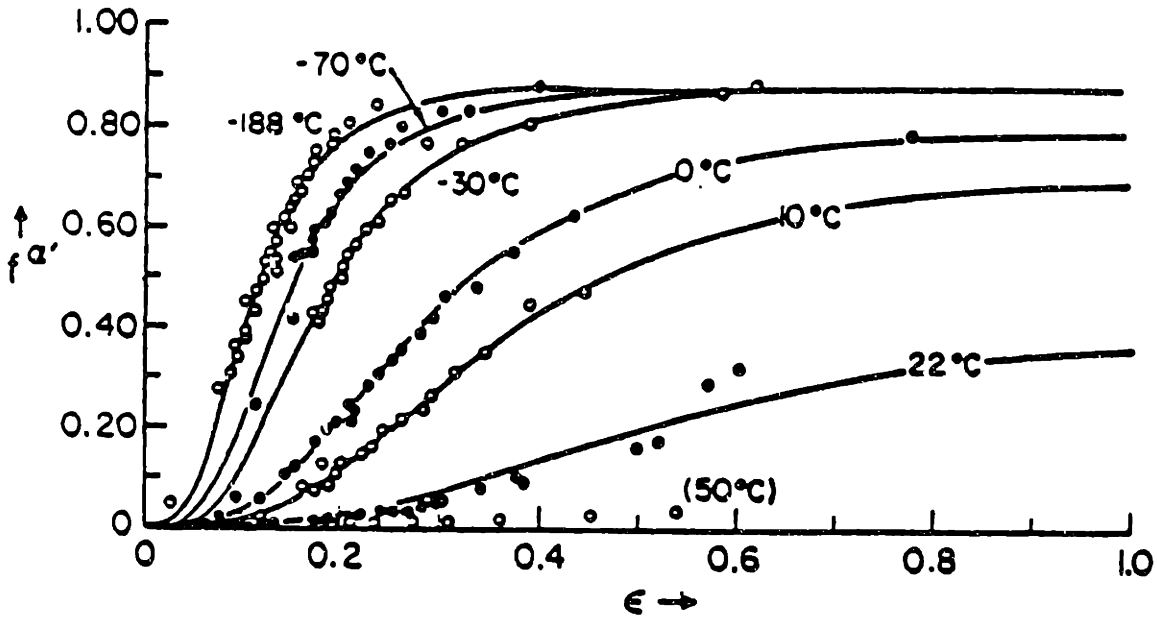

Figure 2.7 Comparison of calculated transformation curves with data of Angel [53] for a 304 stainless steel. Experimental data are indicated by points. The solid curves represent predictions obtained using the model of Olson and Cohen [20].

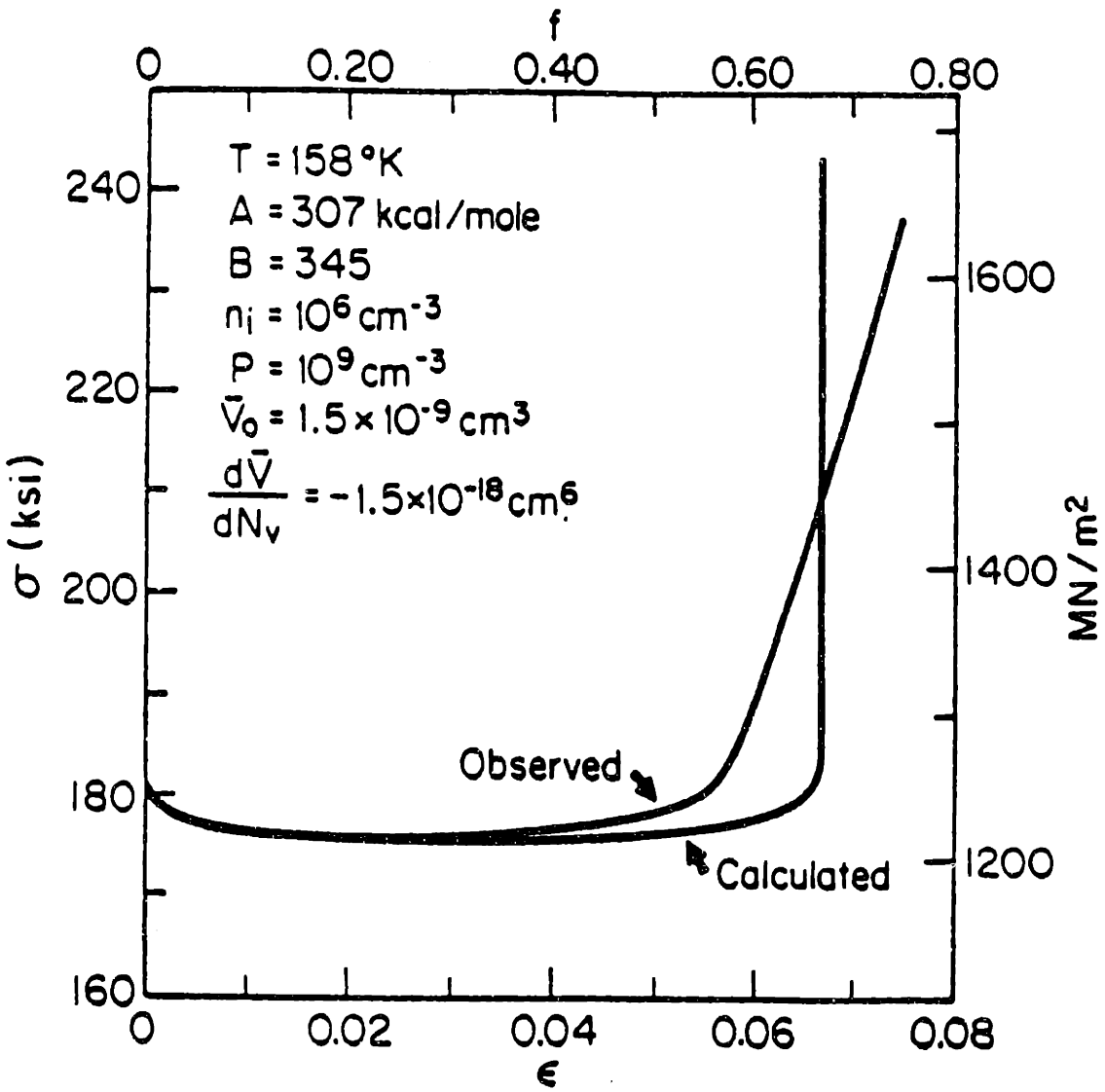

Figure 2.8 Comparison of model predictions obtained from eq. (2.4) with observed stress-strain behavior for a high strength metastable austenitic steel steel which exhibits stress-assisted nucleation (taken from [32]).

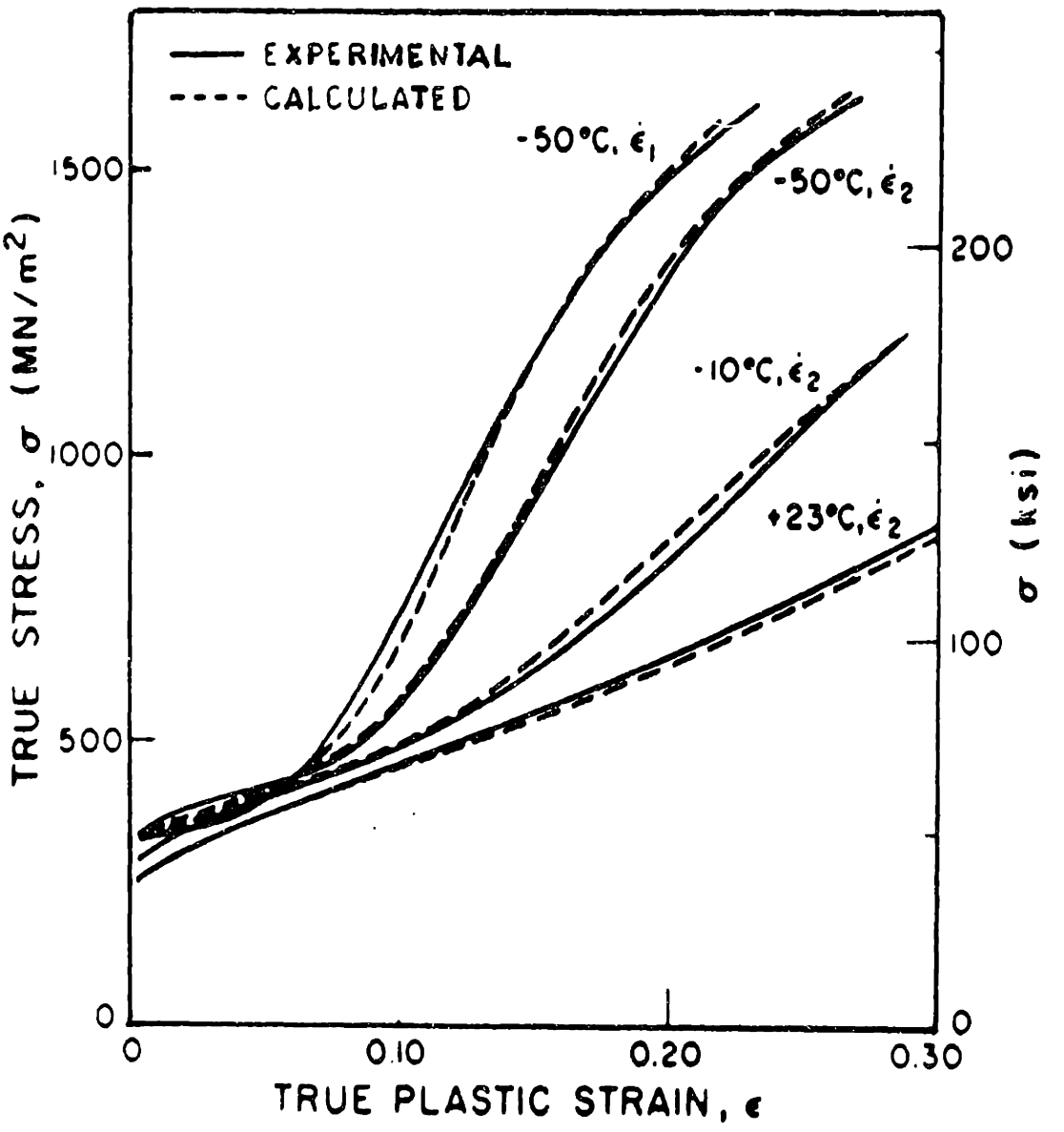

Figure 2.9 Comparison of observed and calculated stress strain curves for 14Ni-7Cr stainless steel studied by Narutani, *et al.* [21].

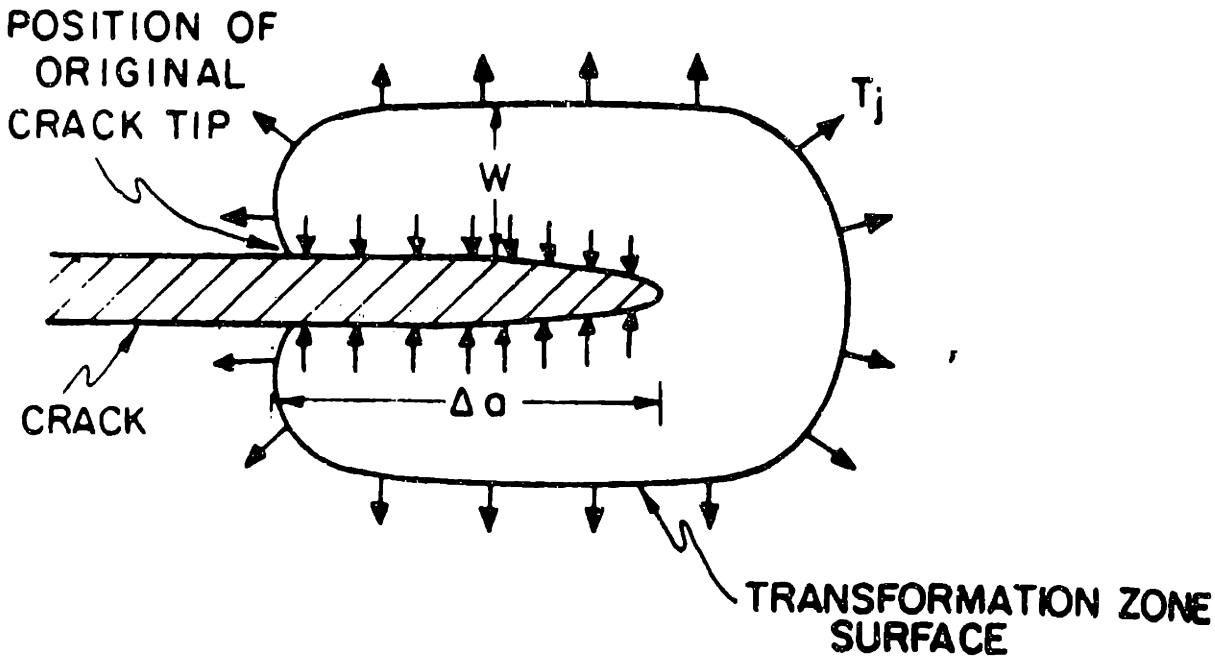

Figure 2.10 Schematic of a crack that has advanced into a prior transformation zone by ΔA; tractions at zone boundary and over crack surface are also shown (taken from [57]).

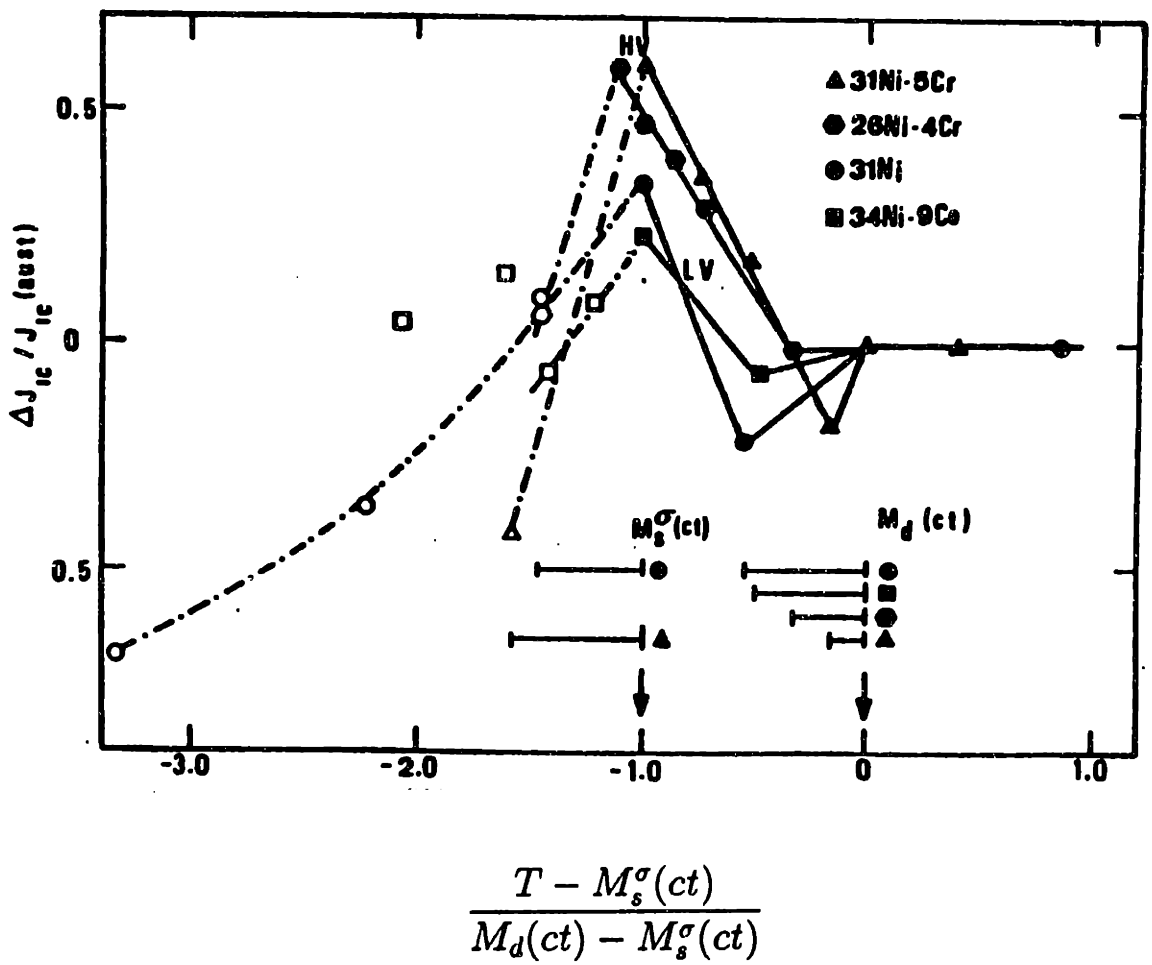

Figure 2.11 Relative enhancement of J-integral toughness versus normalized temperature for the γ'-strengthened metastable austenitic steels studied by Leal [5].

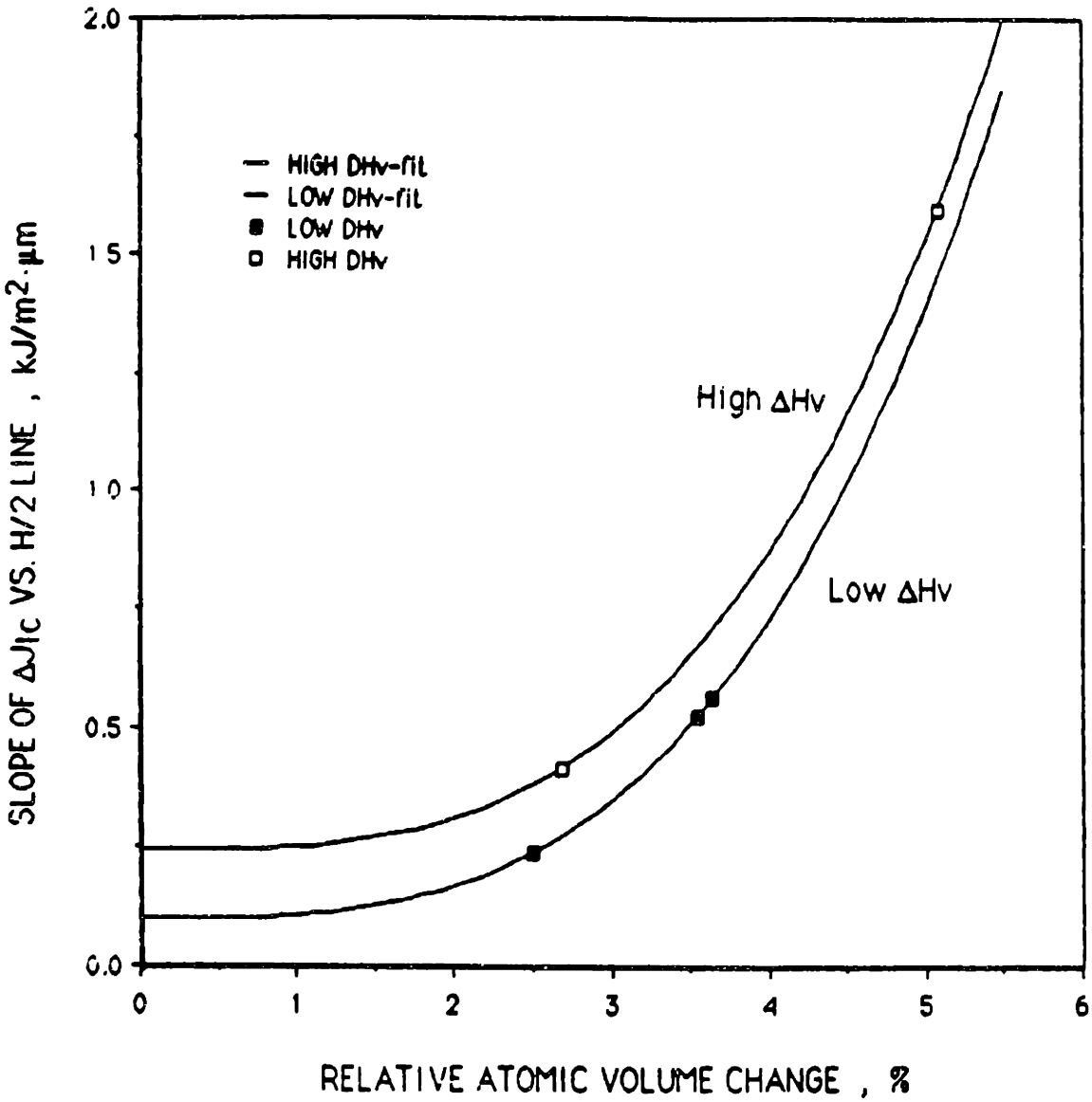

Figure 2.12 Slope of the line relating observed transformation zone half-height ($H/2$) with J_I increment, plotted versus transformation volume change for both high hardness difference (High ΔH_V) and low hardness difference (High ΔH_V) alloys, taken from [6]. The solid lines represent fits to power-law expressions.

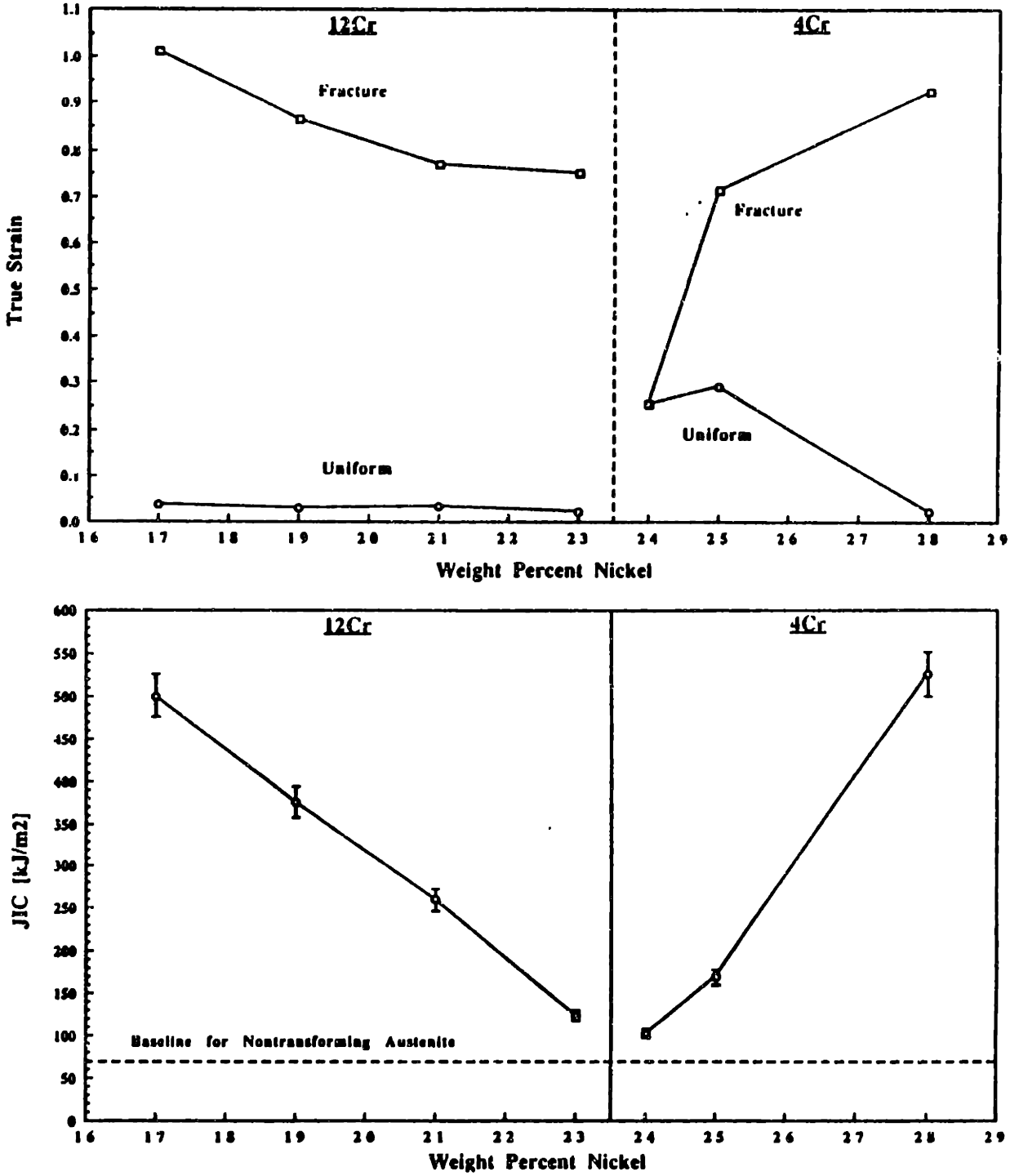

Figure 2.13 Measured uniform strain (above) and J_{Ic} fracture toughness (below), for each of the alloys in the 4% chromium and 12% chromiun. series studied by Stavehaug [7].

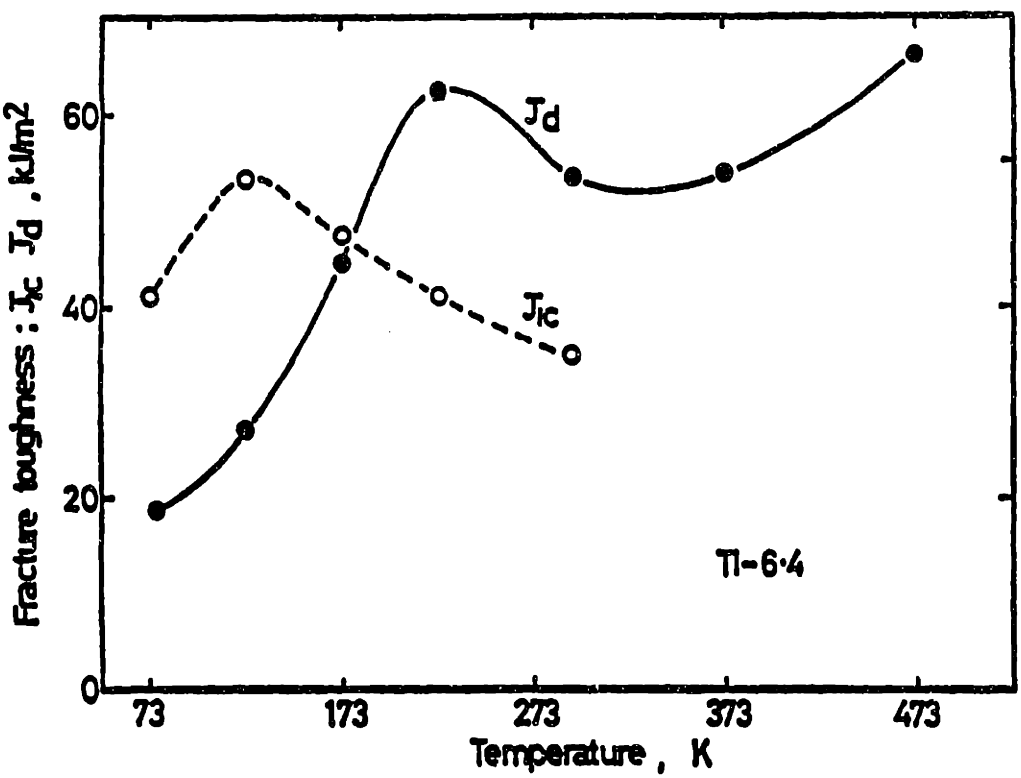

Figure 2.14 Relationship between test temperature and J_{Ic}, J_d (dynamic fracture toughness) for an as-quenched Ti-6Al-4V alloy [62], demonstrating the variation of toughness within the strain-induced temperature regime. M_s^σ and M_d temperatures were not given in [62].

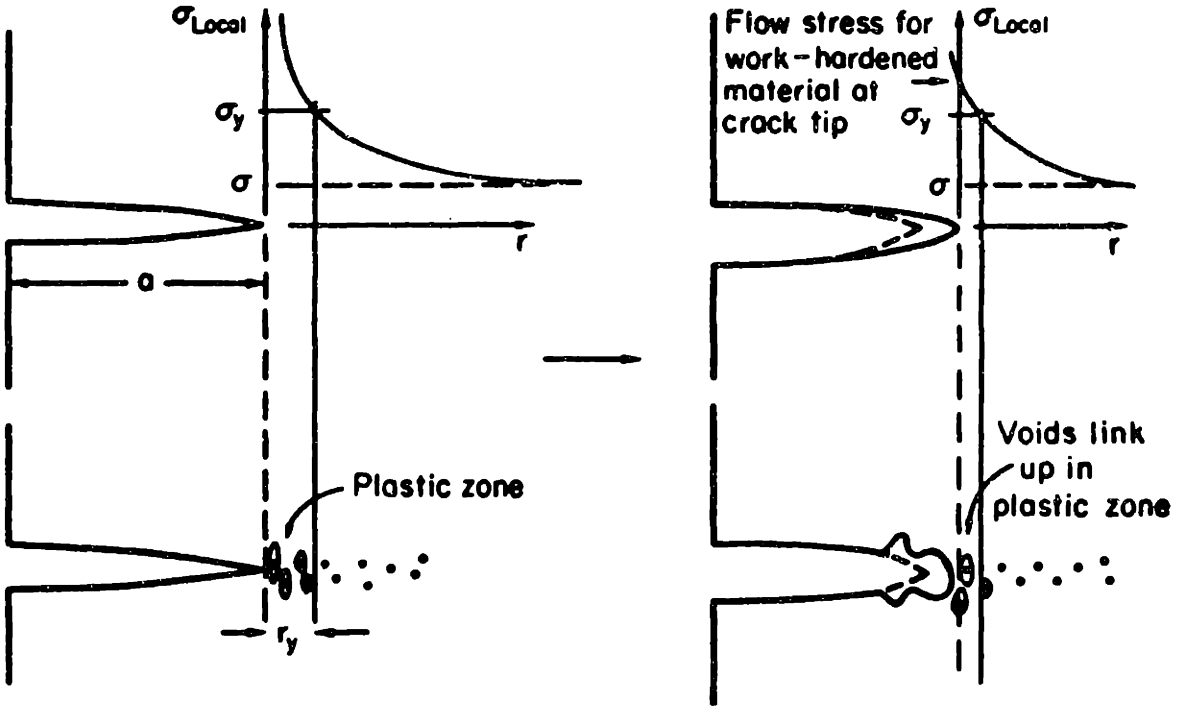

Figure 2.15 Schematic of ductile failure process, wherein voids ahead of the crack tip eventually link up and cause ductile tearing [70].

Figure 2.16 Crack-tip micrograph of a 4340 steel fracture toughness specimen studied by Van den Avyle [72], illustrating the characteristic zig-zag mode of fracture observed in high strength steels.

Figure 2.17 Crack-tip micrograph of the three point bend fracture toughness specimen studied by Stavehaug [1], exhibiting local transformation, crack tip branching and tremendous blunting for his extremely high fracture toughness 12Cr-17Ni material.

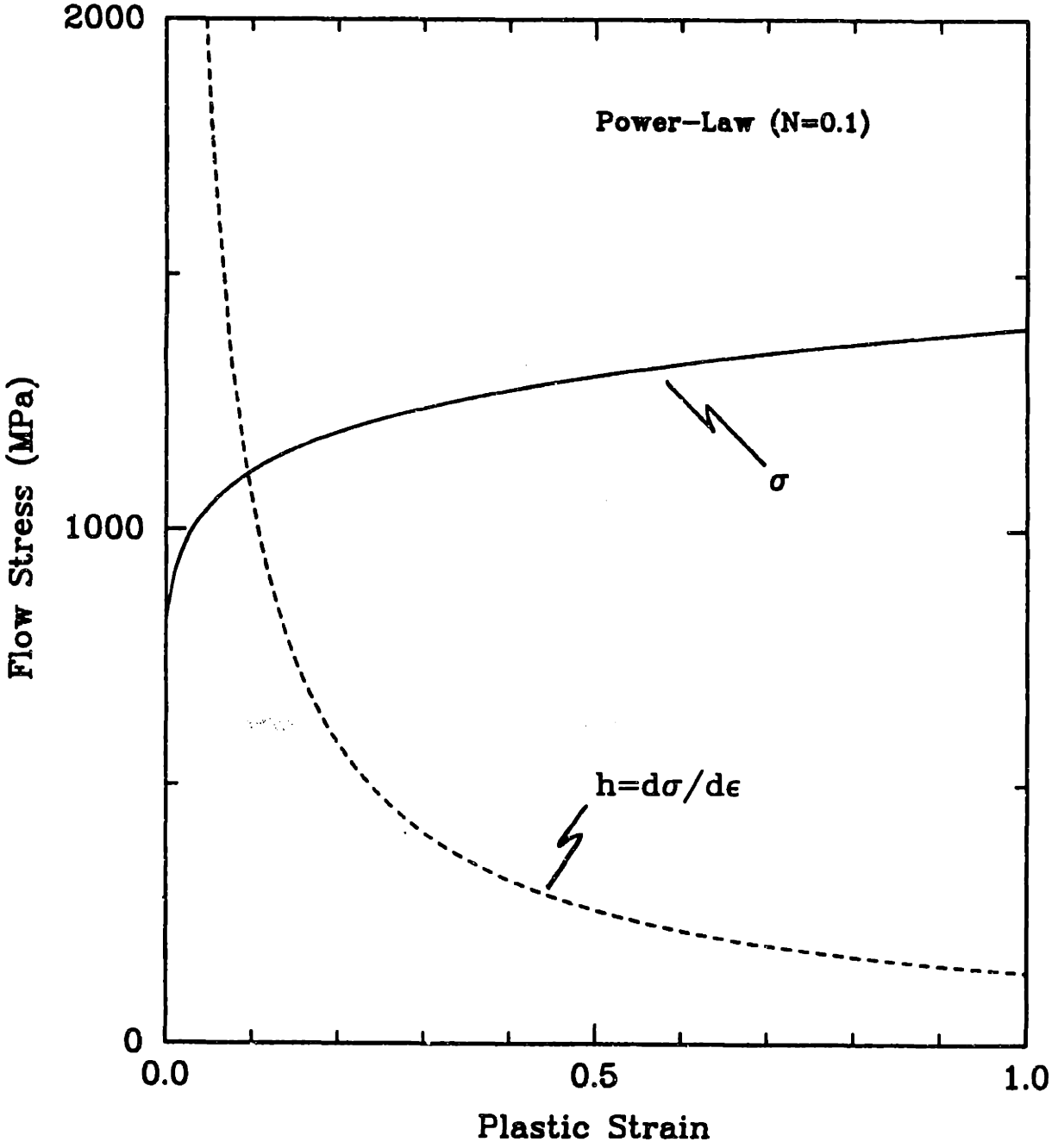

Figure 2.18 Flow stress, σ, and strain hardening rate, h, for a power-law material ($N = 0.045$).

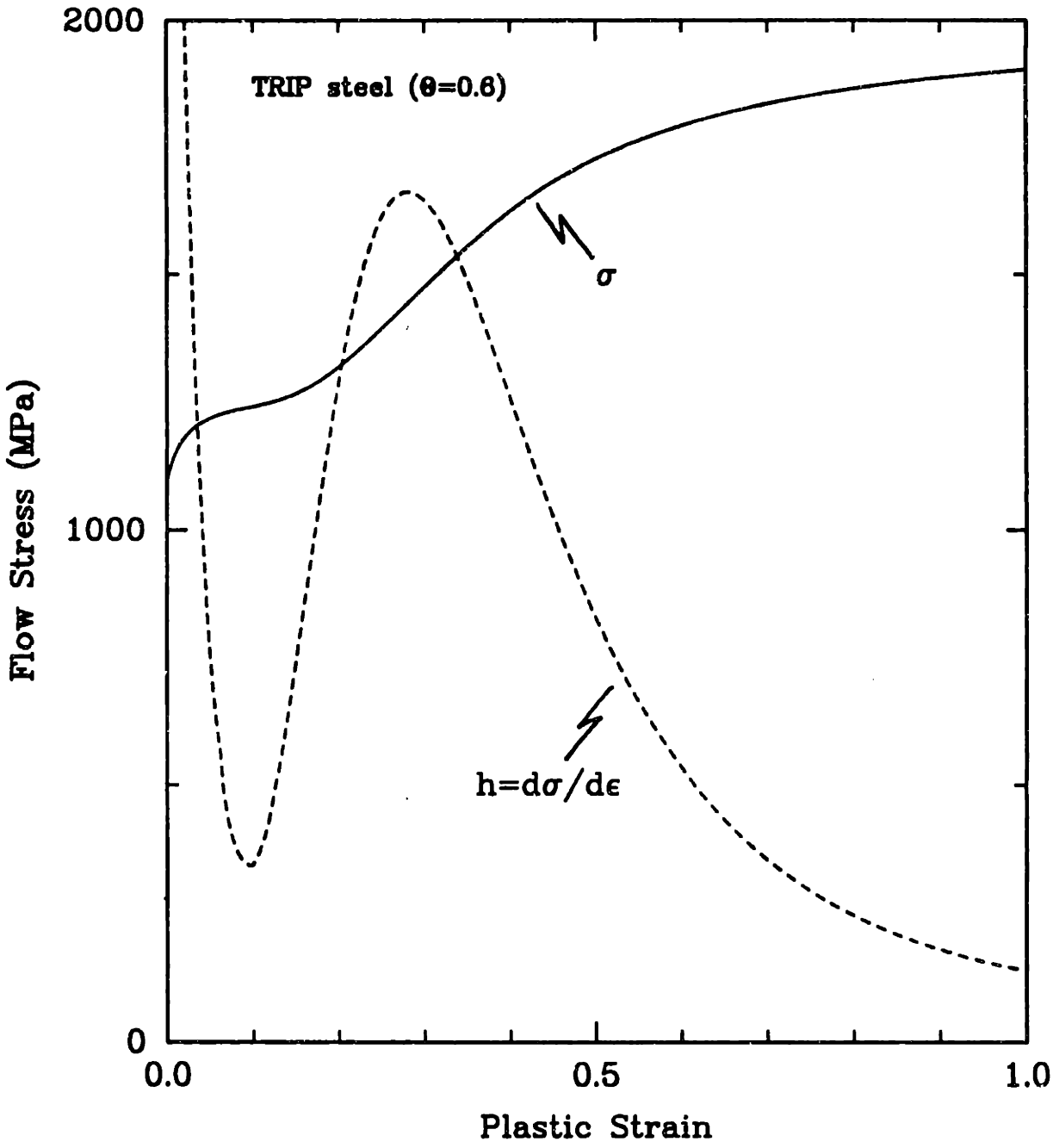

Figure 2.19 Flow stress, σ, and strain hardening rate, h, for a typical transforming material at normalized temperature $\Theta = 0.6$.

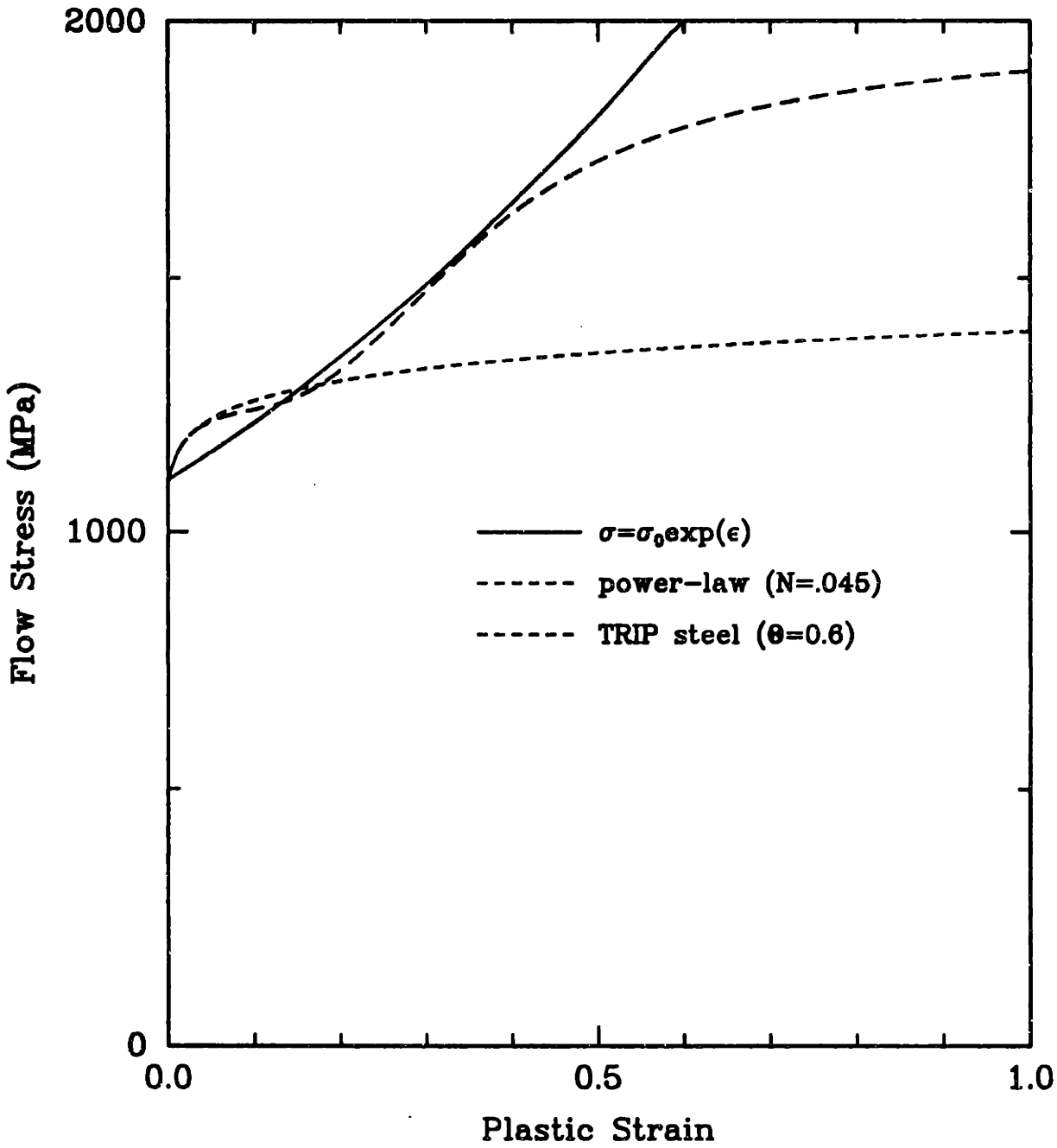

Figure 2.20 Flow stress curves for an "ideal hardening" material, a non-transforming (power-law) material and a transforming material.

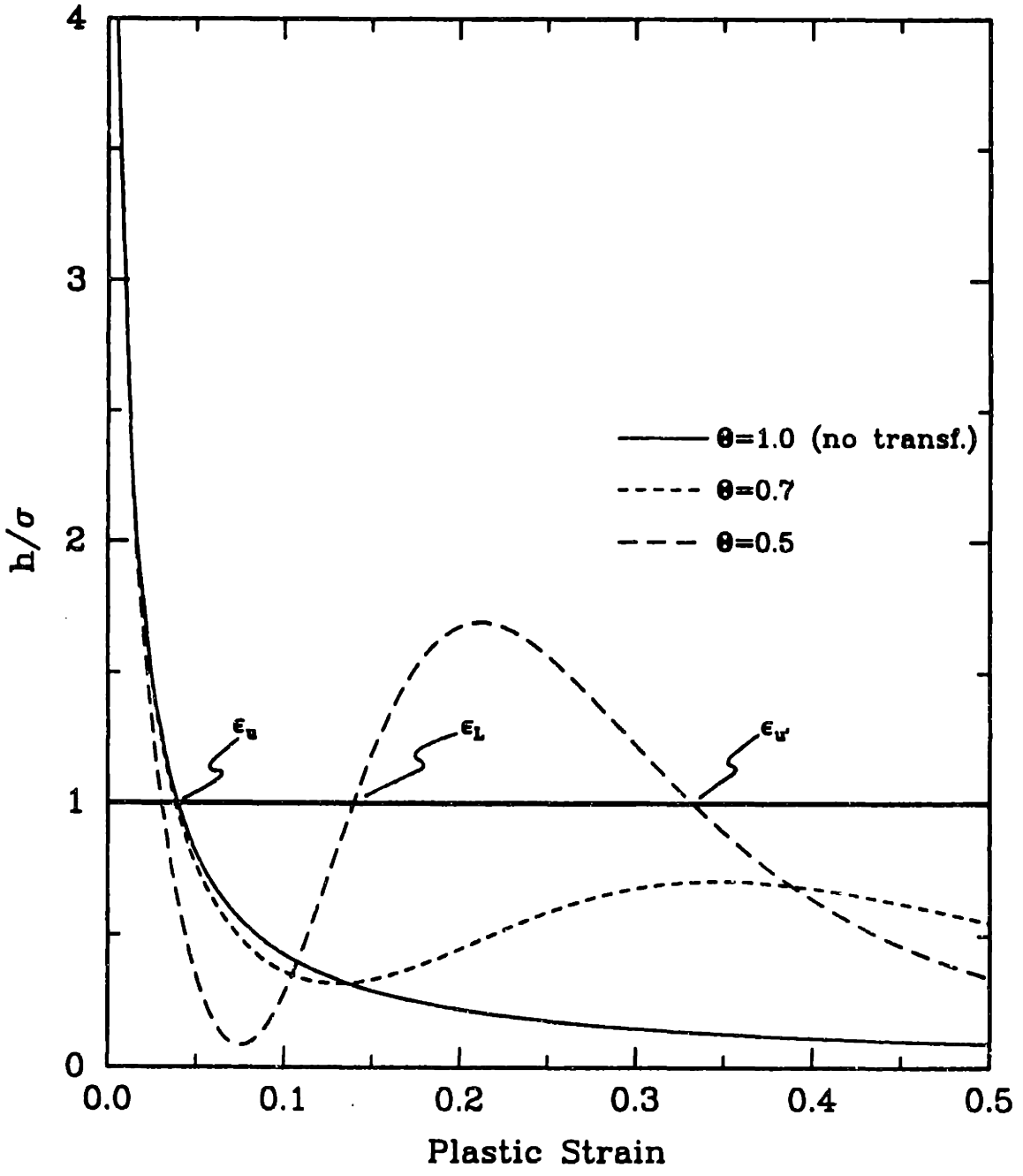

Figure 2.21 Instability parameter, h/σ, for $\Theta = 0.5$, $\Theta = 0.7$ and $\Theta = 1.0$ (no transformation).

Chapter 3

Constitutive Model

3.1 Introduction

In this chapter, we present a constitutive model for transformation plasticity in the strain-induced temperature range suitable for incorporation into a computer program for numerical analysis of boundary value problems.

We first present an updated form of the Olson-Cohen [20] model for strain-induced martensitic transformation kinetics, in which we have accounted for the stress-state sensitivity of the transformation process. Under isothermal conditions, the volume fraction of martensite formed is then a function of both plastic strain and the local stress state.

With a knowledge of the functional dependence of martensite evolution in hand, we then present a straightforward analysis for the prediction of the stress-strain properties of the evolving two-phase composite. A simple model for the stress-strain behavior of steels which exhibit strain-induced transformation plasticity was proposed by Narutani, *et al.* [21]. In this model, a first estimate of the flow stress is made using a Voigt method, where the strains in the two phases are assumed equal. This leads to predicted stress-strain curves which overestimate the actual behavior. A correction accounting for the effect of the transformation process is then introduced; the transformation shape strain leads to strain-softening. In this manner, composite flow stress predictions are obtained which are in reasonable agreement with experimental data for low strength austenitic steels deformed in uniaxial tension; however, the hardness

differences between austenite and martensite are often so large that the assumption of equal strains in the two phases leads to grossly inaccurate predictions of composite behavior. Furthermore, the functional form of the constitutive models used in [21] to account for the effects of transformation strain have often, in our experience, led to numerical difficulties when used for the modeling of boundary value problems.

We have therefore developed a self-consistent model which not only partitions the strains in the two phases according to their relative hardnesses, but is also better conditioned for numerical analysis. Moreover, the structure of the model is amenable to the incorporation of transformation strain in a straightforward manner.

We first derive a general model suitable for a multiphase material, but applicable only to materials with fixed phase fractions. We then specialize the model to the case of a two-phase material in which the volume fraction of each phase evolves with time and where transformation strain is accounted for. This modified model is less rigorous than the model for fixed phase fractions, but nonetheless leads to reasonable fits to experimental data. Several assumptions are made in deriving a model for this complex mechanical process, and these are discussed.

After illustrating a few of the features of the self-consistent model predictions for two-phase steels with fixed phase fractions, we compare model predictions with experimental data taken from [74] for dual-phase steels. More significantly, we then compare model predictions for metastable austenite/martensite steels with data taken from [7] and [21], and illustrate a few of the one-dimensional features of the transformation in terms of the resulting kinetics and flow response under various loading conditions.

Finally, in order to model the failure process directly, we extend the model to account for the continuum effects of void nucleation and growth. The influence of void nucleation and growth becomes evident only at high strain and triaxiality, where porosity evolution leads to strain-softening. With a few additional assumptions, these processes are easily incorporated into the framework of the original model.

3.2 Preliminaries

3.2.1 Notation

For the discussion of our constitutive relationships, we have adopted the tensor notation of Gurtin [75]. Scalars are written in regular type (e.g., γ, $\bar{\sigma}$). Vectors are written in boldface lowercase Roman (e.g., $\mathbf{e}, \mathbf{t}$) and 2^{nd} order tensors are written in boldface uppercase Roman and boldface lowercase Greek (e.g., $\mathbf{T}$, $\boldsymbol{\sigma}$). 4^{th} order tensors are written as capitalized calligraphic letters (e.g., $\mathcal{I}$, $\mathcal{L}$). Given an orthonormal vector basis, $\mathbf{e}_i$, 2^{nd} and 4^{th} order tensors can be defined as follows:

$$\mathbf{A} = A_{ij}\mathbf{e}_i \otimes \mathbf{e}_j, \tag{3.1}$$

where repeated indices indicate summation, and

$$\mathcal{C} = C_{ijkl}\mathbf{e}_i \otimes \mathbf{e}_j \otimes \mathbf{e}_k \otimes \mathbf{e}_l, \tag{3.2}$$

where the tensor product $\mathbf{a} \otimes \mathbf{b}$ of two vectors $\mathbf{a}$ and $\mathbf{b}$ is a 2^{nd} order tensor, defined such that for any vector $\mathbf{v}$,

$$(\mathbf{a} \otimes \mathbf{b})\,\mathbf{v} = (\mathbf{b} \cdot \mathbf{v})\,\mathbf{a}, \tag{3.3}$$

where the dot product of vectors $\mathbf{b}$ and $\mathbf{v}$, $\mathbf{b} \cdot \mathbf{v}$, is defined to equal $b_i v_i$. Second order tensors are linear maps which assign vectors to vectors. Similarly, 4^{th} order tensors are linear maps which assign 2^{nd} order tensors to 2^{nd} order tensors, etc. The following notation is used to denote this mapping:

$$\mathbf{u} = \mathbf{A}\,[\mathbf{v}]\,, \tag{3.4}$$

$$\mathbf{B} = \mathcal{C}\,[\mathbf{A}]\,. \tag{3.5}$$

Some standard operators are defined as follows: The inner product $\mathbf{A} \cdot \mathbf{B}$ of two 2^{nd} order tensors $\mathbf{A}$ and $\mathbf{B}$ is a scalar, and can be written in component form as follows:

$$\mathbf{A} \cdot \mathbf{B} = \sum_{i,j} A_{ij} B_{ij}. \tag{3.6}$$

The magnitude of $\mathbf{A}$ can now be defined as

$$\|\mathbf{A}\| = \sqrt{\mathbf{A}^{\mathbf{T}} \cdot \mathbf{A}}\,. \tag{3.7}$$

The tensor product $\mathbf{A} \otimes \mathbf{B}$ of two 2^{nd} order tensors $\mathbf{A}$ and $\mathbf{B}$ is a 4^{th} order tensor which is defined such that for any second order tensor $\mathbf{V}$,

$$(\mathbf{A} \otimes \mathbf{B})[\mathbf{V}] = (\mathbf{B} \cdot \mathbf{V})\,\mathbf{A}. \tag{3.8}$$

In component form,

$$(\mathbf{A} \otimes \mathbf{B})_{ijkl} = A_{ij}B_{kl}. \tag{3.9}$$

Two identity tensors can now be defined. The second order identity, $\mathbf{1}$, is defined such that

$$\mathbf{1} = \delta_{ij}\mathbf{e}_i \otimes \mathbf{e}_j, \tag{3.10}$$

where δ_{ij} is the Kronecker delta. The fourth order identity, $\mathcal{I}$, is defined such that

$$\mathcal{I} = \frac{1}{2}\left(\delta_{ik}\delta_{jl} + \delta_{il}\delta_{jk}\right)\mathbf{e}_i \otimes \mathbf{e}_j \otimes \mathbf{e}_k \otimes \mathbf{e}_l. \tag{3.11}$$

Identity tensors have the property that they map vectors or tensors into themselves: $\mathbf{1}[\mathbf{u}] = \mathbf{u}$; $\mathcal{I}[\mathbf{A}] = \mathbf{A}$.

Finally, the deviatoric part of tensor $\mathbf{A}$ can now be defined as

$$\mathbf{A}' = \mathbf{A} - \left(\frac{1}{3}tr\mathbf{A}\right)\mathbf{1}\,, \tag{3.12}$$

where $tr\mathbf{A} = \sum_k A_{kk}$ is the trace of $\mathbf{A}$.

3.2.2 Kinematics

Using the above notation, we give definitions for a few standard kinematical quantities which are referenced in the derivation of the model: If we let $\mathbf{x}$ be the position of a particle in the current configuration at time t; then the following quantities can be defined in terms of $\mathbf{x}$:

$\mathbf{v}(\mathbf{x},t)$ ..... spatial description of velocity,

$\mathbf{L}(\mathbf{x},t) = \frac{\partial}{\partial \mathbf{x}}\mathbf{v}(\mathbf{x},t)$ ..... velocity gradient,

$\mathbf{D} = \frac{1}{2}\left(\mathbf{L} + \mathbf{L}^T\right)$ ..... stretching,

$\mathbf{W} = \frac{1}{2}\left(\mathbf{L} - \mathbf{L}^T\right)$ ..... spin,

$\boldsymbol{\sigma}(\mathbf{x},t)$ ..... Cauchy (true) stress,

ρ_0 ..... Mass density in reference undeformed configuration,

$\rho_t(\mathbf{x},t)$ ..... Mass density in current configuration,

$\mathbf{T}(\mathbf{x},t) = \frac{\rho_t}{\rho_0}\boldsymbol{\sigma}$ ..... Kirchhoff stress.

$\dot{\mathbf{T}}(\mathbf{x},t) = \frac{\mathcal{D}}{\mathcal{D}t}(\mathbf{T}(\mathbf{x},t))$ ..... material time derivative of $\mathbf{T}$,

The following definitions are also used frequently throughout the remainder of the text: The Mises equivalent tensile stress, $\bar{\sigma}$, is defined as follows:

$$\bar{\sigma} = \sqrt{\frac{3}{2}\mathbf{S}\cdot\mathbf{S}}\,, \tag{3.13}$$

where $\mathbf{S} \equiv \mathbf{T}'$. The hydrostatic pressure, p, is defined as

$$p = -\frac{1}{3}tr\mathbf{T}\,. \tag{3.14}$$

The equivalent strain, ϵ, is given by:

$$\epsilon = \int \dot{\epsilon}dt, \tag{3.15}$$

where $\dot{\epsilon}$ is defined such that:

$$\dot{\epsilon} = \sqrt{\frac{2}{3}\mathbf{D}\cdot\mathbf{D}}\,. \tag{3.16}$$

Similar definitions can be given for the equivalent shear stress, τ and the equivalent shear strain rate $\dot{\gamma}$:

$$\tau = \sqrt{\frac{1}{2}\mathbf{S}\cdot\mathbf{S}}. \tag{3.17}$$

$$\dot{\gamma} = \sqrt{2\mathbf{D}\cdot\mathbf{D}}. \tag{3.18}$$

3.3 Transformation Kinetics

In previous studies, Olson and Cohen [20,30] reviewed the kinetic aspects of transformation plasticity in the strain-induced regime. They argued that the kinetics and morphology found in the strain-induced temperature range are a result of the continuing generation, by the intersection of slip bands in the austenite, of a population of sufficiently potent embryonic nuclei for triggering the martensitic transformation. The potency of a given distribution of slip-band intersections in activating the transformation process depends on the local temperature and stress state. Olson and Cohen [20] developed a model for the kinetics of strain-induced martensitic transformation which was based strictly on the above nucleation hypothesis; it is hereafter denoted as the OC model. The stress-state sensitivity of the transformation kinetics was not explicitly considered in the original OC model formulation; only temperature and plastic strain were considered as the parameters controlling martensite evolution. In their application of the OC model, Olson and Cohen considered only uniaxial tensile states of stress under isothermal conditions. In this case, the volume fraction of martensite formed becomes a function, through some temperature-dependent parameters, of plastic strain only. This single-variable dependence leads to an integrable form for the martensite evolution equation. This approach is not, however, sufficiently general to encompass the noted dependence of the transformation kinetics on the stress state. In light of the unknown histories of stress, strain and temperature to which material points in the vicinity of blunt notches, crack tips, *etc.* are subjected, it is important to establish more general evolution equations for martensite volume fraction. The proposed model will therefore incorporate stress-state sensitivity into the general framework of the OC model of transformation kinetics, utilizing results of Haezebrouck's [76] recent investigation of this matter. The incorporation of pressure sensitivity as a second independent quantity necessitates a reformulation of the OC evolution law into an incremental form, because the extent of martensite evolution at a material-point depends on its stress-state history.

Model Formulation

The rate of increase in the volume fraction of martensite, $\dot{f}$, is proportional to the rate of increase in the number of martensitic embryos per unit austenite volume, $\dot{N}_m$:

$$\dot{f} = (1 - f)\,\bar{v}_m \dot{N}_m \,, \tag{3.19}$$

where $\bar{v}_m$ is the average volume per martensitic unit, which is assumed to be constant. The factor $(1 - f)$ represents the decreasing volume fraction of austenite available for transformation.

The OC model is based on the observation that strain-induced nucleation occurs predominantly at shear-band intersections. The number of operational nucleation sites, N_m, is taken to be equal to the number of shear-band intersections per unit volume, N_I, multiplied by the probability, P, that a shear band intersection will act as a nucleation site. $\dot{N}_m$ is thus given as

$$\dot{N}_m = P\dot{N}_I + N_I \dot{P} H\left(\dot{P}\right) \,, \tag{3.20}$$

where $H(\dot{P})$ is the Heaviside step function, reflecting the fact that the transformation is irreversible [1]. N_I can be defined as

$$N_I = \frac{f_I}{\bar{v}_I} \,, \tag{3.21}$$

where f_I is the volume fraction of shear-band intersections, and $\bar{v}_I$ is the average volume of a shear-band intersection. The parameter f_I is assumed to be related to the volume fraction of austenite occupied by shear-bands, f_{sb}, through a power-law expression of the form

$$f_I = C(f_{sb})^{r_I} \,, \tag{3.22}$$

where C is a geometric constant, and the exponent $r_I = 2$ models a random orientation of shear-bands. Olson and Cohen pointed out that these shear-bands tend to be

[1] The form of (3.20) is adequate for most probability histories; however, in some cases it leads to double accounting of nucleation sites. A short illustration of such a case and its effect on the formation of martensite is given at the end of this section.

initially parallel, reducing the initial rate of intersection, so that a value greater than 2 (typically 4 to 5) is assumed for the exponent r_I.

Consistent with available data for the special case where the shear bands consist of hcp ϵ-martensite, the remaining austenite volume fraction of shear-bands, f_{sb}, is taken to evolve with plastic shear strain in the austenite, γ_a, as follows:

$$\dot{f}_{sb} = (1 - f_{sb})\,\alpha\dot{\gamma}_a \,. \tag{3.23}$$

Equation (3.23) is based on the assumption of a constant rate of shear-band production. The factor $(1 - f_{sb})$ accounts for the diminishing austenite volume available to produce new shear-bands. The parameter α represents the rate of shear band formation, $df_{sb}/d\gamma_a$, at low strains. It is dependent upon stacking-fault energy, and since lower levels of stacking-fault energy promote shear-band (planar slip) deformation modes [20], α generally increases with decreasing stacking fault energy. The α-parameter is temperature-dependent through the variation of stacking fault energy with temperature.

Integrating (3.23) under isothermal conditions, we obtain

$$f_{sb} = 1 - e^{-\alpha\gamma_a} \,. \tag{3.24}$$

Substituting for f_{sb} in (3.22) and using (3.21) provides

$$N_I = \frac{C}{\bar{v}_I}\left(1 - e^{-\alpha\gamma_a}\right)^{r_I} \,, \tag{3.25}$$

or, differentiating,

$$\dot{N}_I = \left[\frac{r_I C\alpha}{\bar{v}_I} e^{-\alpha\gamma_a}\left(1 - e^{-\alpha\gamma_a}\right)^{r_I - 1}\right]\dot{\gamma}_a \,. \tag{3.26}$$

Consistent with available strain-induced transformation kinetics data [20], the probability parameter, P, is determined assuming that there exists a Gaussian distribution of shear band intersection potencies (where "potency" is defined to be the minimum thermodynamic driving force at which a given nucleation site can be activated). P is thus cast in the form of a cumulative probability distribution function,

$$P = \frac{1}{\sqrt{2\pi}} \int_{-\infty}^{g} exp\left[-\frac{1}{2}\left(\frac{g' - \bar{g}}{s_g}\right)^2\right] dg' \,, \tag{3.27}$$

where $\bar{g}$ is the dimensionless mean of a given probability distribution function and s_g is its standard deviation (both of which are fit to experimental data). P is taken to be a function of temperature *and stress state* through the argument of the distribution function, g. The parameter g is a normalized net thermodynamic driving force, defined as:

$$g = g_0 - g_1\Theta + g_2\Sigma \,, \tag{3.28}$$

where g_0, g_1 and g_2 are dimensionless constants. In eq. (3.28), Θ is a normalized temperature which is related to the absolute temperature, T, according to

$$\Theta = \frac{T - M^{\sigma}_{s,ut}}{M_{d,ut} - M^{\sigma}_{s,ut}} \,, \tag{3.29}$$

where $M^{\sigma}_{s,ut}$ and $M_{d,ut}$ are the absolute M^{σ}_{s} and M_d temperatures for uniaxial tension. The parameter Σ represents a ratio of the volumetric and deviatoric stress invariants:

$$\Sigma \equiv \frac{-p}{\bar{\sigma}} \equiv \frac{-p}{\sqrt{3}\tau} \,. \tag{3.30}$$

We will refer to Σ as the "triaxiality" of the state of stress. The rate of change of the probability function, $\dot{P}$, under isothermal conditions ($\dot{\Theta} = 0$), is thus given by

$$\dot{P} = \frac{g_2}{\sqrt{2\pi}s_g} exp\left[-\frac{1}{2}\left(\frac{g-\bar{g}}{s_g}\right)^2\right]\dot{\Sigma} \,, \tag{3.31}$$

where it can be easily shown that

$$\dot{\Sigma} = \Sigma\left(\frac{\dot{p}}{p} - \frac{\dot{\tau}}{\tau}\right) \,. \tag{3.32}$$

Substituting for $\dot{N}_m$ in (3.19) using (3.20), (3.26) and (3.27), we obtain the following expression for $\dot{f}$:

$$\dot{f} = (1-f)\left(A_f\dot{\gamma}_a + B_f\dot{\Sigma}\right) \,, \tag{3.33}$$

where

$$A_f = \alpha\beta_0 r_I (1-f_{sb})(f_{sb})^{r_I - 1} P \,; \tag{3.34}$$

$$B_f = \frac{g_2}{\sqrt{2\pi}s_g}\beta_0 (f_{sb})^{r_I} exp\left[-\frac{1}{2}\left(\frac{g-\bar{g}}{s_g}\right)^2\right] H\left(\dot{\Sigma}\right) \,, \tag{3.35}$$

where $\beta_0 = C\bar{v}_m/\bar{v}_I$.

Discussion

In the model described in equations (3.19 – 3.35), martensite volume fraction is viewed as a function of temperature, plastic strain and stress state. Temperature affects both the number of shear-band intersections produced, through $\alpha(T)$, and the probability of nucleation, through (3.28). The effects of plastic strain and stress state decouple; plastic strain affects only the number of intersections, while the stress state affects only the probability distribution. The thermodynamic driving force variable, g, of the probability function is a critical parameter determining the extent of transformation under different conditions.

It decreases with increasing temperature but increases with increasing triaxiality. Thus, at fixed temperature, as the triaxiality increases, so does the probability that martensite will nucleate at a potential site. Fig. 3.1 depicts P and $\dot{P}$ as functions of g and the dependence of P on temperature and stress state. The variation of P with stress is seen as one of the most important features of the transformation. For example, as indicated in Fig. 3.1, at fixed temperature, the driving force for transformation under a highly triaxial state of stress is significantly greater than it is under a mildly triaxial state of stress, with the result that the probability of nucleation can increase from a negligible value to a value approaching unity. Following the original Patel-Cohen analysis of the thermodynamics of martensitic transformation under stress [29], the pressure dependence of nucleation scales directly with transformation dilatation, so that the g_2 term in eq. (3.28) is strongly correlated with the relative volume change associated with the transformation,

$$\Delta_V = \frac{(V_m - V_a)}{V_a} , \tag{3.36}$$

where V_a and V_m represent the unstressed relative volumes occupied by the austenite and martensite phases, respectively. Leal [6] found experimentally that $\Delta_V \sim 0.02$ to 0.05 in austenitic steels, depending upon alloy composition.

Stress-state sensitivity enters the present kinetics model through a linear function of the triaxiality ratio, $\Sigma = -p/\sqrt{3}\tau$, so that the probability of nucleating a potential

site is not explicitly biased by the *magnitude* of either p or τ. The use of a linear combination of hydrostatic and deviatoric stress measures (see eq. 2.2) is attractive from a thermodynamic point of view, since these would add to the driving force for the transformation in a consistent manner. In fact, we attempted to implement a model in which a linear combination of p and τ were used in the definition of g. We found, however, that this invariably resulted in far too much transformation at high stress levels. We attribute this result to a disregard of the influence of dislocation hardening on the frictional resistance to martensite interfacial motion [77]. In the present model, the thermodynamic contribution of the net deviatoric stress (applied stress minus athermal friction stress) can be regarded as residing primarily in the constant g_0, with some contribution to the temperature coefficient g_1 through the temperature dependence of the flow stress.

One final note regarding the functional form of eq. (3.20): the Heaviside step function, $H(\dot{P})$, is added to account for the irreversibility of the transformation. The resulting incremental predictions of $\Delta N_m \approx \dot{N}_m \Delta t$ are accurate for most stress-state histories. More specifically, (3.20) is accurate when Σ (and thus P) is a concave function of plastic strain (*i.e*, P increases and then decreases). However, whenever Σ is a convex function (*i.e.*, it decreases and then increases), the form used in (3.20) leads to double accounting of N_I. This difficulty could be overcome if the entire history of P was tracked, in which case

$$\Delta N_m = P \Delta N_I + \int_0^t H\left[P - P_{max}(t')\right]\left[P - P_{max}(t')\right] \Delta N_I(t') dt', \tag{3.37}$$

where P_{max} is the maximum probability seen by each ΔN_I. Storing the history of P is impractical from a computational point of view. In light of the rare instances in which the stress state history — and thus the history of P — exhibits this kind of behavior, the form of (3.20) is sufficient for our model. Fig. 3.2 compares the more accurate integrated form (3.37) with the approximate form (3.20), in terms of the effect on the resulting $f - \gamma_a$ behavior, for a hypothetical probability history, $P = \frac{1}{2} + \frac{1}{4} sin(5\pi\gamma_a)$. The difference between the predictions of (3.20) and (3.37) does not manifest itself until P begins to increase for the second time at $\gamma_a = 0.3$. The

maximum error in this extreme example is only about 5%, so that we can consider the approximate form (3.20) adequate for our purposes.

In section 3.6.2, below, we present a comparison of model predictions of martensite volume fraction versus plastic shear strain with uniaxial tension and compression data measured by Young [7].

3.4 Stress-strain Behavior

A constitutive law which adequately describes the behavior of this unique class of steels must be able to model a finitely-deforming, dynamically-evolving, two-phase elastic-plastic composite having the following significant features: 1. each phase is strain-hardening, and there are generally large contrasts between the plastic resistances of each phase, leading to substantial differences between the average plastic strains in each phase; 2. the evolution of martensite, as we argued in the previous section, is a strong function of temperature, plastic strain, and stress state; 3. the transformation process generates a "nucleation" strain having both deviatoric and hydrostatic components; 4. the incrementally-formed martensite, as shown, for example, in ausforming studies [78], "inherits" the dislocation substructure of its parent austenite, so that the martensite formed at higher levels of plastic strain will be harder than that formed at lower levels of plastic strain.

Any model attempting to account for all of these features will have a certain complexity; however, if a few appropriate assumptions are made, these features can be directly incorporated into a straightforward model.

3.4.1 Constitutive Formulation

An isotropic hypoelastic formulation is used to define the evolution of the stress state as a function of the rate kinematics. This choice renders the model properly frame-indifferent, as is necessary when large deformations are considered. Anand [79] has shown that the hypoelastic form is a good approximation to the proper hyperelastic form when elastic stretches are small. The evolution equation for the average stress

in the composite, $\mathbf{T}$, is thus given by:

$$\overset{\nabla}{\mathbf{T}} = \mathcal{L}^e [\mathbf{D} - \mathbf{D}^p] \ , \tag{3.38}$$

where the stretching tensor, $\mathbf{D}$, which is the symmetric part of the velocity gradient tensor, $\mathbf{L}$, has been decomposed into its elastic and plastic parts: $\mathbf{D} = \mathbf{D}^e + \mathbf{D}^p$. The Jaumann derivative of stress, $\overset{\nabla}{\mathbf{T}}$, is defined as:

$$\overset{\nabla}{\mathbf{T}} = \dot{\mathbf{T}} - \mathbf{W}\mathbf{T} + \mathbf{T}\mathbf{W} \ . \tag{3.39}$$

The 4th order isotropic elasticity tensor $\mathcal{L}^e$ is defined as:

$$\mathcal{L}^e = 2G\mathcal{I} + (K - \frac{2}{3}G)\mathbf{1} \otimes \mathbf{1} \ , \tag{3.40}$$

where G is the shear modulus, and K is the bulk modulus. The elastic properties of the austenite ($\mathcal{L}^e_a$) and martensite ($\mathcal{L}^e_m$) are virtually equal, so we take $\mathcal{L}^e = \mathcal{L}^e_a = \mathcal{L}^e_m$.

We can further decompose the stretching tensor into deviatoric and hydrostatic parts:

$$\mathbf{D} = \mathbf{D}' + \frac{1}{3}(tr\mathbf{D})\mathbf{1} \ , \tag{3.41a}$$

or

$$\mathbf{D} = \frac{1}{\sqrt{2}}\dot{\gamma}^T\mathbf{M} + \dot{e}^T_v\mathbf{1} \ , \tag{3.41b}$$

where $\dot{\gamma}^T = \sqrt{2}\,\|\mathbf{D}'\|$ is the total equivalent shear strain rate, $\mathbf{M} = \mathbf{D}'/\|\mathbf{D}'\|$ is the unit deviatoric tensor coaxial with $\mathbf{D}'$, and $\dot{e}^T_v = \frac{1}{3}tr\mathbf{D}$ is the total dilatation rate. We can likewise decompose the plastic stretching into deviatoric and hydrostatic parts:

$$\mathbf{D}^p = \mathbf{D}^{p'} + \frac{1}{3}(tr\mathbf{D}^p)\mathbf{1} \ , \tag{3.42a}$$

$$= \frac{1}{\sqrt{2}}\bar{\dot{\gamma}}^p\mathbf{N} + \dot{e}^p_v\mathbf{1} \ , \tag{3.42b}$$

where $\bar{\dot{\gamma}}^p = \sqrt{2}\,\|\mathbf{D}^{p'}\|$ is the equivalent plastic shear strain rate (the bar indicates that this is a quantity averaged over the composite), $\dot{e}^p_v$ is the rate of plastic dilatation, and $\mathbf{N}$ is the unit deviatoric tensor coaxial with $\mathbf{D}^{p'}$. Within the scope of our isotropic model, $\mathbf{D}^{p'}$ is chosen to be coaxial with $\mathbf{S}$, so that $\mathbf{N}$ is given by

$$\mathbf{N} = \frac{\mathbf{S}}{\sqrt{2}\bar{\tau}} \ . \tag{3.43}$$

Using (3.38 - 3.43), the time rates of $\bar{\tau}$ and p can be expressed as

$$\dot{\bar{\tau}} = \frac{1}{\sqrt{2}}\overset{\nabla}{\mathbf{T}} \cdot \mathbf{N} = G\left(\beta\dot{\gamma}^T - \dot{\bar{\gamma}}^p\right) ; \tag{3.44}$$

$$\dot{p} = -\frac{1}{3}\overset{\nabla}{\mathbf{T}} \cdot \mathbf{1} = -K\left(\dot{e}_v^T - \dot{e}_v^p\right) , \tag{3.45}$$

where $\beta = \mathbf{M} \cdot \mathbf{N}$. (It can be shown that the tensor dot products of the second and third terms of the r.h.s of (3.38) with $\mathbf{N}$ and $\mathbf{1}$ vanish.)

The set of equations (3.44, 3.45) for the rates of stress invariants $\dot{\bar{\tau}}$ and $\dot{p}$ can be completed by constitutively expressing $\dot{\bar{\gamma}}^p$ and $\dot{e}_v^p$ — and thus $\mathbf{D}^p$ — in terms of $\dot{\bar{\tau}}$, $\dot{p}$ and internal variables, including f and the hardnesses of the two phases, s_a and s_m. In order to obtain these relationships, we first introduce the following further decomposition of the plastic stretching:

$$\mathbf{D}^p = \mathbf{D}^{slip} + \mathbf{D}^{nucl} , \tag{3.46}$$

where the deviatoric tensor $\mathbf{D}^{slip}$ is the part of the plastic stretching which is due to slip in the austenite and martensite phases and $\mathbf{D}^{nucl}$ is an additional inelastic strain rate resulting from the transformation process. In the remainder of this section, we give complete descriptions of $\mathbf{D}^{slip}$ and $\mathbf{D}^{nucl}$ — and thus $\dot{\bar{\gamma}}^p$ and $\dot{e}_v^p$ — in terms of $\dot{\bar{\tau}}$, $\dot{p}$, f, s_a and s_m.

3.4.2 Modeling Transformation Strain

A critical aspect of the transformation process is the strain softening which occurs as a result of the transformation strain. We have incorporated strain softening into the model simply by considering an additional "nucleation" rate contribution to the total strain rate in a manner similar to that used by Hutchinson and Tvergaard [80] for modeling softening due to void nucleation. In their constitutive model, the softening effects of void nucleation are accounted for by considering an additive strain rate term proportional to the rate of increase of the void volume fraction. Similarly, we propose the following form to account for the plastic softening due to martensitic nucleation:

$$\mathbf{D}^{nucl} = \dot{f}\left\{\frac{1}{\sqrt{2}}A\mathbf{N} + \frac{1}{3}\Delta_V\mathbf{1}\right\} . \tag{3.47}$$

The dilatational term in (3.47) accounts for the positive transformation volume change. We assume that $\mathbf{D}^{slip}$ is deviatoric, thus (3.47) directly provides that $\dot{e}_V^p = \Delta_V \dot{f}$. The deviatoric term models the transformation shape strain, where $\mathbf{N}$, as stated, is proportional to $\mathbf{S}$. Thus, within the framework of our isotropic model, we assume that the deviatoric part of the nucleation strain rate should be biased in the direction of the applied stress deviator.

The dimensionless coefficient A in (3.47) reflects an ensemble effect of the shape strains over an isotropic distribution of nucleation sites as considered by Olson, Tzusaki and Cohen [41]. Some sites will generate local shape strains in the direction of $\mathbf{N}$. Others will generate shape strains orthogonal to $\mathbf{N}$. The net shape strains not aligned with $\mathbf{N}$ will tend to cancel themselves, leaving a net shape strain in the $\mathbf{N}$ direction which is *much less than* the total number of transforming sites per unit volume times the shape strain associated with each site; hence the need for the factor A. Consistent with data from tests where inelastic flow is controlled by the stress-assisted mode of transformation [14], A is taken to depend on the stress level. For our present development, we chose the following simple form for A:

$$A = A_0 + A_1 \left(\frac{\bar{\tau}}{s_a^*} \right) , \tag{3.48}$$

where A_0 and A_1 are constants and s_a^* is a reference austenite hardness. Fig. 3.3 shows several values of A plotted versus $\bar{\tau}$, which have been estimated from (linear) curves of volume fraction martensite versus plastic strain given in [7] and [14]; these data were measured at different levels of transformation stress in the stress-assisted regime. Since the kinetics and morphology of stress-assisted and strain-induced transformations are different, we can expect that values for the parameter A obtained from experimental data in the stress-assisted regime may differ slightly from the values of A that are appropriate for the strain-induced regime. However, for lack of direct measurement in the strain-induced regime, we have used these data, trusting that they represent reasonable upper bounds for the A coefficient in the strain-induced regime. The solid line shown Fig. 3.3 represents the value taken for A which is used later in this work to fit available tensile data given in [21] for a 14Ni-7Cr metastable

austenitic steel.

3.4.3 Estimation of Composite Stress-strain Behavior

The most critical step in the development of our model involves the partitioning of the plastic strain rate into its contributions from slip in each phase and a contribution from the transformation itself. We use a self-consistent model for this purpose. In this section, we first develop a general model for multiphase materials with fixed phase fractions. We then specialize the model to two phases and modify it to incorporate evolving phase fractions and transformation strain. The more general model for fixed phase fractions is useful in its own right for estimating nonlinear composite behavior and is also useful for illustrating, for example, the effect of phase hardness difference on the partitioning of strain and the resultant predictions of the composite flow stress. We therefore devote a significant portion of this chapter to the development of the general model and a discussion of its predictions.

A Self-consistent Model for Multiphase Materials with Fixed Phase Fractions

Various methods have been used to predict the elastic–plastic stress–strain behavior of multi-phase materials. The simplest and most often used is the Taylor [81] method, in which the strain levels in individual phases are each assumed to equal the average macroscopic strain. This approach yields an upper bound for the composite stress. An approach that has received considerable attention in recent years is the so-called "self-consistent" method. In application of the self-consistent method to multiphase media, each phase is successively represented by a single ellipsoidal inclusion embedded in an infinitely extending equivalent matrix which has properties representing the average of the phases. A uniform stress or strain rate is applied at "infinity" to determine the conditions in each included phase. Composite properties are determined in terms of the known average properties of each phase.

The self-consistent method was first proposed by Hershey [82] and Kröner [83] for

estimating elastic properties of polycrystal aggregates. Krōner's approach is based on Eshelby's [84] solution to the problem of an ellipsoidal inclusion embedded in an infinite medium. Budiansky and Wu [85] formulated an early, simple elastic-plastic model, but a more general formulation of the method was first proposed by Hill [86] and later implemented by Hutchinson [87].

In recent years, the self-consistent method has been used extensively in the study of polycrystalline deformation and texture development (*e.g.*, [88,89]) and two-phase metal plasticity (*e.g.*, [90,91]). Other means of estimating composite properties have also been proposed, such as the approach of Mori and Tanaka [92], which was recently applied to metal plasticity by Tandon and Weng [93]. These models make somewhat different assumptions regarding the composite averaging scheme. Rigorous bounds on the composite behavior which are tighter than those of uniform strain or stress have also been developed — in earlier work by Hashin and Shtrikman [94] for linear constitutive behavior, and more recently for nonlinear behavior in work such as that by Talbot and Willis [95] and Ponte Castañeda and Willis [96]. Finally, specialized self-consistent models of nonlinear behavior have been developed for the limiting cases of materials with voids or with rigid inclusions [97–99].

In this section, we present a straightforward analysis for the prediction of the composite properties of a multiphase rigid-plastic material using a viscoplastic, self-consistent model in the manner of Molinari, Canova and Ahzi [100], who employed a related approach in the modeling of large deformation polycrystalline plasticity texture development. Our approach is quite similar in structure to the method utilized by Chen and Argon [101] in their analysis of creep in heterogeneous materials with coarse grain structure. The approach is also similar to the simple method outlined by Berveiller and Zaoui [90] for estimating composite properties of incompressible, isotropic two-phase metals. This last method relies on an estimate of the ratio of total values of stress and (small) strain through the use of "secant" moduli, and is therefore approximate and not incremental in nature. Elasticity is neglected in our model, but since we are primarily concerned with large deformation applications, this

seems a reasonable simplification. Incompressibility is also assumed.

Consider now a material with N distinct phases, each of which is isotropic, viscoplastic and incompressible. The following relationship is assumed to hold for material points within each individual phase:

$$\mathbf{S} = 2\mu\,\mathbf{D}\,, \tag{3.49}$$

where $\mathbf{S}$ is the deviator of the stress tensor $\mathbf{T}$, $\mathbf{D}$ is the plastic stretching tensor and μ is the local value of the "effective viscosity". Note that since we are modeling materials with nonlinear behavior, μ will vary not only from phase to phase, but also *within* each phase, depending on the local magnitude of deformation.

We postulate an isotropic distribution of each phase in the form of spherical inclusions embedded in a homogenized equivalent medium; thus the overall behavior is also isotropic viscoplastic. This assumption leads to an analogous relationship for the composite:

$$\overline{\mathbf{S}} = 2\overline{\mu}\,\overline{\mathbf{D}}\,, \tag{3.50}$$

where here and throughout, "barred" quantities refer to the composite material. Incompressibility requires that $tr\,\mathbf{D} = tr\,\overline{\mathbf{D}} = 0$.

For the simplified case of an isotropic, incompressible spherical inclusion of shearing modulus (viscosity) μ_i embedded in an infinitely extended incompressible isotropic matrix of *uniform* shearing modulus $\overline{\mu}$, Eshelby demonstrated that the deformation within the inclusion is uniform, *i.e.*, $\mathbf{D} = \mathbf{D}_i$ = constant, and $\mathbf{S} = \mathbf{S}_i$ = constant. The following relations can be derived between these local quantities and the macroscopic strain rate and stress deviator fields of the composite (*e.g.*, [101]):

$$\mathbf{D}_i = \frac{5\overline{\mu}}{3\overline{\mu} + 2\mu_i}\,\overline{\mathbf{D}}\,; \tag{3.51a}$$

$$\mathbf{S}_i = \frac{5\mu_i}{3\overline{\mu} + 2\mu_i}\,\overline{\mathbf{S}}\,. \tag{3.51b}$$

Equations (3.51a) and (3.51b) are precise only for a spherical inclusion embedded in a *linear* viscous matrix. We intend to extend the application of a suitably defined generalization of the localization law (3.51) to *non-linear* viscous materials, for which

the deformation $\mathbf{D}$, the stress state $\mathbf{S}$, and the viscosity μ within the inclusion are no longer uniform. The *inclusion* strain rate and stress deviator must then be considered as *volume averages* within the inclusion, *i.e.*,

$$\mathbf{D}_i = \frac{1}{V_i}\int_{V_i} \mathbf{D}\, dV_i \; ; \tag{3.52a}$$

$$\mathbf{S}_i = \frac{1}{V_i}\int_{V_i} \mathbf{S}\, dV_i \; . \tag{3.52b}$$

These two tensors are assumed to be related through a phase-average viscosity parameter μ_i^*, defined by

$$\mathbf{S}_i = 2\mu_i^* \mathbf{D}_i \; . \tag{3.53}$$

The averaged quantities $\mathbf{D}_i$, $\mathbf{S}_i$ and μ_i^* will satisfy (3.51*a*) and (3.51*b*) only approximately. Furthermore, the composite stress-strain rate relationship (3.49) will now only be satisfied approximately.

Self-consistency is enforced by requiring macroscopic fields to equal volume-averages of local fields, *i.e.*,

$$\overline{\mathbf{D}} = \frac{1}{V}\int_V \mathbf{D}\, dV \; = \; \frac{1}{V}\sum_{i=1}^{N}\int_{V_i} \mathbf{D}\, dV_i \; ; \tag{3.54a}$$

$$\overline{\mathbf{S}} = \frac{1}{V}\int_V \mathbf{S}\, dV \; = \; \frac{1}{V}\sum_{i=1}^{N}\int_{V_i} \mathbf{S}\, dV_i \; . \tag{3.54b}$$

Using the definitions (3.52*a*) and (3.52*b*), (3.53*a*) and (3.53*b*) simplify to

$$\overline{\mathbf{D}} = \sum_{i=1}^{N} f_i \mathbf{D}_i \; ; \tag{3.55a}$$

$$\overline{\mathbf{S}} = \sum_{i=1}^{N} f_i \mathbf{S}_i \; , \tag{3.55b}$$

where $f_i \equiv V_i/V$ is the volume fraction of the i^{th} phase. For consistency,

$$\sum_{i=1}^{N} f_i = 1 \; . \tag{3.56}$$

The assumption of isotropic symmetry allows us to introduce the equivalent plastic shear strain rate, $\dot{\gamma}$ (see eq. 3.18), and the equivalent shear stress, τ (see eq. 3.17). Scalar constitutive equations isotropically equivalent to (3.49,3.50) can now be written as

$$\overline{\tau} = \overline{\mu}\, \dot{\overline{\gamma}} \; ; \tag{3.57a}$$

$$\tau_i = \mu_i \dot{\gamma}_i \ , \tag{3.57b}$$

where $\dot{\gamma}_i$ and τ_i are volume averages of the scalar invariants τ and $\dot{\gamma}$ over the ith phase, *i.e.*,

$$\dot{\gamma}_i = \frac{1}{V_i} \int_{V_i} \dot{\gamma} \, dV_i \ ; \tag{3.58a}$$

$$\tau_i = \frac{1}{V_i} \int_{V_i} \tau \, dV_i \ . \tag{3.58b}$$

In (3.57*b*), an alternative phase-average viscosity parameter μ_i is used. Since $\dot{\gamma}_i$ and τ_i are not scalar invariants of the volume average tensor quantities given by (3.52*a*) and (3.52*b*) (*i.e.*, $\dot{\gamma}_i \neq \sqrt{2\mathbf{D}_i \cdot \mathbf{D}_i}$) $\tau_i \neq \sqrt{\frac{1}{2}\mathbf{S}_i \cdot \mathbf{S}_i}$), we find that $\mu_i \neq \mu_i^*$ in general.

The Eshelby equations (3.51) relating local and macroscopic quantities can be recast in an approximate sense as relating macroscopic and phase-average invariants of stress and strain rate:

$$\dot{\gamma}_i = \frac{5\overline{\mu}}{3\overline{\mu} + 2\mu_i} \dot{\overline{\gamma}} \ ; \tag{3.59a}$$

$$\tau_i = \frac{5\mu_i}{3\overline{\mu} + 2\mu_i} \overline{\tau} \ . \tag{3.59b}$$

A brief discussion regarding the validity of this approximation with respect to the degree of nonlinearity and the inhomogeneity between matrix and inclusion properties is given at the end of section 3.6.1.

Let $\chi_i = \dot{\gamma}_i / \dot{\overline{\gamma}}$ represent the ratio of the average equivalent strain rate within the ith phase to the composite equivalent strain rate. A self-consistency condition equivalent to (3.55*a*) can now be given in terms of χ_i as:

$$\sum_{i=1}^{N} f_i \chi_i = 1 \ . \tag{3.60}$$

A similar rearrangement of the Eshelby equation for equivalent strain rates (3.59*a*) yields

$$\chi_i \left(\frac{3}{5} + \frac{2}{5} \frac{\mu_i}{\overline{\mu}} \right) = 1 \ . \tag{3.61}$$

To close the system, we must provide explicit viscoplastic constitutive equations for each phase. Rate dependence can be expressed in the following simple power law form:

$$\frac{\dot{\gamma}}{\dot{\gamma}_0} = \left(\frac{\tau}{s} \right)^M \ , \tag{3.62}$$

where s represents a reference shear strength level, $\dot{\gamma}_0$ a reference strain rate, and $M \geq 1$ is a material constant. At low homologous temperatures ($T_H < 1/3$), the strain-rate dependence of the flow stress is quite low, because plastic flow is slip controlled; thus we expect $M \gg 1$ [102]. The shear strength s evolves with plastic deformation according to

$$\dot{s} = h\dot{\gamma} \,, \tag{3.63}$$

where $h = \hat{h}(s, \ldots)$ is the hardening rate. Although more complex viscoplastic models relating the volume averages of the scalar invariants τ and $\dot{\gamma}$ could be chosen, let us consider each phase to behave according to (3.62), so that the relation between τ_i and $\dot{\gamma}_i$ will be

$$\frac{\dot{\gamma}_i}{\dot{\gamma}_0} = \left(\frac{\tau_i}{s_i}\right)^M \,. \tag{3.64}$$

With each phase exhibiting this type of power law response, the composite will behave according to

$$\frac{\dot{\overline{\gamma}}}{\dot{\gamma}_0} = \left(\frac{\overline{\tau}}{\bar{s}}\right)^M \,, \tag{3.65}$$

where $\bar{s}$ represents a composite hardness. From (3.64) and (3.65), we can solve for the viscosity ratios,

$$\frac{\mu_i}{\overline{\mu}} \equiv \frac{\tau_i/\dot{\gamma}_i}{\overline{\tau}/\dot{\overline{\gamma}}} = \frac{s_i}{\bar{s}} \left(\chi_i\right)^{\frac{1}{M}-1} \,. \tag{3.66}$$

Let $\Pi_i = s_i/\bar{s}$ represent the ratio of the average phase hardness to the composite hardness. Substituting expression (3.66) for $\mu_i/\overline{\mu}$ into (3.61) and simplifying the result, we obtain

$$\chi_i = \frac{5}{3} - \frac{2}{3}\Pi_i \chi_i^{\frac{1}{M}} \,. \tag{3.67}$$

The set (3.67), together with the self-consistency condition (3.60), yields a closed system of equations for the unknowns χ_i and $\bar{s}$, provided that $\overline{\tau}$ (or $\dot{\overline{\gamma}}$), f_i and s_i are given, along with material constants M and $\dot{\gamma}_0$. Integration of this system in conjunction with the hardening rules (3.63) provides a solution for $\overline{\tau}$ *versus* $\overline{\gamma}$. Either $\overline{\tau}$ or $\dot{\overline{\gamma}}$ can be used as the independent control variable. Note that defining a composite hardness, $\bar{s}$, as we have in (3.65), implies that the rate exponent M is the same in all phases. An equivalent form of (3.67) can be reached without using (3.65); however,

in this alternative formulation, one of the unknowns will be $\overline{\mu}$, which does not offer an interpretation as immediate as that offered by $\bar{s}$.

A Modified Self-consistent Model for Evolving Phase Fractions Accounting for Transformation Strain

Returning now to our dynamically evolving metastable austenite/martensite system, let us define $\dot{\gamma}^{slip} = \sqrt{2}\,\mathbf{D}^{slip}/\|\mathbf{D}^{slip}\|$ and separate it according to its contribution from the individual phases:

$$\dot{\gamma}^{slip} = f\dot{\gamma}_m + (1-f)\,\dot{\gamma}_a\ , \tag{3.68}$$

where $\dot{\gamma}_a$ and $\dot{\gamma}_m$ represent average equivalent shear strain rates due to slip in the austenite and martensite phases, respectively. Using (3.42), (3.46), (3.47) and (3.68), the equivalent plastic shear strain rate can now be written as

$$\dot{\overline{\gamma}}^p = f\dot{\gamma}_m + (1-f)\,\dot{\gamma}_a + A\dot{f}\ . \tag{3.69}$$

Apportionment of the plastic strain rate between the individual phases is of critical importance. As stated earlier, previous models for strain-induced transformation plasticity were based on the Voigt concept, an upper bound approximation for the composite stress in which it is assumed that $\dot{\gamma}_m = \dot{\gamma}_a = \dot{\overline{\gamma}}^p$. Because of the high hardness differences between the austenite and martensite, Voigt predictions lead to overestimates of the composite stress. Applying the model outlined in the previous section to this system, a loose condition of self-consistency of strain rates is enforced by requiring the macroscopic strain rate to equal the volume-averages of the local strain rates plus the transformation strain rate. This condition is automatically satisfied by (3.69). Self-consistency of stresses would require that $\overline{\tau} = f\tau_m + (1-f)\,\tau_a$. This condition must be relaxed, however, in order to satisfy (3.57, 3.59). In particular, model predictions of $\overline{\tau}$ will generally be less than $f\tau_m + (1-f)\,\tau_a$ by an amount proportional to $A\dot{f}\overline{\tau}/\dot{\overline{\gamma}}^p$. This term can be seen by first noting that (3.59) requires that $\tau_i/\overline{\tau}$ and χ_i are related as follows:

$$\frac{\tau_i}{\overline{\tau}} = \frac{5}{2} - \frac{3}{2}\chi_i\ . \tag{3.71}$$

Thus,

$$f\tau_m + (1-f)\,\tau_a = \overline{\tau}\left\{\frac{5}{2} - \frac{3}{2}\left[f\chi_m + (1-f)\,\chi_a\right]\right\} \ . \tag{3.72}$$

But, by (3.69),

$$f\chi_m + (1-f)\,\chi_a = 1 - A\frac{\dot{f}}{\dot{\overline{\gamma}}^p} \ , \tag{3.73}$$

so that, solving for $\overline{\tau}$:

$$\overline{\tau} = \left[f\tau_m + (1-f)\,\tau_a\right]\left[1 - \frac{3}{2}A\frac{\dot{f}}{\dot{\overline{\gamma}}^p}\right] \ . \tag{3.74}$$

The factor $\frac{3}{2}A\dot{f}/\dot{\overline{\gamma}}^p$ is of precisely the same form as the "dynamic softening" factor postulated by Narutani, *et al.* [21] to account for the softening effects of the transformation, which they supported with experimental data. The discrepancy between (3.74) and the self-consistency condition for stress will be large only when $A\dot{f} = \dot{\gamma}^{trans}$ is large compared with $\dot{\overline{\gamma}}^p$.

We also assume that apportionment of the plastic strain rates is not affected by either the elastic strain rates or by the hydrostatic part of the transformation strain rate (recall the assumption of composite incompressibility). Since $\dot{f}\Delta_V$ is generally much smaller than $\dot{\overline{\gamma}}^p$, the error introduced by this assumption is generally negligible. When $\dot{f}$ is large, however, $\dot{f}\Delta_V/\dot{\overline{\gamma}}^p$ can be sizable, and the predictions for $\dot{\gamma}_a$ and $\dot{\gamma}_m$ may lose a certain degree of accuracy. Nevertheless, the predicted values of $\dot{\gamma}_a$ and $\dot{\gamma}_m$ will still be much better than those obtained using a Voigt model. Also, due to the small strain hardening in these materials, composite stress predictions are relatively insensitive to small changes in the strain levels in the individual phases.

Let $\chi_i = \dot{\gamma}_i/\dot{\overline{\gamma}}^p$, where the subscript "i" refers to each of the two phases, and let $\chi_f = \dot{f}/\dot{\overline{\gamma}}^p$. Dividing (3.69) by $\dot{\overline{\gamma}}^p$ and substituting for $\dot{\gamma}_a/\dot{\overline{\gamma}}^p$, $\dot{\gamma}_m/\dot{\overline{\gamma}}^p$ and $\dot{f}/\dot{\overline{\gamma}}^p$ provides a self-consistency condition in terms of χ_a, χ_m and χ_f:

$$f\chi_m + (1-f)\,\chi_a + A\chi_f = 1 \tag{3.75}$$

Equation (3.75) together with (3.67) yields a closed system of three equations for the unknowns χ_a, χ_m and $\bar{s}$, provided that f, s_a and s_m are given, along with the material constant M. The equivalent plastic strain rate, $\dot{\overline{\gamma}}^p$, can then be expressed in

terms of $\overline{\tau}$, $\bar{s}$ and the material properties M and $\dot{\gamma}_0$ using (3.65). Thus we now have a system of equations for $\dot{\gamma}_a$ and $\dot{\gamma}_m$ in terms of f, s_a and s_m, $\overline{\tau}$, M and $\dot{\gamma}_0$.

An alternative constitutive formulation can be obtained by assuming that the self-consistent model accounts only for the slip strain-rates of the two phases. The transformation strain-rate term, $A\dot{f}$, is then added as an additional strain-rate that does not affect the apportioning of the slip strain-rates or the predictions of $\overline{\tau}$. The resultant stress–strain curve is, in effect, simply moved to the right by a distance Af relative to the stress–slip strain curve. With this approach, we do not directly violate either of the two self-consistency conditions. In an earlier modelling effort, we did, in fact, implement the model in such a manner, but found that we could not produce fits to experimental curves for $\overline{\tau}$ versus $\overline{\gamma}^p$ that were in reasonable accordance with the corresponding curves for f versus $\overline{\gamma}^p$. Experimental data for f and $\overline{\tau}$ are given in terms of $\overline{\gamma}^p$, but our model predicts $\dot{f}$ as a function of $\dot{\gamma}_a$. Thus, both f versus $\overline{\gamma}^p$ and $\overline{\tau}$ versus $\overline{\gamma}^p$ must be fit simultaneously, since $\dot{\gamma}_a$ is a quantity that must be evaluated within the model.

3.4.4 Phase Hardening Laws

The individual constituents are assumed to behave as power law hardening type materials, whose hardening rates can be expressed in the following general form:

$$h_i = \hat{h}_i(s_i) = \frac{s_i}{\sum_{j=1}^{L} C_j n_{ij} \left(\frac{s_i}{s_i^*}\right)^{n_{ij}}} , \tag{3.76}$$

where C_j, s_i^* and n_{ij} are constants. In most cases, a single exponent can be used ($L = 1$), yielding the more familiar form in which

$$h_i = \frac{s_i}{n_i} \left(\frac{s_i^*}{s_i}\right)^{n_i} , \tag{3.77}$$

and the second subscript of the hardening exponent is omitted for clarity.

Using the special form (3.77), an integral form of (3.63) is chosen such that the internal variables s_i are related to the *accumulated* strains γ_i as follows:

$$\left(\frac{s_i}{s_i^*}\right)^{n_i} = \gamma_i + \gamma_i^* , \tag{3.78}$$

where γ_i^* is a reference strain (constant). In a few cases, in order to produce a better fit to the experimental curves of a given phase, two exponential terms ($L = 2$) are employed such that the integrated relation becomes

$$C_1 \left(\frac{s_i}{s_i^*}\right)^{n_{i1}} + C_2 \left(\frac{s_i}{s_i^*}\right)^{n_{i2}} = \gamma_i + \gamma_i^* \ . \tag{3.79}$$

3.4.5 Accounting for the Inherited Dislocation Structure of Newly-formed Martensite

To complete the model, one final feature of the transformation process must be accounted for. It has been established that a unit of martensite which forms at a given plastic strain in the austenite actually *inherits* the strain-hardened dislocation structure of its parent austenite [14,78] Thus, each incrementally-formed bit of martensite is initially harder than the initial hardness of any previously-formed martensite, and substantially harder than the initial hardness of undeformed martensite. This feature is accounted for in the model by keeping a running average of the hardness levels of previously formed martensite. Each incremental unit of martensite is assumed to have an initial hardness which is a function of the plastic strain in the austenite from which it was instantaneously produced. In this manner, the *average* hardness of the martensite continues to increase as initially harder martensite is added, even though (at first) negligible deformation is occurring in the martensite because of its already high hardness. At each increment, all of the prior-formed martensite is assumed to have been exposed to the same "average" strain history, despite the fact that each unit of this group has actually seen a different strain history. The error introduced by this assumption is second order. Assuming a hardening law of the form (3.78) for the martensite, the following incremental hardening law is used to determine the average martensite hardness s_m:

$$s_m = \frac{f_0}{f}\left(s_{m_0} + h_m \dot{\gamma}_m \Delta t\right) + \frac{f - f_0}{f} s_m^* \left(\gamma_m^* + \gamma_a\right)^{n_m} \ , \tag{3.80}$$

where f_0 and s_{m_0} are the value of f and s_m at the previous time increment.

3.4.6 Final Form of the Constitutive Model

Now that we have fully defined the plastic strain rate tensor $\mathbf{D}^p$, we can express the evolution equations for $\dot{\bar{\tau}}$ and $\dot{p}$ in terms of the imposed total rate invariants $\dot{\gamma}^T$ and $\dot{e}^T$, and the unknown phase strain rates, $\dot{\gamma}_a$ and $\dot{\gamma}_m$. Substituting for $\dot{\bar{\gamma}}^p$ from (3.69) and $\dot{f}$ from (3.33) into (3.44, 3.45), and simplifying, we obtain

$$\dot{\bar{\tau}} = G'\left[\beta\dot{\gamma}^T - \{f\dot{\gamma}_m + (1-f)\dot{\gamma}_a\} - A(1-f)\left\{A'_f\dot{\gamma}_a + K'C_f\dot{e}^T\right\}\right] , \quad (3.81)$$

$$\dot{p} = -K'\left[\dot{e}^T - \Delta_V(1-f)\left(A_f\dot{\gamma}_a + D_f\dot{\bar{\tau}}\right)\right] , \quad (3.82)$$

where A_f and B_f are given in (3.34, 3.35) and

$$C_f = B_f/\sqrt{3}\bar{\tau} , \quad (3.83)$$

$$D_f = B_f p/\sqrt{3}\bar{\tau}^2 , \quad (3.84)$$

$$G' = G/[1 + G(1-f)AD'_f)] , \quad (3.85)$$

$$K' = K/[1 + K(1-f)\Delta_V C_f] , \quad (3.86)$$

$$A'_f = A_f[1 - K'(1-f)\Delta_V C_f] , \quad (3.87)$$

$$D'_f = D_f[1 - K'(1-f)\Delta_V C_f] . \quad (3.88)$$

The evolution of stress with strain has now been defined in terms of two scalar evolution equations for the stress invariant quantities $\bar{\tau}$ and p. A solution of these two equations in conjunction with evolution equations for f, s_a and s_m provides a complete description of the constitutive model for these steels.

3.5 Model Implementation

3.5.1 Numerical Procedure

The model has been implemented as a material-law subroutine (UMAT) which can be incorporated into the finite element code ABAQUS [103]. This code gives the user the flexibility of specifying a constitutive law through a "user material" subroutine option. The user is provided with the current level of Kirchhoff stress, $\mathbf{T_0}$, and any user-defined state variables (*i.e.*, for this material, γ_a, f, s_a, and s_m). The strain

increment $\Delta\boldsymbol{\epsilon}$ and the time increment Δt are also provided as an estimate of the kinematic solution for the increment. Within the subroutine, the stress tensor and the other state variables must be updated based on this estimate. We use an Euler backwards difference operator, so that

$$\Delta\mathbf{T} = \overset{\nabla}{\mathbf{T}}\Delta t\,, \tag{3.89}$$

where $\overset{\nabla}{\mathbf{T}}$ is the *updated* value of the Jaumann rate. We also utilize the method of radial-return [104], in which the deviatoric inelastic strain rate, $\mathbf{D}^{p'} = \frac{1}{\sqrt{2}}\dot{\bar{\gamma}}^{p}\mathbf{N}$, is assumed to be coaxial with the elastic predictor of the deviatoric stress, *i.e.*,

$$\mathbf{N} = \frac{(\mathbf{T_0} + 2G\Delta\boldsymbol{\epsilon})'}{\| (\mathbf{T_0} + 2G\Delta\boldsymbol{\epsilon})' \|}\,. \tag{3.90}$$

The complex nature of the proposed constitutive model leads to a relatively involved numerical integration procedure. We have chosen a bi-level structure in which the stress invariants, $\bar{\tau}$ and p, and the state variables f, s_a, s_m, are integrated at the outer level. An estimate of $\bar{\tau}$, p, f, s_a and s_m is first determined. Then, at the inner level, the set of equations which emerges from the self-consistent procedure (3.67, 3.75) is solved for χ_a, χ_m and $\bar{s}$. From this solution, the rate quantities required at the outer level ($\dot{\bar{\tau}}$, $\dot{p}$, $\dot{s_a}$, $\dot{s_m}$ and $\dot{f}$) are calculated. A Newton-Raphson method is used to solve each of these nonlinear sets of equations. After the integration of the material state is successfully completed, a material Jacobian, which represents the change in the increment in stress with respect to a virtual change in the increment in strain, must be computed. This quantity is used in ABAQUS in its global Newton scheme to achieve an accurate assessment of the incremental kinematics. In order to obtain a high rate of convergence, the Jacobian must be consistent with the integration operator.

Detailed time integration and Jacobian calculation procedures for our model are given in Appendix A.

3.5.2 Testing the Constitutive Model

A rather tedious but critical step in the implementation of the numerical model involves the testing of the numerical procedure. Here there are two important issues: the accuracy of the integration of the constitutive equations and the accuracy of each of the three required numerical Jacobians (one for each of the two Newton schemes internal to the UMAT subroutine and one passed back to ABAQUS for use in its global Newton scheme). The accuracy of the Jacobian does not affect the accuracy of the solution, but it can have profound effect on the solution time. An inaccurate Jacobian can also lead to divergence of the global Newton scheme, resulting in cutbacks in ABAQUS's time integration procedure which can bring the entire analysis to an abrupt halt.

Testing of the UMAT is facilitated by using a driver program which simulates the interface between the UMAT and the rest of the ABAQUS code. A listing of the driver used to develop the UMAT subroutine (listed in Appendix A) is given in Appendix B along with some additional details concerning this aspect of the research.

3.6 1-D Model Predictions and Discussion

In this section, we present one-dimensional model predictions, compare these predictions with available experimental data, and discuss the interesting features and the drawbacks of our model. We begin with the case of fixed phase fractions, where it is perhaps easier to demonstrate the salient features of the model and its inherent limitations. We then proceed to the more relevant case of the strain-induced transformations where we can show the effects of temperature and stress state on the response of our system.

3.6.1 Two-phase Materials with Fixed Phase Fractions

For a two-phase material, a useful expression can be developed relating the composite stress and strain rate to corresponding quantities in the respective phases. Let us

denote the softer of the two phases as "phase 1" [2] and the harder as "phase 2". One should expect then that $\tau_2 \geq \overline{\tau} \geq \tau_1$; $\dot{\gamma}_1 \geq \dot{\overline{\gamma}} \geq \dot{\gamma}_2$. Consider the difference in equivalent shear stress between the two phases, normalized by the composite average equivalent shear stress: $(\tau_2 - \tau_1)/\overline{\tau}$. Consider also the difference in the equivalent strain rates in the two phases, normalized by the macroscopic strain rate: $(\dot{\gamma}_1 - \dot{\gamma}_2)/\dot{\overline{\gamma}}$. Substituting for τ_1, τ_2, $\dot{\gamma}_1$ and $\dot{\gamma}_2$ from (3.59), we find that

$$\frac{\tau_2 - \tau_1}{\overline{\tau}} = \frac{5\mu_2}{3\overline{\mu} + 2\mu_2} - \frac{5\mu_1}{3\overline{\mu} + 2\mu_1} \; ; \tag{3.90a}$$

$$\frac{\dot{\gamma}_1 - \dot{\gamma}_2}{\dot{\overline{\gamma}}} = \frac{5\overline{\mu}}{3\overline{\mu} + 2\mu_1} - \frac{5\overline{\mu}}{3\overline{\mu} + 2\mu_2} \; . \tag{3.90b}$$

Dividing (3.90a) by (3.90b), we arrive at a normalized measure of the slope of the line connecting corresponding points, $(\dot{\gamma}_1, \tau_1)$ and $(\dot{\gamma}_2, \tau_2)$, which lie on the stress–strain rate curves of the individual phases. Upon rearrangement, this ratio reduces to the following simple form: [3]

$$\frac{\dfrac{\tau_2 - \tau_1}{\overline{\tau}}}{\dfrac{\dot{\gamma}_1 - \dot{\gamma}_2}{\dot{\overline{\gamma}}}} = \frac{3}{2} \; , \tag{3.91}$$

or

$$\frac{\tau_2 - \tau_1}{\dot{\gamma}_1 - \dot{\gamma}_2} = \frac{3}{2}\overline{\mu} \; . \tag{3.92}$$

Interestingly, when the strain hardening exponents n_1 and n_2 of the two phases are equal, an integrated form of (3.92) can be derived in an approximate manner to relate the equivalent shear stresses and *accumulated* equivalent plastic shear strains of the two phases and the composite; *i.e.*,

$$\frac{\dfrac{\tau_2 - \tau_1}{\overline{\tau}}}{\dfrac{\gamma_1 - \gamma_2}{\overline{\gamma}}} \approx 1.5 \; . \tag{3.93}$$

This approximation holds because of the relationship between $\dot{\gamma}_i$ and $\dot{\overline{\gamma}}$ given by (3.59a) and the fact that the Eshelby-type factors, $5/(3 + 2\overline{\mu}/\mu_i)$, change very little

[2] Here "softer" means lower viscosity: $\mu_1 < \mu_2$.

[3] See appendix C for details.

during the strain history for the case of equal strain-hardening exponents in both phases; therefore:

$$\frac{\gamma_1 - \gamma_2}{\overline{\gamma}} \approx \frac{\dot{\gamma}_1 - \dot{\gamma}_2}{\dot{\overline{\gamma}}} \,. \tag{3.94}$$

It is also interesting to note that an exact form of (3.93) can be derived by assuming the secant modulus relationships proposed by Berveiller and Zaoui [30], lending further credence to their method for small strain applications.

Equation (3.93) provides the geometric interpretation given in Fig. 3.4. The slope of the line connecting corresponding stress–strain points for the individual phases is approximately equal to -1.5 times the ratio of the macroscopic stress to the composite strain (*i.e.*, $\Delta\tau/\Delta\gamma = -1.5\overline{\tau}/\overline{\gamma}$). It is also evident from Fig. 3.4 that the distance between (γ_1, τ_1) and $(\overline{\gamma}, \overline{\tau})$ is equal to f_2 times the distance between (γ_1, τ_1) and (γ_2, τ_2). Likewise, the distance between (γ_2, τ_2) and $(\overline{\gamma}, \overline{\tau})$ is equal to f_1 times the distance between (γ_1, τ_1) and (γ_2, τ_2). Also shown in Fig. 3.4 is an analogous decomposition of the composite stress–strain curve according to a Voigt model, in which case the phase-average stress invariants are similarly weighted to determine the composite stress, but the associated phase-average strain invariants are assumed to be *equal* to that of the composite strain. Note that the self-consistent prediction of the composite stress can be significantly lower than the Voigt upper bound. Note also the slight deviation of the self-consistent prediction of the phase 2 stress from the Voigt prediction. This small difference is due to the slight rate-dependence of this harder phase as predicted by our model; the lower strain rate in the harder phase (relative to $\dot{\overline{\gamma}}$) reduces its flow stress. In general, the smaller the hardening exponents n_i, the closer the approximation. For example, when $f_1 = f_2 = 0.5$, $n_1 = n_2 = 0.06$, $M = 100$ and $s_2^*/s_1^* = 2$, the ratio given by (3.88) is about 1.497 during the entire strain history. For $n_1 \neq n_2$, the ratio is close to 1.5 for small strains, but deviates from 1.5 at larger strains, as shown in Fig. 3.5.

Fig. 3.6 summarizes the results for the two-phase, single exponent case ($L = 1$). The composite stress determined by our self-consistent method differs from the prediction of a Voigt model only when the rate exponent (M) is low and/or the hardness

ratio (s_2^*/s_1^*) between the two phases is high. For constituents which are relatively rate-insensitive ($M \gg 1$) and have small hardness differences, the difference between the stress levels predicted by the self-consistent method and the Voigt model is small. The apparent agreement is misleading, however. A Voigt prediction yields reasonable average *stresses* only because stress–strain curves are generally insensitive to the magnitude of strain apportioned to each phase, due to the small strain hardening exponents of power law relations. Higher hardening exponents, in fact, lead to greater differences between the predictions of the self-consistent and Voigt models, as is evident in Fig. 3.6

Despite the close agreement between the composite stress predictions of the two methods, the predicted *strain* levels in the individual phases are much different. For example, when $f_1 = f_2 = 0.5$, $M = 100$, $s_2^*/s_1^* = 5$, $n_1 = n_2 = 0.06$ and $\overline{\gamma} = 1.0$, the strains in the two phases as predicted by our method are $\gamma_1 = 1.43$ and $\gamma_2 = 0.565$, while the predicted normalized composite stress level at this strain, $\overline{\tau}_{SC}/s_1^* = 2.80$, does not differ appreciably from the Voigt prediction, $\overline{\tau}_V/s_1^* = 2.91$. Often, the softer phase has a much higher hardening exponent than the harder phase. For such materials, the differences between self-consistent predictions and Voigt predictions are generally even smaller. For example, if n_1 above is changed to 0.30, then $\overline{\tau}_{SC} = 2.79$, while $\overline{\tau}_V = 2.85$. The sizable strain difference between the two phases is an aspect of the problem that is lost using a Voigt model.

Comparison with Experiments

An extensive experimental study of stress–strain behavior in a class of dual-phase steels was performed by Wojewodzki [74]. She considered ferrite-martensite alloys with both banded and homogenized microstructures and varying phase fractions. These were 1.6Mn-0.75Si-0.20Mo alloys with carbon content varying from 0.052 to 0.42 weight percent, which enabled the volume fraction of the ferrite phase to vary while keeping the carbon content of the austenite constant at the critical annealing temperature. (The austenite transformed to martensite upon quenching.) The

banded microstructure was obtained from an intercritical annealing process which resulted in a complete dissolution of carbides present in the pearlite phase of the as-received steel and produced a dual-phase structure, but did not eliminate the heavily banded structure of the pearlite. The homogenized microstructure was obtained by a homogenization of the austenite for 50 hours at $1250C$ before quenching, which effectively eliminated the banding of the pearlite and produced a randomly dispersed microstructure.

We implemented our model using power law fits to Wojewodzki's experimental data. The one-term power law hardening relationship (3.78) was used to fit the data for the softer ferrite phase, while the two-term form (3.79) was employed to fit the martensite phase. Values for all constants are given in Table 3.1. Note that the hardnesses of the respective martensite phases of the dual-phase alloys differed from the hardness of the 100% martensite measured by Wojewodzki. This difference is due to the varying carbon content of the martensite phase in its single-phase state and in each of the dual-phase states. The martensite hardness versus plastic strain curves listed in Wojewodzki's thesis — to which we fit our power law model — were interpolated from the actual data using the carbon content measured during both the dual-phase tests and the pure martensite tests.

	Ferrite — see eq. (3.78)						
	s_1^*(MPa)	γ_1^*	n_1				
for all cases	384.	0.492	3.33				
	Martensite — see eq. (3.79)						
	f_2	s_2^*(MPa)	γ_1^*	C_1	C_2	n_{21}	n_{22}
banded	0.12	1273.	0.0197	0.01145	0.00171	1.1	23.5
"	0.27	1273.	0.0191	0.01175	0.00089	1.1	22.7
"	0.56	1273.	0.0166	0.01064	0.00044	1.1	23.6
"	0.86	1273.	0.0225	0.01353	0.00148	1.1	24.2
homog.	0.27	1263.	0.0140	0.00683	0.00252	1.1	13.6
"	0.64	1206.	0.0184	0.01064	0.00159	1.1	17.6
"	0.88	1211.	0.0170	0.01006	0.00125	1.1	19.4

Table 3.1 Constants used to fit Wojewodzki's [74] data.

A comparison between our model predictions and experimental results is given in Fig. 3.7 for the banded alloy and Fig. 3.8 for the homogenized alloy. Included in these curves are the predictions using the method of Tomota, *et al.* [105], as calculated by Wojewodzki, as well as predictions using a Voigt model (based on our fit to Wojewodzki's data). The values predicted by the self-consistent model for the banded alloy (Fig. 3.7) with 12% and 27% martensite are low in comparison with experiment and the predictions of the other models. This is a result of the extremely low strain levels predicted by the self-consistent model for the much harder martensite phase and the high hardening-rate of the martensite at these composite strain levels. At a given composite strain level, the self-consistent prediction of the martensite contribution to the composite flow stress is lower than that of the Tomota and Voigt models because the predicted martensite strain is lower and thus, because of the high hardening-rate, the predicted flow stress is much lower. In defense of the self-consistent predictions, however, the martensite stress versus plastic strain data taken from Wojewodzki was not well defined, especially at these extremely low strains. Not only were the martensite curves interpolated from actual data, as noted, but the given plastic strains were obtained by subtracting an estimate of the elastic strains from the measured values. It should also be noted that the austenite to martensite transformation has been shown to cause hardening of the surrounding ferrite material as a result of accommodation strains, leading to an increased composite hardness [106]. This effect is more significant at lower martensite volume fractions shown here, where the ferrite contribution to the total flow stress is greater.

Despite these two somewhat low values, it is clear from these curves that the self-consistent method described herein yields equal or better agreement to the experimental data than the Voigt or Tomota models. At very small strains, the Tomota model yields somewhat better agreement, but at the larger strains for which the model is intended to apply, the improvement is considerable in some cases. In fact, the Voigt model is not even strictly applicable at strain levels which are higher than

the strain at which experimental data for the martensite phase ceases (presumably because of fracture). The strain decomposition of the self-consistent method allows for predictions of composite behavior at strains which are also considerably higher than those which can be predicted using the Tomota model, further illustrating the usefulness of the method.

Discussion

The results which have been presented in this section for a two-phase, constant f_i material are clearly qualitatively correct: the harder phase is apportioned less strain than the composite and the softer phase is apportioned more strain according to how much harder or softer each phase is with respect to the composite hardness. The model leads to results that are more accurate than those obtained using a Voigt model, and are as good or better than those obtained by means of other, more complex models. (Note that Reuss [equal stress] predictions were not included in any of the figures; these greatly underestimate the composite behavior when the hardness differences are large.) As the rate exponent, M, approaches one, the localization law (3.59) becomes precise, and model predictions should be quite accurate. Similarly, as $\Pi_i = s_i/\bar{s}$ approaches one for each phase, model predictions become precise for all M.

The important question, then, is how reliable are model predictions when M is much greater than one (nearly rate-independent behavior), and Π_i differs significantly from one? Namely, how accurate is (3.59) for these cases? In response to this question, we compare our predictions for the strain-rate ratios, χ_i, at different values of M and Π_i with the finite element predictions of Gilormini and Germain [107]. Their calculations are based on a variational formulation for incompressible power law viscous materials, suggested by Hill [86], which they applied to the case of a power law spherical inclusion embedded within a power law matrix of the same exponent,

but different hardness ($\Pi_i \neq 1$). The results of this comparison are shown in Fig. 3.9. Note that their model provides data for the variation of $\dot{\gamma}$ within the inclusion, and the finite element predictions for χ_i shown in Fig. 3.9, represent averages of the numerical results over the inclusion volume. As one might expect, current model predictions of χ_i become increasingly different from the finite element calculations as $1/m$ approaches zero. The differences also grow larger as Π_i departs from one. These differences suggest that our model generally overestimates the strain in the harder phase and underestimates the strain in the softer phase. The differences appear to be greater for harder phases, $\Pi_i > 1$, than for softer phases, implying that, when roughly equal amounts of all phases are present, our estimates of the strain in harder phases are generally less accurate than our estimates of the strain in softer phases.

The trends shown in Fig. 3.9 suggest that, for near rate-independent, two-phase materials, stress–strain behavior can be quite reasonably predicted for phases whose hardnesses differ by a factor of about three or less, *i.e.*, $s_2/s_1 = \Pi_2/\Pi_1 < 3$. When s_2/s_1 becomes much larger than three, the accuracy provided by the localization law (3.59) becomes increasingly worse (assuming that the finite element calculations are accurate for large values of M). It will always, however, be much better than that obtained from a Voigt prediction ($\chi_i \equiv 1$). Furthermore, the errors in predicted strain will tend to cancel themselves out (just as they do in the Voigt model), in that an overestimate of strain in the harder phase will always be accompanied by an underestimate of the strain in the softer phase. The predictions of composite stress will thus be relatively insensitive to errors owing to the use of an inaccurate localization law, especially for low strain-hardening materials in which the flow stress is already insensitive to changes in strain.

The austenite-ferrite data shown in Figs. 3.7 and 3.8 suggest that reasonable predictions of composite behavior can be obtained even when the hardnesses of the hard and soft phases differ by a factor of 4 or 5. A more accurate localization law which partitioned less strain to the harder phase would probably bring the 86% and

56% martensite curves of Fig. 3.7 and the 88% and 64% martensite curves of Fig. 3.8 into better agreement with the experimental data, but not by much. The low values obtained for the 12% and 27% cases shown in Fig. 3.7 would probably not be improved by a better localization law; as mentioned previously, the errors here are more likely attributable to an inaccurate fit to the 100% martensite data at low strain.

The variational principles outlined in [107], which are the basis of the finite element calculations given in Fig. 3.9, may lend themselves to the development of an improved localization law which is applicable for near rate-independent materials having large hardness differences. A model derived from such a variational formulation, if tractable, offers itself as an attractive alternative to the simple model presented here. The development and implementation of such a model remains a topic for further investigation.

Finally, it is interesting to note that, in the limiting case of a rigid inclusion ($\mu_2 \to \infty$) embedded in a nonlinear viscous matrix, (3.59) and (3.67) can be simplified to produce the following relationship between Π_1 and χ_1:

$$\Pi_1 = \frac{\chi_1^{1-\frac{1}{m}}}{1 - \frac{2}{5} f_2} \,. \tag{3.95}$$

This relationship is equivalent to one given by Ponte Castañeda and Willis [96] as part of an upper bound estimate of composite behavior which they derived using a different variational principle. In light of these investigations, our estimated strain decomposition likely leads to an upper bound approximation which is much better than the Voigt prediction, but perhaps can be improved upon in cases where the hardness differences are large.

The simple model presented here for multiphase materials with fixed phase fractions yields quite reasonable agreement with experimental data in the application considered, despite the limitations inherent in its simplicity. The approximate nature of the localization law used in the model limits its applicability in cases where the

rate sensitivity of the constituent phases is low and the hardness differences are also high. One might argue that a lack of consideration of such effects as particle shape or local effects due to the size scale of the microstructure also limits the usefulness of the model. Nevertheless, these generally good results suggest that the model can be effective in appropriate situations. One should, however, be careful when applying such a model to materials in which the size scale of the individual phases is so small that the material model outlined here, which is meant to apply to coarse microstructures, is not representative of the material behavior of each phase in regions of fine microstructure.

3.6.2 Metastable Austenite/Martensite Transforming Materials

Comparison with Experiments

The most complete set of data for strain-induced martensitic transformation kinetics in uniaxial tension, covering a wide range of test temperatures, is the data of Angel [53], obtained on an annealed type 304 stainless steel. It was to this data set that the Olson-Cohen kinetic model was originally fit [20]. In the case of isothermal deformation at constant stress state, Σ, the original and present model are equivalent, so that the current model will fit the Angel data equally well.

For the high strength austenitic steels in which transformation toughening has been studied, Young [7] has measured martensite evolution with plastic strain during both uniaxial tension and compression tests. The particular alloy studied is a 10Ni-16Cr-0.5Mn-0.33P-0.25C phospho-carbide strengthened austenitic stainless steel. The results of the tests are shown in Fig. 3.10 along with a fit to the data using the present model. Parameters used for our calculations are listed in Table 3.2. The proposed model is able to fit these data reasonably well. Compared to the case of lower strength austenitic steel [53], high strength data are rather limited at higher

temperatures. This is due to the very small extent of uniform elongation seen at these temperatures before a necking instability occurs. Due to the Bridgman effect, reliable data cannot be determined past necking because the stress state becomes progressively nonuniform.

$T\ (°K)$	304	338	369	373	388	399
α	13.0	10.1	7.5	7.5	7.0	6.9
β_0	r	g_0	g_1	g_2	$\bar{g}$	s_g
4.42	4.0	-2120	1450	490	3230	290

Table 3.2 Constants used to fit Young's [7] data.

As discussed earlier, the high-strength austenitic steels employed in toughening studies and for which the kinetic data of Fig. 3.10 were generated [7], show high uniform ductility over a rather limited temperature range. Available flow property data for the individual phases are also limited. For lower strength austenitic steels, however, the thorough investigation of tensile deformation behavior by Narutani, Olson and Cohen [21] provides extensive data for a series of compositions, including the directly measured properties of austenite and martensite. A comparison of model predictions with the experimental data for a 14Cr-7Ni metastable austenitic steel are shown in Fig. 3.11. Values for all constants used in the model are listed in Table 3.3, including the kinetics constants which fit the data for the martensite volume fraction versus plastic strain given. The constant values (A_0, A_1) chosen for the A coefficient produce the solid line given in Fig. 3.3, which is in reasonable accordance with the given experimental data. The modified self-consistent method clearly yields a solution which matches the shape of the experimental curves quite well, including the early softening associated with transformation deformation, most noticeable in the $T = 223K$ curve. Note that although the combined influences of the softening/hardening effects of transformation give the stress-strain curve a sigmoidal shape qualitatively similar to that of the volume fraction martensite-strain curve, the inflection point of the former occurs at significantly higher strain than the latter.

austenite hardening parameters — see eq. (3.78)						
$T(°K)$	s_a^* (MPa)	γ_a^*	n_a			
223	697.	0.275	1.0			
263	581.	0.300	1.0			
296	496.	0.355	1.0			
martensite hardening parameters — see eq. (3.79)						
$T(°K)$	s_m^* (MPa)	γ_m^*	C_1	C_2	n_{m1}	n_{m2}
223	865.0	0.052	0.1965	0.8035	5.0	19.9
263	841.0	0.052	0.3107	0.6893	5.6	20.7
296	815.0	0.040	0.0552	0.9448	1.8	18.9
martensite evolution constants						
$T(°K)$	α	$\beta = \beta_0 P$	r_I			
223	8.4	4.2	4.0			
263	4.0	4.0	4.0			
296	2.7	2.6	4.0			
shape-strain constants			rate constants			
$T(°K)$	A_0	A_1/s_a^* (MPa)$^{-1}$				
223	0.02	1.72×10^{-5}	$M = 100$			
263	0.02	1.72×10^{-5}	$\dot{\gamma}_0 = 0.007/s$			
296	0.02	1.72×10^{-5}				

Table 3.3 Constants used to fit Narutani, *et al.'s* [21] data. Note that the indicated austenite hardening parameters produce a linear fit to the near-linear austenite stress-strain data given in [21]. Note also that since only tensile $f - \overline{\gamma}^p$ and $\overline{\tau} - \overline{\gamma}^p$ data were measured, driving force constants g_0, g_1, g_2, $\bar{g}$ and s_g could not be distinguished. Thus, values for $\beta = \beta_0 P$ were chosen simply to yield the best fit to the $f - \overline{\gamma}^p$ data shown in Fig. 3.11.

An Example Problem

To illustrate the importance of the stress-state sensitivity of the transformation, we performed a few numerical analyses using the ABAQUS program. We first considered a very simple one-element model under the following states of stress: plane strain tension, simple tension, pure shear, simple compression, and plane strain compression. Each of these five cases is characterized by a different level of triaxiality (Since Poisson's ratio for these steels is not equal to one-half ($\nu \approx 0.3$), in plane strain the triaxiality evolves to a certain extent; thus the values given for plane strain are only

approximate):

$$\begin{aligned} \text{plane strain tension :} \quad & \Sigma \approx 0.577 \ ; \\ \text{simple tension :} \quad & \Sigma = 0.333 \ ; \\ \text{simple shear :} \quad & \Sigma = 0.0 \ ; \\ \text{simple compression :} \quad & \Sigma = -0.333 \ ; \\ \text{plane strain compression :} \quad & \Sigma \approx -0.577 \ . \end{aligned}$$

In each case, we loaded the element under displacement control, until equivalent shear strain levels of order one-half were reached. The results from these five cases are summarized in Figs. 3.12 and 3.13. Material parameters used for these calculations were estimated for the high-strength austenitic steel studied by Young [7] using the kinetic parameters of Fig 3.10, with flow parameters estimated from available data. The model temperature for each case was $373K$, which is about halfway between the experimentally estimated values of $M^{\sigma}_{s,ut}$ and $M_{d,ut}$ for this material. The evolution of martensite with equivalent plastic strain, shown in Fig. 3.12, indicates dramatic differences between the extreme cases of plane strain tension versus plane strain compression. Recall that the triaxiality level affects the formation of martensite only through the driving force argument g of the probability function P. As mentioned earlier, the significance of these data is that they suggest that at higher triaxialities, such as near a crack tip, where $\Sigma > 2.0$, significant amounts of martensite can form even at temperatures that are well above the M_d temperature for uniaxial tension.

Fig. 3.13 shows how dramatically the martensite changes the equivalent stress-strain curve. In plane strain compression, for example, very little martensite forms and the resulting stress-strain curve differs little from the curve for 100% austenite. On the other hand, in plane strain tension, significant martensite evolution results in a stress-strain curve with a unique "S"-shape that ultimately approaches the curve for 100% martensite at this temperature. Note the early strain-softening in this case, where the plane strain tension curve dips well below the curve for plane strain compression, and thus well below the pure austenite curve. This is a result of the transformation strain-rate term which was incorporated into the model (see eq. 3.48). Note that the dip in the curve occurs at the same strain level at which the volume fraction curve has the steepest slope, *i.e.*, where $df/d\bar{\gamma}^p$ reaches its maximum value.

Discussion

Uniaxial tension and compression represent a fairly narrow spectrum of possible triaxialities ($\Sigma = -1/3$ for simple compression and $\Sigma = 1/3$ for simple tension). Of utmost interest are the triaxialities near the tip of a crack ($\Sigma > 2.0$). The linear form of the triaxiality ratio, as it appears in (3.28), when extrapolated to crack-tip triaxialities, appears to overestimate the extent of martensite formed in such a region, based upon indirect calculations which utilize experimentally-predicted crack-tip M_s^σ measurements [6,7] For this reason, an alternative quadratic form for (3.28), in which

$$g = g_0 - g_1\Theta + g_2\Sigma - g_3\Sigma^2 \,, \tag{3.96}$$

has also been considered, based on statistical analysis of nucleation site orientation effects [29]. The size scale of the highly stressed regions near the tip of a crack is too small to obtain reliable direct measurements of martensite evolution with respect to strain and stress state; in particular, the gradients of f are too large near the tip to be measured accurately. An experimental investigation using notched tensile specimens is currently in progress in order to evaluate the extent of transformation at intermediate levels of triaxiality [108]. This study should provide more data along the triaxiality spectrum with which to fit the net driving force parameter g.

Nevertheless, the data of Fig. 3.10 clearly illustrate the need to consider the stress-state dependence of transformation kinetics in a constitutive model for transformation plasticity. Of course, the ability to obtain reasonable agreement with experimental data is not the primary motivation for the development of this model. Its value lies in its ability to model the phenomenon of strain-induced transformation plasticity under complex states of stress.

It might be further argued that the proposed model suffers from a lack of consideration of such effects as particle shape — the martensite phase which forms during transformation plasticity in the strain-induced regime is certainly not spherical, but rather rodlike — or local effects due to the size scale of the microstructure.

Perhaps a better model of the flow behavior of this system might also be arrived at by directly solving the Eshelby-type problem of a matrix with an inhomogeneous

inclusion which undergoes a transformation strain. The solution to such a problem would likely produce a set of Eshelby-type equations analogous to (3.59) which leads to self-consistency conditions for both the strain-rates (including the transformation strain-rate) and the stresses. It is not clear, however, whether such a model would lead to more reasonable predictions than those presented here. Given the complexity of the constitutive behavior that we have considered here, several assumptions must be made in deriving any tractable model, and model predictions must ultimately be fit to experimental data through adjustable model parameters.

Finally, we note that, in formulating the model as we have, we restrict ourselves to proportional loading histories. When slip occurs in the austenite matrix near in the proximity of the much harder martensite phase, the interaction of dislocations with the hard martensite particle leads to an increase in the resistance to slip. This is indirectly accounted for in the model through the stress-dependence of the A-coefficient (eq. 3.47). Upon reversal of loading, however, the opposite will be true — it will be much easier for dislocations to propagate past the martensite particles, and thus the overall resistance to slip will decrease. Incorporation of this feature into the model would require the use of a tensorial internal variable which would track changes in local loading direction and adjust the flow resistance accordingly. Although such a variable could be incorporated into the model relatively easily, it would not be of much help in the analysis of the types of boundary problems that we are considering in this thesis. We therefore leave the incorporation of this feature as a future modeling effort that will be necessary when more complicated loading histories are encountered.

The reasonable fits to experimental data for both martensite evolution versus strain and stress versus strain indicate that this relatively simple model can be useful for numerical study of boundary value problems. In particular, this model reasonably represents the unusual property of pressure-sensitive strain-hardening in these materials, a feature that must be accounted for in examining the sources of their remarkable fracture toughness.

3.7 A Continuum Model for Void Nucleation and Growth

The constitutive model introduced in section 3.4 does not account for the strain-softening and subsequent destabilizing effects of void nucleation, growth and coalescence. As such, any insight into the failure process must be gathered in terms of localization and/or nucleation criteria, such as that offered by Needleman and Rice [23] (see section 2.5.2). In order to *directly* account for these mechanisms, we must incorporate the porosity evolution provided by nucleation and growth into our continuum model. Because of the already complex nature of the model, we assume that there is no interaction between transformation dilatation and void nucleation.

3.7.1 Theory

Following the techniques which have been used in numerous recent investigations [22, 109–113], we propose to account for porosity evolution using the model of Gurson [24,25], as modified by Needleman and Tvergaard [22]. Based on his solution for an incompressible matrix with a spherical cavity, Gurson proposed a plastic potential function, Φ, accounting for the effect of porosity on plastic flow. The functional form of Φ has since been modified by Needleman and Tvergaard [22] so that a complete loss of stress-carrying capacity is predicted at a reasonable value of void volume fraction. The modified plastic potential function, Φ, is given by:

$$\Phi(\overline{\tau}, \overline{\tau}_M, \rho) = \frac{\overline{\tau}^2}{\overline{\tau}_M^2} + 2\rho^* q_1 \cosh\left(\frac{3}{2} q_2 \Sigma_M\right) - 1 - (q_1 \rho^*)^2 = 0 \,, \qquad (3.97)$$

where $\overline{\tau}_M$ is the *matrix* equivalent shear stress, $\overline{\tau}$ is the now interpreted as the *effective* average macroscopic equivalent shear stress, Σ_M is the *matrix* triaxiality and q_1, q_2 are constants. Tvergaard [114] showed that $q_1 = 1.5$ yields good agreement with numerical studies of periodically distributed spherical voids. Further modification of Φ to account for material failure through void coalescence is accomplished through an effective porosity function, $\rho^*(\rho)$, defined as:

$$\rho^* = \begin{cases} \rho & \rho \leq \rho_c \\ \rho_c + K_\rho (\rho - \rho_c) & \rho > \rho_c \end{cases} \,, \qquad (3.98)$$

where ρ is the void volume fraction, ρ_c is the critical value of ρ at which void coalescence is first observed, and K_ρ is an "acceleration" function, which accounts for the increased damage due to void coalescence, given by

$$K_\rho = \frac{\rho_U^* - \rho}{\rho_F - \rho_c} , \tag{3.99}$$

where $\rho_U^* = 1/q_1$ is the void volume fraction at which the plastic potential function (3.97) predicts a complete loss of stress-carrying capacity and ρ_F is the actual void volume fraction associated with a complete loss of stress-carrying capacity. Experimental investigations have shown that the ligaments connecting neighboring voids fail when the voids have grown in size to the order of their spacing. Consistent with the calculations of Brown and Embury [115], we take $\rho_c = 0.15$. We further assume that $\rho_F = 0.25$, a value that has been determined through numerical analyses [116], and is consistent with experimental observations of failure in AISI 4340 alloy steel [68]. The values $\rho_c = 0.15$ and $\rho_F = 0.25$ are commonly used in the literature (*e.g.*, [109,114]).

In normalized stress space ($\overline{\tau}/\overline{\tau}_M$ versus $-p/\overline{\tau}_M$), this potential function produces the loci of points shown in Figure 3.14 for various values of ρ^*. When $\rho^* = 0$, the potential surface follows a horizontal line, indicating a lack of pressure dependence. As ρ^* increases, the potential surface approaches the origin. Plastic flow becomes pressure dependent — the shear stress necessary for plastic flow at fixed void volume fraction decreases with increasing negative pressure. The direction of plastic flow is taken to be normal to the potential surface, so that the plastic strain rate tensor is given by

$$\mathbf{D}^p = \dot{\lambda}\frac{\partial \Phi}{\partial \mathbf{T}} , \tag{3.100}$$

where $\dot{\lambda}$ is a scalar quantity that must be determined from the work hardening properties of the matrix. In the absence of transformation dilatation, macroscopic normality of plastic flow is a direct consequence of matrix normality [117].

Analogous to (3.42), (3.100) can be separated into deviatoric and hydrostatic parts as

$$\mathbf{D}^p = \dot{\lambda}\left[\frac{1}{\sqrt{2}}\frac{\partial \Phi}{\partial \overline{\tau}}\mathbf{N} + \frac{\partial \Phi}{\partial p}\mathbf{1}\right] . \tag{3.101}$$

Requiring the macroscopic plastic work rate equal the matrix plastic work rate yields

$$\mathbf{T} \cdot \mathbf{D}^p = (1 - \rho^*)\overline{\tau}_M \dot{\overline{\gamma}}^p_M \,, \tag{3.102}$$

where $\dot{\overline{\gamma}}^p_M$ is the equivalent plastic strain rate *in the matrix.* Substituting for $\mathbf{D}^p$ in (3.102) from (3.101) and solving for $\dot{\lambda}$ yields:

$$\dot{\lambda} = \left[\frac{(1 - \rho^*)\overline{\tau}_M}{\overline{\tau}\frac{\partial \Phi}{\partial \overline{\tau}} + p\frac{\partial \Phi}{\partial p}}\right] \dot{\overline{\gamma}}^p_M \,. \tag{3.103}$$

The rate of porosity evolution, $\dot{\rho}$, is taken to have a contribution from nucleation of new voids and growth of existing voids:

$$\dot{\rho} = \dot{\rho}_{nucleation} + \dot{\rho}_{growth} \,. \tag{3.104}$$

The rate of void nucleation is further seen as a general function of three terms: a strain-based term and two stress-based terms (a deviatoric term and a hydrostatic term):

$$\dot{\rho}_{nucleation} = A_n\left(\overline{\gamma}^p_M\right)\dot{\overline{\gamma}}^p_M + B_n\left(\overline{\tau}, p\right)\dot{\overline{\tau}}_M + C_n\left(\overline{\tau}, p\right)\dot{p} \,. \tag{3.105}$$

As we discussed briefly in section 2.5, nucleation is likely predicated on a stress-based criterion. An approximate correspondence with the maximum normal interfacial stress criterion is provided by setting $A_n = 0$, $C_n = -1/\sqrt{3}B_n$. In certain cases, however, numerical procedures are simplified by assuming a strain-controlled nucleation criterion ($B_n = C_n = 0$). In analyzing problems in which the gradients in triaxiality are not severe, stress-based nucleation criteria and strain-based nucleation criteria lead to similar results. However, in cases where gradients in triaxiality are steep, namely ahead of the tip of a crack, these two assumptions lead to significantly different material behavior. In these cases, the arguments presented in section 2.5 strongly suggest that a stress-controlled nucleation criterion should be used.

Following Chu and Needleman [118], we assume that for strain-controlled nucleation there exists a Gaussian distribution for the critical nucleation strain, such that

$$A_n = \frac{\rho_N}{\sqrt{2\pi}s_N} exp\left[-\frac{1}{2}\left(\frac{\overline{\gamma}^p_M - \overline{\gamma}^p_N}{s_N}\right)^2\right] \,, \tag{3.106}$$

where ρ_N is the total volume percentage of nucleating particles, $\overline{\gamma}^p_N$ is a mean nucleation strain and s_N is a standard deviation about that mean. Similarly, for stress-controlled nucleation, we assume a Gaussian distribution for the critical nucleation stress, such that

$$B_n = -\sqrt{3}C_n = \frac{\rho_N}{\sqrt{2\pi}s_N} exp\left[-\frac{1}{2}\left(\frac{\left(\sqrt{3\overline{\tau}} - p\right) - \sigma_N}{s_N}\right)^2\right], \tag{3.107}$$

where σ_N is a mean nucleation stress and s_N is the corresponding standard deviation.

In the absence of transformation dilatation, growth of voids subsequent to nucleation follows from the plastic incompressibility of the matrix:

$$\dot{\rho}_{growth} = (1 - \rho^*)(tr\mathbf{D}^p) \tag{3.108}$$

Following [112], in order to avoid problems arising from a flow stress which approaches zero, the void volume fraction ρ is maintained at a constant level when it reaches the value $\rho = 0.95\rho_F$. Phase hardness levels s_a and s_m are also fixed at this point.

Finally, the effect of porosity evolution on *elastic* response is determined using a self consistent model, whereby the elastic constants G and K become functions of the volume fraction of voids, and the matrix elastic constants G_M and K_M. We use self-consistent estimates of elastic behavior derived by Budianksy [119] for an isotropic random distribution of spherical voids. Following [119], the elastic moduli are taken to satisfy the following set of simultaneous equations:

$$\rho^*(1-a)^{-1} + (1-\rho^*)[1 - a + a(K_M/K)]^{-1} = 1, \tag{3.109}$$

$$\rho^*(1-b)^{-1} + (1-\rho^*)[1 - b + b(G_M/G)]^{-1} = 1, \tag{3.110}$$

where

$$a = \frac{1}{3}\left(\frac{1+\nu}{1-\nu}\right), \tag{3.111}$$

$$b = \frac{2}{15}\left(\frac{4-5\nu}{1-\nu}\right), \tag{3.112}$$

$$\nu = \left(\frac{3\kappa - 2\mu}{6\kappa + 2\mu}\right). \tag{3.113}$$

The model for porosity evolution that we have outlined in this section is incorporated into our constitutive procedure simply by taking $\dot{\overline{\gamma}}^p$ in (3.44) equivalent to

$\dot{\lambda}(\partial\Phi/\partial\overline{\tau})$ and $\dot{e}^p_V$ in (3.45) is equivalent to $\dot{\lambda}(\partial\Phi/\partial p)$. In addition, the power law expression (3.65) relating composite stress and strain-rate must now be taken to hold for the *matrix* quantities, *i.e.*,

$$\frac{\dot{\overline{\gamma}}^p_M}{\dot{\gamma}_0} = \left(\frac{\overline{\tau}_M}{\bar{s}}\right)^M . \tag{3.114}$$

The modified final form of the constitutive model (3.81, 3.82) then becomes

$$\dot{\overline{\tau}} = G'\left[\beta\dot{\gamma}^T - Z_1\left\{f\dot{\gamma}_m + (1-f)\dot{\gamma}_a\right\} - A(1-f)\left\{A'_f\dot{\gamma}_a + K'C_f\dot{e}^T\right\}\right], \tag{3.115}$$

$$\dot{p} = -K'\left[\dot{e}^T - Z_2\dot{\overline{\gamma}}^p_M - \Delta_V(1-f)\left(A_f\dot{\gamma}_a + D_f\dot{\overline{\tau}}\right)\right] , \tag{3.116}$$

where, using (3.101 and 3.103),

$$Z_1 = \left[\frac{(1-\rho^*)\overline{\tau}_M\frac{\partial\Phi}{\partial\overline{\tau}}}{\overline{\tau}\frac{\partial\Phi}{\partial\overline{\tau}} + p\frac{\partial\Phi}{\partial p}}\right] , \tag{3.117}$$

$$Z_2 = \left[\frac{(1-\rho^*)\overline{\tau}_M\frac{\partial\Phi}{\partial p}}{\overline{\tau}\frac{\partial\Phi}{\partial\overline{\tau}} + p\frac{\partial\Phi}{\partial p}}\right] . \tag{3.118}$$

Numerically, integration of the constitutive equations becomes much simpler if we assume that

$$Z_1^{k+1} = Z_1^k , \tag{3.119}$$

$$Z_2^{k+1} = Z_2^k , \tag{3.120}$$

$$\rho^{*,k+1} = \rho^{*,k} , \tag{3.121}$$

where the superscript k indicates the value of the parameter at the beginning of the increment, and $k+1$ indicates its value at the end of the increment. Assuming that the increment size is small, this approximation should not greatly affect model predictions.

3.7.2 One-dimensional Effects of Void Nucleation and Growth

In this section, we present several figures showing the effects of void nucleation and growth on model predictions for uniaxial stress states. As a baseline for these examples, we choose the following for strain-based nucleation parameters: $\rho_N = 0.04$,

$\overline{\gamma}^p_N = 0.5$ and $s_N = 0.10$. These choices are approximately equivalent to values often used in the literature for high strength steels (*e.g.* [110,112]). All other material parameters are the same as given in Tables 3.2 and 3.3. Unless indicated, these analyses were carried out for the non-transforming material.

Fig. 3.15 shows the evolution of $\rho_{nucleation}$, ρ_{growth}, ρ and ρ^* with equivalent plastic strain, $\overline{\gamma}^p$ determined from a one-element, plane strain finite element analysis. The curve for $\rho_{nucleation}$ takes the shape of a cumulative Gaussian function corresponding to the chosen ρ_N, $\overline{\gamma}^p_N$ and s_N. Growth of voids becomes significant when about one-half of the particles have nucleated (*i.e.*, $\rho = 0.02$); ρ_{growth} then evolves in a relatively smooth fashion. The void volume fraction, $\rho = \rho_{nucleation} + \rho_{growth}$ increases accordingly until it reaches its ultimate numerical value: $\rho = 0.95\rho_F = 0.2375$, where it abruptly levels off. The function ρ^*, as per (3.99), is equal to ρ until it reaches the critical value, $\rho_c = 0.15$, at which point the acceleration due to coalescence begins to take effect, and ρ^* begins to increase at a much faster rate. It too reaches a constant value where $\rho = 0.95\rho_F$.

Figure 3.16 compares the stress-strain response for cases where: nucleation is not accounted for; only nucleation is accounted for, and when both nucleation and growth are accounted for. There is little difference between model predictions with and without void nucleation until strains of about 40% are reached. Thus, void nucleation and growth should not greatly affect the fits to experimental data given in Fig. 3.11. The curve illustrating the effects of nucleation (only) drops as $\rho_{nucleation}$ increases, but then increases again as $\rho_{nucleation}$ reaches its saturation value, ρ_N. In the relatively low triaxiality stress state of plane strain, a build-up of 4% porosity results in a an 8% decrease in the flow stress, as (3.98) would predict. With both nucleation and growth accounted for, porosity continues to evolve, and the flow stress drops with increasing strain. The onset of coalescence is noticeable here as the point where the flow stress begins to decrease at a much faster rate. Finally, when $\rho = 0.95\rho_F$, the stress levels off at value which is about 13% of yield stress.

Figs. 3.17 and 3.18 illustrate the effect of altering the nucleation parameters $\overline{\gamma}^p_N$ and ρ_N. Increasing $\overline{\gamma}^p_N$ pushes both the $\rho - \overline{\gamma}^p$ and the $\overline{\tau} - \overline{\gamma}^p$ curves toward the right.

Increasing ρ_N (Fig. 3.18) causes the slope of the $\rho - \overline{\gamma}^p$ curve to increase, and thus increases the extent of softening relative to the case where $\rho_N = 0$.

The effect of triaxiality is illustrated in Fig. 3.19. Increasing triaxiality produces an effect similar to that produced by increasing ρ_N: the slope of the $\rho - \overline{\gamma}^p$ curve increases and so does the extent of strain-softening. Note that the $\Sigma = 1$ curve shown here was obtained using the driver program (see appendix B) and not from a finite element analysis.

Finally, the effect of martensitic transformation (at fixed triaxiality) on the slope of the stress-strain response is summarized in Fig. 3.20 for three temperatures: $T = 773K$ (no transformation), $T = 423K$ ($\Theta \approx 0.8$), and $T = 373K$ ($\Theta \approx 0.6$). For purposes of illustration, the phase hardening parameters for each case were assumed to equal that of the $T = 373K$ case. Because the model for porosity evolution used in these examples is strictly strain-based, transformation has little or no effect on the evolution of ρ. For this reason, void coalescence causes acceleration of softening at about the same strain level ($\overline{\gamma}^p = 2.0$) and, ultimately, the response at all three temperatures is controlled by this process. Prior to the onset of void coalescence, however, it is evident that transformation, and its associated strain-hardening, can lead to a 2 to $2\frac{1}{2}$ times increase in the strain at which strain-softening (*i.e.*, $d\overline{\tau}/d\overline{\gamma}^p < 0$) first occurs.

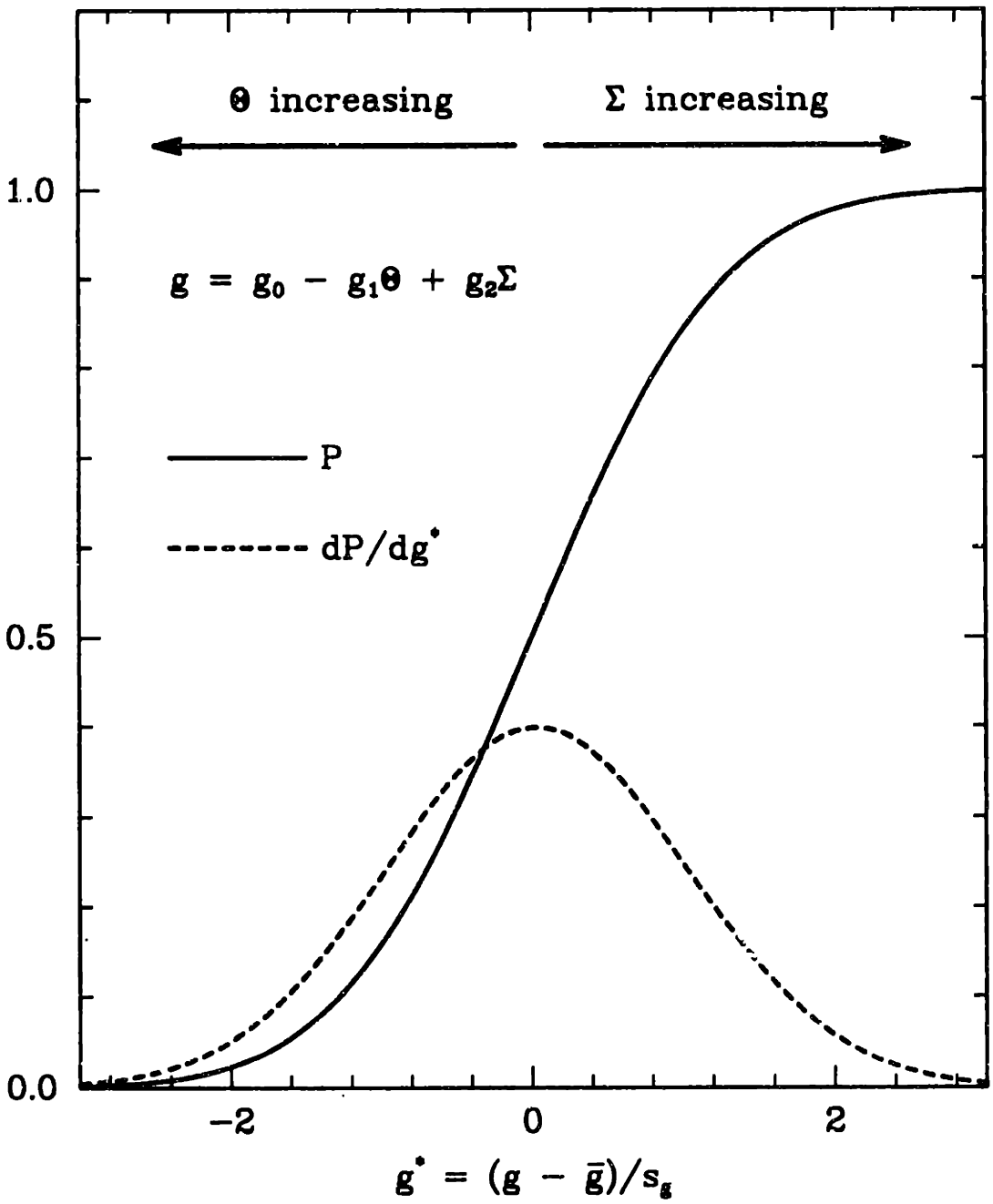

Figure 3.1 Probability function, P, and its derivative with respect to a normalized driving force, $(g-\bar{g})/s_g$, illustrating the effect of normalized temperature (Θ) and triaxiality (Σ) on the driving force for transformation.

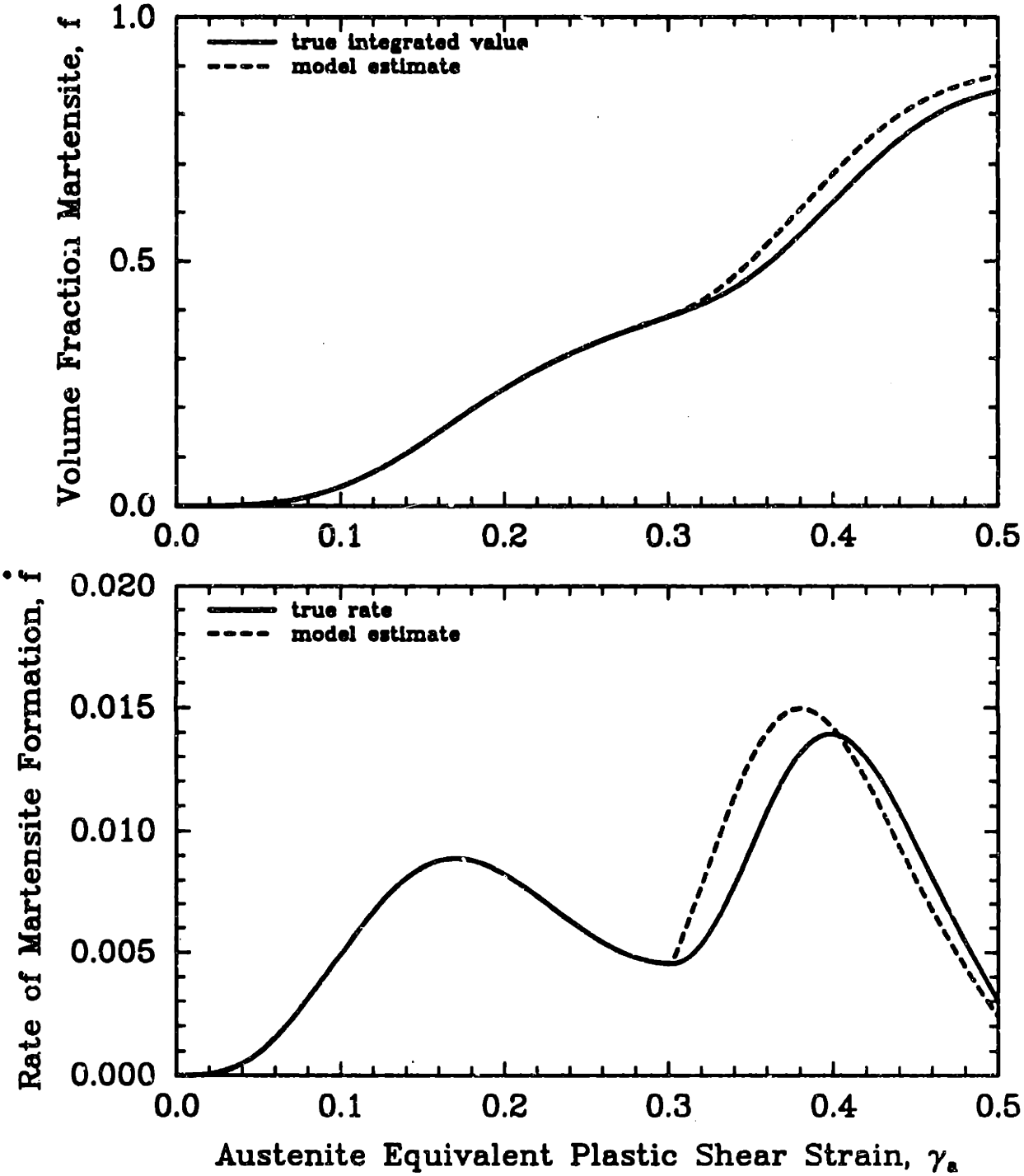

Figure 3.2 Comparison of model predictions for martensite volume fraction, f, and rate of martensite formation, $\dot{f}$, obtained using (3.20) with the more accurate integrated values obtained using (3.37) for a hypothetical "worst case" probability history function, $P = \frac{1}{2} + \frac{1}{4}sin(5\pi\gamma_a)$.

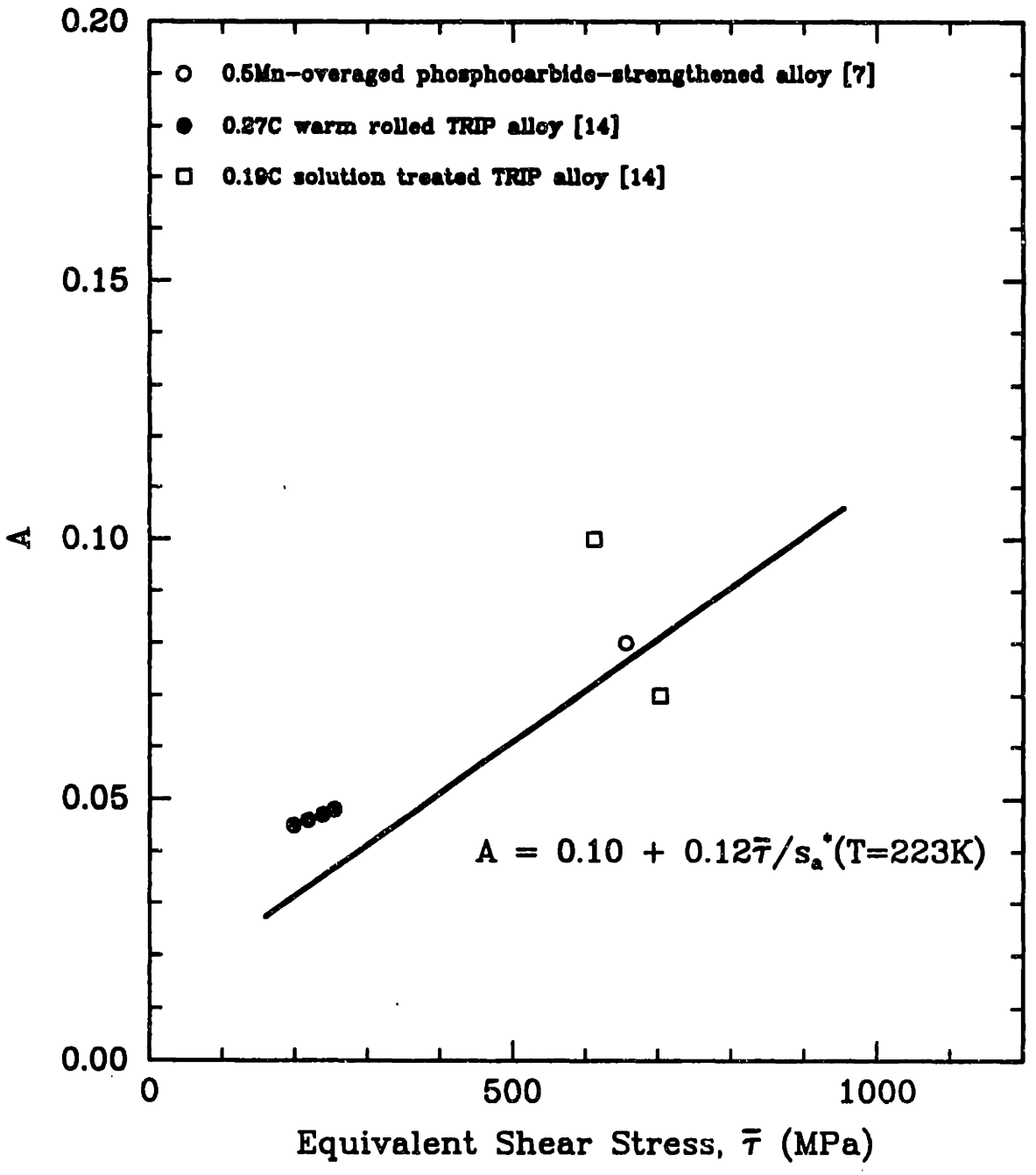

Figure 3.3 Estimate of A dependence on $\bar{\tau}$ (eq. 3.48), based on experimental data of Olson and Azrin [14], and Young [7]. The solid line represents values of A used to fit Narutani, *et al.* [21] stress-strain data (Fig. 3.11).

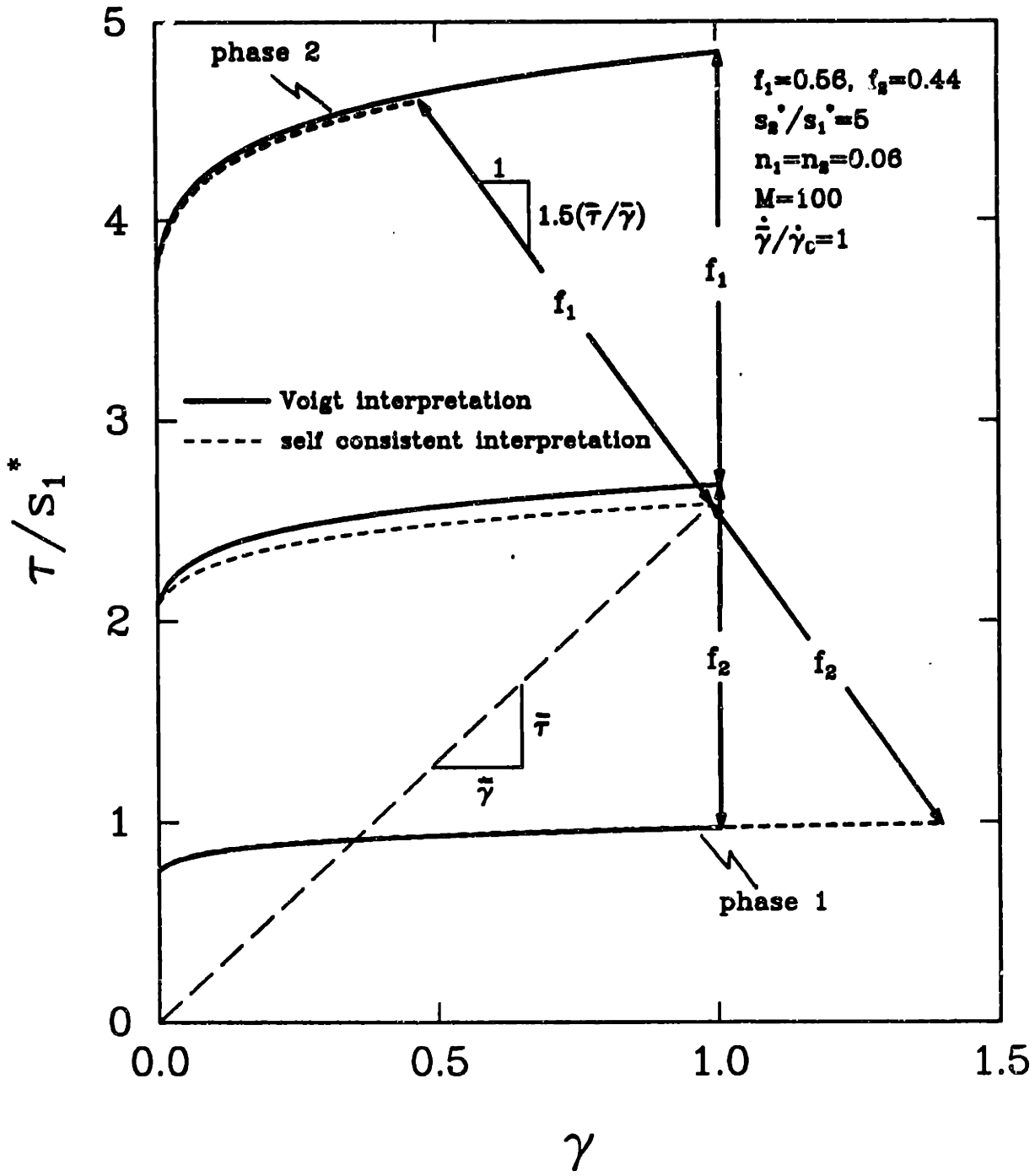

Figure 3.4 Geometric interpretation of (3.88). For equal and relatively small strain-hardening exponents, the slope of the line connecting (τ_1, γ_1) and (τ_2, γ_2) is approximately equal to $-1.5\bar{\tau}/\bar{\gamma}^p$, as shown. In addition, the relative distances between $(\bar{\tau}, \bar{\gamma})$, (τ_1, γ_1) and (τ_2, γ_2) are as shown.

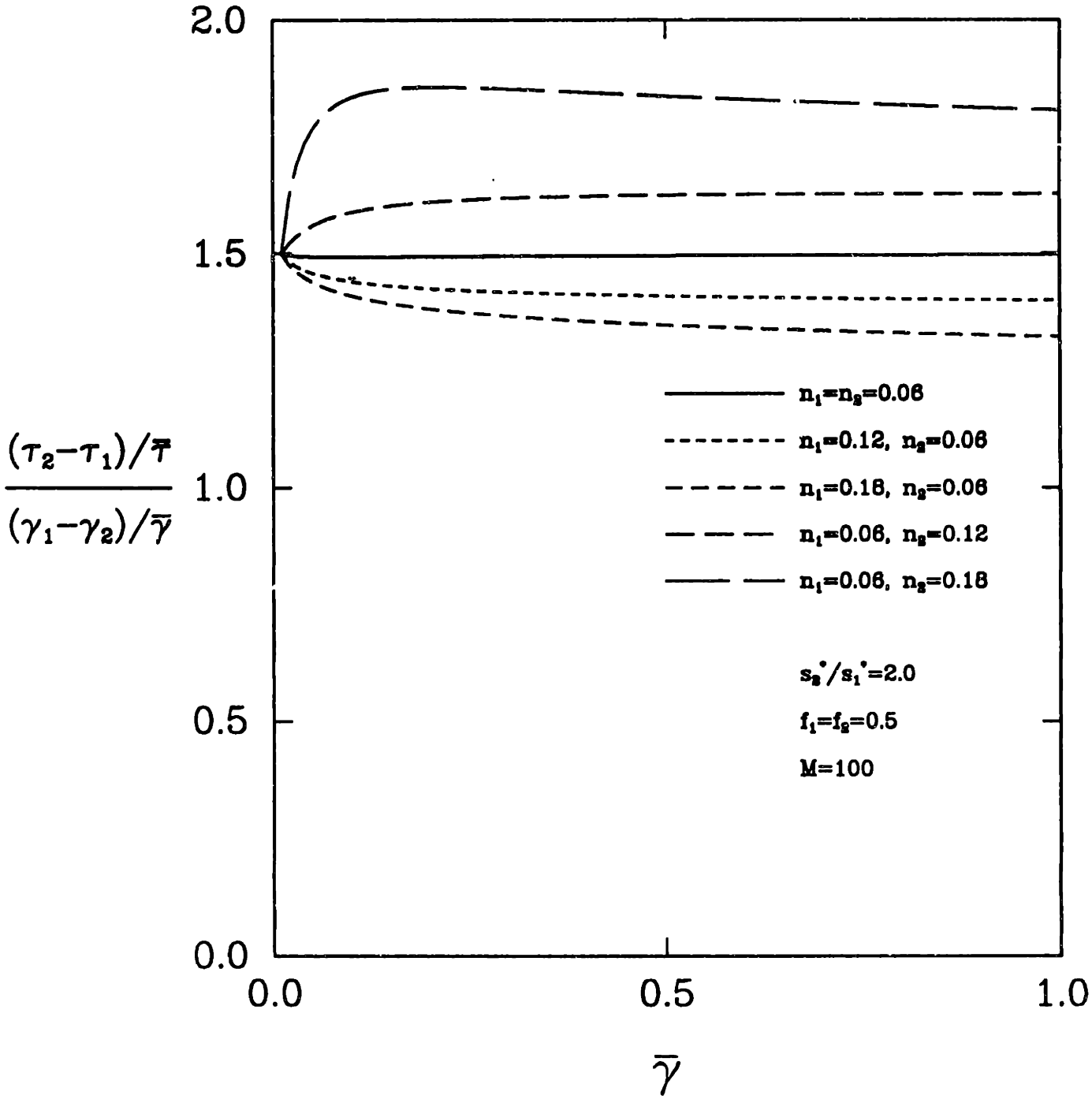

Figure 3.5 Deviation from the value 1.5 for various combinations of individual phase strain-hardening exponents.

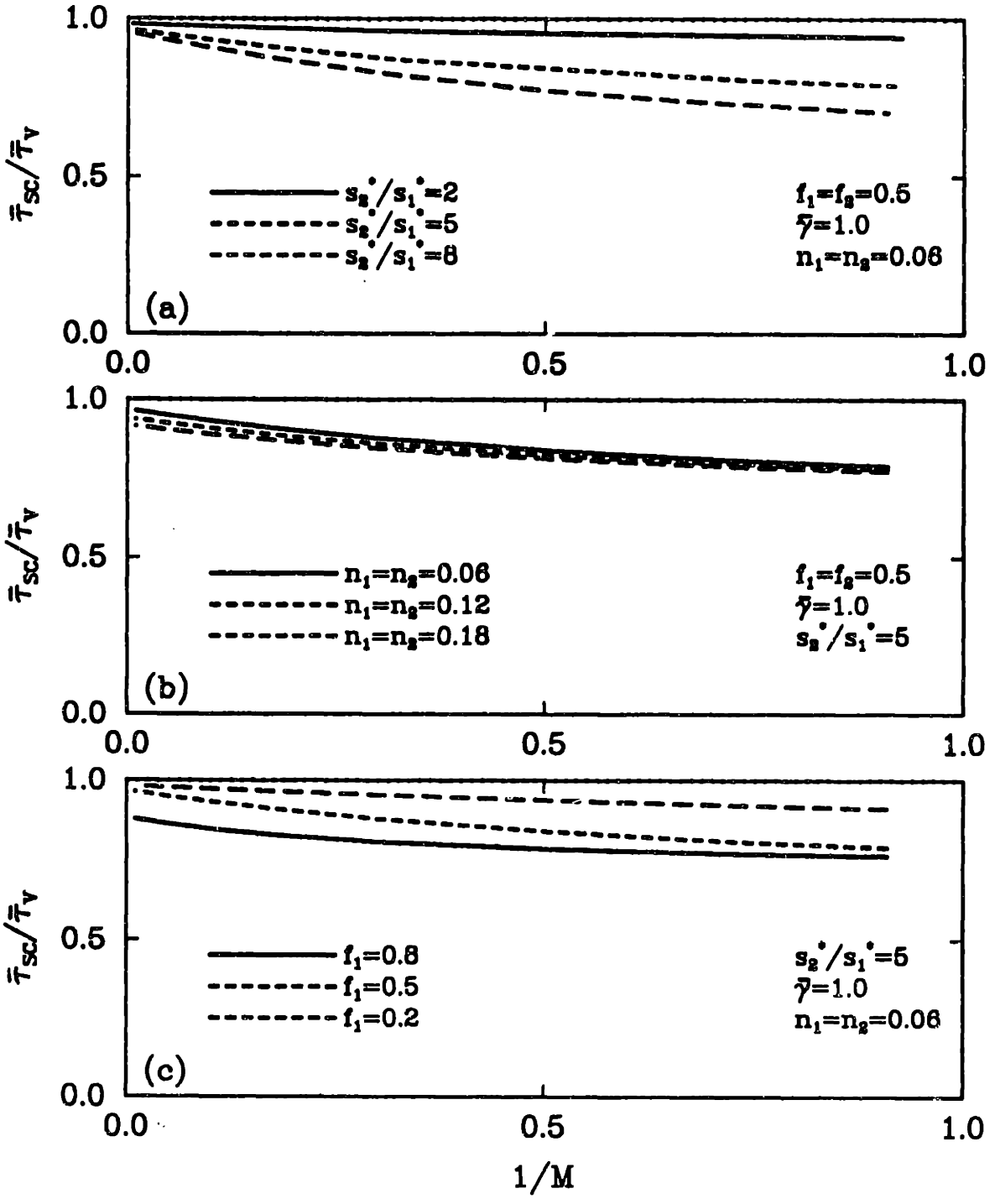

Figure 3.6 Comparison of viscoplastic self-consistent and Voigt model predictions for a wide range of rate exponents M: (a) Variation with phase hardness difference; (b) Variation with strain-hardening exponent magnitude; (c) Variation with phase fraction.

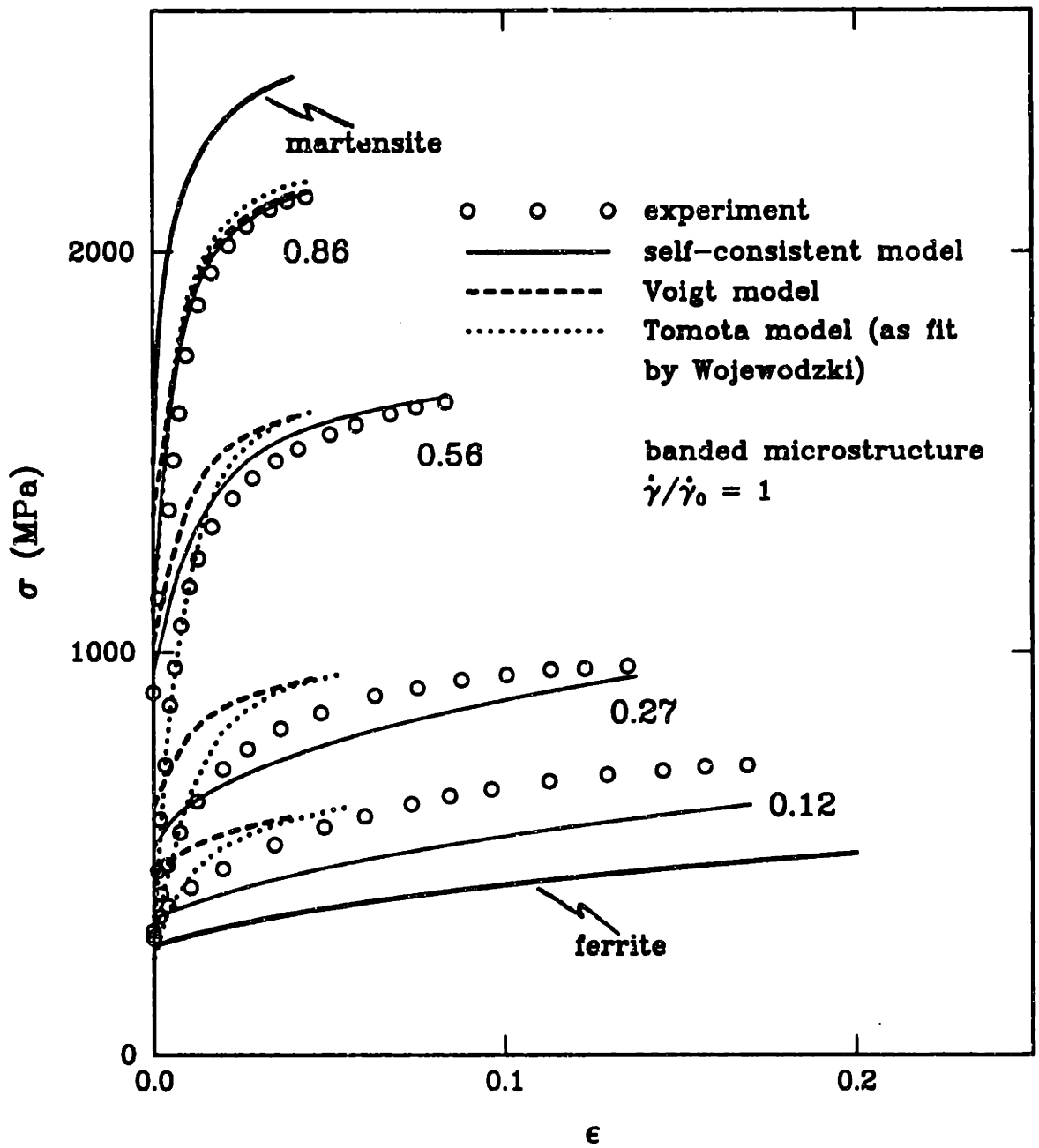

Figure 3.7 Comparison of model prediction with experimental results for a *banded* martensite-ferrite dual-phase steel at martensite fractions of 0.12, 0.27, 0.56 and 0.86. Also shown for reference are model predictions using the method of Tomota, *et al.* [105] and the Voigt model (taken from [74]). Note that the martensite curve shown here represents our fit to Wojewodzki's data for behavior of the martensite in the $f_2 = 0.12$ composition. The estimated martensite hardnesses at the other phase fractions can be found using equation (3.79) and the data of Table 3.1. For comparison, the martensite tensile stress levels at 4% plastic strain are 2431, 2503, 2567 and 2430 MPa for phase fractions of 0.12, 0.27, 0.56 and 0.86, respectively.

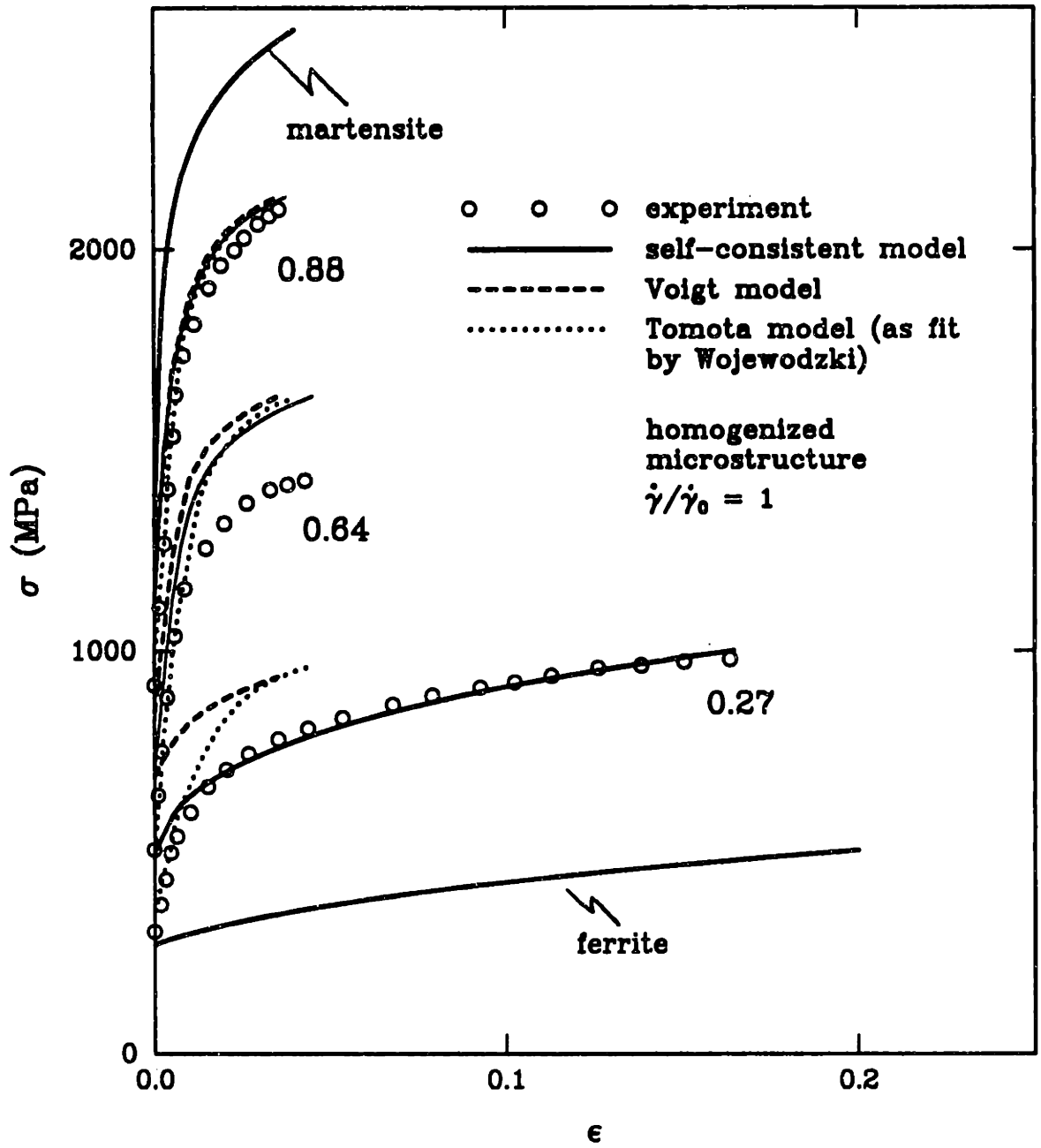

Figure 3.8 Comparison of model prediction with experimental results for a *homogenized* martensite-ferrite dual-phase steel at martensite fractions of 0.27, 0.64 and 0.88. Also shown for reference are model predictions using the method of Tomota, *et al.* [105] and the Voigt model (taken from [74]). Note that the martensite curve shown here represents our fit to Wojewodzki's data for the behavior of the martensite in the $f_2 = 0.27$ composition. The estimated martensite hardnesses at the other phase fractions can be found using equation (3.79) and the data of Table 3.1. For comparison, the martensite tensile stress levels at 4% plastic strain are 2544, 2388, and 2400 MPa for phase fractions of 0.27, 0.64 and 0.88, respectively.

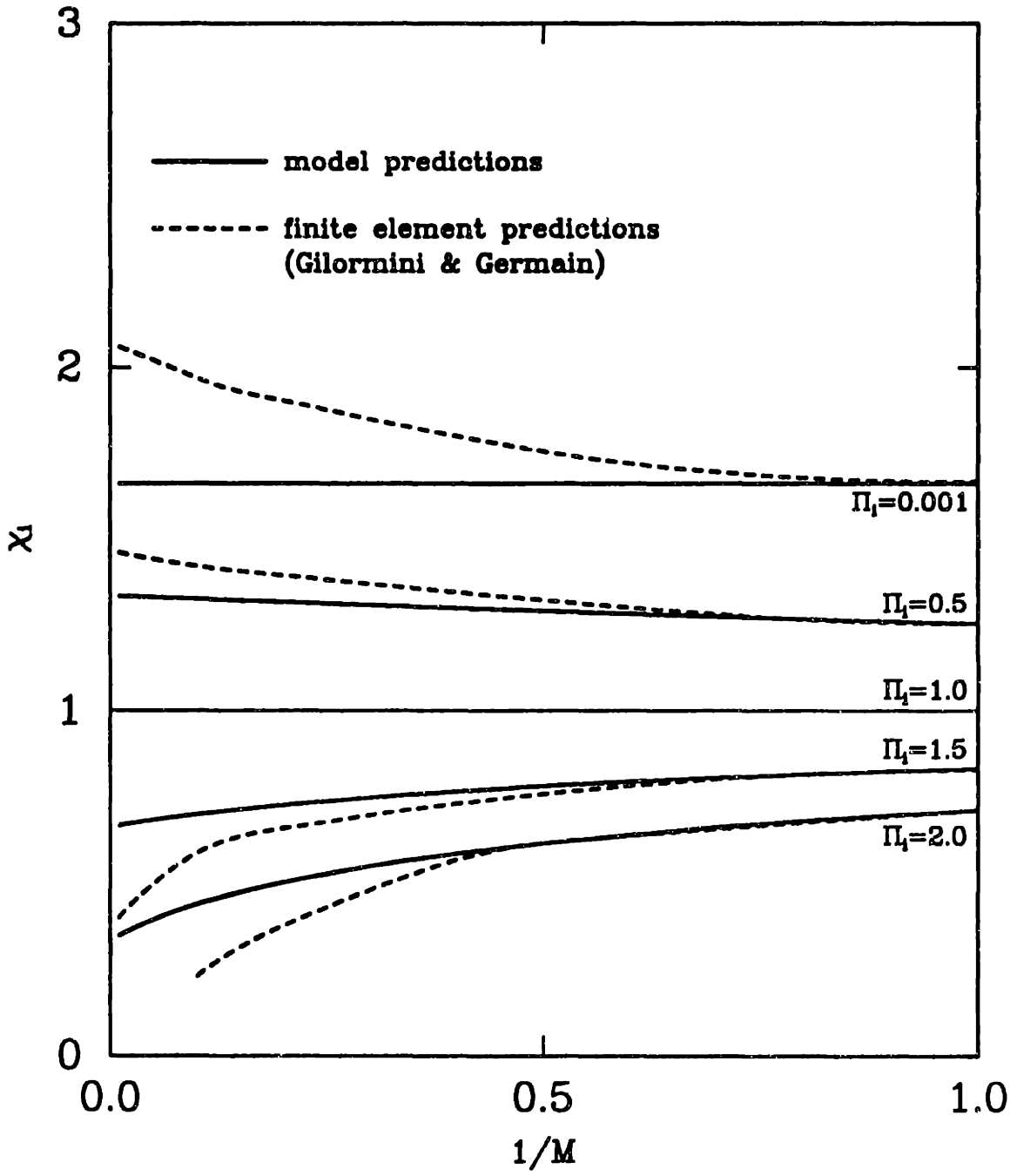

Figure 3.9 Comparison of model estimates of $\chi_i = \dot{\gamma}_i/\dot{\bar{\gamma}}$ as a function of $1/M$ with the finite element calculations of Gilormini and Germain [107] for various values of $\Pi_i = s_i/\bar{s}$. Model predictions are obtained by solving (3.67) explicitly. Finite element predictions represent numerical volume averages according to (3.58*a*).

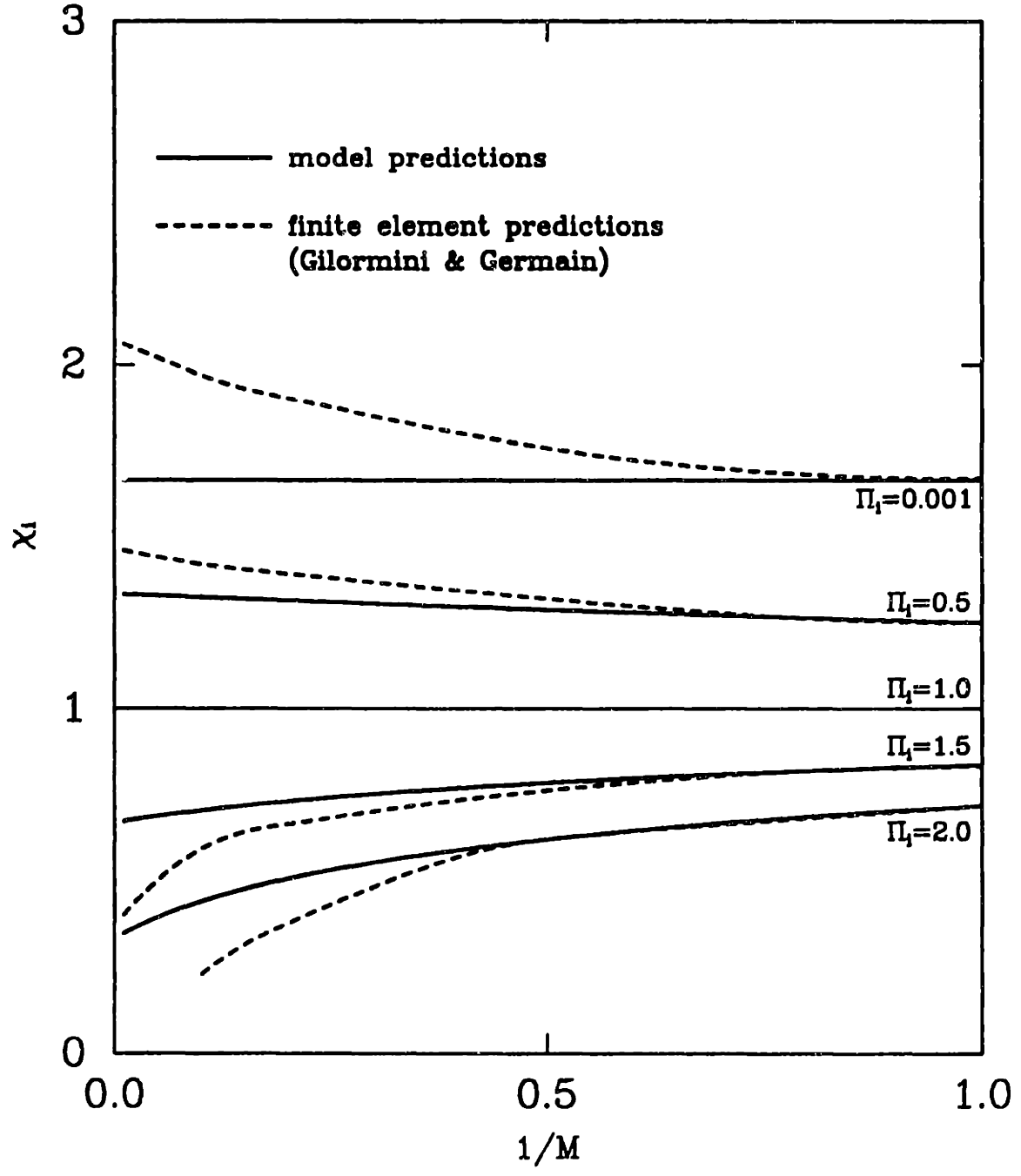

Figure 3.9 Comparison of model estimates of $\chi_i = \dot{\gamma}_i/\dot{\bar{\gamma}}$ as a function of $1/M$ with the finite element calculations of Gilormini and Germain [108]. for various values of $\Pi_i = s_i/\bar{s}$. Model predictions are obtained by solving (3.67) explicitly. Finite element predictions represent numerical volume averages according to (3.58a).

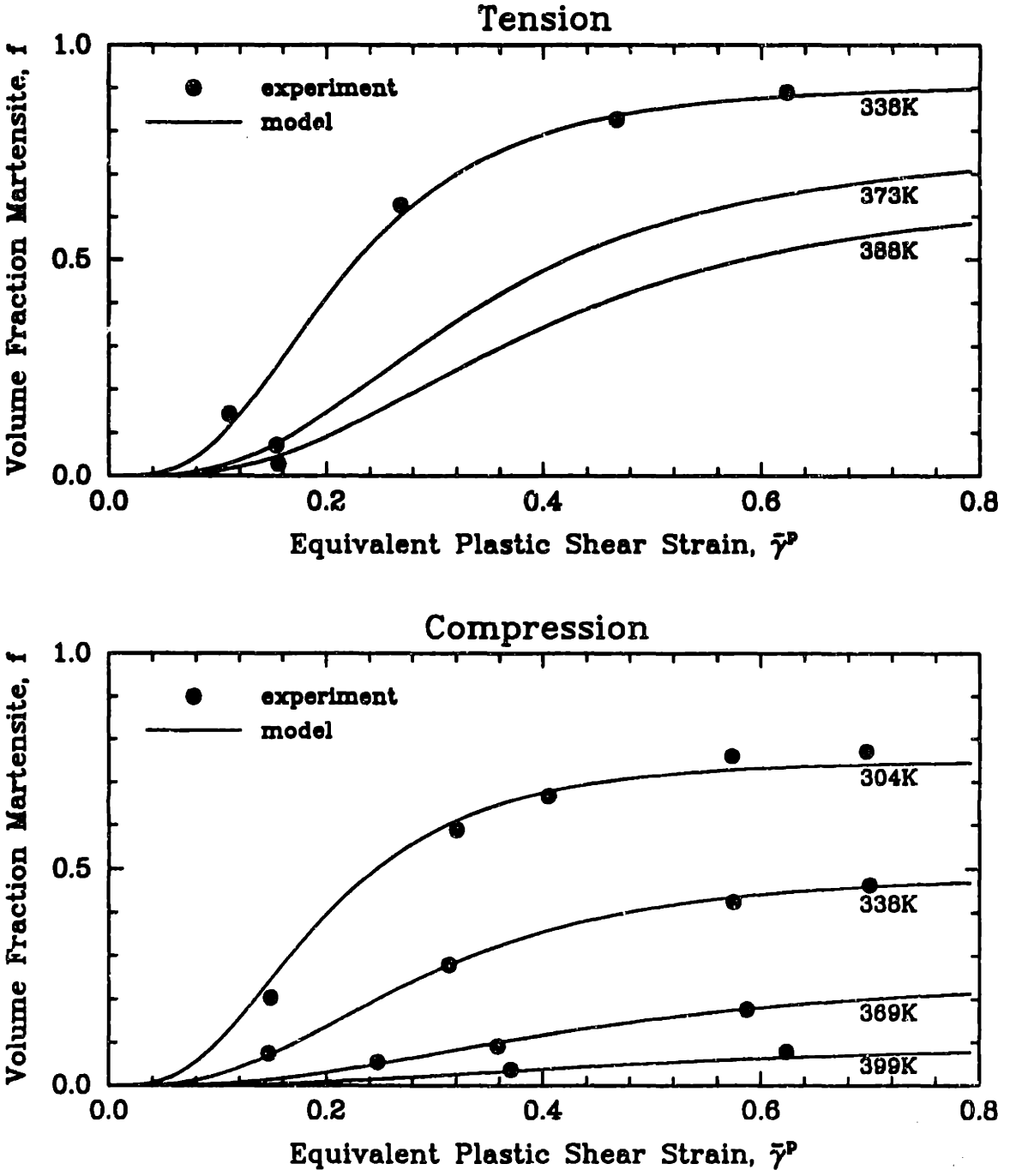

Figure 3.10 Comparison of model predictions for volume fraction martensite versus equivalent plastic strain. Experimental points represent data measured during simple tension and compression tests for a 0.5 Mn overaged phospho-carbide strengthened alloy [7]. Model parameters are listed in Table 3.2.

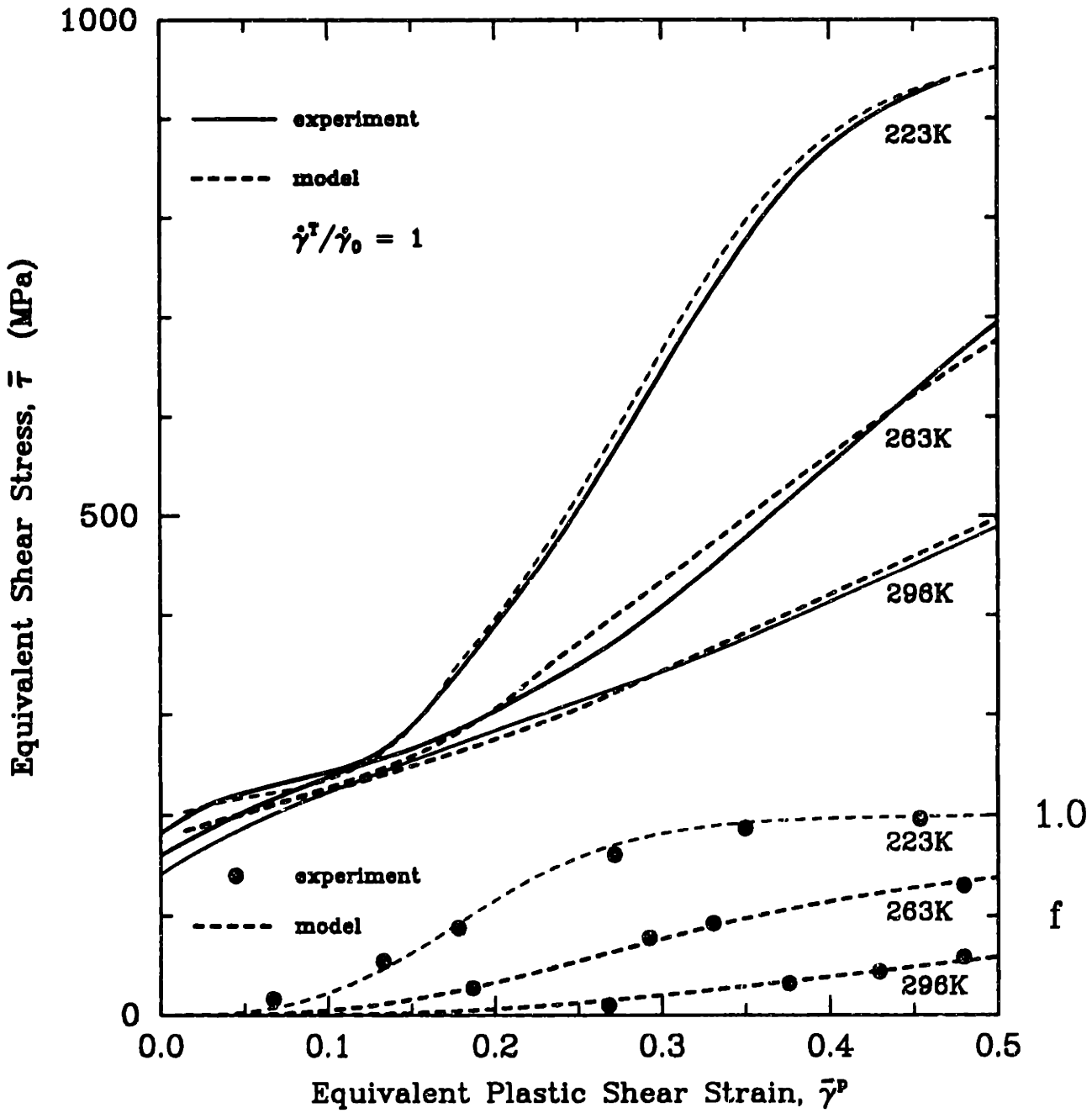

Figure 3.11 Comparison of model predictions for equivalent shear stress, $\bar{\tau}$, versus equivalent plastic strain, $\bar{\gamma}^p$. Experimental points represent data measured in simple tension tests for a 14Cr-7Ni SITP alloy [21]. Model parameters are listed in Table 3.3.

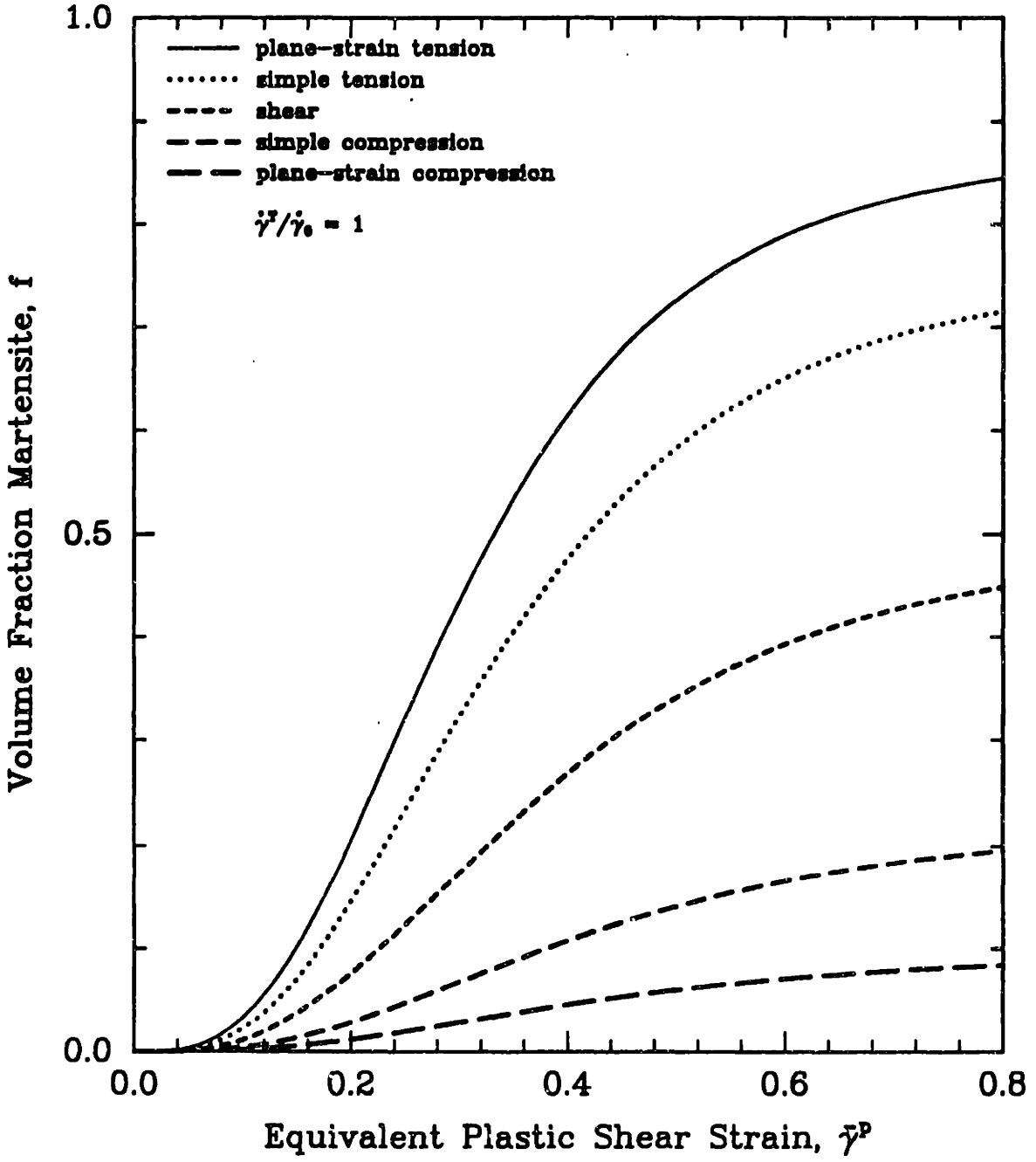

Figure 3.12 Martensite volume fraction, f, plotted versus equivalent plastic strain, $\bar{\gamma}^p$, for five one-element loading conditions: plane-strain tension, simple tension, pure shear, simple compression and plane-strain compression. Kinetics data are taken from [7] and are given in Table 3.2. $T = 373K$.

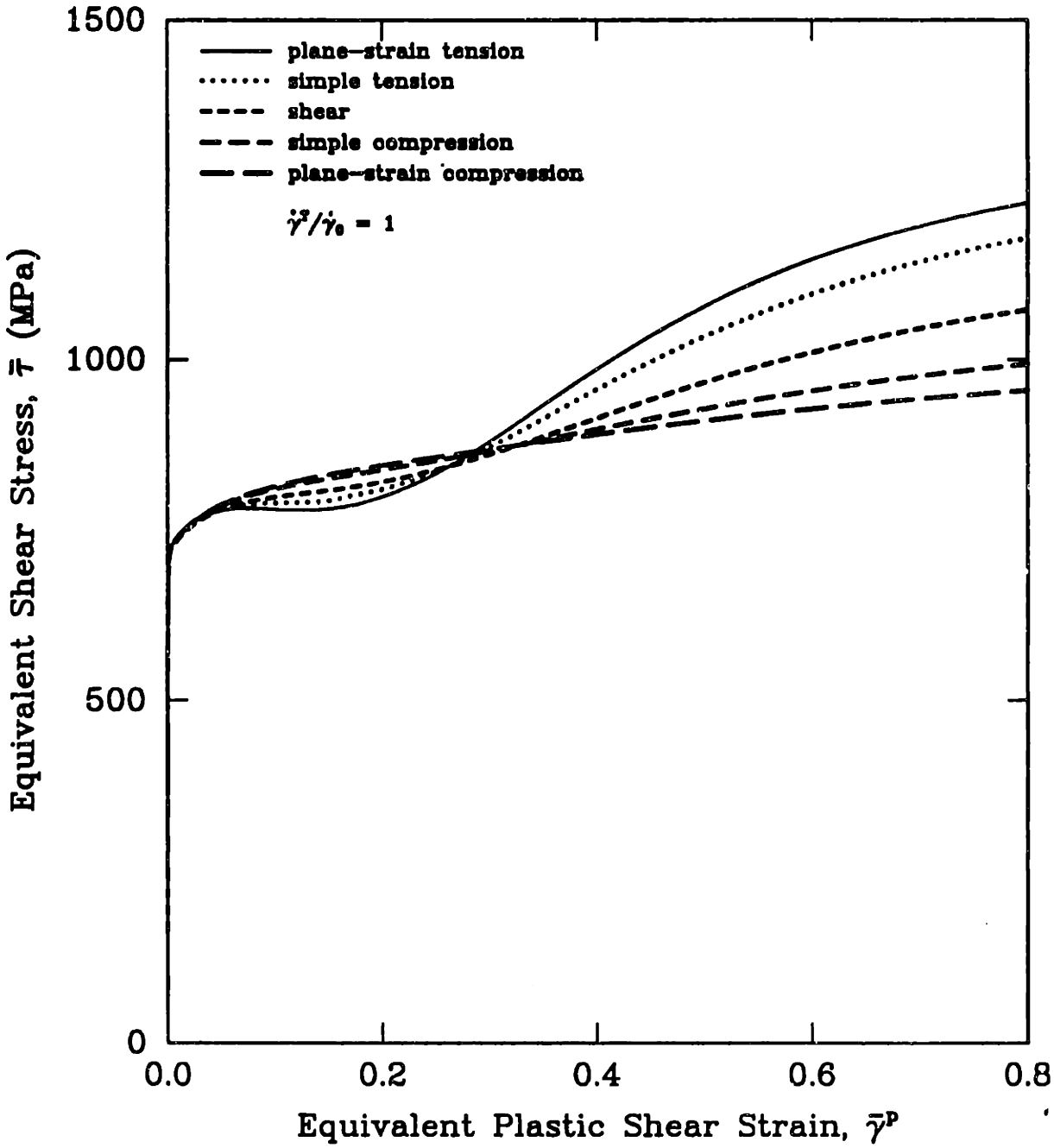

Figure 3.13 Equivalent shear stress, $\bar{\tau}$, plotted versus equivalent plastic strain, $\bar{\gamma}^p$, for five loading conditions: plane-strain tension, simple tension, pure shear, simple compression and plane-strain compression. Model parameters are taken from [7]: $T = 373K$, $s_a^* = 903$, $s_m^* = 1307$, $\gamma_a^* = 0.013$, $\gamma_m^* = 0.019$, $n_a = 0.06$, $n_m = 0.12$, $A_0 = 0.02$, $A_1 = 0.02$, $\Delta_V = 0.0$, $M = 100$, $\dot{\gamma}_0 = 0.007/s$, $\dot{\gamma}^T/\dot{\gamma}_0 = 1$.

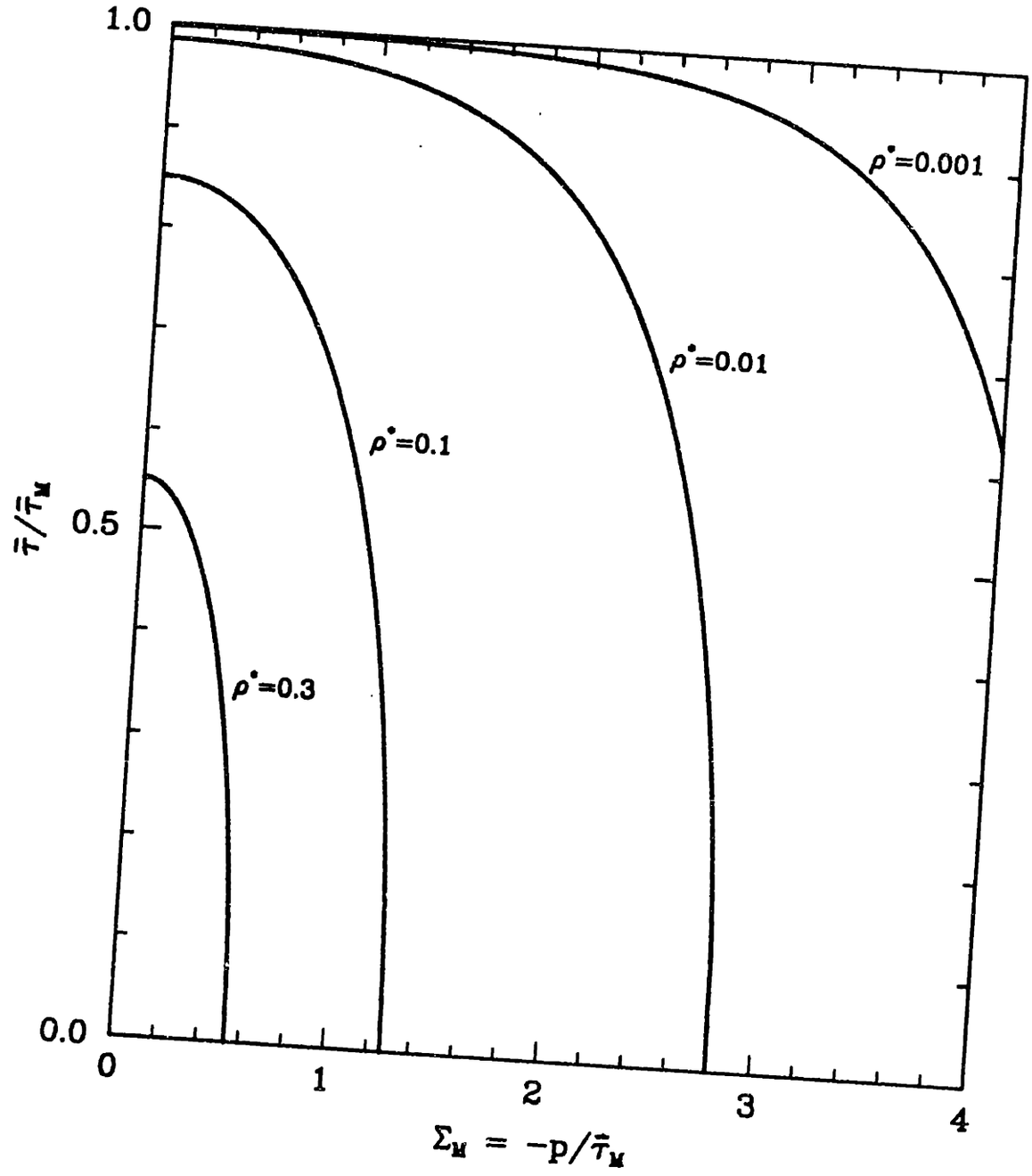

Figure 3.14 Yield locus obtained from (3.97), plotted in normalized stress space ($\bar{\tau}/\bar{\tau}_M$ versus $-p/\bar{\tau}_M$), for several values of ρ^*.

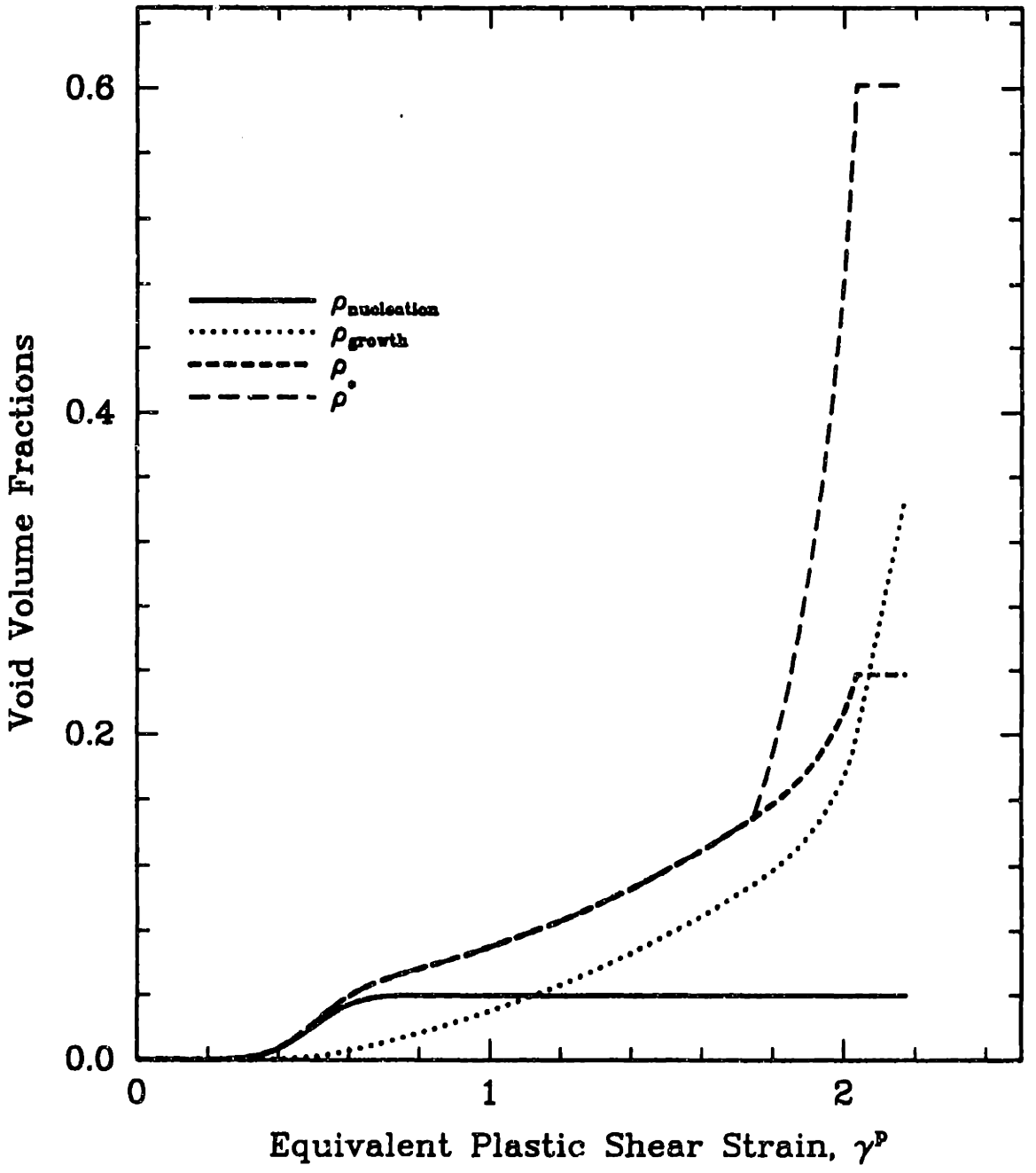

Figure 3.15 Model predictions for evolution of $\rho_{nucleation}$, ρ_{growth}, ρ and ρ^* with equivalent plastic strain, obtained from a one-element, plane-strain finite element analysis. Material parameters are taken from Tables 3.2 and 3.3; nucleation parameters are as follows: $\rho_N = 0.04$, $\overline{\gamma}^p_N = 0.5$ and $s_N = 0.10$.

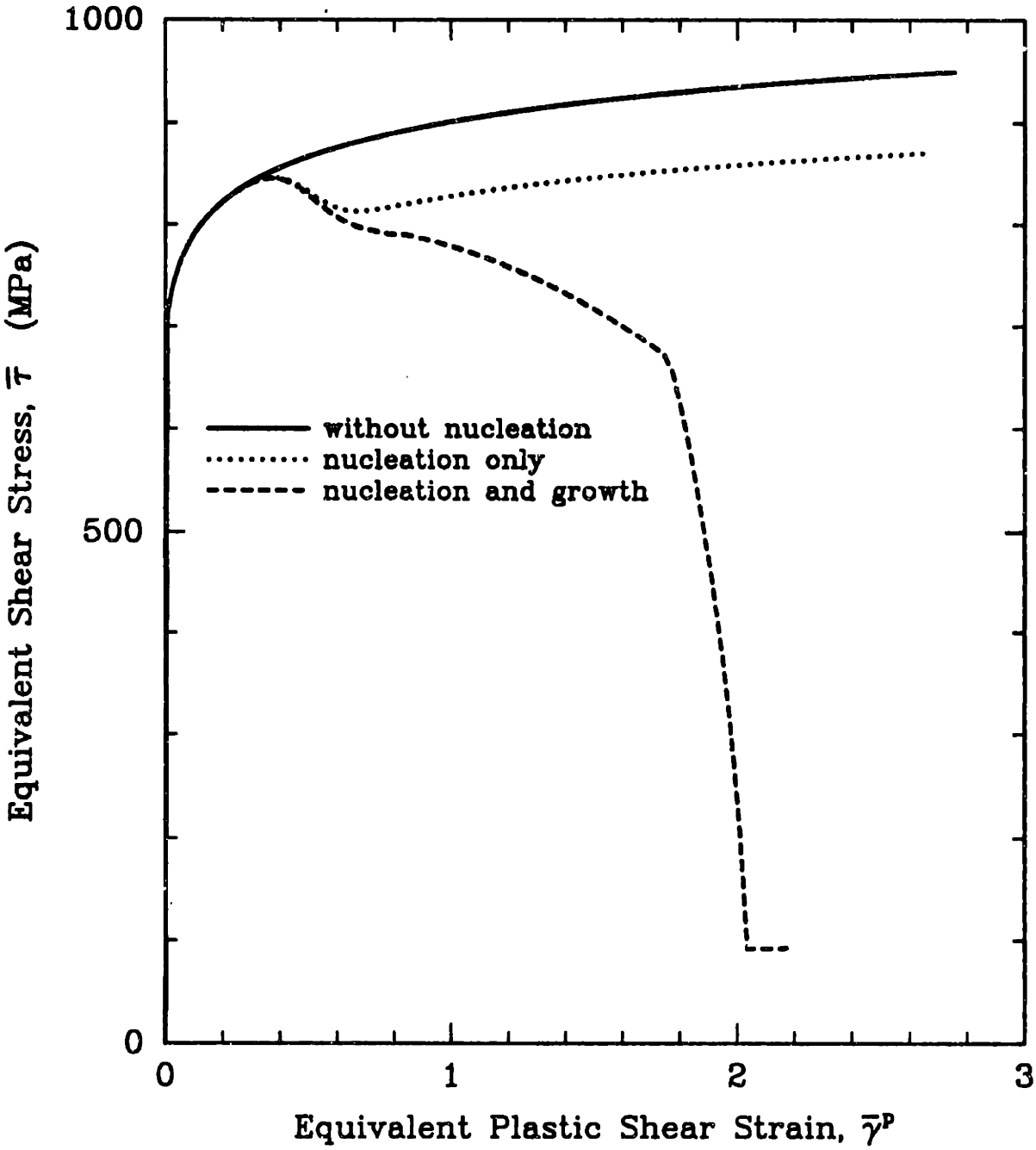

Figure 3.16 Effect of nucleation and growth on model predictions of stress-strain response. Material parameters are taken from Tables 3.2 and 3.3; nucleation parameters are as follows: $\rho_N = 0.04$, $\bar{\gamma}^p_N = 0.5$ and $s_N = 0.10$.

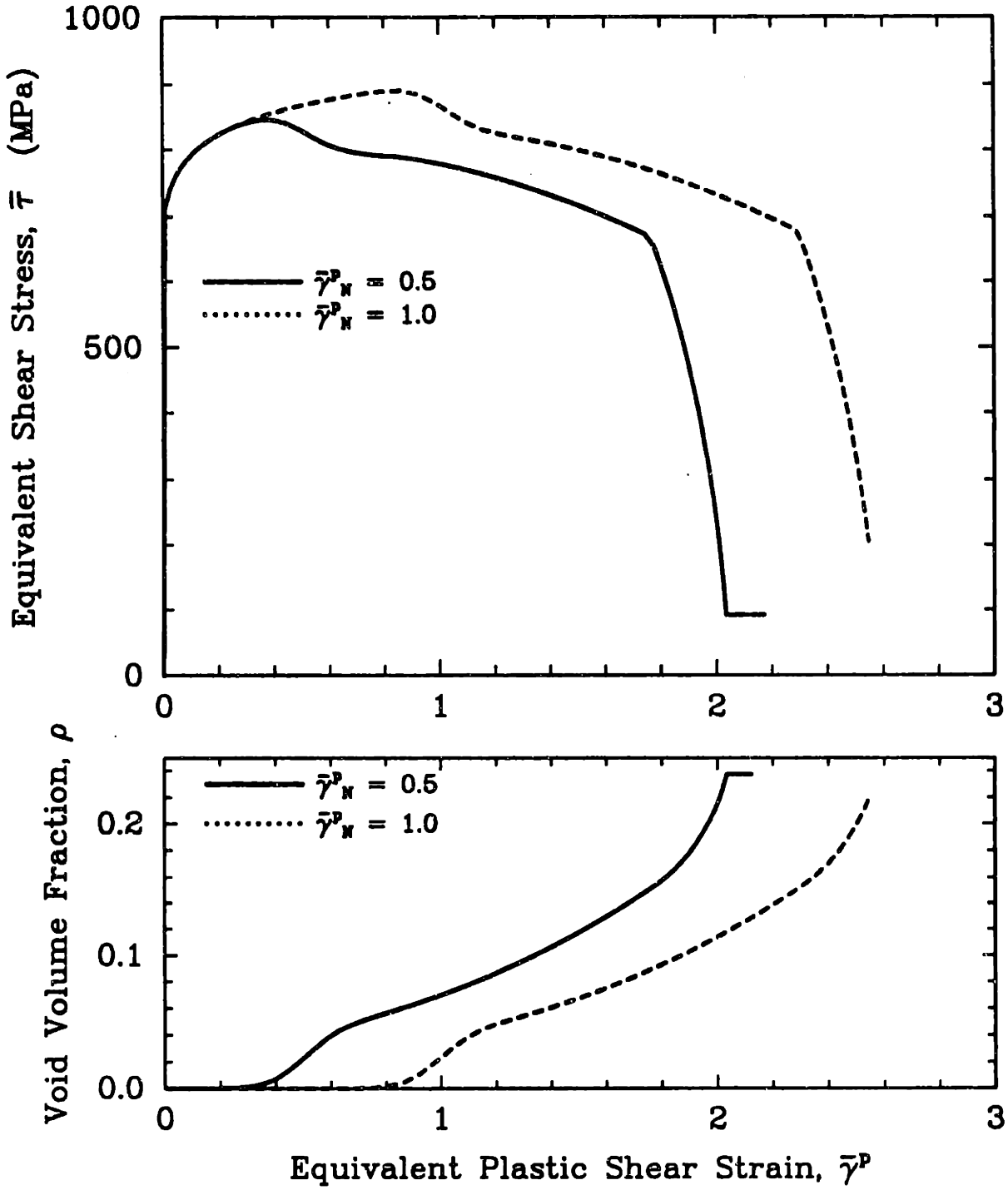

Figure 3.17 Effect of altering $\bar{\gamma}^p_N$ on porosity evolution (below) and the resultant stress-strain behavior (above).

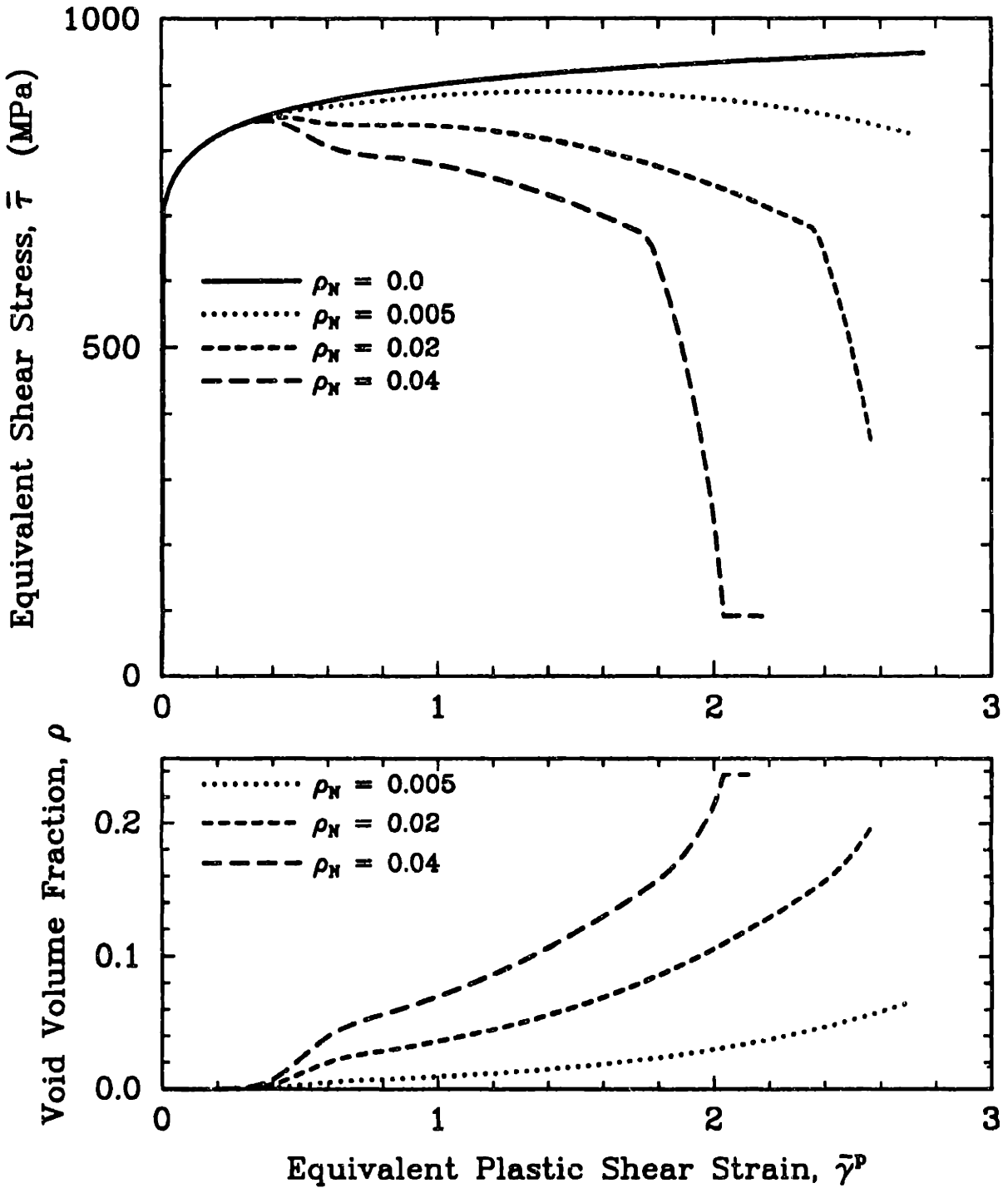

Figure 3.18 Effect of altering ρ_N on porosity evolution (below) and the resultant stress-strain behavior (above).

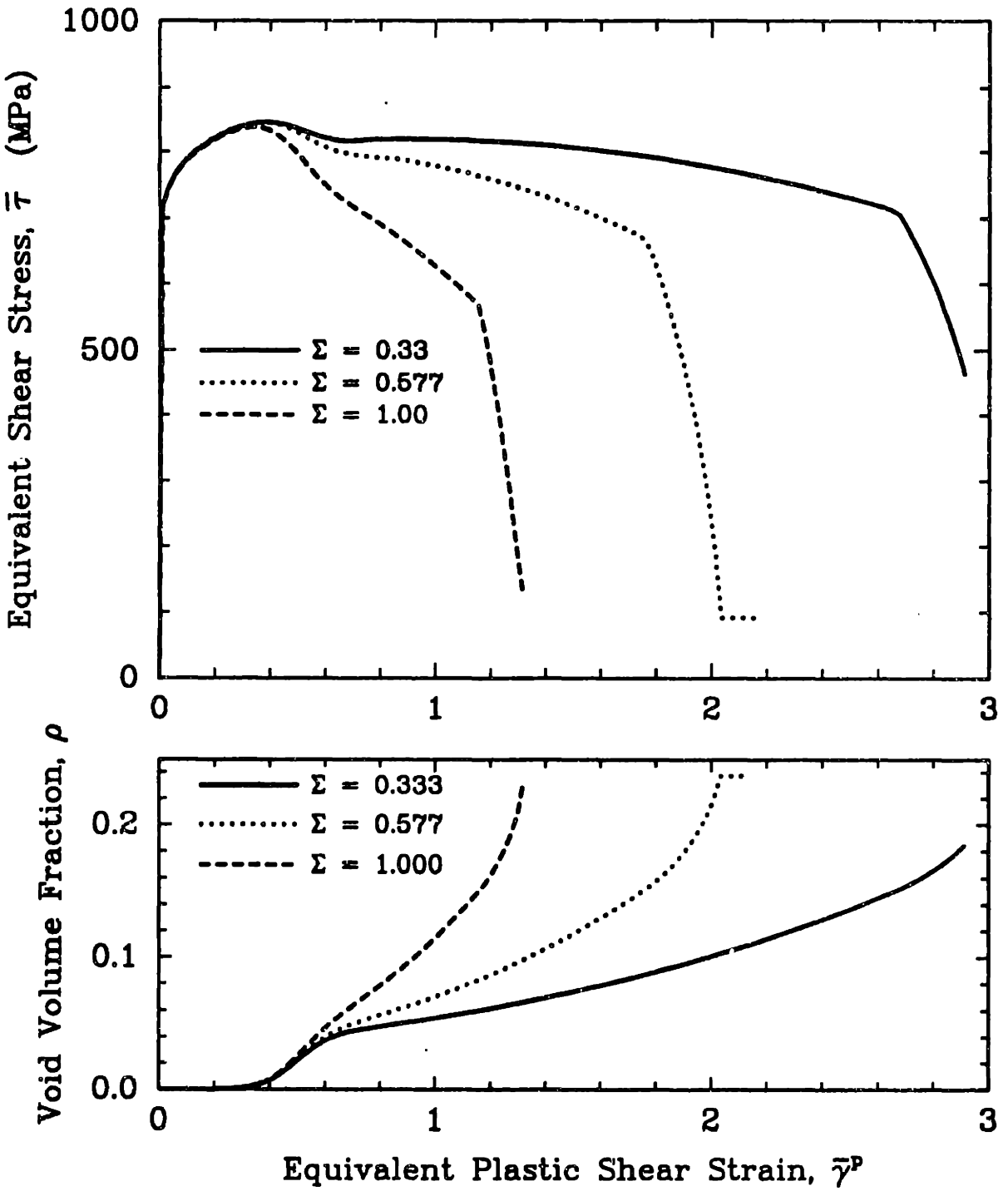

Figure 3.19 Effect of triaxiality on porosity evolution (below) and the resultant stress-strain behavior (above).

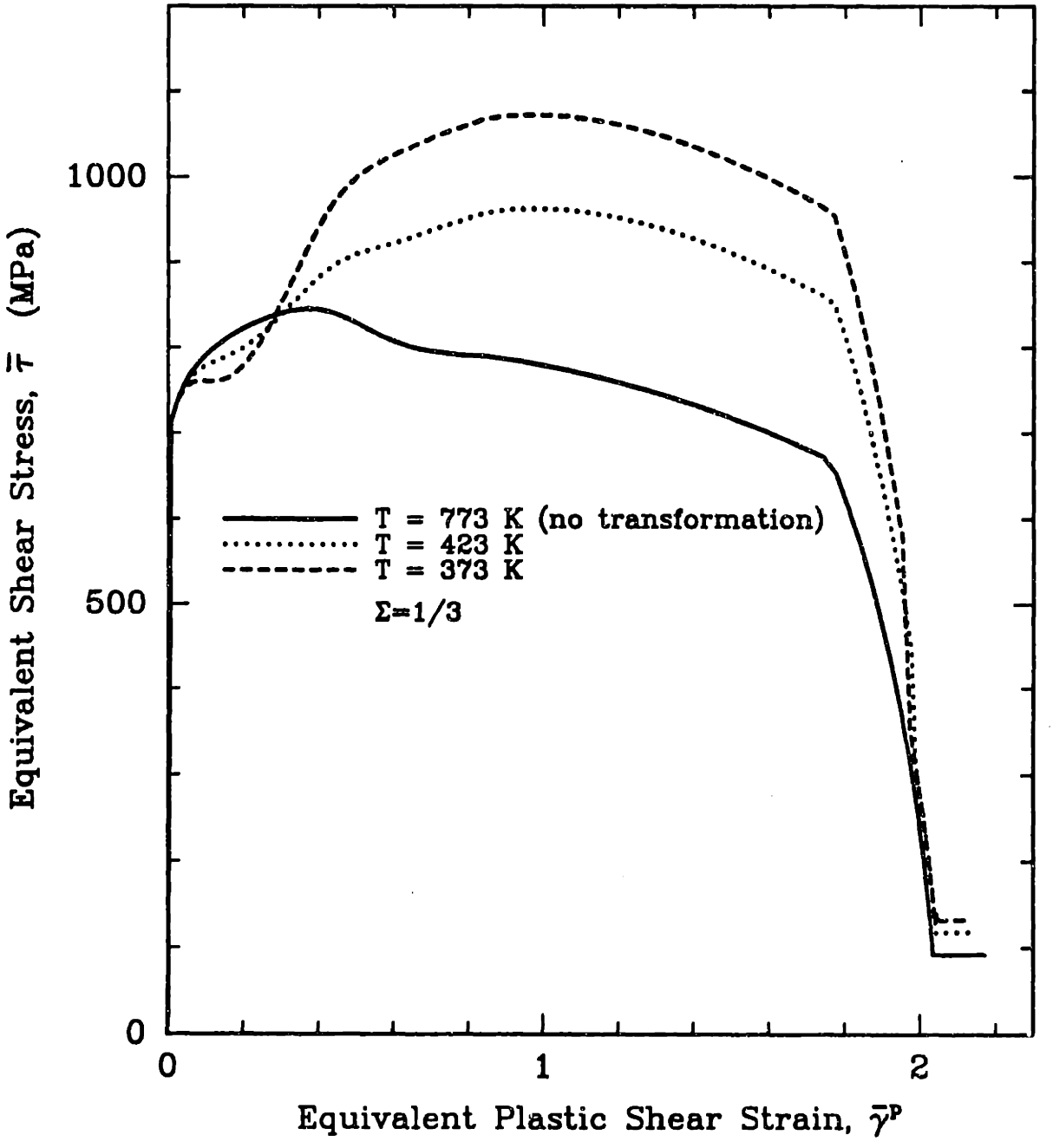

Figure 3.20 Combined effect of nucleation of martensite and nucleation and growth of voids on stress-strain behavior for three different model temperatures. The temperature dependence of austenite and martensite hardening parameters (see Table 3.3) has been neglected here for purpose of illustration.

Chapter 4

Analysis of Continuum Fields: Comparison of Nontransforming and Transforming Material Behavior

4.1 Introduction

In this chapter, we discuss the results of several numerical analyses of boundary value problems for which we have used the material model outlined in sections 3.3 and 3.4 (*i.e.*, void nucleation and growth are not included). Here, we examine the influence of transformation on the continuum response of three mechanical subsystems, each of which is characterized by a different length scale. We first consider the material response in a simulated uniaxial tension test. We then focus in by several orders of magnitude to the smallest length scale over which our model can reasonably be applied, to consider the stress and strain fields surrounding an isolated elastic particle embedded in an infinite matrix, subject to a remote stress. At this level, we examine the particle/matrix interfacial fields in order to assess to what extent, if any, transformation affects the void nucleation process. Finally, at an intermediate length scale, we consider the fields surrounding a smoothly blunting crack tip subject to mode I loading. Here, our objective is to gain insight into the effect of transformation on the continuum crack-tip fields and attempt to relate these findings to tendencies toward inhibition of plastic flow localization.

Each of these boundary value problems was previously considered in [13], where our preliminary model, which did not account for the stress-state sensitivity of the transformation kinetics, was not able to completely capture the physics of the phenomena. We concluded that the lack of an accounting of the stress-state sensitivity in our preliminary model for transformation kinetics limited the usefulness of our results. We therefore re-examine these fields using the current model in an effort to identify the mechanical sources of the observed transformation toughening.

Calculations performed in [13] indicated that transformation dilatation does not *directly* alter mechanical response to a significant degree. The state of stress and strain in the composite is not substantially modified when the Δ_V term is introduced into the model. Current model calculations support these preliminary findings. For example, for the problem we present in section 4.4, setting $\Delta_V = 0.04$ resulted in a change in the peak normal stress ahead of the crack tip of less that 1% relative to the $\Delta_V = 0$ case. Transformation dilatation is rather thought to be *indirectly* associated with increased toughness through the correlation between transformation dilatation and the stress-state sensitivity of transformation kinetics, as discussed in section 3.3, a notion that still needs to be experimentally verified. Moreover, plastic dilatation leads to a numerical Jacobian that is nonsymmetric, necessitating the use of the nonsymmetric solver routines of ABAQUS, which severely increases computation time. We therefore set the transformation dilatation term, Δ_V, to zero for all the calculations described in this chapter and the next.

4.2 Numerical Simulation of the Uniaxial Tension Test

4.2.1 Introduction

The tension test has been extensively used to determine the stress-strain behavior of materials. The data from these tests often serve as the basis for critical evaluations regarding the performance of the material in actual engineering applications. When materials are tested well past their yield point, they often exhibit a localization of

deformation at some point along the specimen, leading to the formation of a *neck*. In most cases, the neck grows (*i.e.*, the necked cross-section becomes smaller) and fracture ensues with little further elongation of the specimen. In some materials, however, the neck stops growing, and instead propagates down the entire length of the specimen. In either case, the presence of a neck is an indication that the stress and strain fields that were once homogeneous throughout the specimen are no longer uniform, and inferred stress-strain data which are based on the assumption of homogeneity lose validity as the neck grows.

Until the 1940's, the methods used to interpret data from tension tests did not account for the nonhomogeneity of flow associated with the onset of necking. Bridgman [120,121] and Davidenkov and Spiridonova [122] were the first to suggest corrections to tension test data based on the effects of geometry changes on the state of stress in the neck. These corrections, however, were based on simplifying assumptions concerning the state of strain in the neck which are not generally valid. The development of the finite element method and other numerical techniques has greatly improved the ability to evaluate the stress and strain fields in the neck and to predict how they will affect the overall stress-strain behavior of the material. Nonetheless, the interpretation of tensile data is still a difficult problem, and it is even more challenging for TRIP steels and other materials, such as polymers, which have unusual mechanical properties that often lead to propagation of the neck, or *cold drawing*. Experimentally, the neck forms but does not grow, and, instead, propagates down the length of the specimen, at which point a second period of uniform elongation ensues, followed by formation of a second neck prior to final fracture.

Using the constitutive model developed in the first part of chapter 3, we simulated a uniaxial tension test in order to compare the behavior of a model "transforming" steel with that of a "nontransforming" steel which has material properties equivalent to those of the austenite phase of the transforming steel.

An analysis of this type is useful for several reasons. First, it serves as a check on whether the constitutive model is capable of simulating the necking/cold drawing behavior of these alloys. In addition, an analysis of this type provides macroscopic

details related to the features of transformation that lead to the observed increases in uniform ductility and fracture strain during tension tests at certain temperatures in the strain-induced range (*e.g.*, [1,6]). Since the finite element method provides a good estimate of the stress and strain fields throughout the specimen and especially in the neck, these analyses provide insight into the features of transformation that lead to this enhanced behavior.

In a more general sense, this problem is useful because it provides a better understanding of the state of stress and strain which develop during necking (and drawing) in tension tests. The results of these tests are often the sole basis for determining the stress-strain properties of the material, and these properties are in turn used in more complicated numerical analyses. Therefore, it is important that the methods used to interpret test data are accurate and reliable. In tests of this kind, stress-strain data are generally formulated under the assumption of uniform stress and strain fields. In some instances a Bridgman correction factor is used to account for the nonuniformities which are thought to be present. In recent times, difficulties in obtaining accurate data from tension tests has led many investigators to use compression tests instead. These tests have problems of their own, namely "bulging" of cylindrical specimens from frictional end constraints. An additional concern arises for strain-induced transforming steels, because of the demonstrated stress-state dependence of transformation kinetics. It is worthwhile, therefore, to be able to test the accuracy of tensile data using these simulated tests. This can be accomplished by comparing stress-strain predictions obtained through pointwise averages with those obtained using load-displacement data and the correction factors of Bridgman [120,121] or Davidenkov and Spiridonova [122], as must be done experimentally.

4.2.2 Problem Description

Using the finite element code ABAQUS in conjunction with the UMAT subroutine listed in Appendix A, we simulated the geometry and loading conditions of an actual simple tension test. The specimen modeled here is round, and has gauge length L_0 and initial diameter $D_0 = 0.3L_0$ as shown in Fig. 4.1a.

A model of the round tensile specimen is shown in Fig. 4.1b. Symmetry about the centerline allows us to model only one-half of the specimen. In order to promote necking at the center of the specimen, a perturbation is introduced along the outside of the mesh which reduces the cross-sectional area at the mid-plane of the specimen. This "flaw" causes a reduction in the cross-sectional area of the specimen at the mid-plane, increasing the axial stress, so that localization of deformation occurs first in this region. This perturbation is meant to model natural imperfections which are invariably present in an actual specimen. The particular perturbation used in this analysis takes the form of a sine function with a period equal to the total specimen length, L_0, defined to reach its maximum value of $0.0025D_0$ at the middle of the specimen. Preliminary calculations in [13] indicated that a perturbation of this size is large enough to be sensed by the numerical procedures of the finite element analysis, but small enough so that it does not significantly affect the results aside from causing the neck to form in a predetermined location. The undeformed radius, $R_0(z)$, of the model specimen takes the following form:

$$R_0(z) = \frac{D_0}{2}\left(1 - .005 \sin \frac{\pi z}{L_0}\right), \tag{4.1}$$

where z is measured from the end of the specimen. The corresponding finite element mesh, as shown in Fig. 4.1c, utilizes 900 4-node axisymmetric, isoparametric quadrilateral (ABAQUS CAX4) elements in a 15 by 60 grid pattern. These elements are formulated such that mesh *locking*, a deleterious phenomenon which might otherwise arise due to the constraint of incompressibility, is prevented [123]. The mesh is designed so that the refinement is greatest near the outside edge of the specimen in order to adequately model the large deformations which occur in this region during the necking and drawing process. Symmetry conditions are applied at nodes along the specimen centerline. The nodes along the axis are, by definition, constrained to have zero radial displacement, while the nodes along the end of the specimen are constrained to have equal axial displacements. The calculations were performed on a Sun microsystems *SPARCstation 1* computer using version 4.7 of the ABAQUS finite element code.

Material parameters, incorporated into the analyses via the PROPS vector of the

UMAT subroutine (see Appendix A), are given in Table 4.1. The model material is based, as closely as possible, on the kinetics and stress-strain data of Young [7]. Model temperatures are given in absolute (Kelvin) units. For reference, Young estimated that $M^{\sigma}_{s,ut} \approx 323K$ and $M_{d,ut} \approx 448K$. Solutions were obtained under displacement control, with a constant normalized displacement rate, $\Delta L/(L_0 \Delta t) = 0.005/sec$, applied at the end nodes.

It was shown in [13] that, in order to obtain a solution to this problem in a reasonable amount of CPU time, it was necessary to utilize the modified RIKS method [124–126], available in ABAQUS as an optional solution procedure. The RIKS algorithm is designed to solve problems in which the load-displacement behavior is such that the load and/or the displacement may decrease as the incremental solution develops, as is the case in necking problems. The routine is based on the assumption that all loads scale with a single scalar parameter. The method then looks for an equilibrium path which is defined by nodal variables and the loading parameter. The solution follows this path until the desired displacement is reached. Details of the theory upon which the method is based can be found in the ABAQUS theory manual [123].

location in PROPS	material parameter	value	equation reference
1	K	175000 MPa	3.40
2	G	80000 MPa	3.40
3	r_I	4.0	3.22
4	n_a	0.06	3.78
5	n_m	0.12	3.78
6	s_a^*	904. MPa	3.78
7	s_m^*	1307. MPa	3.78
8	γ_a^*	0.013	3.78
9	γ_m^*	0.019	3.78
10	α	4.33	3.23
11	Δ_V	0.0	3.47
12	$\bar{g}$	3230.	3.27
13	s_g	292.	3.27
14	β_0	4.42	3.34
15	Θ	1.16	3.28
16	g_0	3400.	3.28
17	g_1	4.7	3.28
18	g_2	493.	3.28
19	M	100.	3.62
20	$\dot{\gamma}_0$	$0.007/s$	3.62
21	A_0	0.02	3.48
22	A_1	0.02	3.48
23	ρ_N	0.00	3.106
24	$\overline{\gamma}_N^p$	0.00	3.106
25	$s_N(\gamma)$	0.00	3.106
26	σ_N	0.00	3.107
27	$s_N(\sigma)$	0.00	3.107

Table 4.1 Contents of the PROPS vector of material parameters used by ABAQUS as input to the UMAT material-law subroutine (Appendix A) for $T = 225K$ ($\Theta = 1.16$). Changes to these values with changes in temperature will be indicated for each analysis. The corresponding source and the equation where the parameter first appears are given for reference.

4.2.3 Results and Discussion

Since we already analyzed this problem in considerable detail in [13], we restrict attention here to the differences in model predictions due to incorporation of the

stress-state sensitivity of transformation kinetics into the model. We discuss results for four cases: a nontransforming material; a transforming material at a temperature, $T = 448K$ ($\Theta \approx 0.8$), that is not low enough relative to $M_{d,ut}$ to resist neck formation; a transforming material at a temperature, $T = 423K$ ($\Theta \approx 0.7$) near that at which a transition from necking behavior to drawing behavior occurs, and a transforming material at a sufficiently low temperature, $373K$ ($\Theta \approx 0.3$), for transformation hardening to result in tensile neck propagation.

Effect of the Transformation on Uniaxial Behavior

Figs. 4.2 through 4.5 compare deformation behavior for the nontransforming and transforming materials. In Fig. 4.2, the deformed "specimen" (which is actually the mesh shown in Fig. 4.1c mirrored about the longitudinal and transverse axes) is plotted at several points during deformation for the nontransforming case. Here classical necking behavior is demonstrated: the neck forms (at the point of the initial "flaw") near maximum load and continues to grow. In marked contrast to the behavior for the nontransforming material, Fig. 4.3 shows the deformation of the model transforming material at $373K$, a model temperature at which a recovery in tensile stability occurs. At this temperature a completely different pattern of deformation is observed. The neck forms at the center of the specimen just as it did for the nontransforming case. However, instead of continuing to grow, the neck propagates down the length of the specimen, at which point a substantial period of uniform elongation takes place. Finally, a second neck forms at the center of the specimen, and this neck grows without recovery. The final result is a dramatic increase in the total elongation of the specimen, characterized by the difference in length between the deformed meshes of Figs. 4.2 and 4.3, as shown together in Fig. 4.4.

The behavior described in the previous plots can be explained in terms of the loss

and recovery of plastic flow stability as explained in section 2.5.2 (see Fig. 2.20). In this section, we introduced a "stability" parameter, h/σ, lending qualitative insight into the tendencies for plastic flow localization. Within the context of our viscoplastic model, the hardening rate, "h", must now be interpreted as an incremental hardening rate, $h = \Delta\bar{\sigma}/\Delta\bar{\epsilon} = 3\Delta\bar{\tau}/\Delta\bar{\gamma}^p$. Since these materials are relatively rate insensitive, strain-rate-hardening effects are minimal, thus $h/\bar{\sigma}$ does not lose its qualitative significance. The neck first forms when the uniaxial strain reaches ϵ_u (where the stability parameter h/σ falls below unity), and it continues to grow until the the average strain across the minimum section reaches ϵ_L, at which point $h/\bar{\sigma}$ increases above unity once again. At this point the neck stops growing in this region, but in a neighboring region the initial necking strain ϵ_u has been achieved, and so the neck forms at this new location and grows there until ϵ_L is reached. This continuous process causes the neck to travel down the specimen until the end of the gauge section is reached. At this juncture, a second stage of uniform deformation begins, during which the strain in the specimen increases from ϵ_L to $\epsilon_{u'}$. The incremental stability parameter $h/\bar{\sigma}$ is greater than 1.0 during this stage of deformation, so the flow is stable. The final loss of stability first occurs again at $\epsilon_{u'}$ at the center of the specimen (which still has a reduced cross-sectional area relative to other locations as a result of the initial perturbation). As recovery is no longer possible at still higher strains, this neck grows until, in an actual specimen, fracture occurs.

Actually, the strain at which the neck propagates must be somewhat greater than ϵ_L, because the propagating region has a reduced cross-section relative to the adjacent material. Therefore, additional hardening is required to offset the differences in cross-sectional areas of the drawn-out band and the neighboring material. In other words, the load carrying capacity must be greater in the band than outside the band, and the extra strain-hardening is required for this purpose.

At the higher temperature ($448K$), the formation of martensite in the necked

region is not sufficient to cause a recovery of stability, and the neck grows rather than propagating. However, a comparison of specimen profiles (*i.e.*, the displaced position of the nodes along the outer edge of the deformed mesh) for the nontransforming material and this higher temperature transforming material (Fig. 4.5) at equivalent reduced sections $R/R_0 = 0.734$, (and thus equal diametral strain levels), reveals that the transforming material has a more diffuse neck — transformation has redistributed the deformation away from the mid-specimen plane.

Fig. 4.6 compares the distribution of scalar fields $\overline{\gamma}^p$, Σ, and f for the $T = 448K$ transforming material and the nontransforming material at this same reduced section, $R/R_0 = 0.734$. It is well-known that the formation of a tensile neck is accompanied by a concentration of strain and an increase in triaxiality (over its level in uniaxial tension) at the center of the neck. As a result of the increased triaxiality, the probability of martensite nucleation is enhanced. The resulting levels of martensite volume fraction are a direct consequence of the combined effect of the strain and triaxiality fields.

Fig. 4.7 shows the variation of $\overline{\gamma}^p$, Σ and f across the minimum section at this same reduced section, $R/R_0 = 0.734$. Equivalent strain and triaxiality are both maximum at the center of specimen and decrease smoothly towards the edge of the specimen. The increased triaxiality at the center of the neck has led to an enhanced driving force for transformation, and hence higher f. The corresponding increase in flow stress at the the specimen center has, at the same time, lowered the triaxiality at the center with respect to the nontransforming case. Comparing the variation of triaxiality across the minimum section for the nontransforming and transforming cases (Fig. 4.8) indicates that diffusion of the neck for the transforming material results in substantially decreased triaxiality at the center of the neck relative to the nontransforming value. This trend becomes even stronger at the lower temperature, $T = 423K$, where, at a minimum reduced section, $R/R_0 = 0.734$, the triaxiality at the

center of the specimen, was 27% lower than the peak for the nontransforming case, compared to 17% reduction for the $T = 448K$ case. For the still lower temperature case, $T = 373K$, an early restabilization of plastic flow resulted in very little build-up in triaxiality prior to propagation. The experimental observations of Young are consistent with model predictions neck diffusion with transformation, as shown in Fig. 4.9.

The enhancement of martensite formation is more clearly evident in Fig. 4.10, where we plotted the strain history of f of a material point at the neck center. For reference, we have also plotted predictions of f versus $\overline{\gamma}^p$ obtained from constant triaxiality analyses conducted under uniaxial and plane strain conditions. As Σ increases, f_{neck} departs from its uniaxial value, and continues to increase at an enhanced rate, eventually crossing the reference plane strain curve as Σ_{neck} nears its plane strain value. Fig. 4.11 shows the corresponding stress-strain curves of this material point. The resulting variable triaxiality stress-strain history shows a more steady rate of hardening than do the reference constant triaxiality curves.

Another consequence of the triaxiality-dependence of of martensite formation is that the temperature at which the transition from necking behavior to drawing behavior occurs is increased above the value predicted by the non-stress-dependent model of [13]. Our calculations indicate that that this transition occurs near $T = 423K$. Experimental data from Young [7], as shown in Fig. 4.12, suggest that the transition temperature is lower — around $T = 350K$. This discrepancy might be an indication that the predicted stress-state sensitivity of transformation kinetics, manifested in the model through the g_2 term of (3.28), which we inferred from Young's tension/compression data, may be too high. It could also, however, simply be due to the lack of stress-strain data for this material at these high temperatures. Attempts to fit the one available tensile stress-strain curve of Young [7] resulted in an overprediction of the flow stress. This is likely attributable to the lack of data for the baseline

martensite material, which cannot sustain strains past a few percent. Overprediction of the martensite flow strength is consistent with the higher model predictions for the necking/drawing transition temperature.

4.2.4 Summary

This first application of the constitutive model to a boundary value problem has provided some insight into the macroscopic effects of transformation plasticity in the strain-induced temperature regime as well as more general information concerning interpretation of tensile test data. It is obvious that the formation of martensite can drastically change the overall macroscopic behavior of the material. It has also served to demonstrate the stress-state sensitivity of transformation kinetics.

The most readily apparent beneficial property of the transformation is that it delays the onset of final necking to a much higher strain level. Comparison of the deformed meshes for the nontransforming material and the transforming material at $T = 373K$ indicates tremendous increases in ductility with transformation, as has been observed experimentally.

A less dramatic but equally important feature of the transformation demonstrated here is the diffusion of the necking and lowering of triaxiality in the neck, as demonstrated by the behavior of the transforming material at the higher temperature $T = 423K$. Although the changes in triaxiality are not drastic, it is reasonable to postulate at this point that these differences, coupled with other, more microscopic effects (discussed later — such as the effect of the transformation on the stress and strain fields in the immediate vicinity of particles and its interaction with the flow localization/void nucleation process) are likely the explanation for the observed 20 to 50% increases in fracture strain relative to nontransforming values measured by Leal [6] and Young [7].

4.3 Stress and Strain Fields Around a Stiff Spherical Particle

4.3.1 Introduction

In this section, we consider the fields surrounding an included particle embedded in a transforming/nontransforming matrix, subject to a far-field load. Previously [13], using the constitutive model which did not account for the stress-state sensitivity of transformation kinetics, we analyzed this problem for several normalized temperatures within the strain-induced regime, but only for the case of remote uniaxial tension. Our main findings were that transformation dramatically reduced interfacial strain levels, but that peak normal interfacial stress levels scaled with the level of the higher far-field flow stress. Here, in order to assess the influence of stress-state sensitivity of transformation kinetics, we re-examine this problem using the current model. Stress-state dependence of transformation kinetics allows for transformation near the matrix/particle interface (due to high local triaxiality) at temperatures for which the far-field flow behavior is not significantly affected by transformation.

Since we are primarily interested in the void nucleation process as it occurs in a crack-tip stress field or at the center of a tensile neck, we have also imposed higher far-field triaxiality levels, in order to determine whether transformation leads to different predictions under these conditions.

Because of the small length scales associated with this problem, some justification of the use of a continuum model is required. Typically, the carbide or oxide particles around which voids nucleate are about 0.1 to 0.3 microns in diameter [7]. On the other hand, the critical size of the martensite nucleation sites which might be found near these particles has been determined to be about 50Å [39]. Thus the ratio of particle size to nucleation site size is of the order of at least 20:1. It seems, therefore, that a continuum model is at least *marginally* justifiable. Of course, another concern

that arises when considering such small length scales is that the entire domain of the analysis lies within one grain of the material. Thus, the concepts of polycrystalline plasticity also become suspect. Nonetheless, substantial insight can be gained by applying continuum concepts to this problem.

Spherical particle problems were first studied by Goodier [127]. Eshelby [84] later solved analytically the problem of an elastic ellipsoidal particle embedded in an elastic matrix and determined that the stresses and strains are uniform inside the particle, as discussed in chapter 3. More recent studies have been devoted to numerical calculations of particles in rigid elastic-plastic matrices. Thompson and Hancock [128] considered rigid spherical particles in elastic-perfectly plastic and elastic power-law hardening materials. Needleman [129] studied rigid spherical particles in an isotropic hardening elastic-viscoplastic matrix. Wilner [130] solved the problem of an elastic particle embedded in a plastically-deforming matrix under the assumption of small strains.

4.3.2 Problem Description

The boundary value problem considered here models an infinite series of stacked cylinders with spherical particles, as pictured in Fig. 4.13. Tvergaard [131] proposed that this problem closely represents the problem of a three dimensional array of hexagonal cylinders with spherical particles. The model is axisymmetric, and due to symmetry about the midplane of the cell, only one representative section need be modeled (as indicated in solid black). Fig. 4.13 depicts the isolated cell. Boundary conditions along the four sides of the model provide the necessary symmetry and periodicity conditions for modeling the infinite series of stacked cells. The boundary conditions are as follows: symmetry conditions are applied along the midplane of the cell, i.e., the nodes along the midplane are constrained to move only in the radial

direction; the nodes along the top of the cell are constrained to have equal axial displacements— the prescribed displacement increments which control the loading in the problem are enforced on these nodes; the nodes along the outer edge of the cell are constrained to have equal radial displacements; and the nodes along the pole (z-axis) are, by definition, constrained to have zero radial displacement. In this analysis, the ratio of particle diameter to cell diameter is specified to be $a/b = 1/20$. This ratio yields approximately a 0.2% volume fraction of particles, thus representing a nearly isolated particle. Thus, for this small volume fraction, the representation of this model as a series of stacked cells is not critical, because particle interaction is essentially nonexistent.

Three separate loading conditions were considered: a uniaxial case; and two cases where higher levels of triaxiality were imposed. For the latter two cases, triaxiality was imposed by applying a negative pressure along the outer radius of the cell. In order to keep the level of the far-field triaxiality constant throughout the loading history, these pressures were defined, via the DLOAD subroutine of ABAQUS (see Appendix D), to scale with the far-field flow stress. Because the solution was obtained under displacement control, we estimated the far-field flow stress by assuming it to be a power-law function (using austenite hardening parameters) of the applied axial strain, ϵ_{zz}^{∞}. This assumption, which neglects the effects of elasticity and of any far-field evolution of martensite, nonetheless resulted in triaxiality levels that varied by less than 1% throughout the deformation history.

The finite element grid used for this problem is shown in Fig. 4.15. In this mesh, the elements are concentrated near the interface on the matrix side, in order to capture the steep gradients in the various fields which occur along the elastic-plastic side of the interface. The particle, which is modeled as an elastic carbide particle with Young's modulus $E = 210$ MPa and Poisson's ratio $\nu = 0.36$ [132], did not require such refinement.

Several test cases were performed in order to determine which of the many axisymmetric elements available in ABAQUS yielded the most reliable results. Four node isoparametric quadrilateral axisymmetric elements, as used in the previous series of problems, were not able to adequately represent a state of constant elastic strain when both the particle and the matrix were given the same material properties, and a constant displacement was imposed along the top edge of the mesh. Standard eight-noded elements failed to provide accurate conversion of the normal and shear stresses along the interface, due to the tendency of these elements to lock under the constraint of incompressible plastic flow. Eight-noded hybrid elements and eight-noded reduced integration elements both seemed to solve the locking problem. Hybrid elements, for which the pressure stress is interpolated independently from the deviatoric stress throughout each element, were finally chosen because they provided better convergence of the tractions along the particle-matrix interface. With this choice of element type, the mesh uses 428 elements with 1400 nodes. Due to the convergence problems inherent in this highly constrained, large deformation, elastic-plastic analysis, the solutions required substantial computation time. Solutions were obtained under displacement control, with a constant normalized displacement rate, $\Delta z/(b\Delta t) = 0.5/sec$, applied at the upper nodes of the cell.

The following discussion considers the results of this problem for two cases: a nontransforming case; and a transforming case at a temperature, $T = 448K$ ($\Theta \approx 1.0$), for which the driving force for transformation under uniaxial conditions is quite small (*i.e.*, far-field $f < 0.001$).

4.3.3 Results and Discussion

We begin by reviewing the results of the preliminary study [13], so that we may then focus directly upon the influence of the stress-state sensitivity of transformation

kinetics on the near-particle and the interfacial fields, with special attention given to the higher triaxiality cases.

In the preliminary analysis, we only considered the case of far-field uniaxial tension ($\Sigma^\infty = 0.33$). As it should be expected, most of the nonhomogeneous plastic flow occurs in an area very close to the particle-matrix interface. At very low far-field strains (3%), the results were quite consistent with the work of Wilner [130]. The plastic zone shapes, the location of the peak traction, and the distribution of intense straining were all qualitatively similar. Fig 4.16 summarizes model predictions of interfacial fields at a far-field strain axial level, $\epsilon_{zz}^\infty = 0.125$, obtained in the preliminary analysis. Peak strain levels are dramatically reduced for the transforming cases. Since the old kinetics model was strictly strain-based, martensite formed as shown in the figure, peaking at the the location of maximum strain at $\phi = 45°$ (where ϕ is measured from the r-axis, transverse to the direction of loading — to the z-axis, parallel to the direction of loading). Peak triaxiality and peak normal stress occurred at about $\phi = 75°$. Interfacial triaxiality is significantly enhanced from its far-field value, $\Sigma^\infty = 0.33$. Fig. 4.17 depicts the strain history of maximum normal interfacial stress, σ_{rr}^{max}. In Fig. 4.17a, σ_{rr}^{max} is normalized by the initial austenite flow strength, Y_0, and in Fig. 4.17b, it is normalized by the level of the far-field flow stress, $Y(\epsilon_{zz}^\infty)$. When scaled by the constant, Y_0, the history of peak traction resembles the stress-strain curve of the remote matrix material, and when scaled by the far-field flow stress, $Y(\epsilon_{zz}^\infty)$, the peak traction approaches a steady state-value. Aside from some transient effects, it is clear that the peak interfacial traction is a direct function of the applied far-field load, unaffected by many details of the local fields.

In contrast to these preliminary results, Fig. 4.18 shows current model predictions for the interfacial levels of equivalent plastic shear strain, martensite volume fraction and triaxiality for the transforming case at $\epsilon_{zz}^\infty = 0.12$ under remote uniaxial tension. Due to the interfacial distribution of triaxiality, the peak in martensite volume fraction

is pushed toward the pole of the particle.

Fig. 4.19a shows the distribution of martensite around the particle at $\epsilon_{zz}^{\infty} = 0.09$. This distribution is in reasonable accordance with an experimental observation of enhanced martensite formation around an alumina particle in the phosphocarbide-strengthened alloy of Young [7], as shown in Fig. 4.19b. This micrograph was obtained from a uniaxial tension test at a measured tensile plastic strain level of 9% and temperature of $388K$, sectioned parallel to the direction of applied load. The lower experimental temperature can account for the apparently higher volume fraction of martensite near the pole of the particle.

Figs. 4.20 through 4.23 summarize current model predictions for interfacial fields for the three different applied far-field triaxiality levels. It is immediately obvious that increased triaxiality has a significant effect on interfacial fields: $\overline{\gamma}^p$, and Σ both increase significantly, and therefore so does f. The interfacial values of f indicate that, at the higher far-field triaxialities, the distribution of f becomes less biased toward the point of maximum triaxiality. This is because the driving force for transformation is quite high even at the lower angles, and the probability function has reached the point where it increases much more slowly with increasing driving force (recall Fig. 3.1). More importantly, σ_{rr}^{max} also increases significantly with increasing far-field triaxiality. Fig. 4.24 shows the history of peak interfacial normal traction, scaled by Y_0, for the nontransforming and transforming cases. In the uniaxial case, where the far-field conditions for the transforming and nontransforming cases are essentially equivalent, it is clear that, at these far-field strain levels, transformation leads to a slight reduction in peak traction. This decrease can be attributed to the redistribution of stress and strain near the interface brought about by the formation of the much harder martensite. At the higher remote triaxiality levels, some martensite does form in the far-field. The difference between nontransforming and transforming values for this case can now only be partially attributed to a redistribution of interfacial fields;

the remainder of the difference must be attributed to the decreased far-field flow stress for the transforming case, due to transformation softening. Because of the hardening effect of transformation, the far-field flow stress for the transforming case begin to increase, and the peak interfacial stresses for the transforming case will ultimately reach and surpass the nontransforming curve.

4.3.4 Summary

In assessing the effects of transformation with respect to the void nucleation process, the question that must be addressed is whether or not the critical nucleation stress is reached at a strain level for which transformation suppresses peak local tractions. If so, then transformation clearly suppresses nucleation, and, because of the slow increase in peak normal stress with far-field strain, can lead to significant delays in macroscopic nucleation strain. If not, the redistribution of stress and strain must be weighed against the deleterious effects of far-field transformation hardening. Critical interfacial strength levels are thought to be 0.01 to 0.02 times the material Young's modulus [133] (about 2 to 4 times the material yield strength for these materials), so that nucleation of voids in far-field conditions of high triaxiality probably occurs at relatively low values of remote strain. The results shown in Fig. 4.24 indicate that transformation indeed leads to a reduction of peak tractions relative to the non-transforming case for the given combinations of strain and triaxiality. In view of the tendencies for transformation to delocalize plastic flow and decrease triaxiality, as demonstrated in section 4.2, the simple fact that increased remote triaxiality increases interfacial traction is an encouraging result, at least within the context of the macroscopic behavior manifested in a simple tension test, and lends itself as a further source of explanation for the observed increases in fracture strain.

We must finally mention that the results presented in this section have focussed on the nucleation process from the viewpoint of reaching a critical interfacial stress.

The nucleation process further involves the debonding of the particle prior to complete separation. A question that we do not address here is whether transformation suppresses this "unzipping" process. Transformation clearly decreases the intense straining near the particle, with the result that the partially cavitated transforming and nontransforming materials are quite different. It seems quite plausible that the lower strain levels and associated hardening capability of the transforming material, relative to the transforming material, may act to retard this process as well. The use of cohesive zone models, such as those proposed by Needleman [129], may prove useful in addressing this question.

4.4 A Self-Similar Analysis of Crack-Tip Fields in Small-Scale Yielding

4.4.1 Introduction

The fracture properties of a material clearly depend upon the state of stress and strain in the vicinity of the crack tip. It is important, therefore, to develop an understanding of the effects of the transformation plasticity in the near-tip region in order to better understand how the transformation might lead to retardation of flow localization and subsequent crack extension.

When ductile materials are subject to mode I (tensile opening) loading, the intense strains at the crack tip lead to blunting of the tip. In the vicinity of the crack tip, the material is highly stressed due to the geometric constraints imposed by the presence of the crack. This material plastically deforms, blunting the crack tip, and continues to deform until some criterion is met for localization of flow into shear bands or coalescence of nucleated voids. Experimental observations suggest that blunting can result in formation of sharp vertices at the crack tip [134], or it can be smooth, a mode which was observed by Rawal and Gurland [135] for a pre-fatigued crack in

spheroidized steel. Smooth blunting can be thought of as the limiting case of an infinite number of vertices, and naturally lends itself to analysis of near-tip fields using standard large strain, large displacement finite element methods. A smoothly blunted crack tip with a finite root radius can be modeled as a continuum without creating the numerical difficulties that would otherwise arise for a sharp crack, for which strain rates become singular at the crack tip.

The analysis which follows is patterned after the studies of McMeeking [136] for small-scale yielding (SSY) problems and extended to large-scale yielding problems by McMeeking and Parks [137]. The concept of small-scale yielding implies that the size of the plastic deformation zone is small in comparison to any other relevant length scales, *e.g.*, the length of the crack, or the width of the specimen.

The study of SSY problems is well established. Rice [138] first introduced the concept of the J-integral as a means of characterizing the fields near the crack tip in terms of one parameter, where the J-integral is a measure of the strain energy release rate, based on the fracture theory of Griffith [139]. Rice and Rosengren [140] and Hutchinson [141] developed a methodology for studying crack-tip fields in non-linear problems based on this single parameter, J. Begley and Landes [142] proposed that the J-integral could be used as ductile fracture criterion under certain conditions. The methods of Hutchinson, Rice and Rosengren were extended by Rice and Tracey [143] and Tracey [144] using improved finite element methods. These studies, which ignored large geometry changes, predicted intense levels of shear strain above and below the crack tip and high triaxiality ahead of the tip for plane strain, mode I loading. Because of the singular nature of the models, however, and the assumption of small geometry changes, these methods are not well suited for modeling the blunting of the tip and its effect on the near-tip fields (within a few blunted openings). Rice and Johnson [145], modeling blunting using slip-line techniques, noted that the intense deformation ahead of the crack could only be predicted when finite deformations of

blunting are taken into account. Since transformation plasticity affects stress-strain behavior predominantly at high strains, it is important to consider the effects of the transformation within the blunted zone.

McMeeking's method, on the other hand, does allow for evaluation of the effects of crack-tip blunting. It is based on the results of Rice and Johnson, who noted that, for non-hardening materials under the conditions of small-scale yielding, the shape of the crack tip could be predicted at all times from the steady-state shape of a sharp crack which has been loaded to the same levels. In other words, once a steady-state solution is obtained, the entire solution can be appropriately scaled by the level of the applied load. McMeeking verified these results numerically, and recently his methods have been used extensively in a wide variety of problems (*e.g.*, [146,147]). The unique feature of this technique is that it allows for scaling of results to any desired length scale, including crack-tip openings determined in actual tests, thus allowing for direct comparison between analysis and experiment.

4.4.2 Problem Description

This analysis models the blunting of an initially sharp crack undergoing plane strain, mode I loading. The finite element mesh used in the calculations, however, has been constructed such that, in the undeformed configuration, the crack tip has a finite root radius which is much smaller than the expected plastic zone size or the region of blunting. This apparent contradiction is allowable because when a steady-state solution is reached at a sufficient level of loading, the solution is independent of the original crack-tip notch geometry, as was shown by Rice and Johnson [145]. Since the notch blunts to several times its original radius, the difference between the solutions obtained using an initially rounded crack tip and one which supposes a sharp crack becomes negligible.

For continued loading past the point at which the steady-state is reached, the size but not the shape of the blunted zone changes, and thus the crack-tip opening displacement (CTOD) becomes the only significant characteristic length. McMeeking's results confirmed that if appropriate restrictions are made in regard to the size of the plastic zone with respect to the boundary of the finite element mesh such that the conditions of small-scale yielding are still valid, then the CTOD scales with the applied load. Therefore, the results can be scaled by the magnitude of the far-field load.

A schematic of the boundary value problem considered is shown in Fig. 4.25. The domain of the problem is a fan-shaped area which represents a region surrounding the tip of a crack that is well within the confines of any physical boundaries, such that the body can be considered to be infinite in extent, as shown in Fig. 4.25a. Only one-half of the notch need be modeled due to symmetry about the plane of the crack. Thus, symmetry conditions are applied at the mid-plane, while traction-free conditions are imposed along the free surface of the crack. The mode I load is applied by imposing the linear elastic, asymptotic crack-tip (K_I) displacement field along the outer boundary of the model (Fig. 4.25b). The load is controlled by supplying a value for the stress intensity factor, K_I, at a dummy node. The corresponding relationships between K_I and the far-field displacement field are imposed through an option available in ABAQUS which allows the user to impose constraints via a subroutine MPC which contains these relationships. In this manner the outer boundary displacements are determined according to the relationships governing mode I elastic crack-tip fields, as first derived by Williams [148] and based on the mathematical formulation of Muskhelishvili [149]. The displacement field, in Cartesian form, is given by:

$$u_y = \frac{K_I}{G}\sqrt{\frac{r}{2\pi}}\left\{(3-4\nu-\cos\phi)\sin\frac{\phi}{2}\right\}, \tag{4.2}$$

$$u_x = \frac{K_I}{G}\sqrt{\frac{r}{2\pi}}\left\{(3-4\nu-\cos\phi)\cos\frac{\phi}{2}\right\}, \tag{4.3}$$

where r is the radial distance from the crack tip, ϕ is the angle from the mid-plane, ν is Poisson's ratio, and G is the shear modulus. The displacements imposed at the outer boundary (r_∞), therefore, scale directly with the value of K_I applied at the dummy node according to this relationship. Some details of the derivation of the asymptotic displacement field relationships used in the analysis are given in Appendix E. The MPC subroutine is also listed in Appendix E.

Although the applied boundary conditions are strictly valid only for an elastic problem with small geometry changes, it is evident that both plastic strains and large deformations develop near the crack tip. If, however, the size of the plastic zone is kept small relative to the outer boundary of the mesh upon which these conditions are imposed; i.e., the conditions of small-scale yielding are met, then by St. Venant's principle, the effect of the plasticity in the near-tip region does not affect the validity of the asymptotic boundary conditions applied in the far-field.

In order to accurately model the near-tip solution and yet keep the plastic zone small enough so that SSY conditions are valid, the finite element mesh is designed with a several order of magnitude difference in size between the near-tip elements and the elements near the outer boundary. In order to accomplish this, the mesh, as shown in Fig. 4.26, uses 1340 4-node plane strain isoparametric quadrilateral elements (ABAQUS CPE4) and 1418 nodes, with a 4000:1 ratio between the outer radius of the mesh and the root radius of the crack. Note that in this figure the lower, near-tip mesh fits into the hole in the center of the center mesh which fits into the middle of the top mesh, as indicated by arrows. Although this seems like a radical gradient in length scales, it turns out that this is the minimum acceptable ratio, because the plastic zone must grow to a size of 300 to 400 root radii before the steady state solution is reached in most of the problems analyzed. The large number of elements and the incremental nature of the elastic-plastic solution again necessitated considerable computation time to perform these calculations.

Another feature of the finite element grid is the initial shape of most of the elements, which are oriented such that they are much longer in the radial direction than the circumferential direction. These high aspect ratios, as pointed out by McMeeking [135], are necessary especially near the crack tip, because as the notch is blunted to a size much greater than the original size, the elements near the tip become greatly distorted in the circumferential direction. If the original orientation is not radial, the deformed elements become distorted to the point where computational difficulties arise and accuracy is lost. Fig. 4.27 depicts a representative displaced mesh, which shows the blunting of the crack tip and the severe stretching of the near-tip elements in the circumferential direction, demonstrating the necessity for the oriented shapes of the elements.

4.4.3 Results and Discussion

Reaching the Steady-State

As postulated (and demonstrated by McMeeking [135]), after a sufficient number of increments, the character of the solutions no longer changed. Instead, a series of self-similar states were reached at which point the stress, deformation and state-variable fields, when scaled by the level of the applied load, became asymptotically identical. Fig. 4.28 shows the approach to the steady-state for a representative stress field ($\sigma_{\phi\phi}$ for the non-transforming case). In this graph, the normalized circumferential stress, $\sigma_{\phi\phi}/\sigma_0$, where ϕ is the angle measured from the plane of the crack and σ_0 is yield stress, is plotted versus the distance from the crack tip (in the deformed configuration), R_d, normalized by the load parameter J/σ_0. Here J represents the J-integral, which when measured in an elastic field, is given by the relationship $J = K_I^2/E'$, where $E' = E/(1-\nu^2)$. Calculations in [13] further demonstrate that the relationship between CTOD and J becomes linear as the steady-state solutions is reached. The

CTOD, for which we use the symbol "b", is defined here as the distance between points on opposite flanks of the crack surface which are intersected by a line originating from the crack surface at the mid-plane, and leaving at 45° angles from this point, as schematically illustrated in Fig. 4.29. This measure of b is somewhat arbitrary, but this particular definition keeps the CTOD consistent with respect to the position of the crack tip. This direct correspondence between the blunted opening, b, and the load parameter, J, allows us to present results in terms of b.

As in the previous analyses, we considered both a nontransforming and a transforming material. The model temperature for the transforming material was chosen to be near $M_{d,ut}$ $(448K)$, so that the crack tip region was not far above $M^{\sigma}_{s,ct}$, which was found experimentally in [1,6] to be the optimum for toughness.

Stress and Strain Fields Ahead of the Crack

Fig. 4.30 shows the extent of transformation near the tip of the blunted crack for the $T = 448K$ case. Due to the triaxial nature of the stress-state ahead of the crack tip, a considerable amount of martensite forms in this region, whereas very little martensite forms elsewhere, because of the relatively high temperature. Figure 4.31 shows the variation of equivalent plastic strain, triaxiality and martensite volume fraction on the ligament ahead of the crack tip. Because the strain decays rapidly ahead of the crack tip, the extent of the transformed region is limited; the peak level of martensite thus occurs well before the point at which peak value of triaxiality ($\Sigma \approx 2.3$) occurs. In fact, the peak value of martensite volume fraction occurs at the point where the equivalent shear strain curve intersects the triaxiality curve.

Transformation did not seem to affect the equivalent strain fields and the triaxiality fields, as shown in Figs. 4.32 and 4.33. However, due to the evolution of the much harder martensite phase, an area of increased hardness relative to nontransforming

values is formed directly ahead of the crack tip, as shown in Fig. 4.34.

Significant differences between the non-transforming and transforming cases were found for the parameter $h/\bar{\sigma}$, where $h = \Delta\bar{\sigma}/\Delta\epsilon$, in the context of our viscoplastic model, is the (incremental) hardening rate measured at fixed strain-rate. We again emphasize that the notion of a hardening rate, h, is strictly valid only in the context of rate-independent models. Nevertheless, because of the high rate-sensitivity exponents ($M = 100$) that we have chosen, strain-rate hardening effects are minimal, so that the parameter $h/\bar{\sigma}$ still lends significant qualitative insight into tendencies for plastic flow to become unstable. In Fig 4.35, we have plotted contours of $h/\bar{\sigma}$ for the transforming and non-transforming cases. In the non-transforming case, " stability" (in the Considère sense — recall section 2.5.2) is "lost" at all points where $\bar{\epsilon} > 0.10$. As the crack tip is approached along the ligament, plastic flow becomes more and more unstable. In the transforming case, the loss of stability is limited to a very short region in front of the crack, where the strains are tremendously high. There is a region in front of the crack tip, however, in which the plastic flow is quite stable, due to the strain-hardening influence of the martensite. This region, whose shape — not coincidentally — resembles the shape of the martensite zone, is bounded by a narrow band of low stability, which is a direct consequence of the strain-softening behavior of the transformation at low strain. Another way of viewing this stable region is demonstrated in Fig. 4.36. In this figure, we have plotted pairs of flow stress/equivalent plastic shear strain ($\overline{\tau}$, $\overline{\gamma}^p$) at nodal locations ahead of and approaching the crack (*i.e.* from right to left with reference to Fig. 4.31. When plotted in this manner, these pairs form a "stress-strain" curve of sorts. We have indicated on these curves the location of some of these pairs on the ligament, in terms of their distance from the crack tip. For the nontransforming case, near the crack tip the strain has reached levels which are beyond one-dimensional stability limits for this material. Assuming that one-dimensional stability arguments are qualitatively viable in this multi-dimensional

analysis, it is likely that further plastic flow will be unstable. On the other hand, for the nontransforming case, the strain has reached this critical level only very near the crack tip, and there is a range of equivalent shear strains (analogous to the range of uniaxial strains between ϵ_u and ϵ'_u in Fig. 2.20) — and thus a range of distances ahead the crack tip — for which stability is recovered. This area of stable flow will not be overcome until strain levels have increased by a considerable amount. In fact, since we have reached the steady-state solution, the point at the right end of this stable region will not become unstable until J (or, equivalently, b) increases by a factor of ten.

4.4.4 Summary

It is evident from these figures that transformation, because of the combined effects of strain and triaxiality, leads to the local formation of a region of much harder material, within which plastic flow is quite stable. It will therefore be very difficult for plastic flow to localize across this region. If localization of deformation is to take place, it must either find a path around the hardened zone, or wait for the local strains to increase to the point where this region becomes again unstable. In either case, the crack will be able to sustain much higher amounts of blunting and much higher imposed J's.

The more sophisticated methods which have been developed for predicting the loss of stability under multiaxial stress states, as we discussed in chapter 2, will not lead to qualitatively different predictions than those presented here. The stress-state dependence of the critical hardening rate will likely shift the zones of instability toward the location of peak triaxiality, a few blunted openings away from the crack tip. However, the stable region indicated in Fig. 4.35 will still be stable, since $h/\bar{\sigma}$ will always be well above the critical value here.

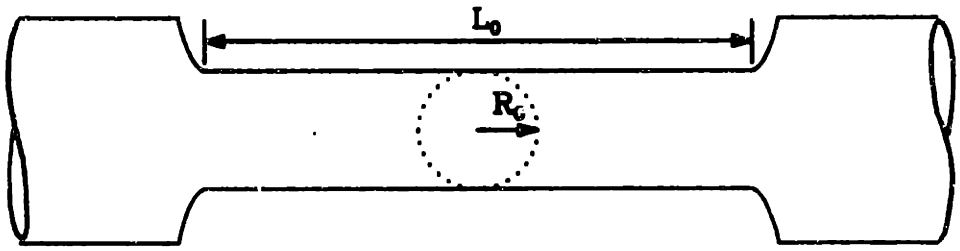

(a)

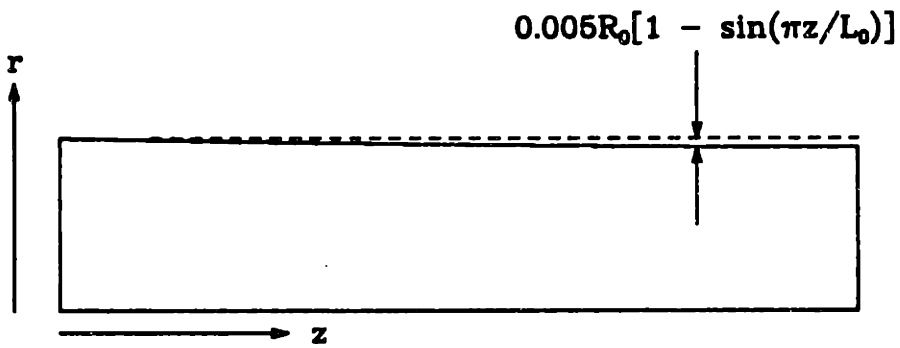

(b)

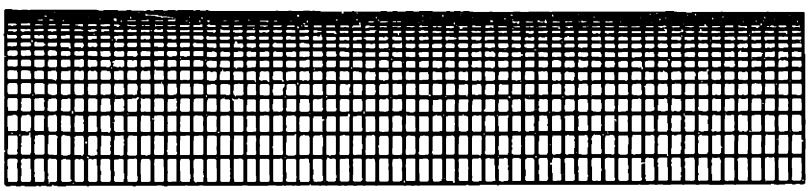

(c)

Figure 4.1 Description of problem studied, showing: (a) the tensile specimen analyzed; (b) a schematic of boundary value problem with initial perturbation; and (c) the finite element model.

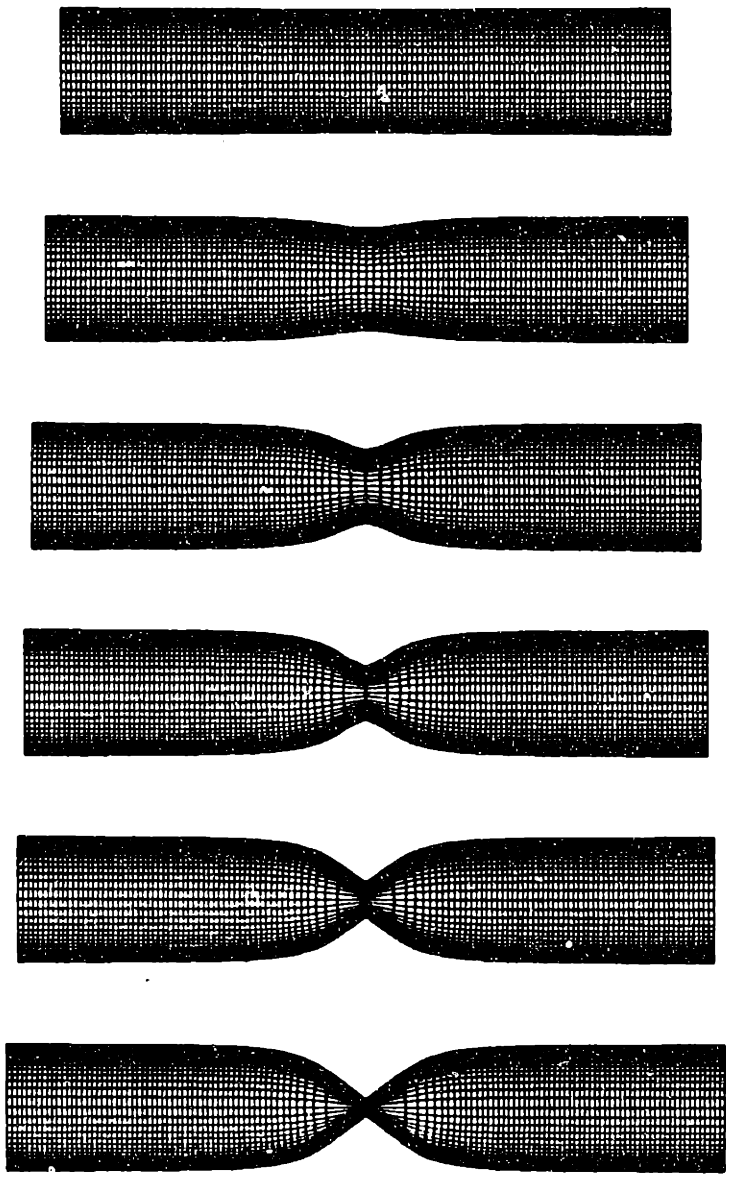

Figure 4.2 Deformed finite element meshes (which have been mirrored about the mid-plane and the longitudinal axis) at several displacement increments for the nontransforming case.

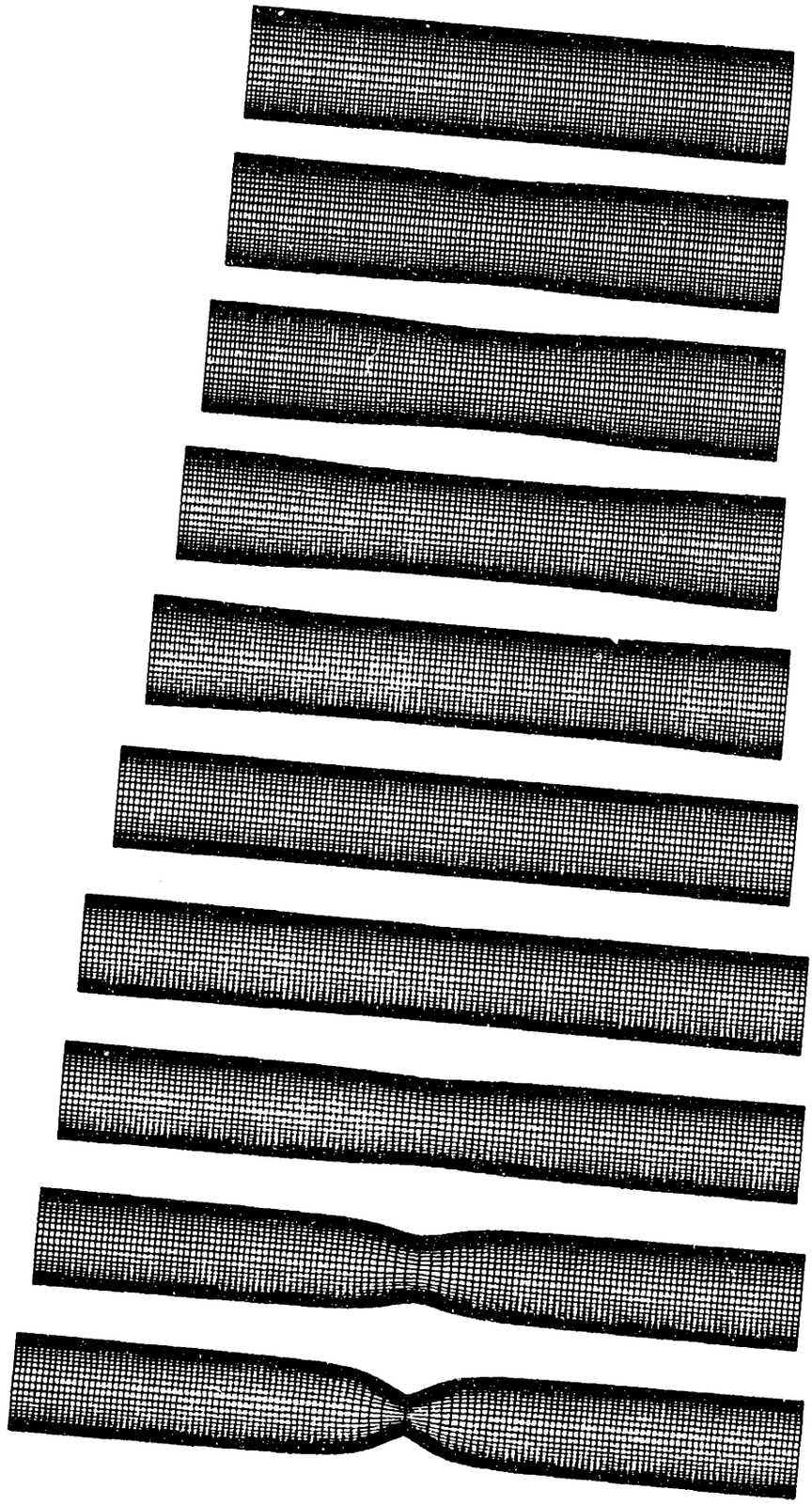

Figure 4.3 Deformed finite element meshes (which have been mirrored about the mid-plane and the longitudinal axis) at several displacement increments for the transforming case, $T = 373K$.

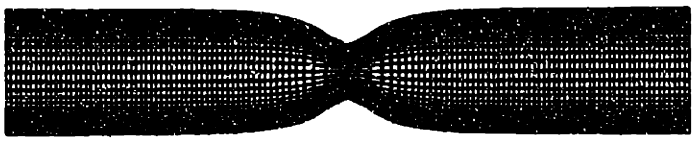

(a)

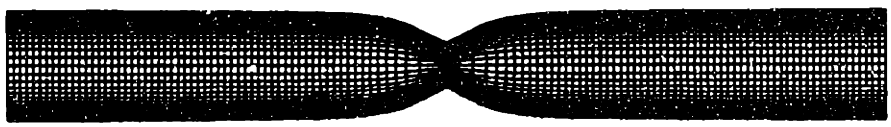

(b)

Figure 4.4 Comparison of deformed meshes at a reduction of approximately $R/R_0 = 0.5$ for: (a) the transforming case and (b) the transforming case, $T = 373K$.

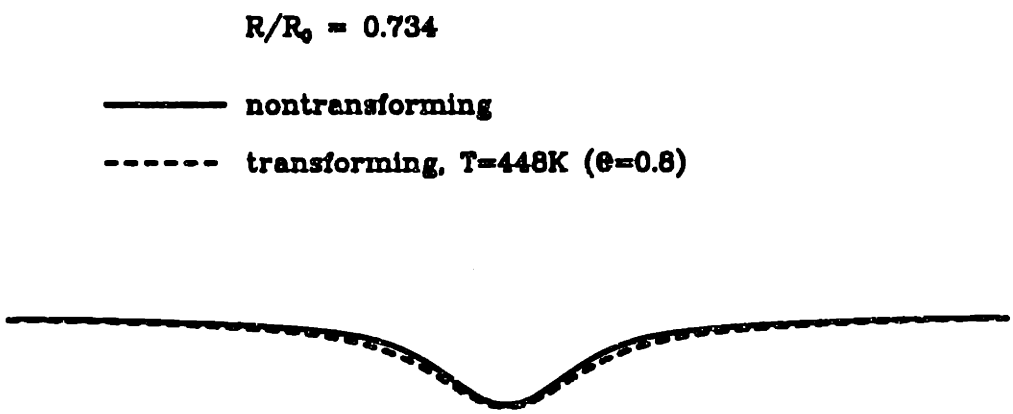

Figure 4.5 Comparison of specimen edge profiles at a reduction of approximately $R/R_0 = 0.734$ for: (a) the transforming case and (b) the transforming case, $T = 448K$. In order to accentuate the differences between the two, the radial position was magnified by a factor of four.

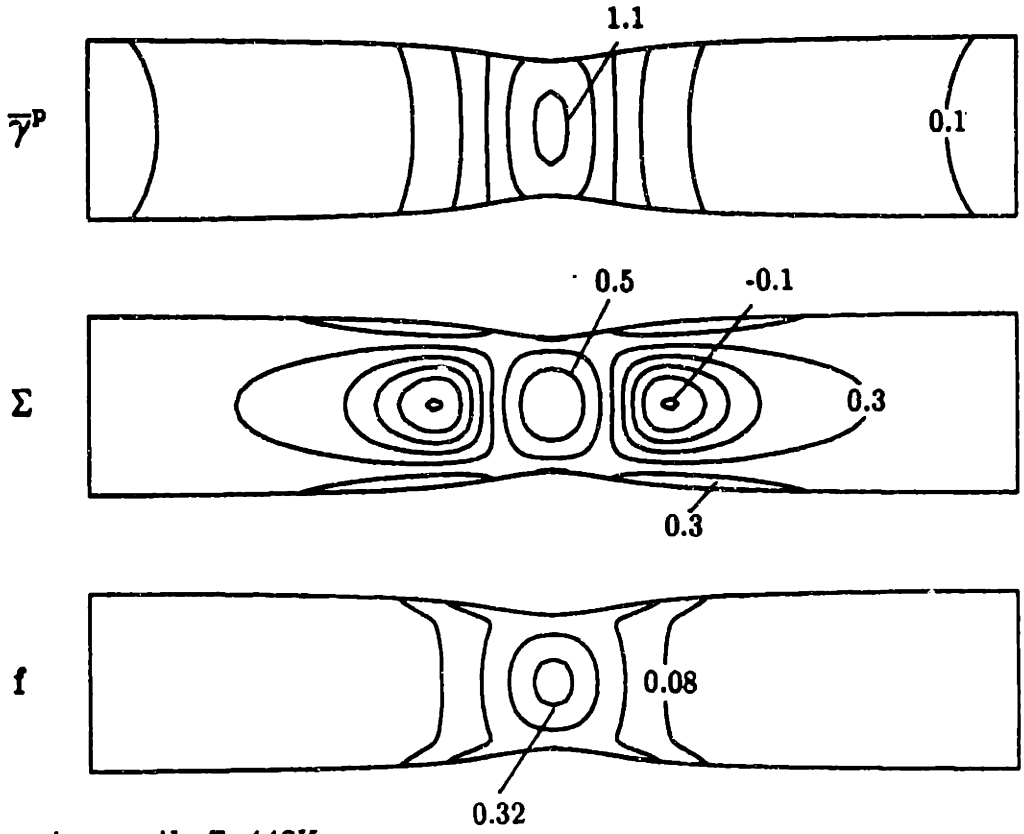

transforming matl., T=448K

---

nontransforming matl.

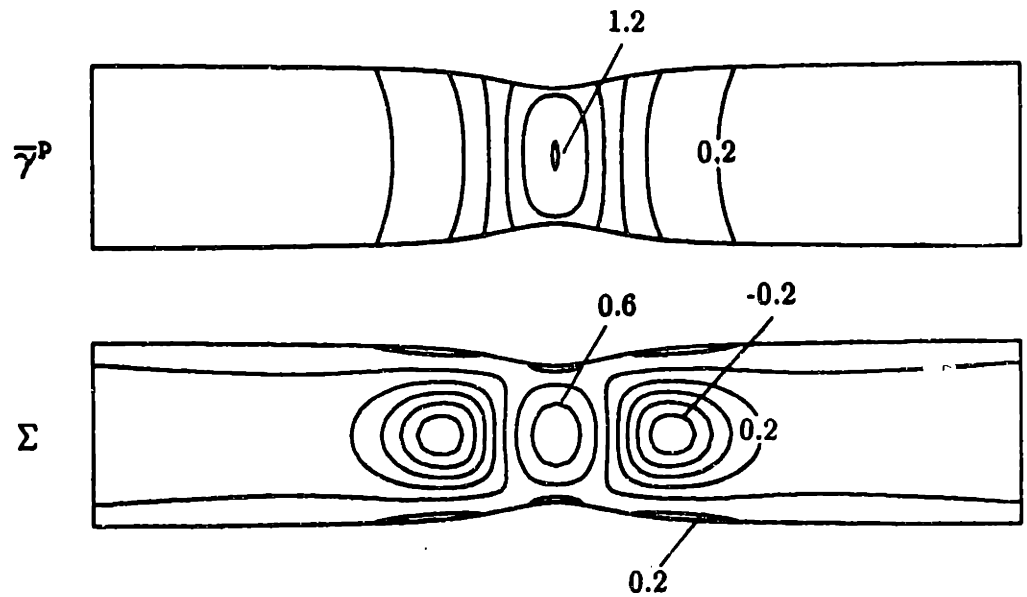

Figure 4.6 Comparison of scalar fields for $\overline{\gamma}^p$, Σ and f at equal minimum section reductions, $R/R_0 = 0.734$, for the transforming ($T = 448K$ [$\Theta = 0.8$]) and nontransforming cases.

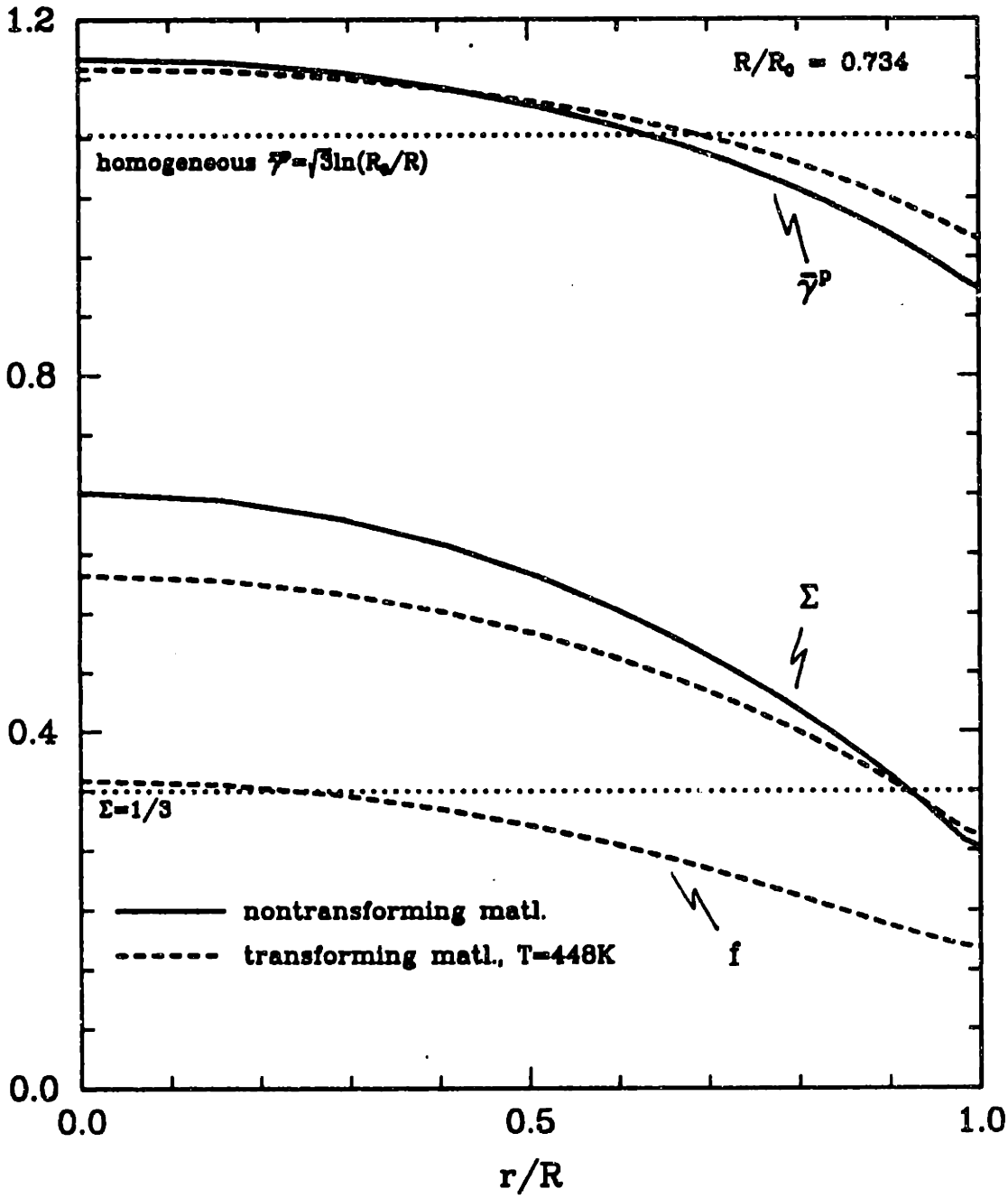

Figure 4.7 Variation of $\bar{\gamma}^p$, Σ and f across the minimum section at area reduction $R/R_0 = 0.734$ for the transforming ($T = 448K$) and nontransforming cases. The increased f at $r = 0$ is the combined result of the corresponding elevated values of $\bar{\gamma}^p$ and Σ.

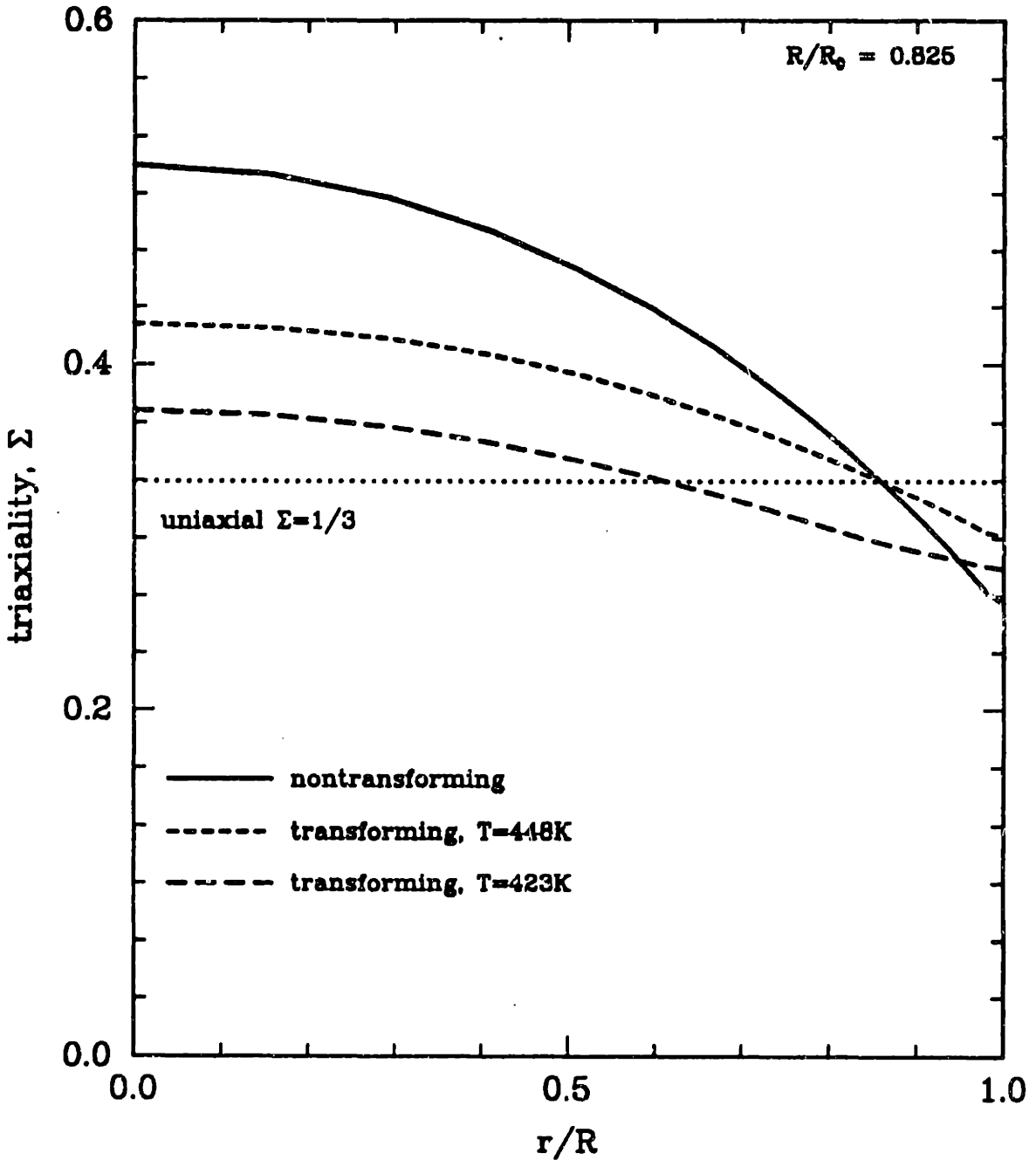

Figure 4.8 Variation of triaxiality, Σ, across the minimum section for the transforming ($T = 448K$ and $T = 423K$) and nontransforming cases, at equal diametral strain levels, $R/R_0 = 0.825$.

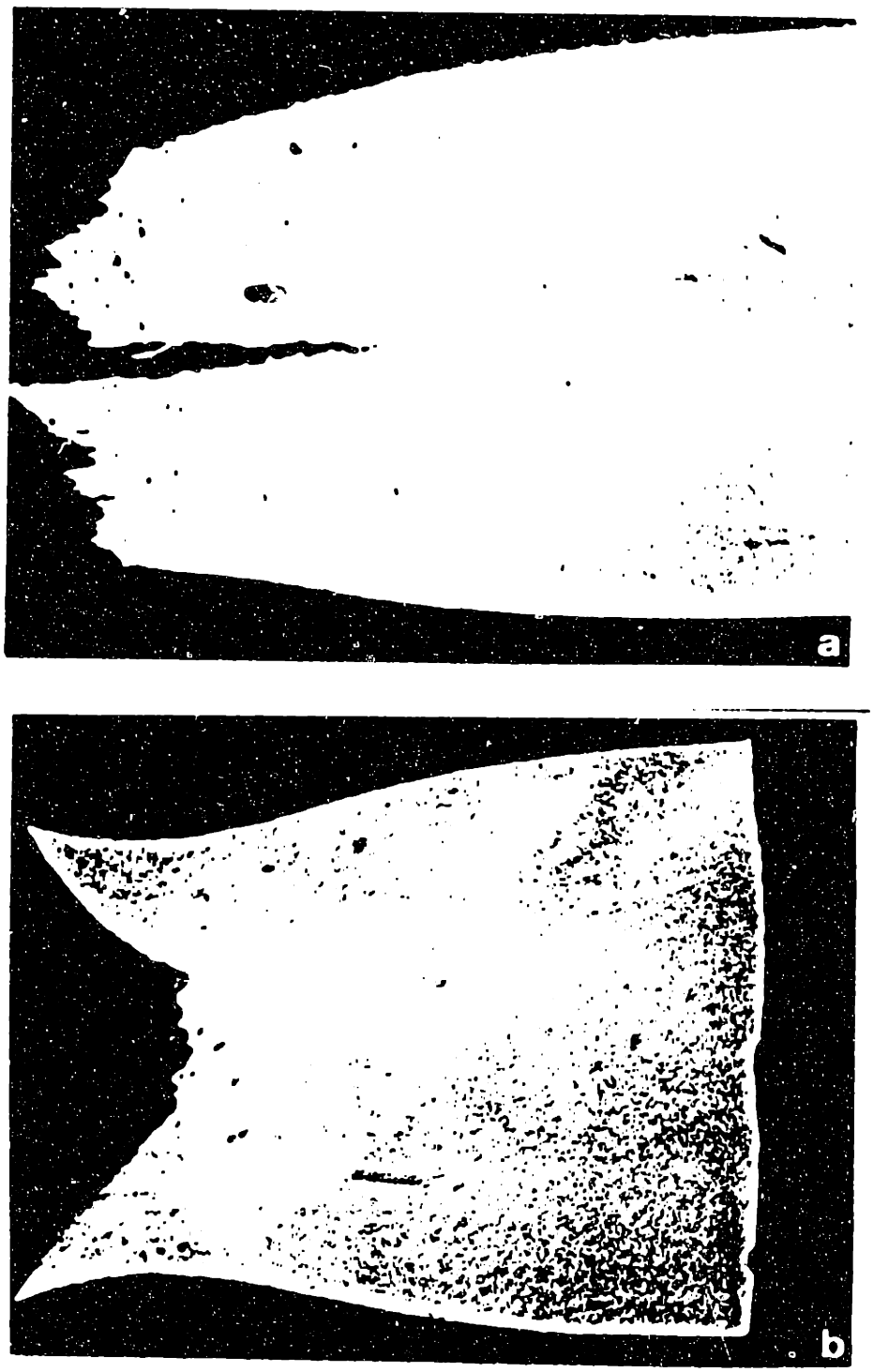

Figure 4.9 Comparison of fractured necks of tensile specimens for the over-aged 0.5Mn phosphocarbide-strengthened alloy of Young, tested at : (a) $T = 388K$, (b) $T = 523K$. These photographs clearly illustrate the decreased curvature of the lower-temperature (transforming) specimen compared to the higher temperature (nontransforming) specimen.

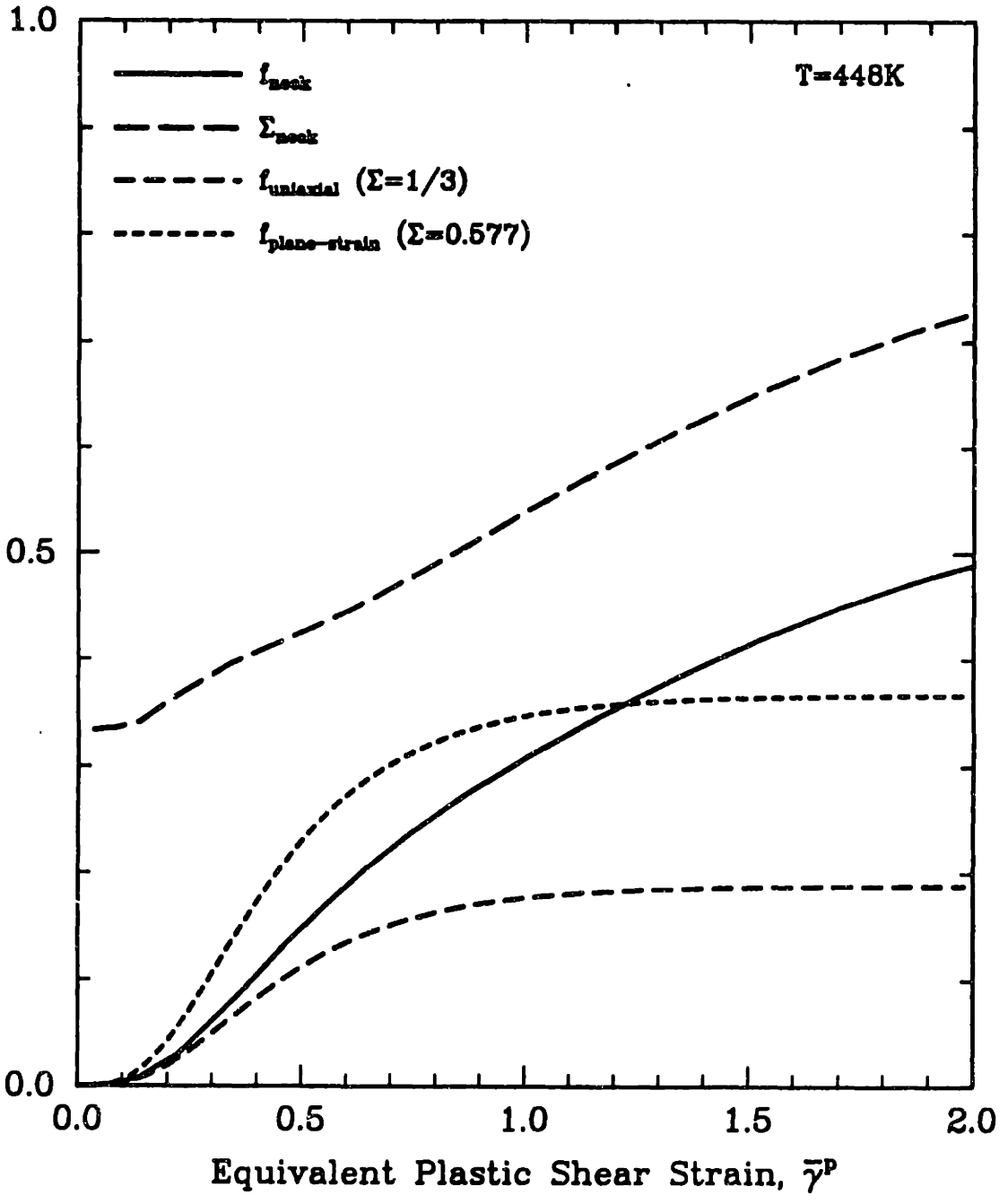

Figure 4.10 Comparison of the strain history of f at the center of the necking tensile specimen with the reference uniaxial and plane strain predictions of f versus $\bar{\gamma}^p$ for the transforming case ($T = 448K$).

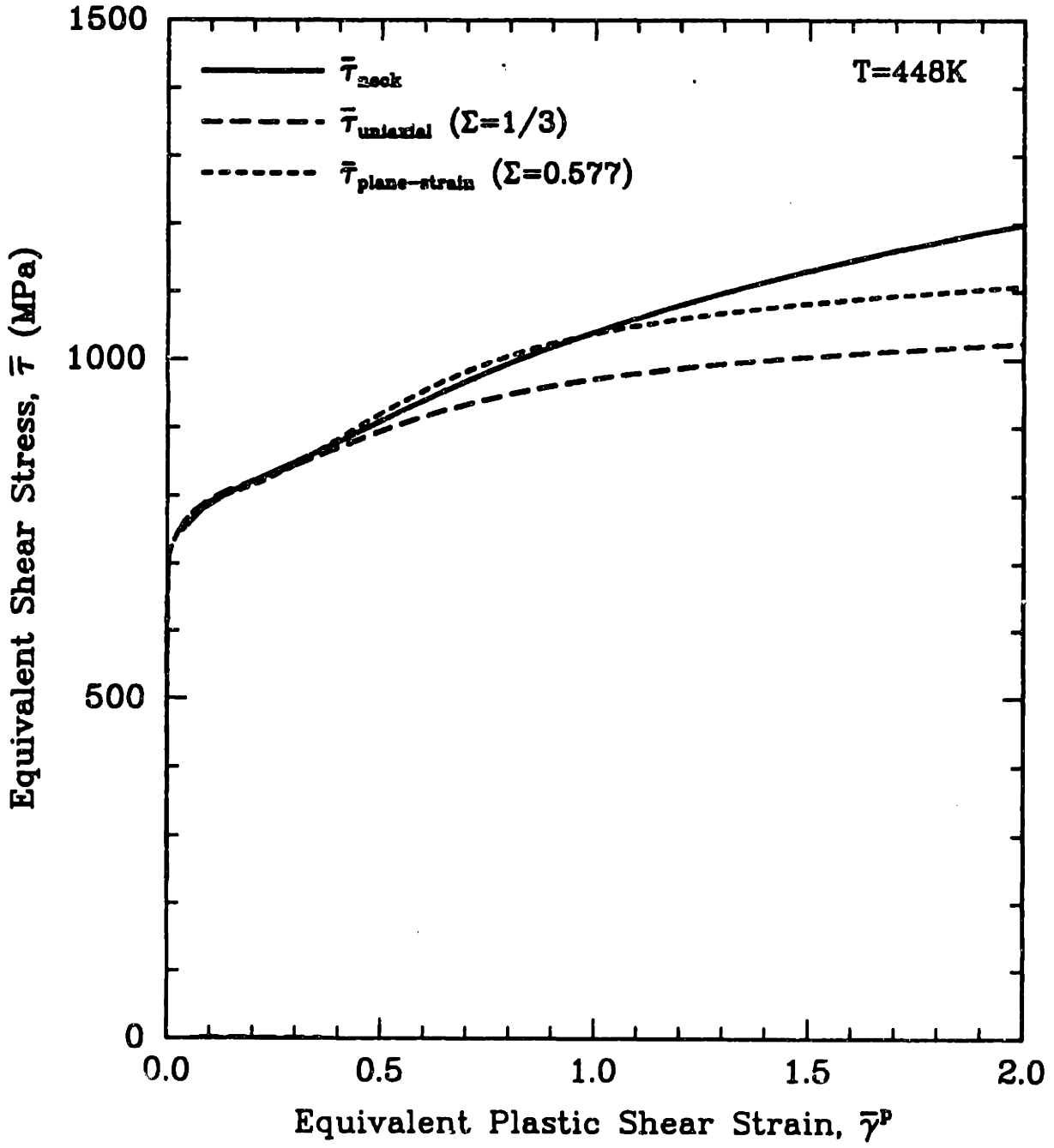

Figure 4.11 Comparison of the history of $\bar{\tau}$ at the center of the necking tensile specimen with the reference uniaxial and plane strain predictions of f versus $\bar{\gamma}^p$ for the transforming case ($T = 448K$).

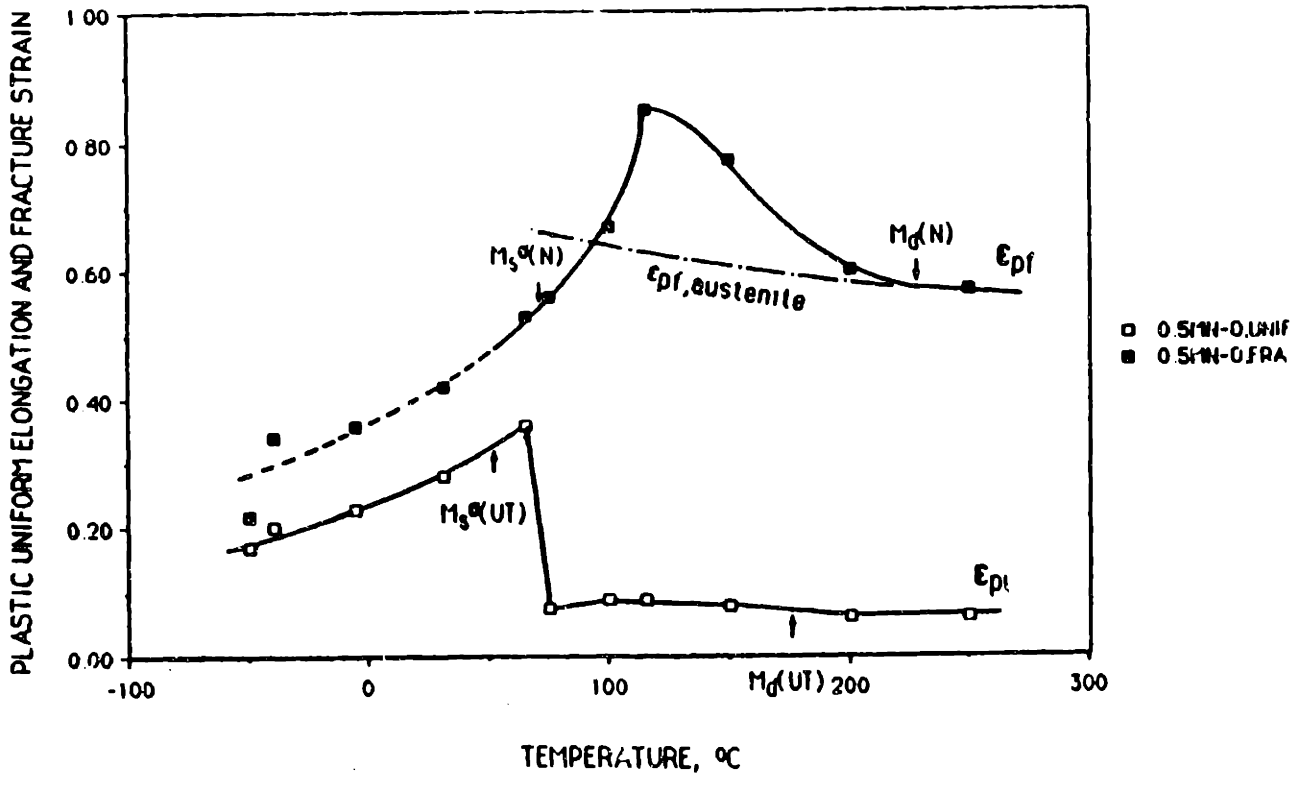

Figure 4.12 Temperature dependence of the plastic strain at fracture (ϵ_{pf}) and uniform plastic strain (ϵ_{pu}) for the overaged 0.5Mn alloy. Arrows indicate mean value of the relative transformation temperatures. The estimated fracture strain of austenite is also shown. Taken from [7].

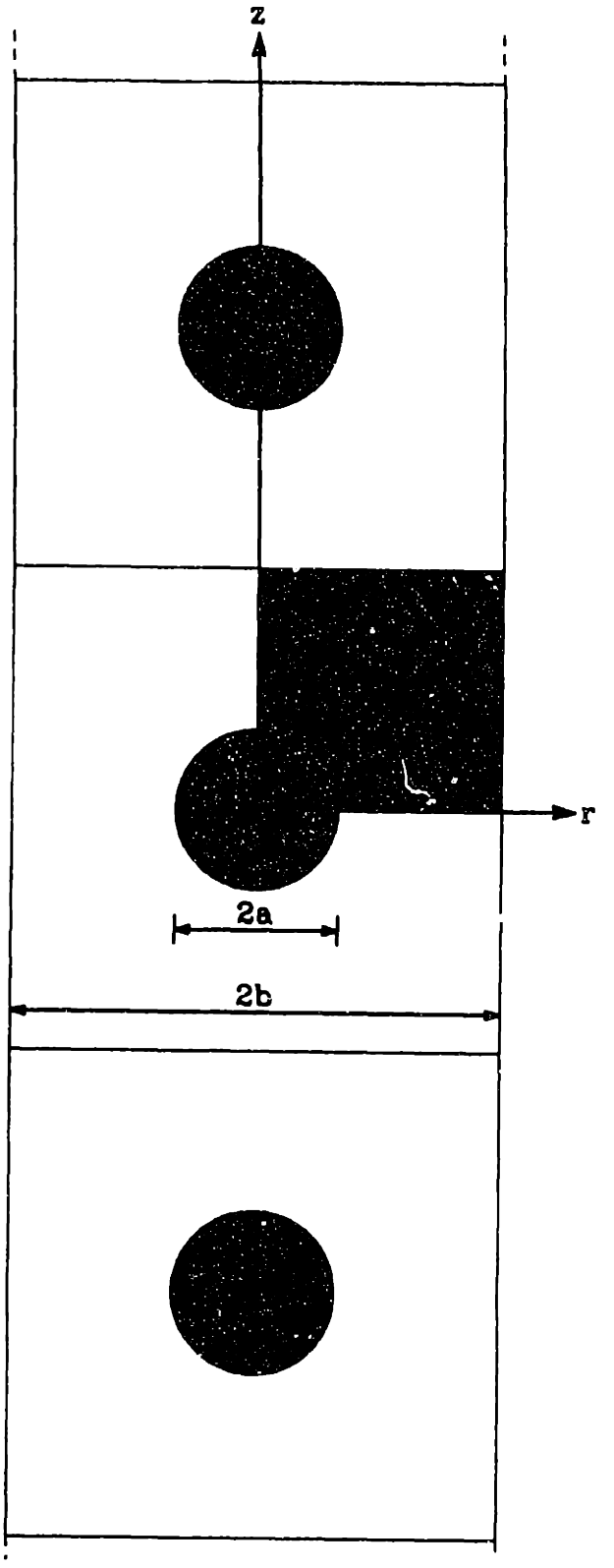

Figure 4.13 Schematic description of an infinite array of stacked cylinders with spherical particles. Only the quarter-cell with the matrix indicated in solid black is modeled in this problem.

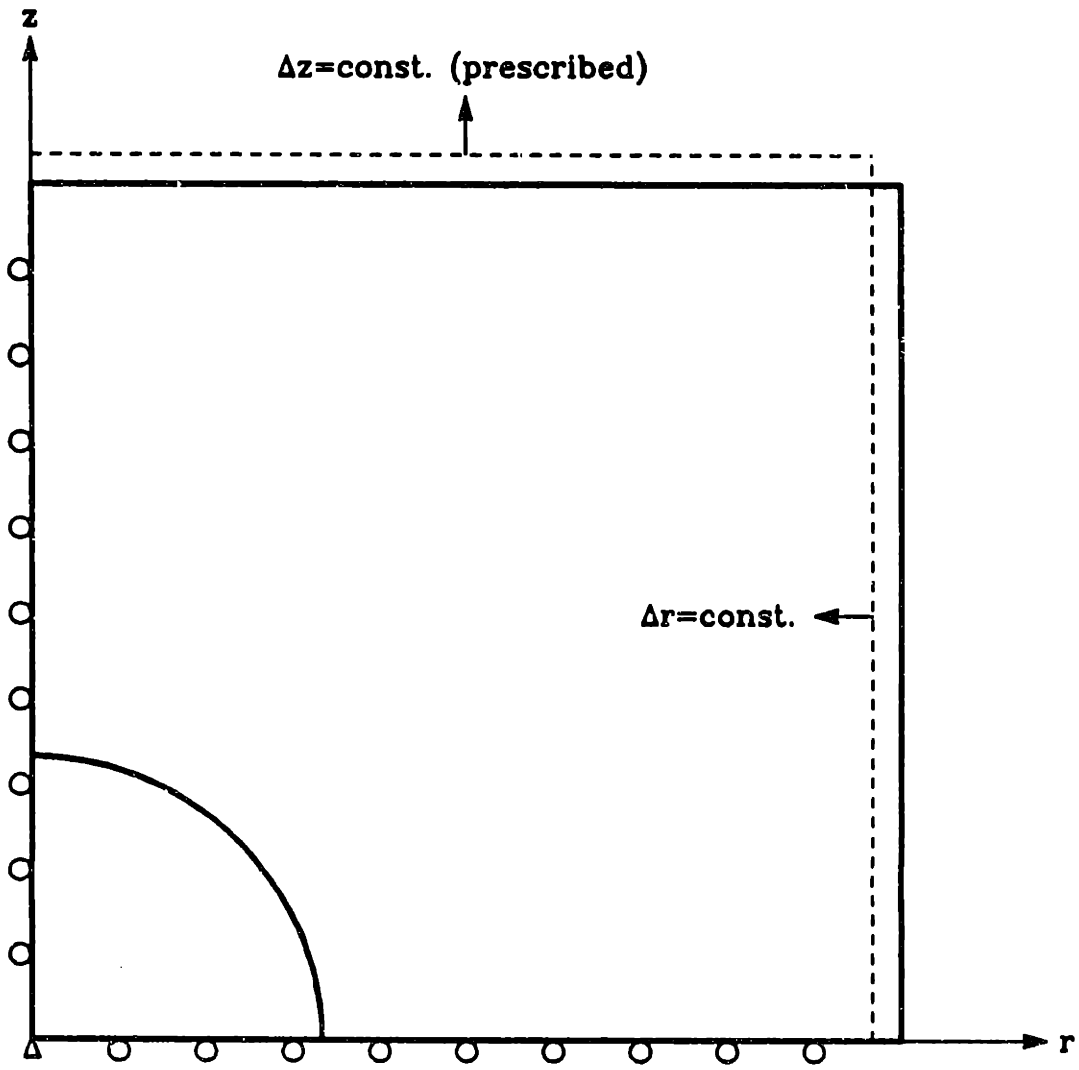

Figure 4.14 Schematic description of the spherical particle problem modeled, with the boundary conditions indicated.

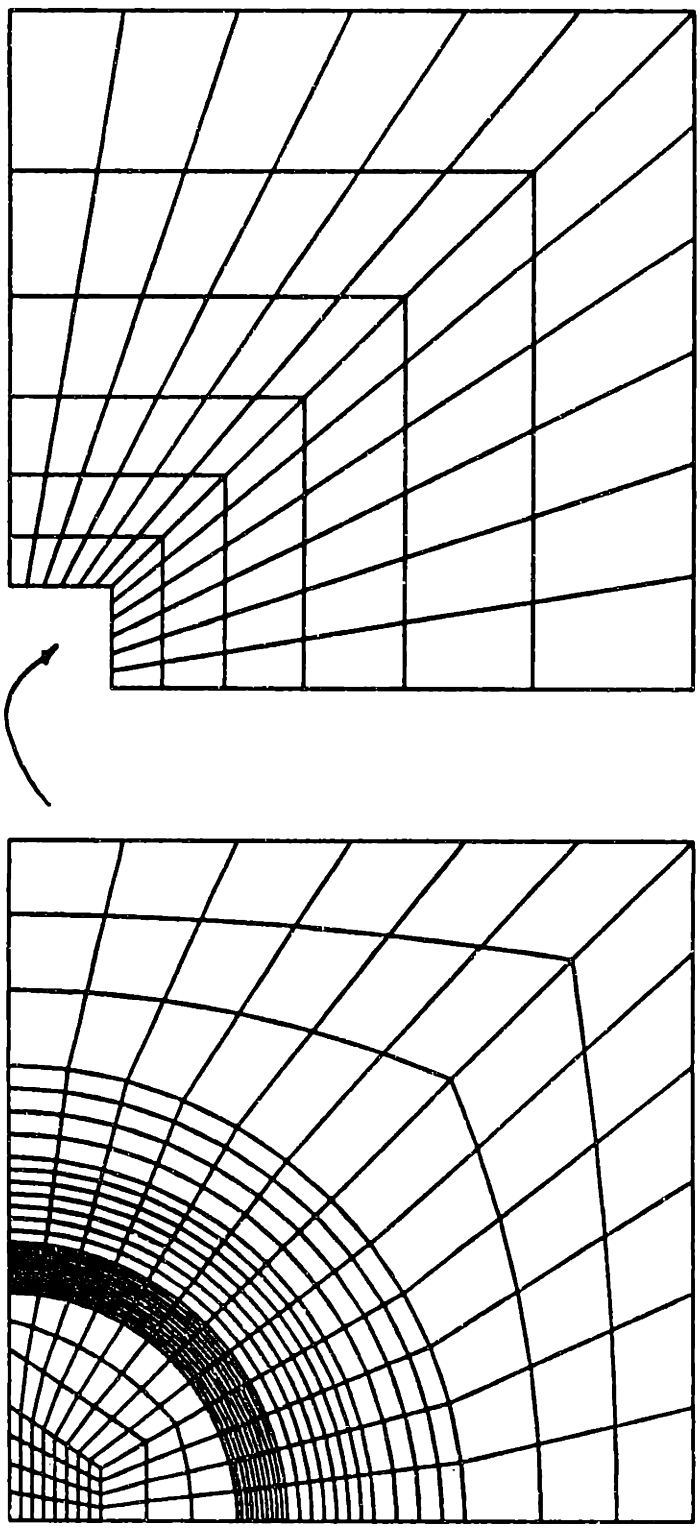

Figure 4.15 Finite element mesh for the spherical particle problem. In this figure, the bottom mesh ("near-particle" region) fits into the indicated area of the top mesh ("nominal far-field" region).

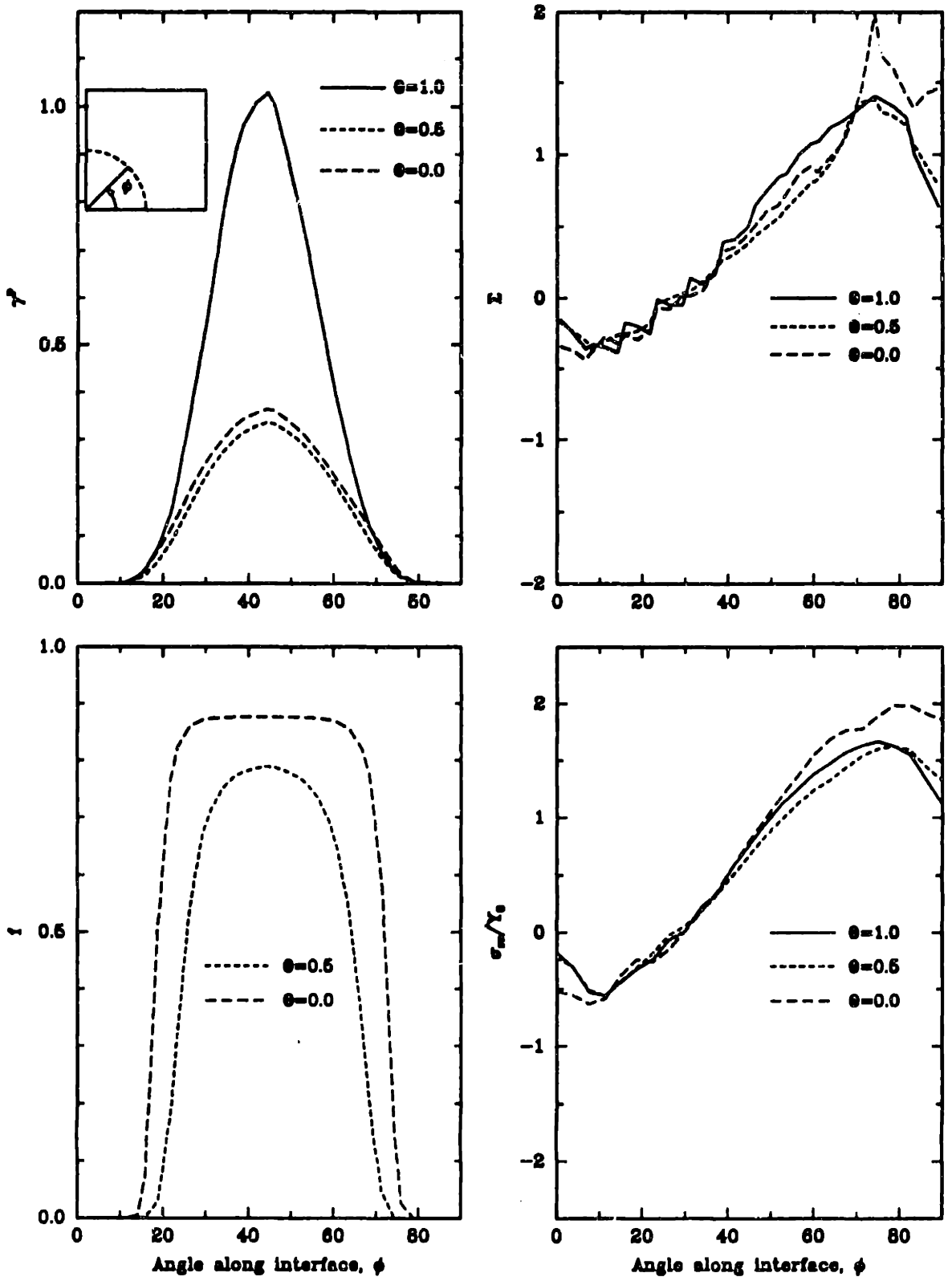

Figure 4.16 Summary of interfacial fields obtained in the preliminary analysis, for which the stress-state sensitivity of transformation kinetics was not considered. (a) equivalent plastic strain; (b) triaxiality; (c) martensite volume fraction; and (d) normal traction, normalized by yield stress [13].

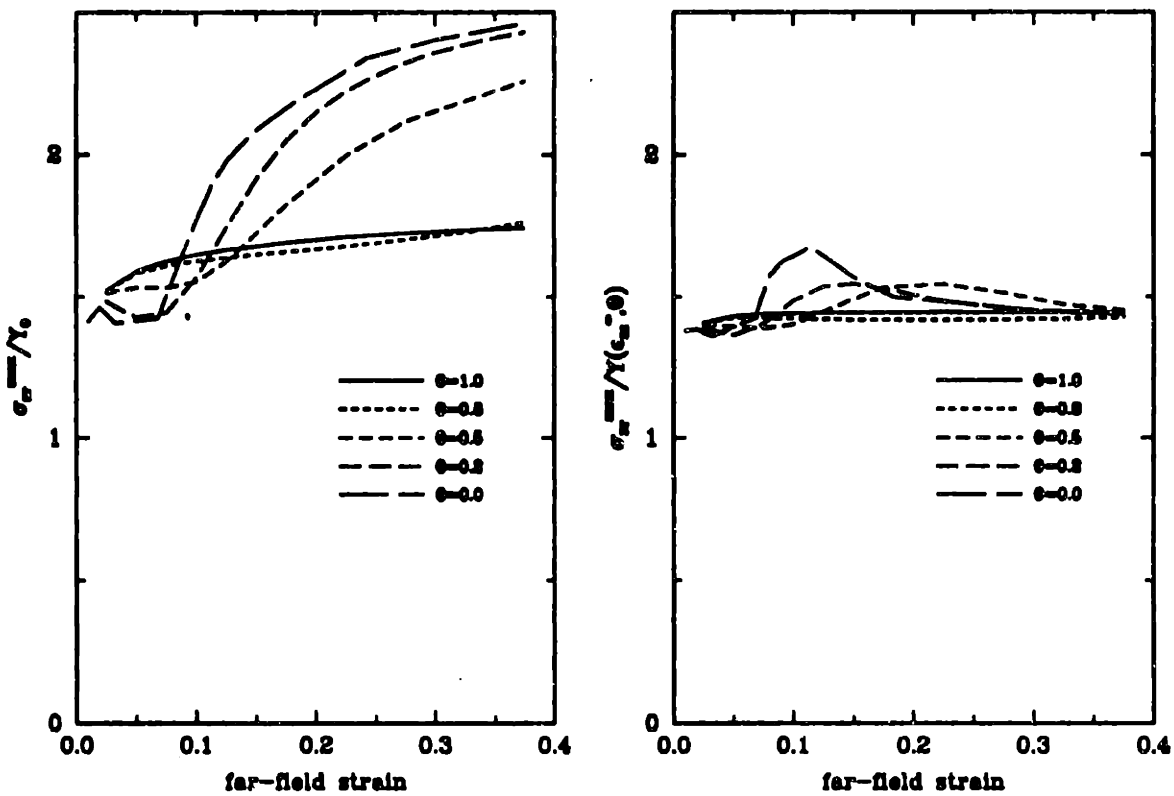

Figure 4.17 History of interfacial normal traction normalized by (a) yield stress, σ_{rr}^{max}/Y_0 and (b) far-field flow stress, $\sigma_{rr}^{max}/Y(\epsilon_{zz}^{\infty}, \theta)$, plotted versus far-field axial strain level, ϵ_{zz}^{∞}, for $\Theta = 1.0$, $\Theta = 0.8$, $\Theta = 0.5$, $\Theta = 0.2$ and $\Theta = 0.0$. Taken from [13].

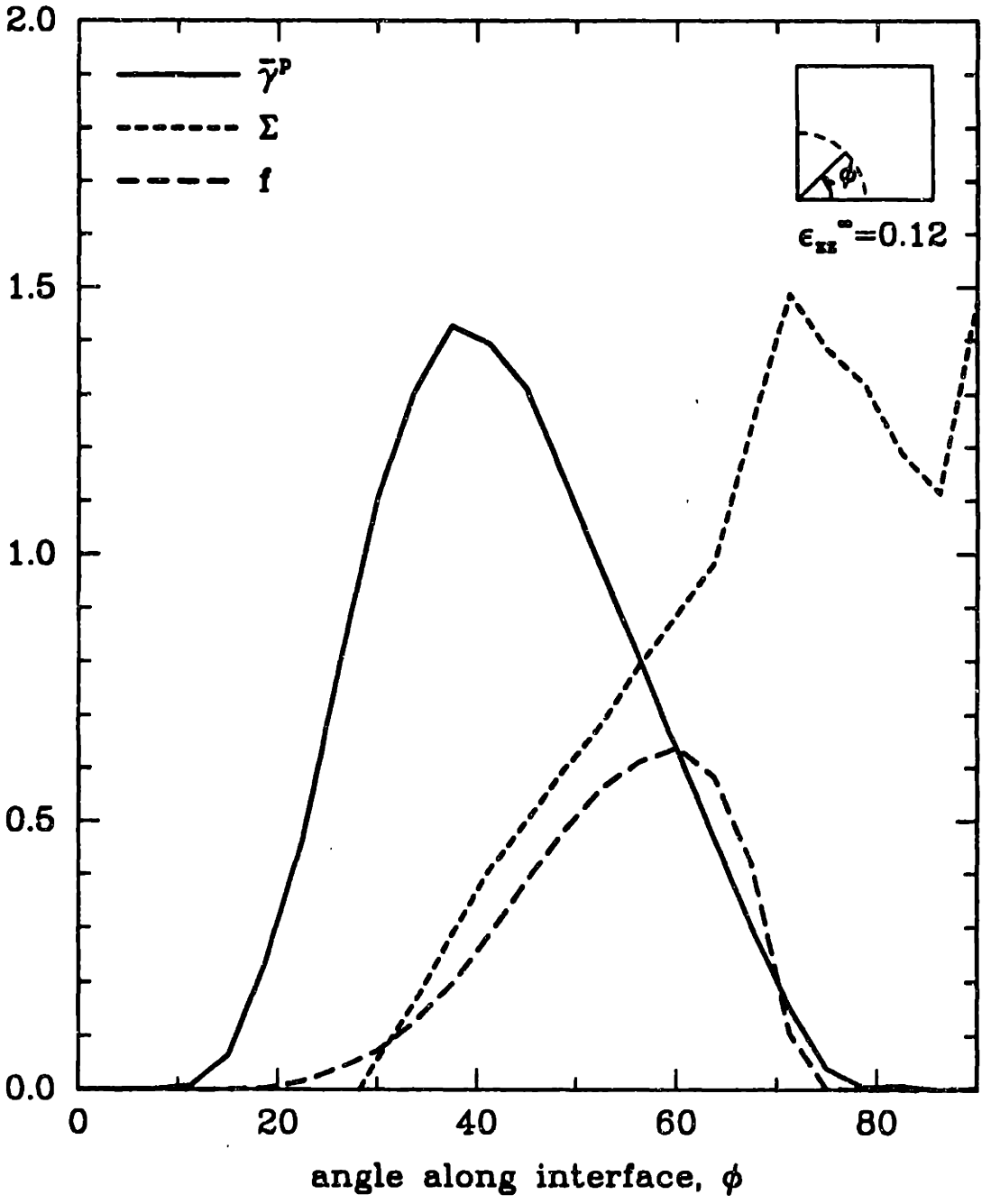

Figure 4.18 *Current model predictions for interfacial distributions of* $\bar{\gamma}^p$, Σ, and f for the transforming case, $T = 448K$ at a far-field strain axial strain level, $\epsilon_{zz}^{\infty} = 0.08$.

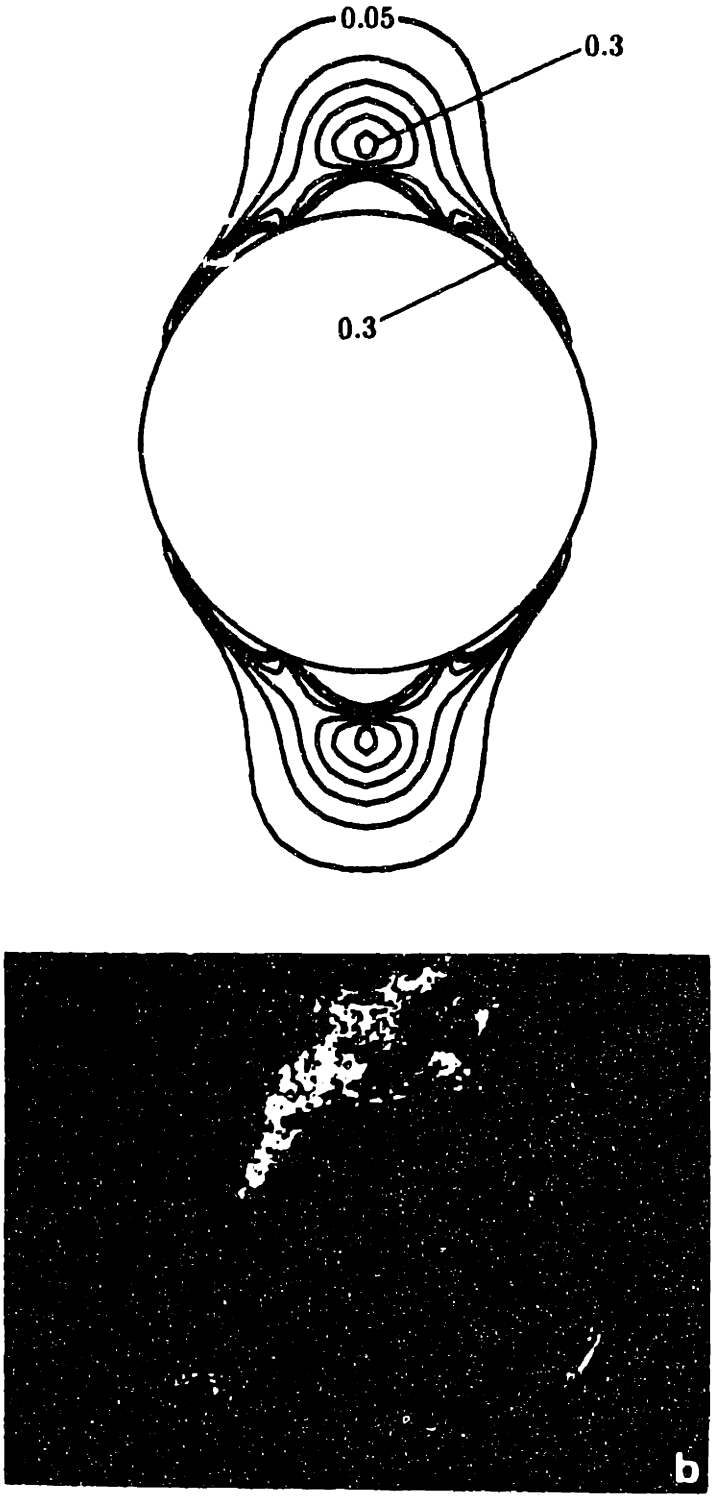

Figure 4.19 (a) Current model predictions for distribution of martensite volume fraction, f, around the particle for the transforming case ($T = 448K$), at a far-field axial strain level, $\epsilon_{zz}^{\infty} = 0.09$. (b) Micrograph taken from a longitudinal cross-section of necked tensile specimen, $T = 115C$, $\epsilon_p = 0.09$, showing preferential formation of martensite (light region in dark field) around an alumina particle [7].

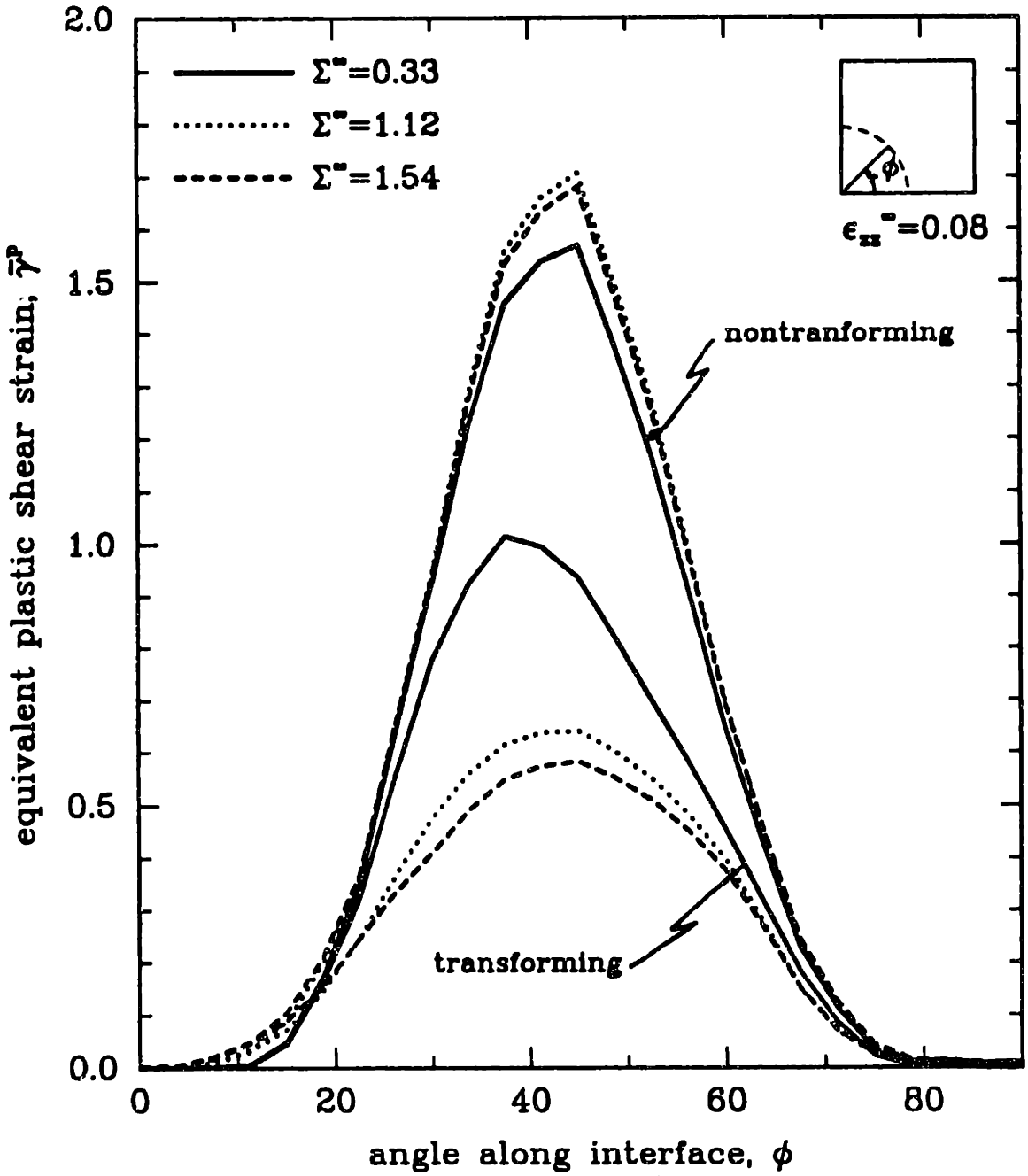

Figure 4.20 Current model predictions of the interfacial distribution of equivalent plastic shear strain, $\overline{\gamma}^p$, for the nontransforming case and the transforming case ($T = 448K$) and the three indicated levels of far-field triaxiality, at a far-field strain axial strain level, $\epsilon_{zz}^\infty = 0.08$.

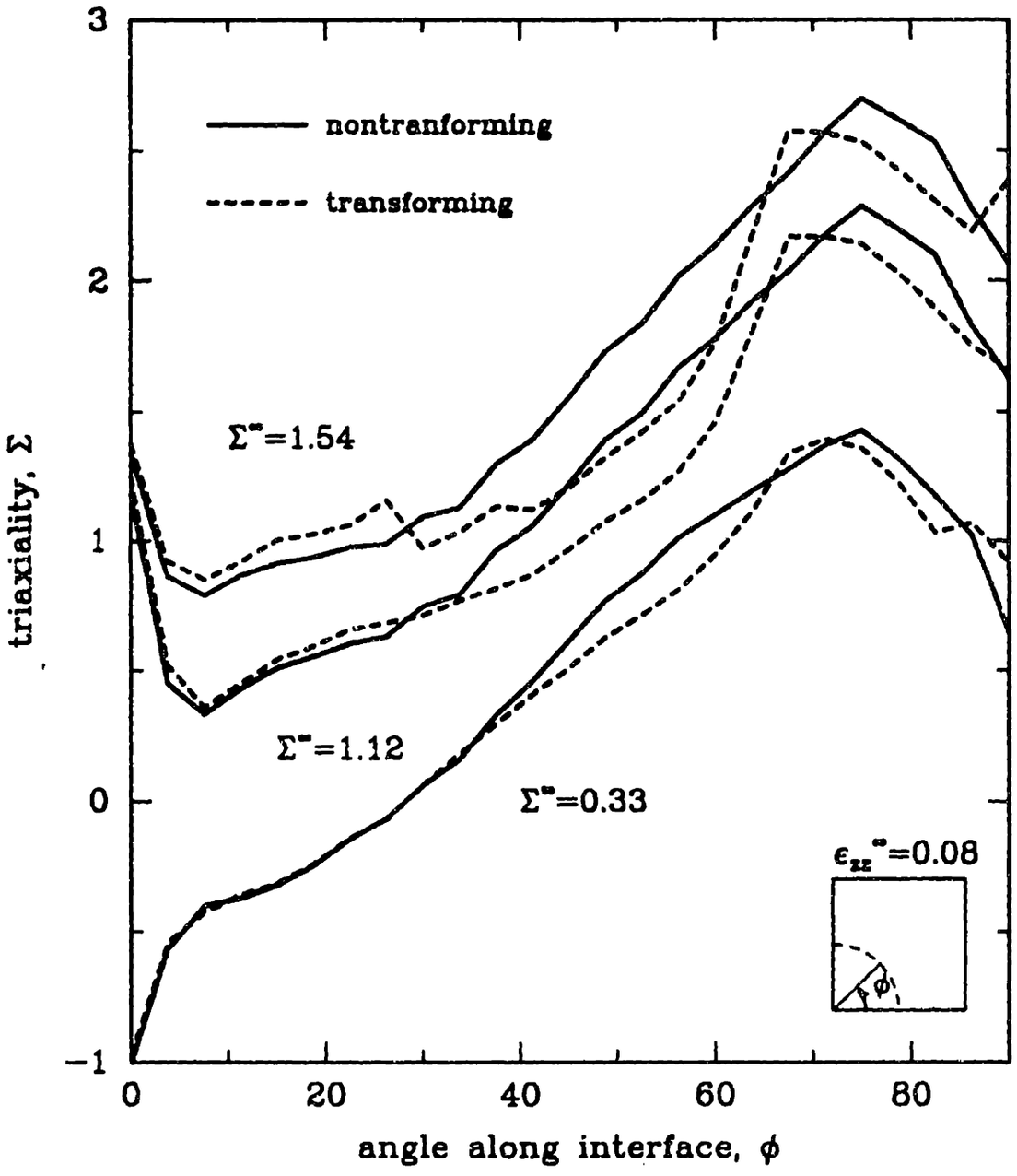

Figure 4.21 Current model predictions of the interfacial distribution of triaxiality, Σ, for the nontransforming case and the transforming case ($T = 448K$) and the three indicated levels of far-field triaxiality, at a far-field strain axial strain level, $\epsilon_{zz}^{\infty} = 0.08$.

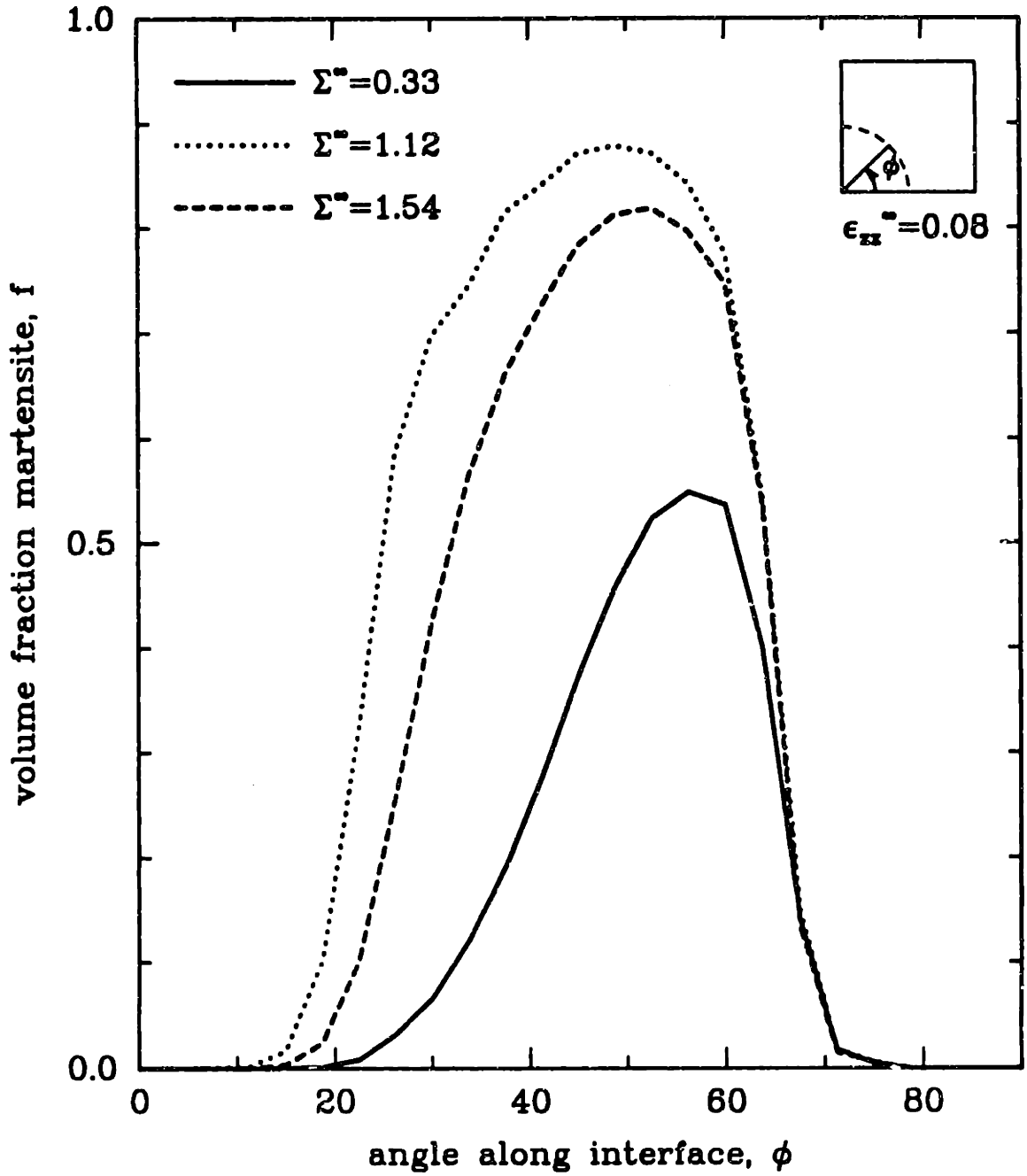

Figure 4.22 Current model predictions of the interfacial distribution of martensite volume fraction, f, for the nontransforming case and the transforming case ($T = 448K$) and the three indicated levels of far-field triaxiality, at a far-field strain axial strain level, $\epsilon_{11}^{\infty} = 0.08$.

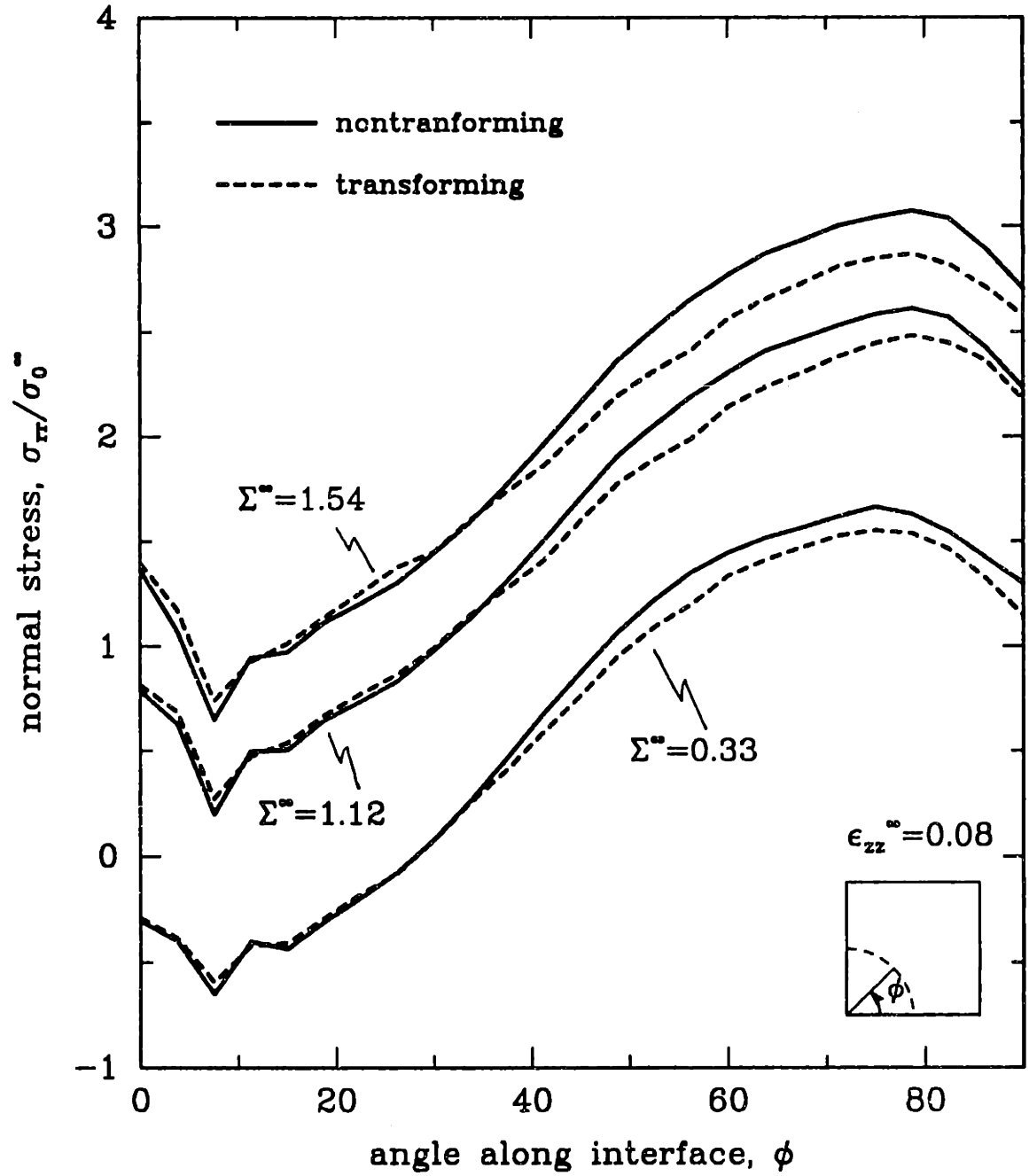

Figure 4.23 Current model predictions of the interfacial distribution of normal traction, σ_{rr}/σ_0, for the nontransforming case and the transforming case ($T = 448K$) and the three indicated levels of far-field triaxiality, at a far-field strain axial strain level, $\epsilon_{zz}^\infty = 0.08$.

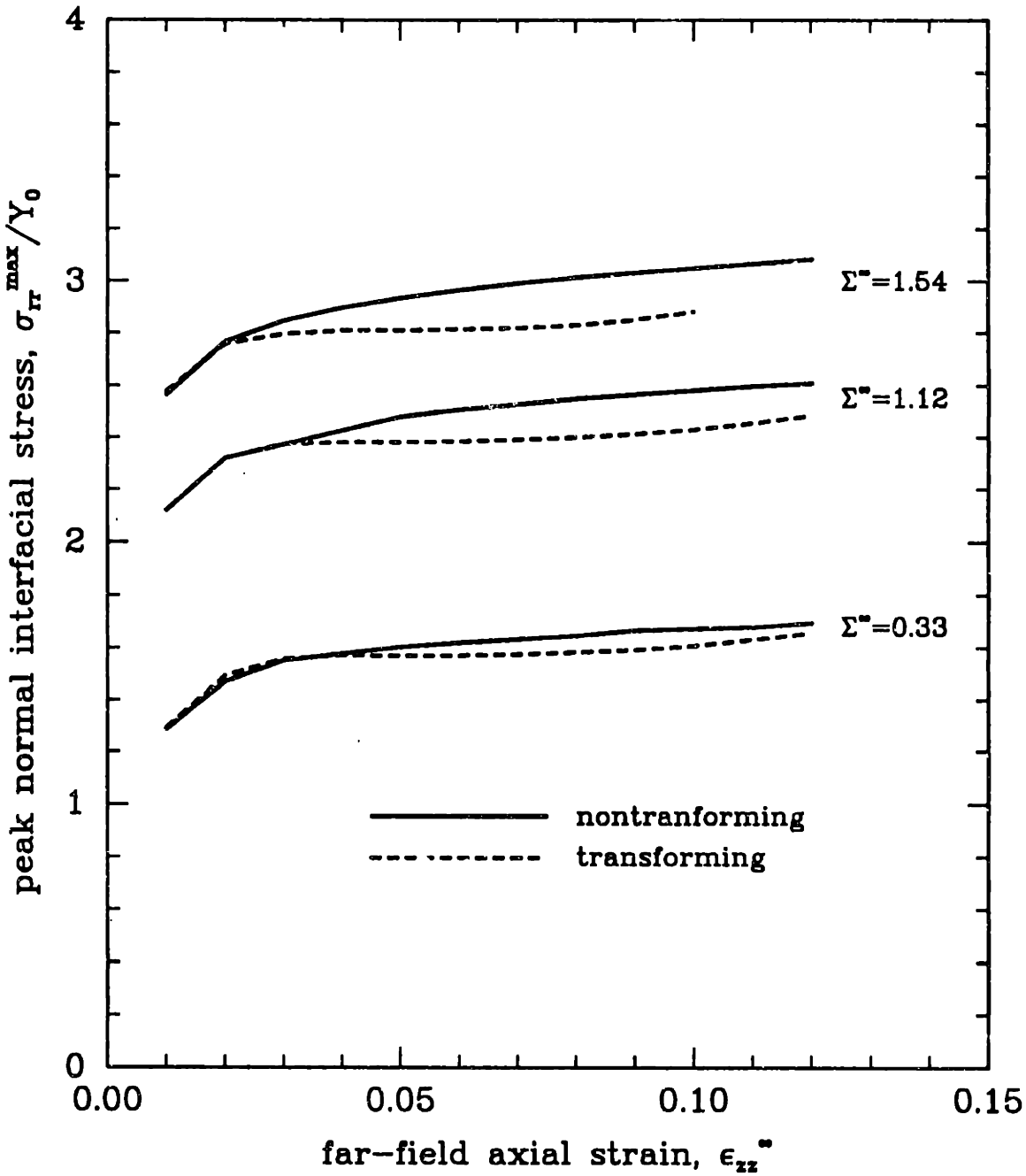

Figure 4.24 Current model predictions for the history of interfacial normal traction normalized by yield stress, σ_{rr}^{max}/Y_0 plotted versus far-field axial strain level, ϵ_{zz}^{∞}, for the nontransforming and transforming cases and the indicated far-field triaxiality levels.

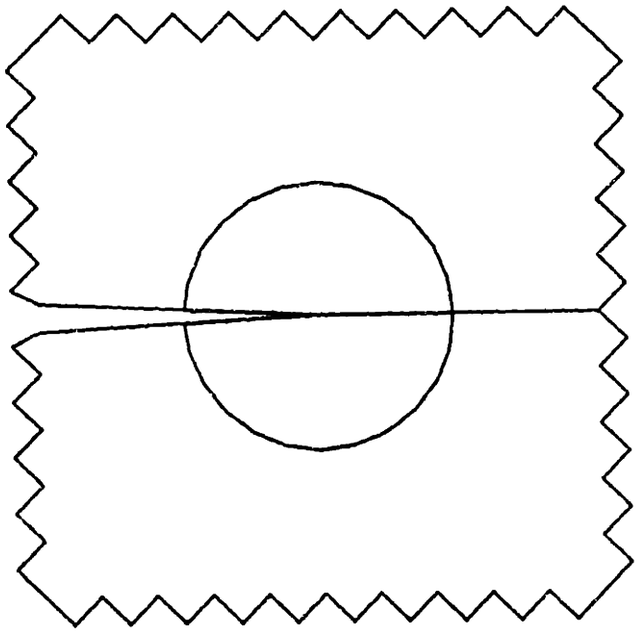

(a)

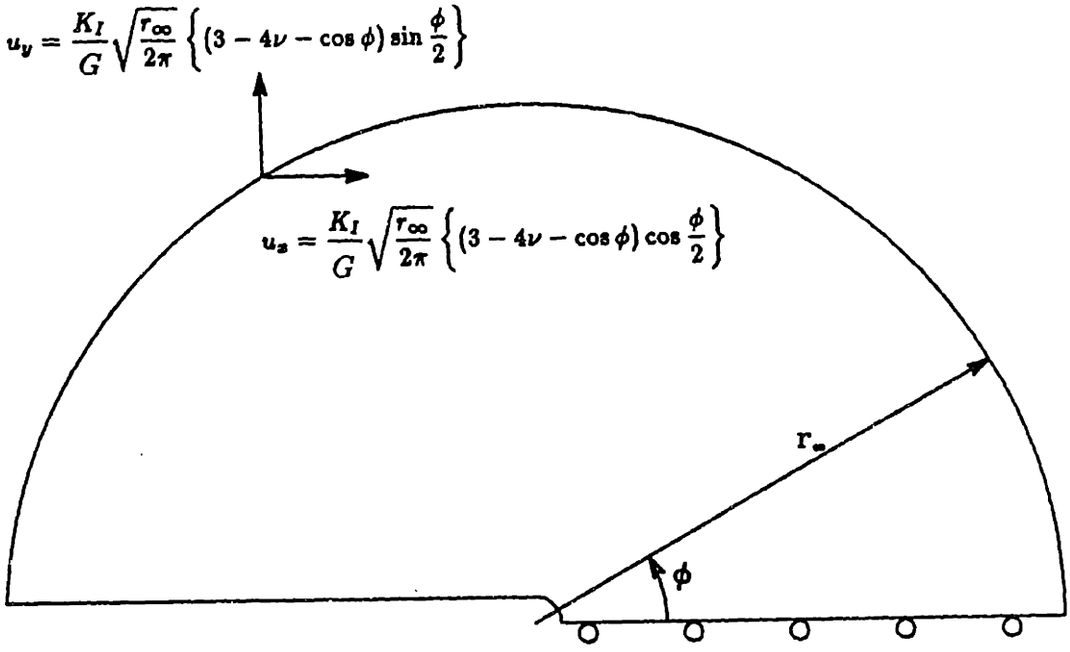

(b)

Figure 4.25 Schematic description of the crack blunting problem. (a) the circular near-tip region modeled, and the manner in which it fits into a body of infinite extent; (b) schematic of the near-tip region modeled, with the imposed displacement field indicated.

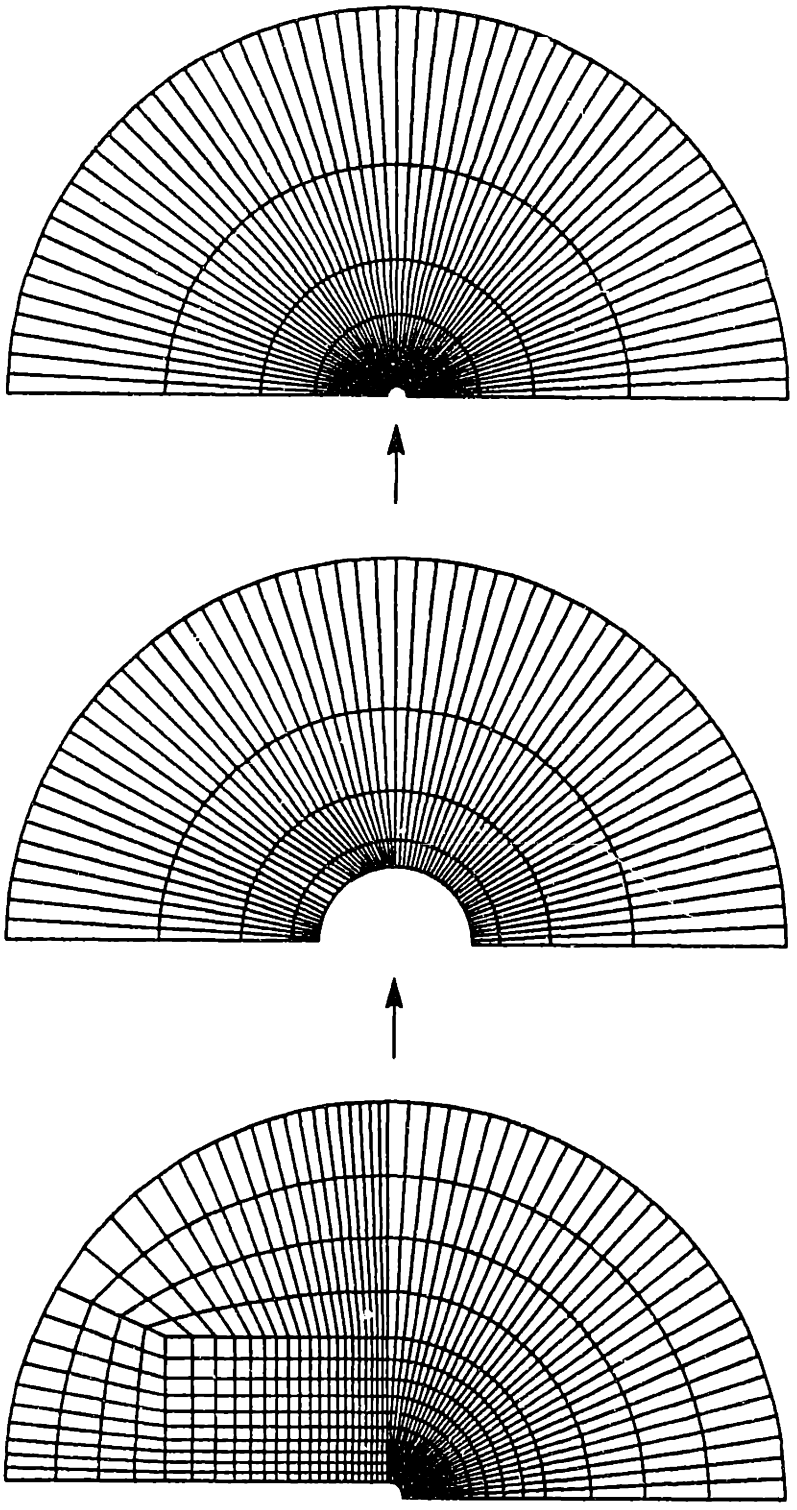

Figure 4.26 Finite element mesh for the crack blunting problem. In this figure, the bottom mesh fits into the center of the middle mesh which fits into the center of the top mesh.

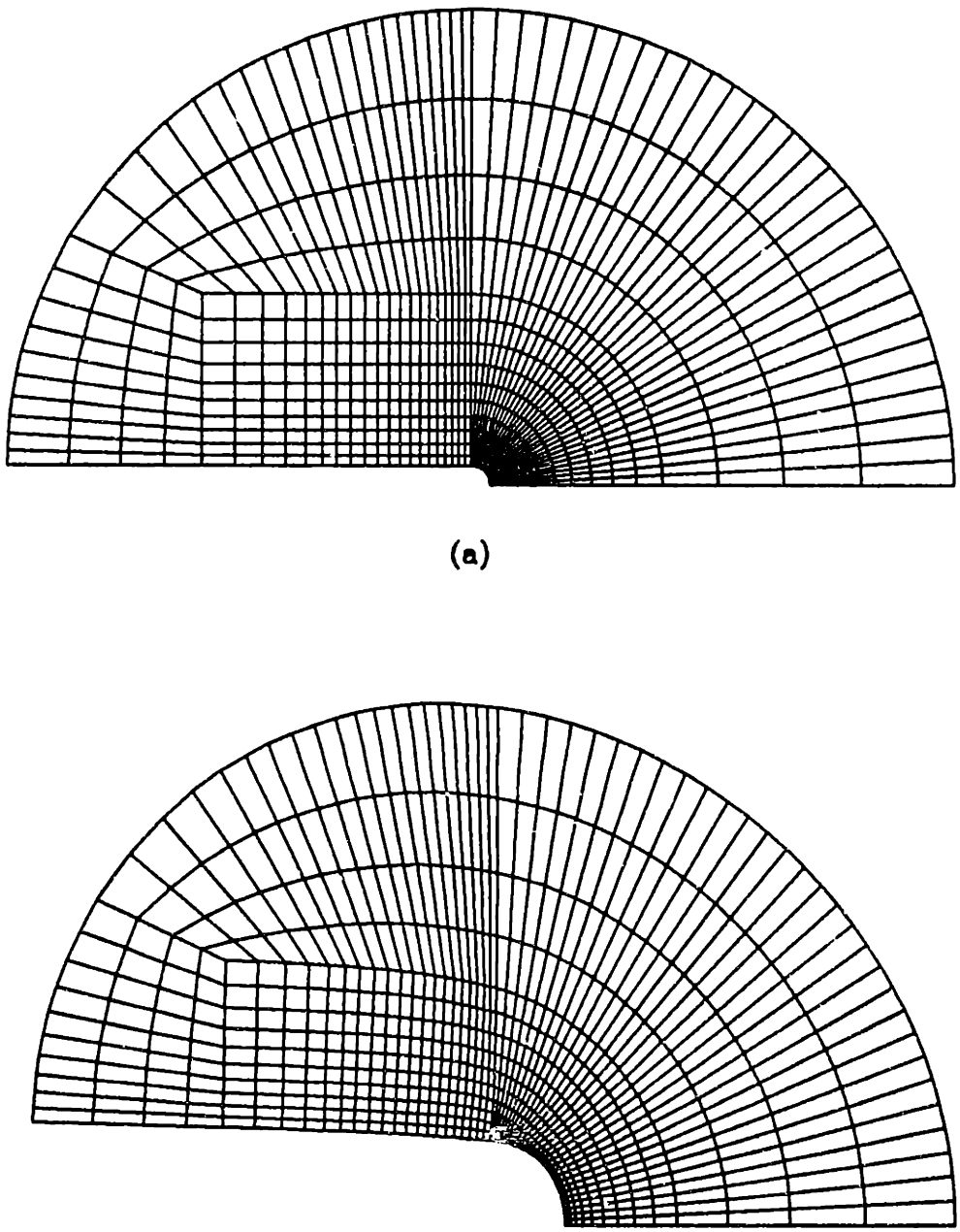

Figure 4.27 Blunting of the crack tip. (a) The undeformed mesh (innermost region only); (b) the deformed mesh, showing the blunting of the crack and the intense deformation of the near-tip elements.

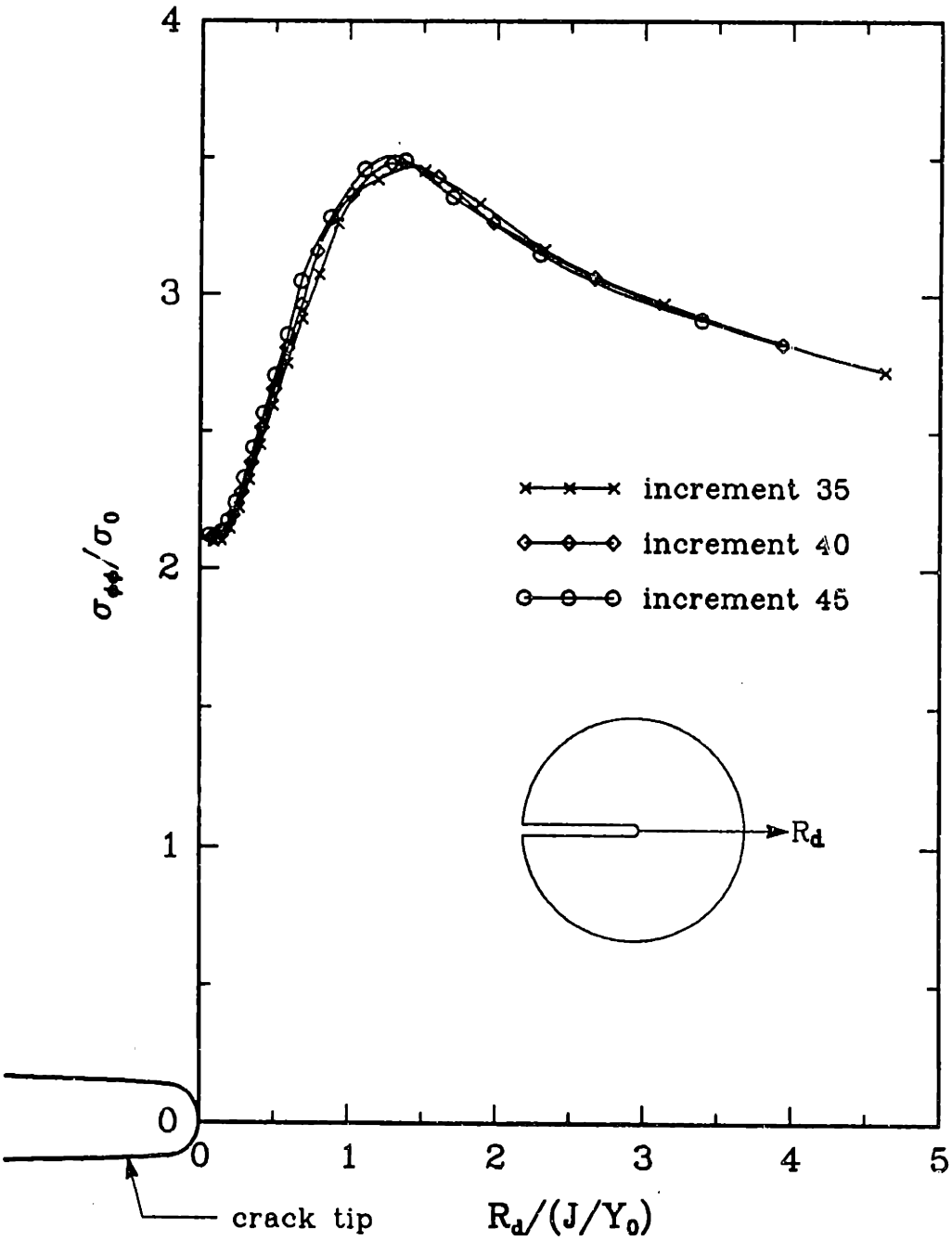

Figure 4.28 Normalized circumferential stress versus the normalized distance ahead of the crack tip, $R_d/(J/Y_0)$, at several load increments, demonstrating the approach to the steady-state solution. Here R_d is represents distance from the notch surface along the crack line, $\phi = 0$, in the *deformed* configuration.

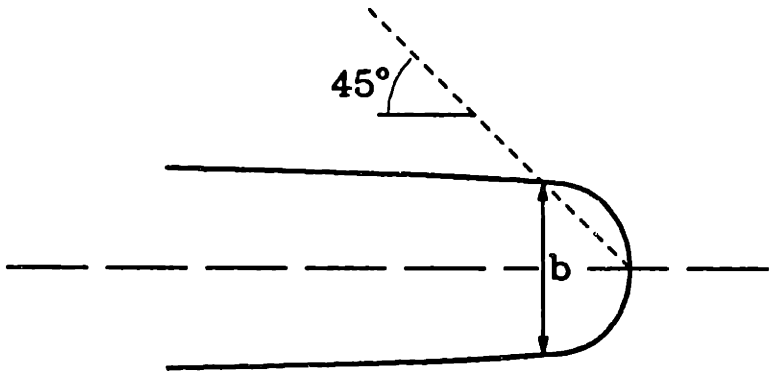

Figure 4.29 Schematic of the 45°-intercept definition for the crack tip opening displacement, b.

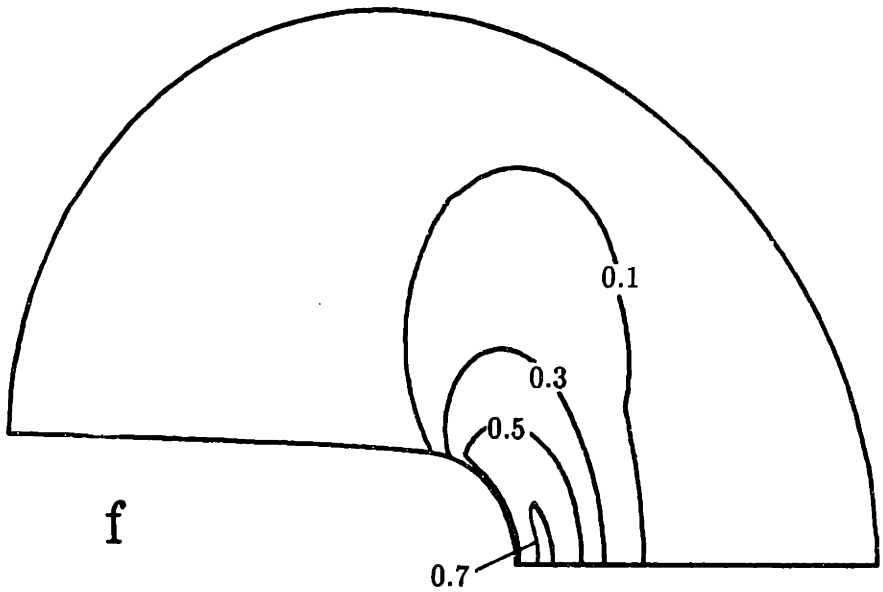

Figure 4.30 Contours of volume fraction martensite, f, ahead of the crack tip ($T = 448K$).

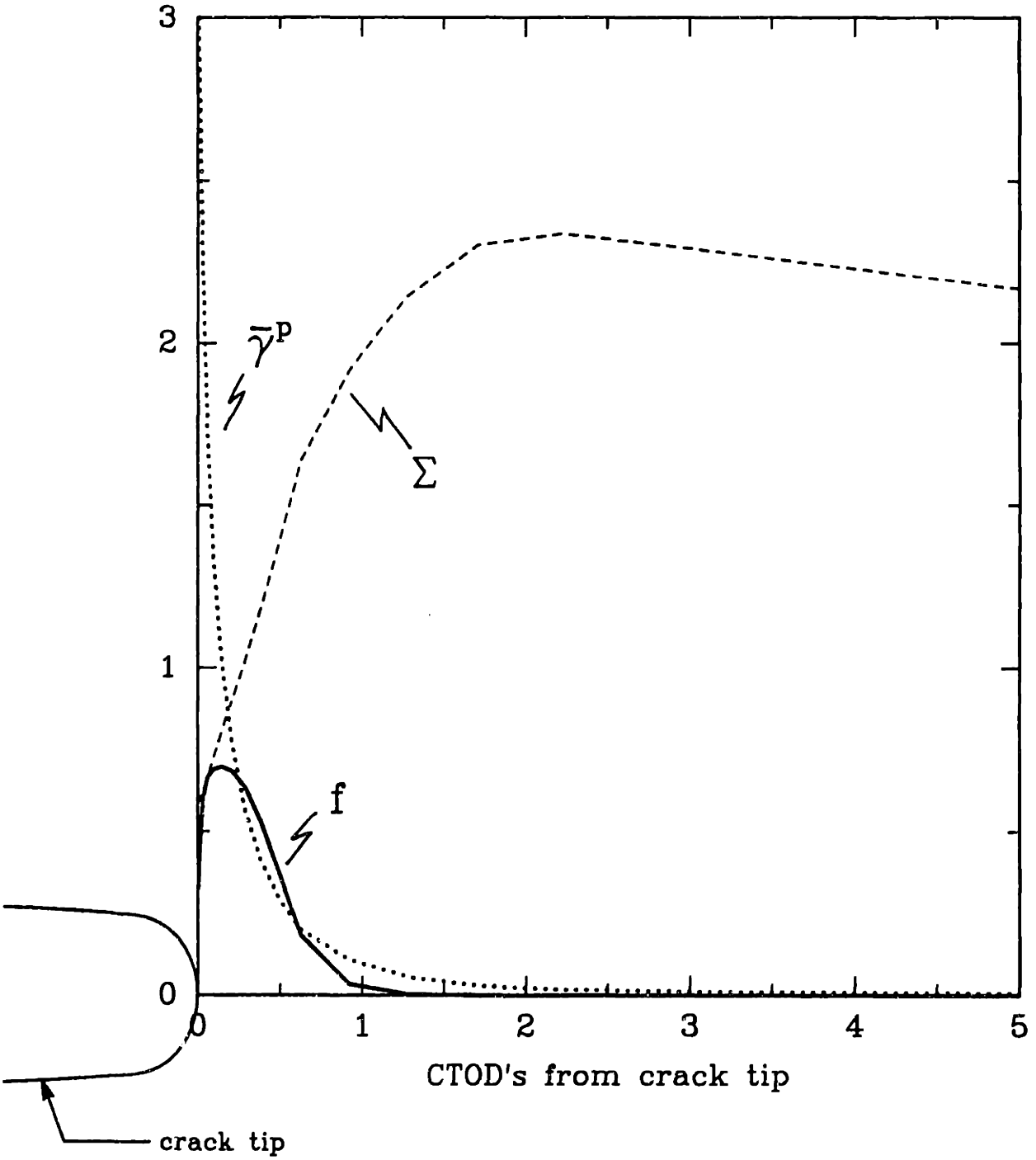

Figure 4.31 Variation of scalar fields $\bar{\gamma}^p$, Σ, and f ahead of the crack tip ($T = 448K$).

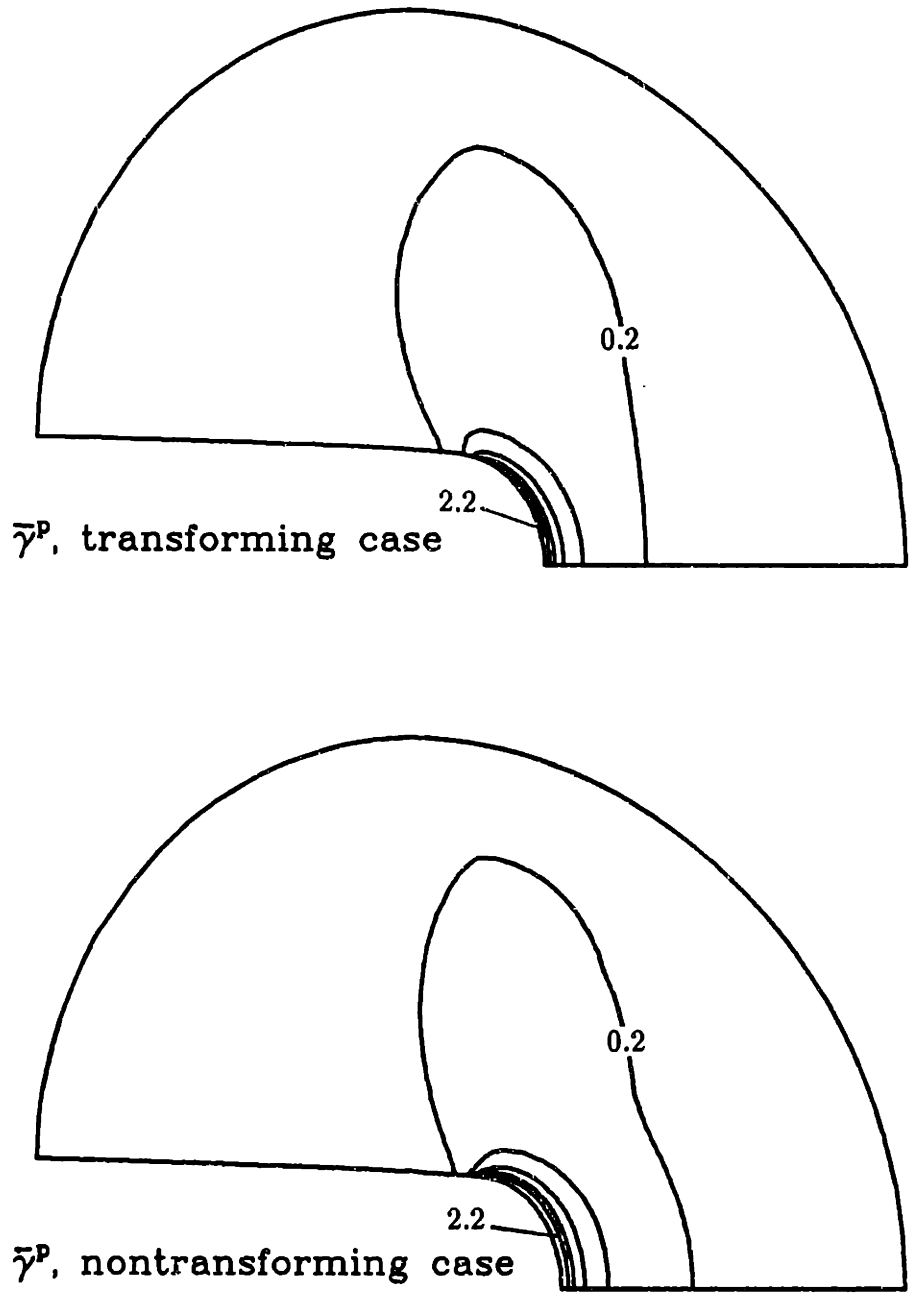

Figure 4.32 Contours of equivalent plastic shear strain, $\bar{\gamma}^p$ near the crack tip for the nontransforming case (above) and the transforming ($T = 448K$) case (below).

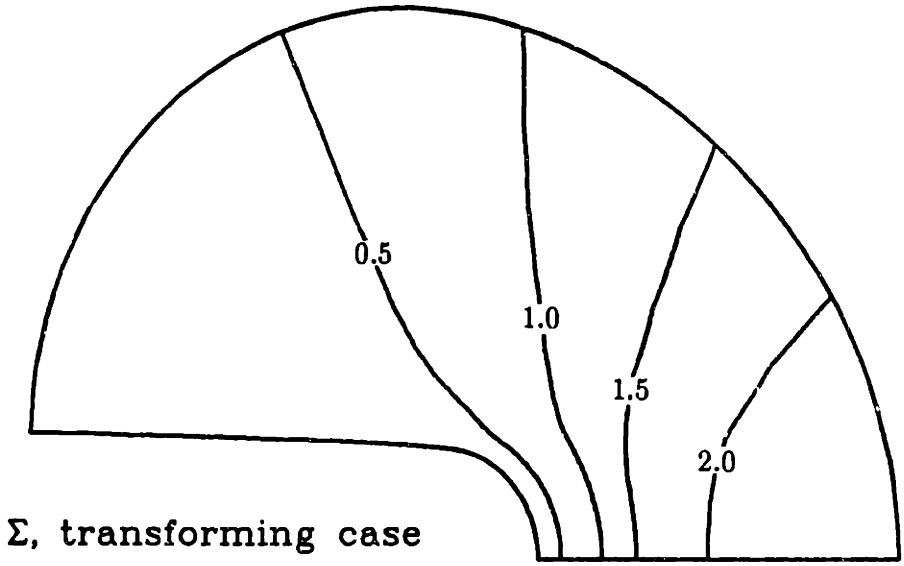

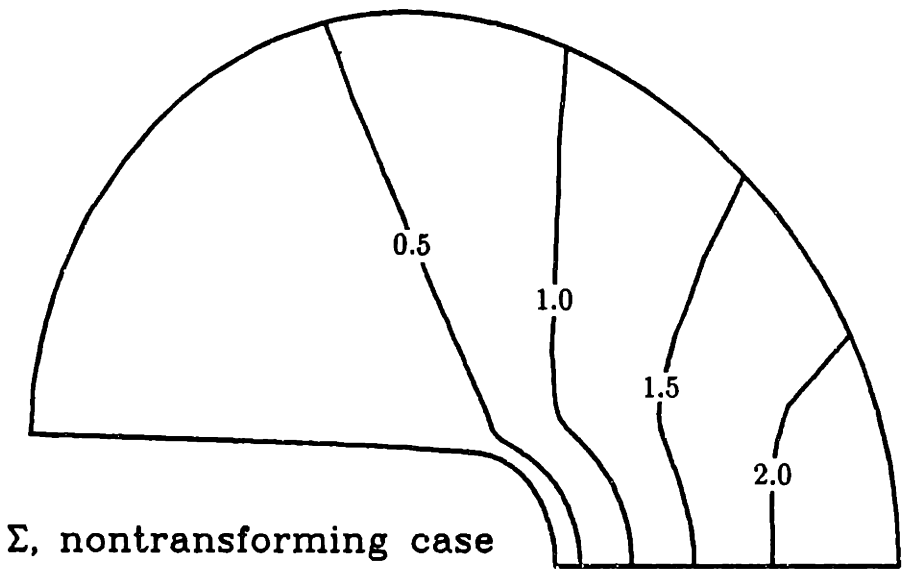

Figure 4.33 Contours of triaxiality, Σ near the crack tip for the nontransforming case (above) and the transforming ($T = 448K$) case (below).

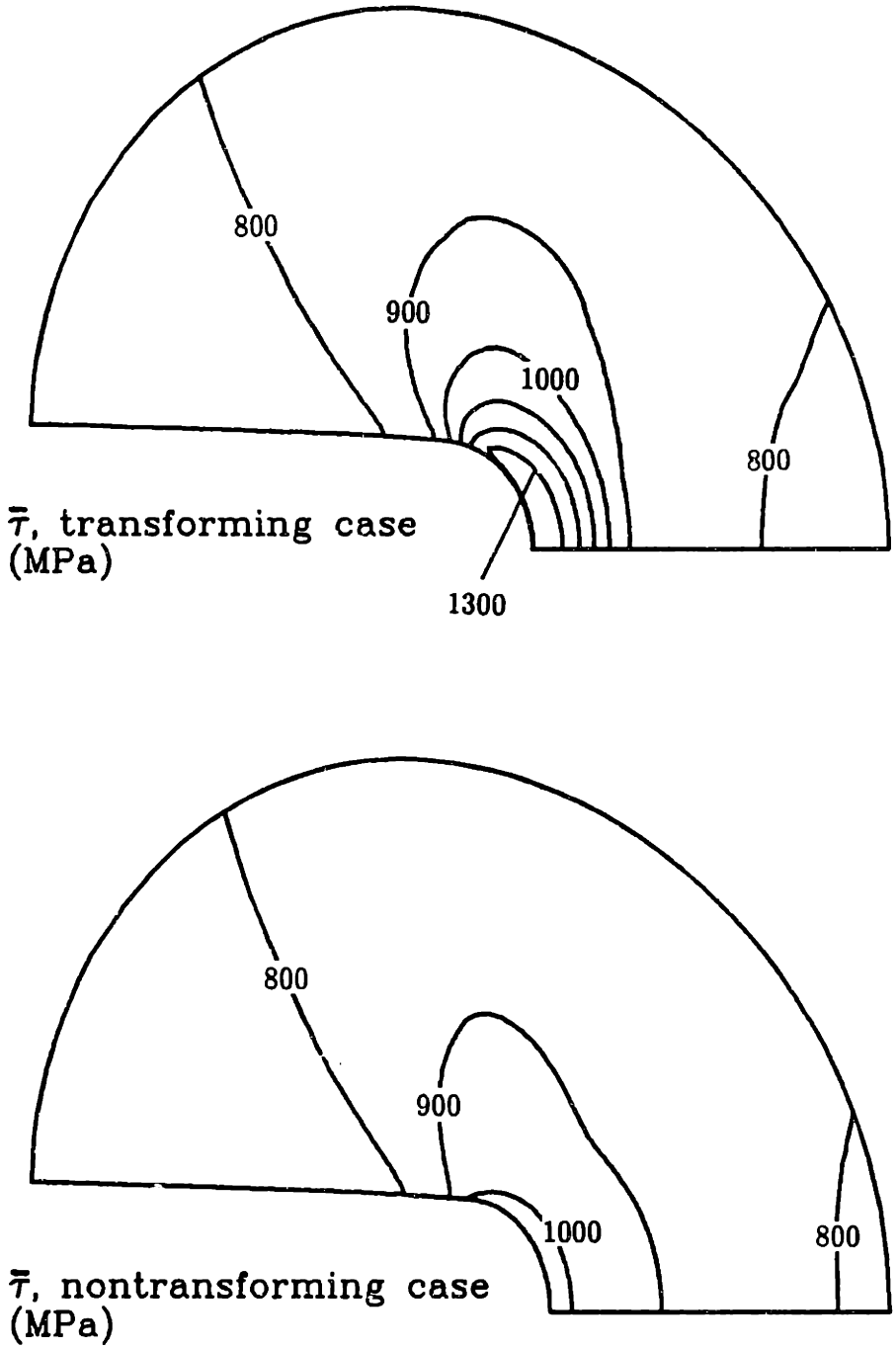

Figure 4.34 Contours of equivalent shear stress, $\bar{\tau}$, near the crack tip for the nontransforming case (above) and the transforming ($T = 448K$) case (below).

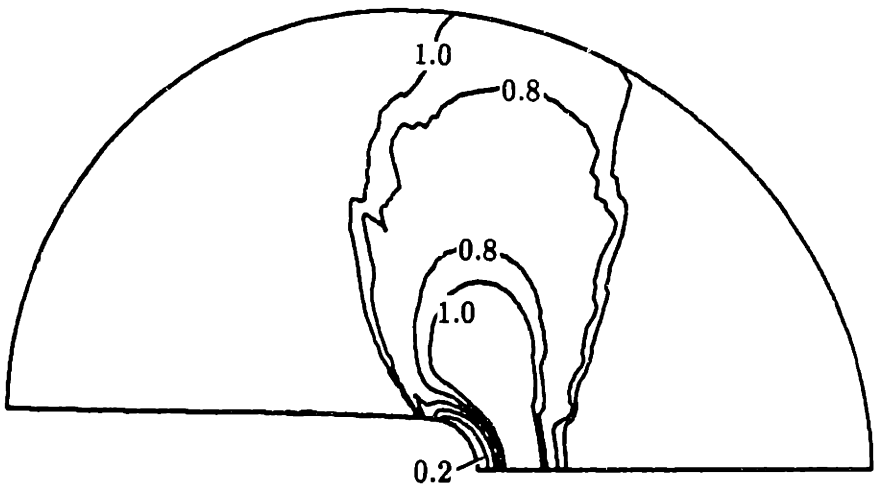

h/$\bar{\sigma}$, transforming case

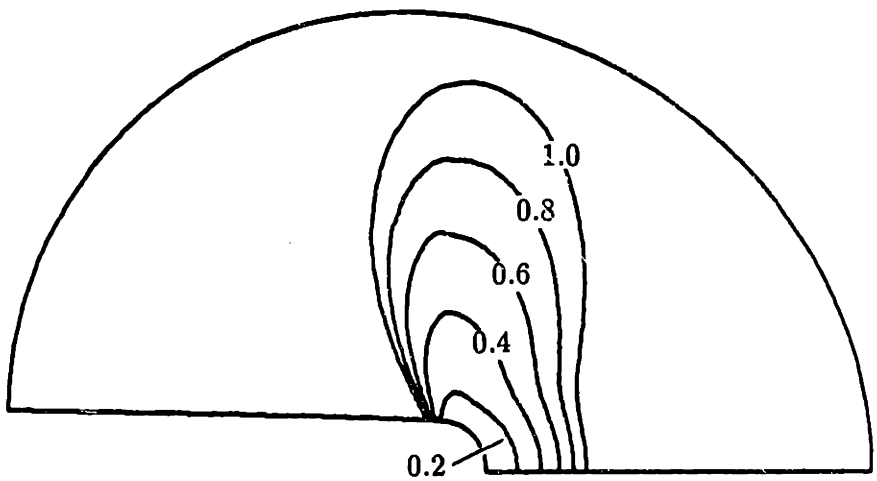

h/$\bar{\sigma}$, nontransforming case

Figure 4.35 Contours of "h"/$\bar{\sigma}$ near the crack tip for the nontransforming case (above) and the transforming ($T = 448K$) case (below). The parameter h is defined as $h = 3\Delta\bar{\tau}/\Delta\bar{\gamma}^p$, with $\dot{\bar{\gamma}} = const.$

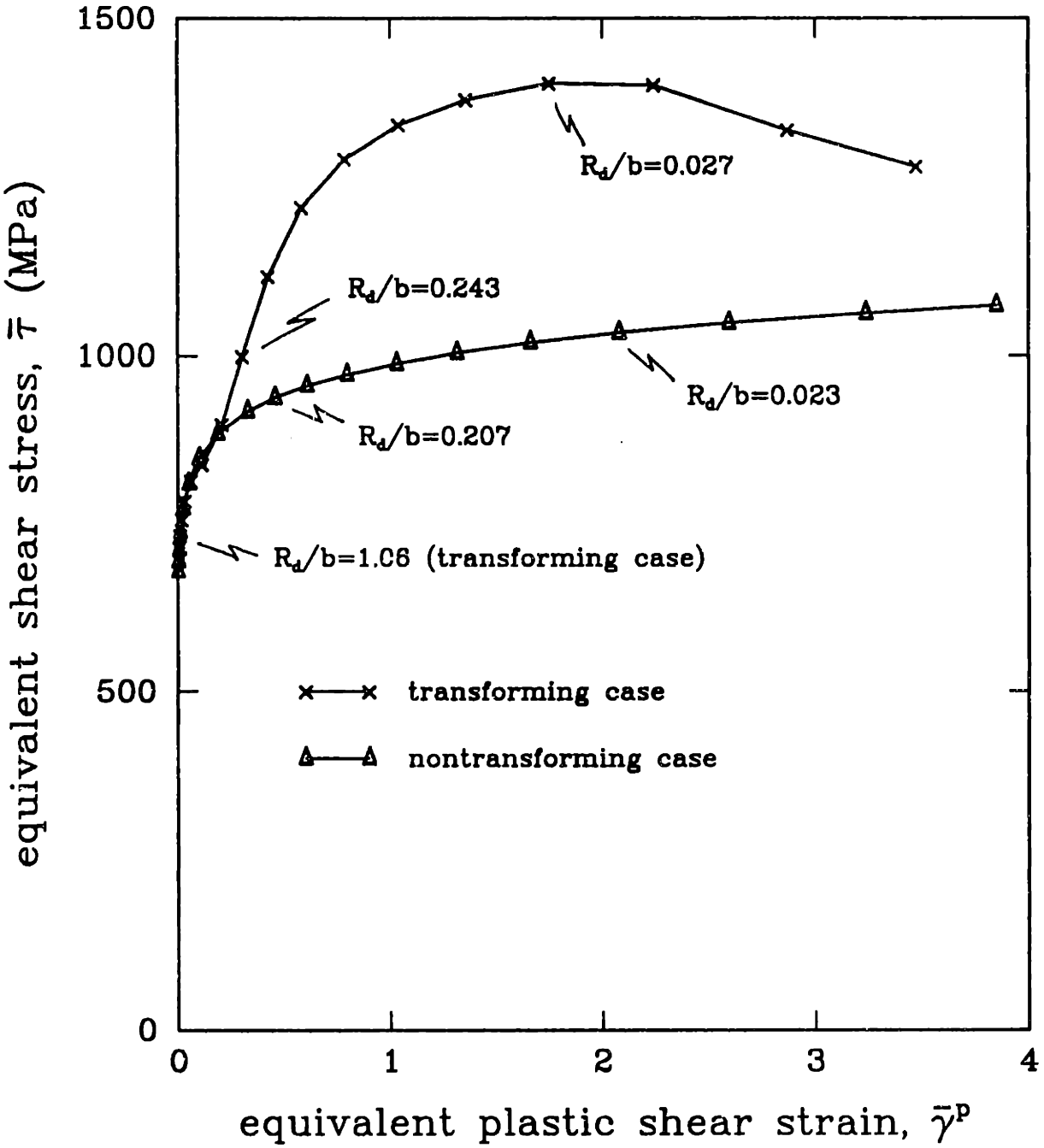

Figure 4.36 Pairs of flow stress/equivalent plastic shear strain ($\bar{\tau}$, $\bar{\gamma}^p$) at nodal locations ahead of and approaching the crack (*i.e.* from right to left in reference to Fig. 4.31). The normalized distance from the crack tip (R_d/b) is indicated for several of the points.

Chapter 5

Analysis of Flow Localization: Nucleation and Growth of Voids

5.1 Introduction

In the previous chapter, we demonstrated that transformation plasticity in the strain-induced temperature regime clearly alters the mechanical response of mechanical subsystems at several different length scales. Moreover, we indicated means by which transformation plasticity leads to enhanced ductility and fracture toughness, through the strain-softening and subsequent strain-hardening behavior caused by the transformation, and their respective abilities to hinder void nucleation and flow localization. In this chapter, we go one step further in evaluating tendencies for suppression of plastic flow localization through numerical analysis of a series of boundary value problems in which the continuum effects of porosity evolution are accounted for via the Gurson/Needleman-Tvergaard model outlined in section 3.7. We have ordered these problems in a sequence characterized by a successively increasing triaxiality of stress-state and more localized flow fields.

In order to illustrate the interaction of transformation with the nucleation/localization process, we begin with the macroscopic, mildly triaxial deformations which occur in a plane-strain tension test. We use this problem not only to illustrate the tendencies for transformation to suppress localization, but also to provide a qualitative assess-

ment of the strain-based void nucleation parameters ρ_N and γ_N. For this analysis, strain-based void nucleation is chosen over stress-controlled void nucleation because it leads to a numerically more stable integration procedure. For the mild gradients in the stress-state which characterize this problem, the two void nucleation modes lead to qualitatively similar predictions. A plane-strain geometry is chosen here because axisymmetric geometries are relatively ineffective for capture of the localization of deformation. We next model the extension of a mildly-notched plane-strain tensile specimen. Here, due to the presence of the notch, the strain and triaxiality fields have natural gradients which are somewhat more severe than those which arise during the extension of a constant cross-section tensile specimen. In spite of the local triaxiality gradients, we again rely on a strain-based nucleation criterion for this problem for the reason noted above. Finally, we consider a sharply-notched tensile specimen, for which the flow fields near the notch are very similar to a those found near a smoothly blunting crack tip. For the sharp-notch problem, we use the numerically more cumbersome, but — in view of the results of section 4.3 — more appropriate assumption of stress-controlled void nucleation. Because of its crack-like geometry, this last case provides qualitative insight into the tendency for transformation to retard flow localization ahead of the notch and the subsequent zig-zag process of crack propagation.

5.2 Numerical Simulation of a Plane Strain Tension Test

5.2.1 Introduction

In this first analysis, we simulate the geometry and loading conditions of a plane strain tension test. All of the tensile specimens tested by Leal [6], Young [7] and Stavehaug [1] were round; we therefore considered an axisymmetric geometry in

the analysis discussed in section 4.2. Despite the axisymmetry in the experiments, Young found that fracture ultimately occurred as a result of shear localization. This can be attributed to anisotropic material behavior (the material was heavily warm-worked), leading to "ovalization" of the specimen. Numerically, we cannot predict these non-axisymmetric deformation patterns using an axisymmetric model. A three-dimensional model could be used to study these phenomena, but a numerical analysis of this sort is computationally intensive, and we leave it as a problem for future study. Here, in order to illustrate the interaction of transformation with the localization/nucleation process, we resort to a plane strain geometry.

5.2.2 Problem Description

The specimen modeled here has width d_0 and gauge length $L_0 = 4d_0$, as shown in Fig. 5.1a. A model of the specimen is shown in Fig. 5.1b. Symmetry about the x and y axes allows us to model only one-quarter of the specimen. As we did for the axisymmetric specimen, we introduce a perturbation along the outer boundary of the mesh, defined analogously to (4.1). The resulting finite element mesh is shown in Fig. 5.1c. It differs from the axisymmetric mesh used in section 4.2 only in the neck region, where the mesh density is increased by a factor of four in order to better capture localized deformation. The nodes along both symmetry axes were constrained to have zero normal displacement, while the nodes along the end of the specimen were constrained to have equal longitudinal displacements. The solution was obtained under displacement control, with the displacement at the end nodes prescribed at each increment. The calculations were performed on a Sun microsystems SPARCstation 1 computer using version 4.7 of the ABAQUS finite element code. Material parameters are the same as given in table 4.1. Additional nucleation parameters are as follows: $\rho_N = 0.04$, $\overline{\gamma}^p_N = 0.5$ and $s_N = 0.1$. As stated in section 3.7, these values are consistent

with those used in several recent investigations. The RIKS algorithm was again used for this analysis. Solutions were obtained under displacement control, with a constant normalized loading rate, $\dot{L}/(L\dot{\gamma}_0) = 0.536$, applied at the end nodes.

We considered two cases: a nontransforming material and a transforming material. The model temperature for the transforming material was chosen to be near $M_{d,ut}$ $(448K)$. At temperatures much lower than $448K$, because of the increased triaxiality of the plane strain geometry with respect to that of axisymmetric tension, the enhanced driving force for transformation and the associated increases in transformation hardening result in cold drawing behavior rather than necking.

5.2.3 Results and Discussion

The evolution of the most significant scalar fields is summarized in Figs. 5.2 through 5.5 for the nontransforming case and in Figs. 5.6 through 5.10 for the transforming case. Only the central, refined part of the deformed finite element mesh is shown in these figures. Each figure shows contours of state variables at four progressively higher transverse strain levels, the last of which was chosen to be the same for both the nontransforming and transforming cases.

The contours of equivalent plastic shear strain, $\overline{\gamma}^p$, for the nontransforming case (Fig. 5.2) demonstrate a transition from a deformation pattern indicative of classical necking to one of shear-band localization. The level of triaxiality, Σ (Fig. 5.3), is again highest in the middle of the specimen; at the higher strain levels, triaxiality also appears to be influenced by the shear localization process: the highest values of Σ are still at the center of the specimen, but the shape of the next-to-the-highest contour line suggests that the entire localized band has reached a relatively high triaxiality. Contours of void volume fraction, ρ^*, shown in Fig. 5.4, also follow this same pattern of evolution. Recall that the void volume fraction is not only a function

of strain, through the strain-based nucleation criterion, but also a function of stress-state, through the triaxiality-dependence of the void growth rate. The final result, best portrayed by the contours of equivalent plastic shear strain rate, $\dot{\overline{\gamma}}^p$ (Fig. 5.5), is a complete loss of stable plastic flow resulting in a band of intense local deformation, within which the porosity is rapidly approaching the critical value for fracture.

In stark contrast to these deformation patterns, the transforming material displays a much more diffuse, stable flow field. Contours of $\overline{\gamma}^p$, shown in Fig. 5.6, show that the transforming material is resisting the bifurcation from classical necking to shear-band formation. The reasons for this behavior can be traced to the formation of martensite in the neck region (Fig. 5.7), which, again, is a result of the combined effect of strain and triaxiality (Fig. 5.8). Even this relatively mild formation of martensite ($f_{max} = 0.35$) leads to dramatically different flow patterns. Transformation has again led to a decrease in triaxiality and an associated diffusion of the neck, as indicated by the much smoother specimen profile. A significant amount of porosity (6%) does develop at the center of the specimen, primarily due to the relatively high strains in that region (Fig. 5.9). This void volume fraction is small, however, compared to the nontransforming case, where ρ^* has reached 20%. This decrease in porosity relative to the nontransforming case is due to both the decrease in strain and the decrease in triaxiality, and, more fundamentally, to the retardation of the flow localization process, manifested by the strain-rate field, which does not show any signs of localization (Fig. 5.10). To emphasize the differences between transforming and nontransforming behavior, we have plotted in Fig. 5.11 contours of equivalent strains and strain-rates for the nontransforming and transforming cases at equal transverse strain levels, $\epsilon_d = ln(d_0/d) = 0.50$, where d_0 is the undeformed width of the specimen and d is the deformed width. It is also worth noting the similarities between the contours of f (Fig. 5.7) and ρ^* (Fig. 5.9). These variables, plotted together in Fig. 5.12, obviously are evolving in a similar fashion.

In terms of macroscopic behavior, Fig. 5.13 shows how transformation affects the load-displacement curves for the nontransforming and transforming materials. In the figure, the applied load P_{app} is normalized by the maximum load for the nontransforming case P^{nt}_{max}. Because of the high temperature for the transforming case, the effects of transformation are mostly confined to the necked region, and, aside from some minor effects due to transformation softening, there is little difference between the nontransforming and transforming materials except at the higher displacement levels, where it is clear that void nucleation-softening has lead to the onset of a rapid drop in load for the nontransforming material, while the load for the transforming material decreases at a much slower rate, because of the much lower porosity and the localized formation of hard martensite across the minimum section.

Finally, if we assume that, after the void porosity has reached its critical value, $\rho^* = 0.15$, negligible macroscopic straining occurs prior to fracture, then, we can interpret the transverse strain at this point as an approximate estimate of the fracture strain. Our calculations show this transverse strain level, $\epsilon_d = 0.364$. This value is well below the value $\epsilon_d = 0.6$ predicted by Young [7]. This discrepancy is not surprising, however, given the inherently higher triaxialities and decreased resistance to flow localization for plane strain geometries relative to axisymmetric geometries. For comparison, we conducted the axisymmetric tension test simulation of section 4.2 using the model accounting for nucleation and growth, with the same nucleation parameters as used here. Because of the symmetry of the problem, shear band formation did not occur; however, we found that porosity reached the critical value, $\rho = 0.15$, at a transverse strain level $\epsilon_d = 0.77$. In light of the the noted ovalization effects that ultimately did lead to shear-band formation in these experiments, this value does not seem unreasonable — shear-band formation likely leads to a decrease in ϵ_d relative to the case where it does not occur. In any event, bracketing the experimental fracture strain, as we have, suggests that the nucleation parameters chosen for this analysis

represent reasonable estimates for these materials, at least in terms of assessing the qualitative differences between transforming and nontransforming behavior.

5.2.4 Summary

The simple analysis presented in this section lends significant qualitative insight not only into the increases in fracture strain observed during tension tests, but also into the more fundamental nature of transformation toughening. As evidenced in the contour plots shown here, transformation, along with its beneficial effects, tends to occur in those places where it is most needed. The similarities between the contours plots of f and ρ^* in Fig. 5.12 illustrate this point quite well.

5.3 Numerical Simulation of a Notched Tension Test

5.3.1 Introduction

In this section, we consider the interaction of transformation and shear localization during the extension of a mildly-notched plane strain tensile specimen. This geometry provides plastic flow and transformation fields that are somewhat more local and constrained than in the plane strain geometry of the previous section, but on a length scale that is still macroscopic enough so that these fields are, in comparison with the fields from sharp notch and crack geometries, relatively easy to assess experimentally. This geometry further imparts a naturally mild gradient to the strain and triaxiality fields that control the transformation kinetics, and thus represents an excellent tool for further verification of model properties, especially in regard to the stress-state sensitivity of the kinetics. At the present time, no experiments have been performed on transforming alloys for this geometry; however, a series of axisymmetric notched tensile specimens are currently under study [108].

Our objective in this analysis is again to illustrate fundamental differences between transforming and nontransforming material behavior. As such, we have considered only one temperature for the transforming material. A more complete parametric study, in which model temperatures and other parameters are systematically varied, so that correlation with experimental data could be refined is an endeavor of critical importance that we leave until more complete experimental data are available.

5.3.2 Problem Description

The model specimen considered here has width, D_0, gauge length, $L_0 = 4D_0$, a semi-circular notch of radius, $r_0 = D_0/4$ and notch ligament $a_0 = D_0/2$, as shown in Fig. 5.14a. Symmetry about the x and y axes again allows us to model only one-quarter of the specimen. The finite element mesh is shown in Fig. 5.14b. A small notch-mesh generator program, capable of generating meshes for various notch geometries, was developed in order to create the mesh. A listing of the program is given in Appendix F. The nodes along both axes were constrained to have zero transverse displacement, while the nodes along the end of the specimen were constrained to have equal axial displacements. The solution was obtained under displacement control, with the displacement at the end nodes prescribed at each increment. The calculations were performed on a Sun microsystems SPARCstation 1 computer using version 4.7 of the ABAQUS finite element code. Material parameters are the same as in the previous section. The RIKS algorithm was used. Solutions were obtained under displacement control, with a constant normalized loading rate, $\dot{L}/(L\dot{\gamma}_0) = 0.178$, applied at the end nodes.

We considered two cases: a nontransforming and a transforming material. The model temperature for the transforming material ($T = 473K$) was chosen to be slightly higher than that of the previous analysis, because of the higher triaxialities

found at the center of the notched cross-section.

5.3.3 Results and Discussion

The evolution of the scalar fields is summarized in Figs. 5.15 through 5.18 for the nontransforming case and in Figs. 5.19 through 5.23 for the transforming case. Only the notch region of the deformed finite element mesh is shown in these figures. As in the previous section, each of these figures shows contours of state variables at four progressively higher transverse notch strain levels. In these figures, the *third* contour plot for the transforming case and the fourth plot for the nontransforming case are at equal transverse notch strain levels. The *fourth* plot for the transforming case is at a still higher strain level. The equivalent plastic strain (Fig. 5.15) and strain rate (Fig. 5.16) contours for the nontransforming case are, again, indicative of a transition from classical necking to shear-band localization. Contours of void volume fraction, ρ^*, shown in Fig. 5.17, are also quite indicative of the intense localization of plastic flow that has occurred. The levels of triaxiality are much higher than they were in the plane strain tension test, due to the curvature of the notch (Fig. 5.18). Note that in the final plot for Σ, a significant amount of numerical noise has appeared within the localized band. This is a result of taking the ratio (Σ) of two quantities, p and $\overline{\tau}$, that, in this region, are both small. It is because of numerical noise of this sort that the calculations eventually broke down.

Once again, in contrast to these deformation patterns, the transforming material displays a much more diffuse, stable flow field. The contours of $\overline{\gamma}^p$ (Fig. 5.19) clearly show that the transforming material is resisting the bifurcation from the classical necking to shear-banding. The triaxiality contours (Fig. 5.20) indicate that, as a result of transformation hardening (see Figs. 5.21 and 5.22), the peak in triaxiality has shifted away from the minimum specimen at some strain levels, forming two small

pockets of peak triaxiality above and below this plane. Finally, despite the relatively small levels of void volume fraction, the high triaxialities, coupled with the relatively small extent of martensite formation across the minimum section, eventually lead to the onset of localization, as indicated by the strain-rate contours of the last plot in Fig. 5.23. Still, transformation has effectively postponed the onset of localization to a significantly higher strain level, and it is likely that, at a lower temperature, where the driving force for transformation is higher, greater martensite formation will lead to even higher strain levels prior to localization. A comparison of nontransforming and transforming strain and strain-rate fields at equal transverse notch strain levels (Fig. 5.24), clearly demonstrate the differences in material response, while a comparison of the transforming case values of ρ^* and f in Fig. 5.25 is indicative of the sources of these differences: transformation occurs in regions of high strain and high triaxiality, and thus regions of high porosity.

Fig. 5.26 shows the differences in load-displacement response for the nontransforming and transforming materials. Apart from some small effects due to transformation softening, there is little difference between the nontransforming and transforming materials except at the higher displacements, where void nucleation-softening manifests itself, and the transforming material, because of its resistance to localization and transformation hardening, clearly follows a more benign path.

5.3.4 Summary

This second example again demonstrates the beneficial effects of martensitic transformations in the strain-induced regime. It also shows, however, that even these materials can localize under certain conditions, emphasizing the need for careful analysis and correlation with experimental results for a wide range of temperatures (or, equivalently, austenite stability parameters), so as to obtain materials that are properly designed for the stress and strain environment to which they will be subjected.

We note in closing this section that our model breaks down when porosity levels reach certain values, thus it cannot account for the significantly increased levels of transformation driving force accompanying the increases in triaxiality within the shear-band due to cavitation. It is likely that transformation will continue to slow down the final stages of localization by further hardening this region.

5.4 Numerical Simulation of a Sharply-Notched-Tension Test

5.4.1 Introduction

In this third and final analysis in which we have employed the additional constitutive features of void nucleation and growth, we consider the interaction of transformation and localization during the extension of a sharply-notched plane strain tensile-specimen. This geometry provides plastic flow and transformation fields that are much more confined to the region around the notch than those found in the mildly-notched geometry of the previous section, and that are characterized by much steeper gradients. Because plastic flow is occurring so close to the notch, these fields are not strongly affected by the other length scales of the problem, *i.e.*, the diameter and length of the bar, and are therefore qualitatively similar to the fields ahead of a smoothly blunting crack tip.

Because of the much steeper gradients of strain and triaxiality inherent to this geometry, we found it necessary to employ a stress-based nucleation criterion. As noted earlier, a stress-controlled nucleation criterion has a more solid physical basis in light of the critical interfacial normal stress criterion for nucleation, discussed in section 4.3. Unfortunately, however, stress-controlled nucleation is numerically more difficult to implement, due to the complex interactions between stress-state, martensite formation, porosity evolution and plastic flow through the potential function, Φ.

Nevertheless, we found that it was necessary to implement the model in this manner in order to properly assess the interactions of transformation and localization of plastic flow ahead of the notch.

5.4.2 Problem Description

The model specimen considered here has width D_0, gauge length $L_0 = 4D_0$, a semicircular notch of radius $r_0 = D_0/40$, and ligament, $a_0 = D_0/2$ as shown in Fig. 5.27a. Symmetry about the x and y axes again allows us to model only one-quarter of the specimen. In order to better capture the localized patterns of deformation, the near-tip area of the finite element mesh was designed so that the grid lines followed the contours of the characteristics of the slip-line field for this geometry [145], as shown in Fig. 5.27b. The remainder of the mesh is displayed in Fig. 5.27c. The program developed to create this mesh is listed in Appendix G.

In all respects, this analysis was carried out in the same fashion as the previous two, *i.e*, displacement control, symmetry conditions, use of the RIKS method. Solutions were obtained under displacement control, with a constant normalized loading rate, $\dot{L}/(L\dot{\gamma}_0) = 0.714$, applied at the end nodes.

We again considered two cases: a nontransforming and a transforming material. The model temperature for the transforming material ($T = 448K = M_{d,ut}$) was chosen to be near the M_s^σ temperature for this geometry (*i.e.*, near $M_{s,ct}^\sigma$). Material parameters are the same as given in table 4.1. Stress-based nucleation parameters: $\rho_N = 0.04$, $\sigma_N = 2.4Y_0 = 2.4 = 2.4s_a^*(\gamma_a)^{n_a}$) and $s_N = Y_0$ were chosen, as representing reasonable values for alloys of these strength levels [150].

5.4.3 Results and Discussion

Figs. 5.28 and 5.29 compare model predictions for the scalar fields ahead of the notch-tip, at a fairly low level of load. Transverse strains lose their significance as measures of such local deformation, so these deformed fields are characterized by equal levels of notch-tip blunting displacements, b, according to the 45°-intercept definition of Fig. 4.29. At this relatively small load level, very little martensite has formed and void porosity levels are quite low, so that these contour plots show little difference between the behavior of nontransforming and transforming materials. The contours of $\overline{\gamma}^p$ and $\overline{\tau}$ are indicative of a classical notch-tip field. The triaxiality field differs from a fully-developed small-scale yielding crack-tip field, in the respect that the peak value of triaxiality is decreased and the location of the peak is only about 1.5 blunted openings ($b = 1.5$) from the notch-tip rather than the $1.9b$ prediction of the slip-line field and the $2.7b$ prediction of the small-scale yielding solution (see Fig. 4.31). This difference is likely a result of the lateral "T"-stress which, in the sharp notch limit of double-edge-cracked tension specimen of comparable geometry, is negative, and thus has the effect of decreasing the peak value of triaxiality and moving the peak towards the notch [151].

At a much higher level of deformation, (Fig. 5.30), the nontransforming material has formed a shear-band between the notch surface and a point on the ligament about 0.5 blunted openings ahead of the notch (Fig. 5.30e). This localization of plastic flow is due to the evolution of porosity (Fig. 5.30d), which, as a result of the imposed stress-controlled nucleation criterion, is greatest along the ligament at the indicated location, where the sum of the deviatoric stress (Fig. 5.30a) and hydrostatic stress (Fig. 5.30c) is greatest. The pattern of localization shown in Fig. 5.30e is indicative of the beginnings of a zig-zag fracture process. Because of the high level of damage and the previously-noted numerical complications caused by stress-based void nucleation,

numerical difficulties prevented us from carrying out the solution to much higher levels of deformation. To the limited extent that we could continue the analysis, we found that the apparent zig-zag pattern of deformation continued, as evidenced in Fig. 5.31. Experimental observations of the crack propagation in the slow-bending of a Charpy V-notch specimen of high strength 4340 steel [152] (Fig. 5.32) indicate that the deformation patterns predicted by our analysis are in reasonable agreement with observed behavior.

Fig. 5.33 summarized the near-tip behavior for the transforming material at a blunted opening ($b = 1.39b_0$) that is already larger than the maximum value reached in our simulation of the nontransforming material ($b = 1.24b_0$). Obviously, flow localization has been completely suppressed by the formation of martensite ahead of the blunting crack tip. The contours of equivalent strain-rate (Fig. 5.33f) have the same general shape as the contours of equivalent strain (5.33a), indicating that flow is still quite stable. A comparison of the contours of f and ρ^* (Figs. 5.33c and e), again indicate that transformation has "come to the rescue" by hardening the area where the void porosity and associated nucleation softening are otherwise promoting the formation of a shear-band. Further deformation resulted in no tendencies to alter these flow patterns prior to a numerical break-down of the solution.

A comparison of the load-displacement curves in Fig. 5.34 indicates that, because of the local nature of the deformation, the effects of transformation are not macroscopically evident, since little transformation is taking place away from the notch tip. The nontransforming curve is, however, starting to show the effects of the onset of localization, as it is beginning to drop in slope very near the top portion of the curve, whereas the curve for the transforming material is giving no signs of decreasing its slope. If we could model crack propagation, we would likely see the curve for the nontransforming case drop abruptly, as is observed experimentally.

5.4.4 Summary

It is clearly evident from the figures shown in this section that transformation is suppressing shear localization, as a result of the softening and subsequent hardening behavior of the transformation. Unfortunately, the complicated nature of the constitutive model, coupled with the limitations of standard finite element methods, made it impossible to carry out the analyses to much higher deformation levels, in order to assess more quantitatively the extent to which localization is suppressed in this problem.

We mention at this point that we did attempt to carry out a simulation of the three-point bend problem which produced the extremely high toughnesses shown in Fig. 1.1. The initial trends from this analysis are very similar to the ones we have shown in this section: in the nontransforming case, the onset of flow localization appears to have occurred, while in the transforming case, the flow fields are much more diffuse. Unfortunately, because of the much larger gradients that develop as the crack-tip field evolves, the solutions broke down too early to make any clear and comprehensive judgments regarding the effects of transformation.

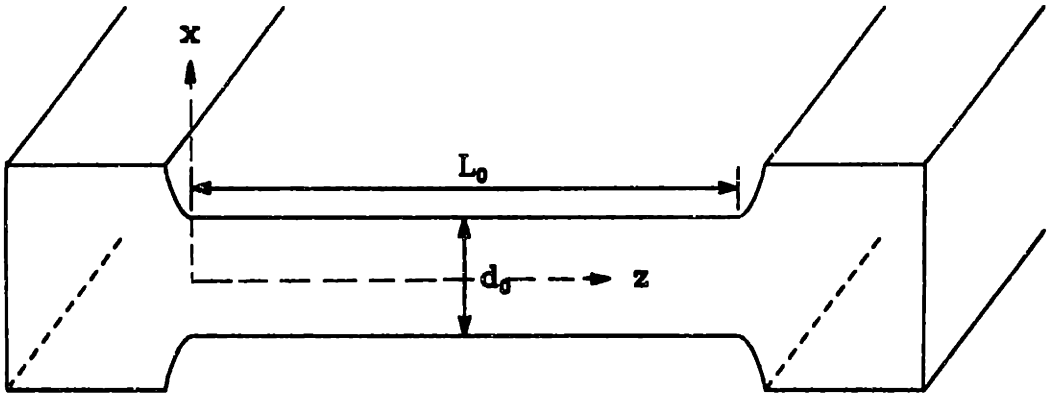

(a)

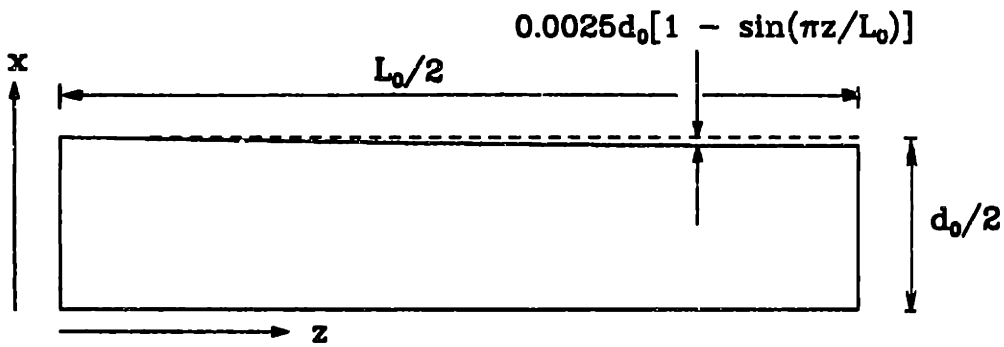

(b)

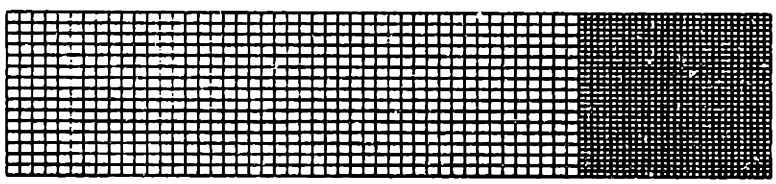

(c)

Figure 5.1 Description of the plane-strain tension problem, showing: (a) the model tensile specimen analyzed; (b) a schematic of boundary value problem with initial perturbation; and (c) the finite element model.

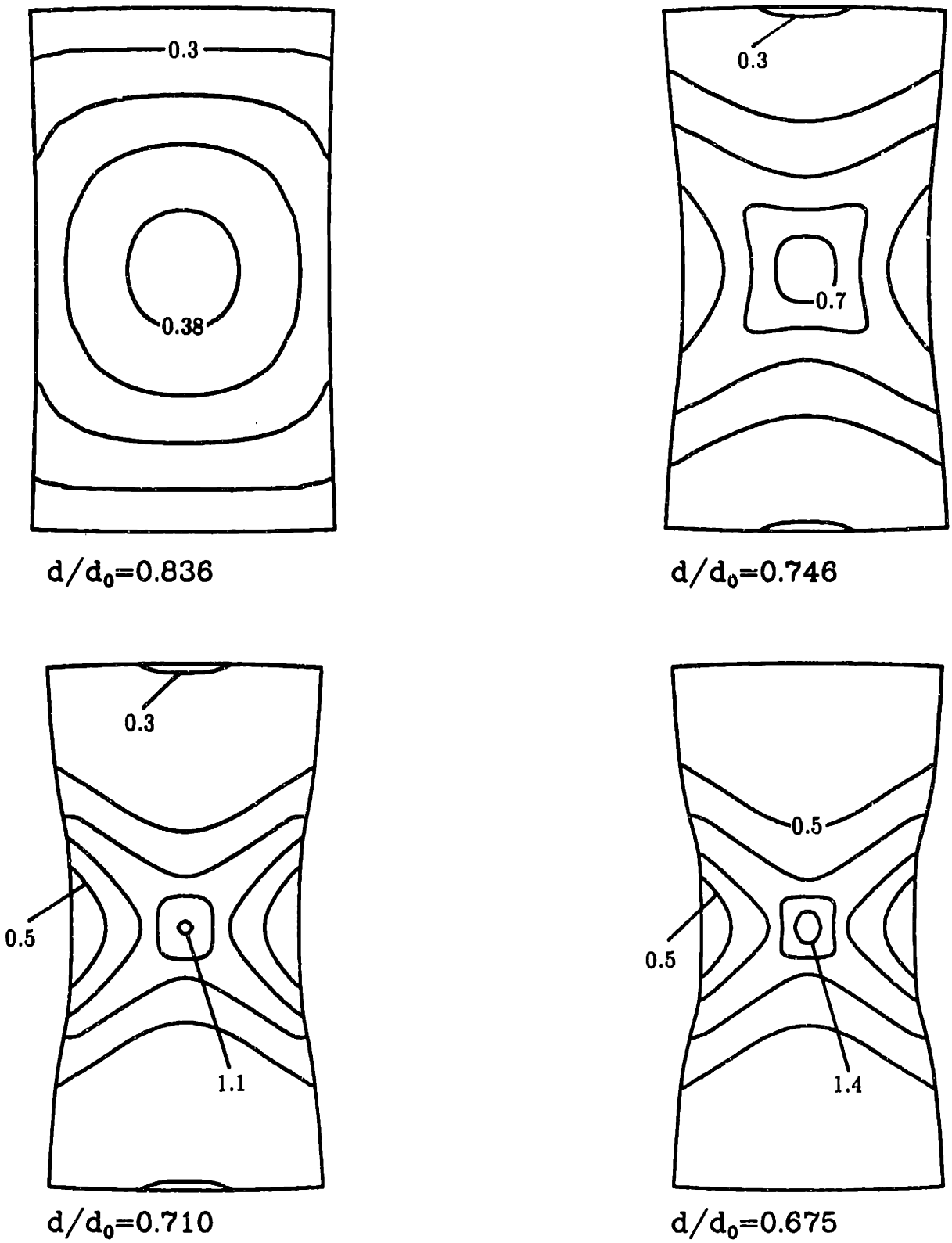

Figure 5.2 Contours of equivalent plastic shear strain, $\overline{\gamma}^p$, plotted on the deformed mesh at the four indicated mid-plane transverse displacement levels (d/d_0), for the *non-transforming* case. Only the refined, central portion of the mesh (which has been mirrored about the mid-plane and the longitudinal axis) is shown in these plots.

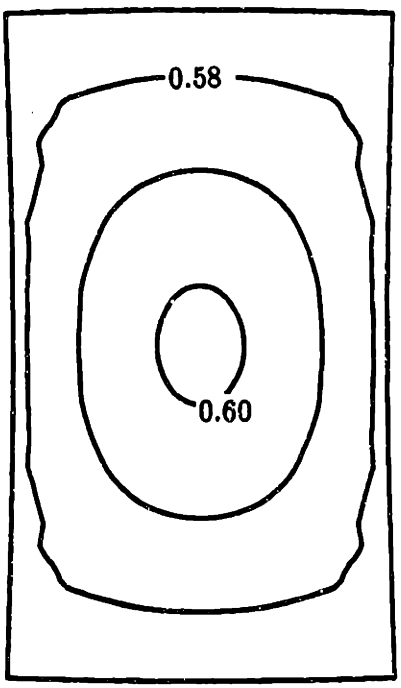

d/d_0=0.836

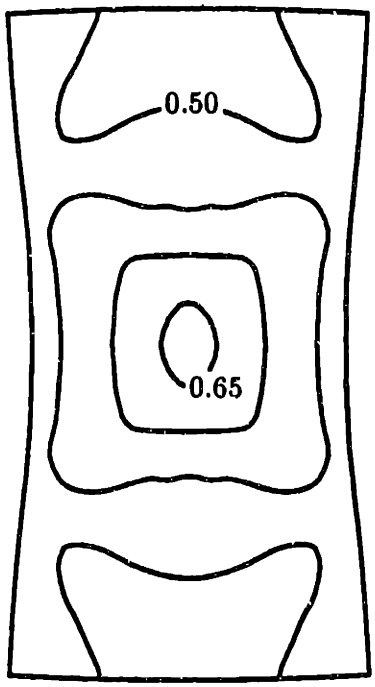

d/d_0=0.746

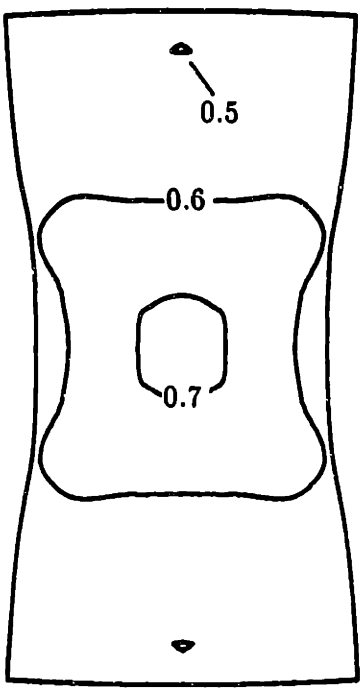

d/d_0=0.710

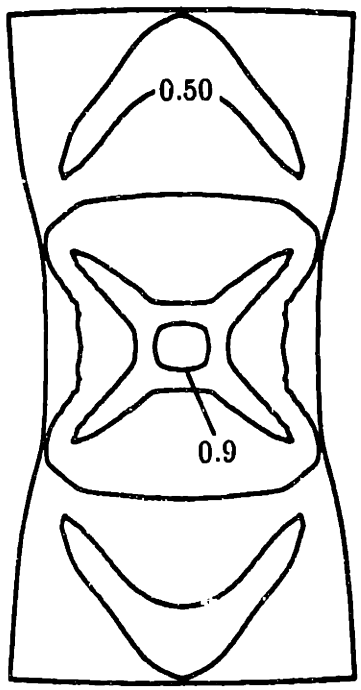

d/d_0=0.675

Figure 5.3 Contours of triaxiality, Σ, at the four indicated mid-plane transverse displacement levels, for the *nontransforming* case.

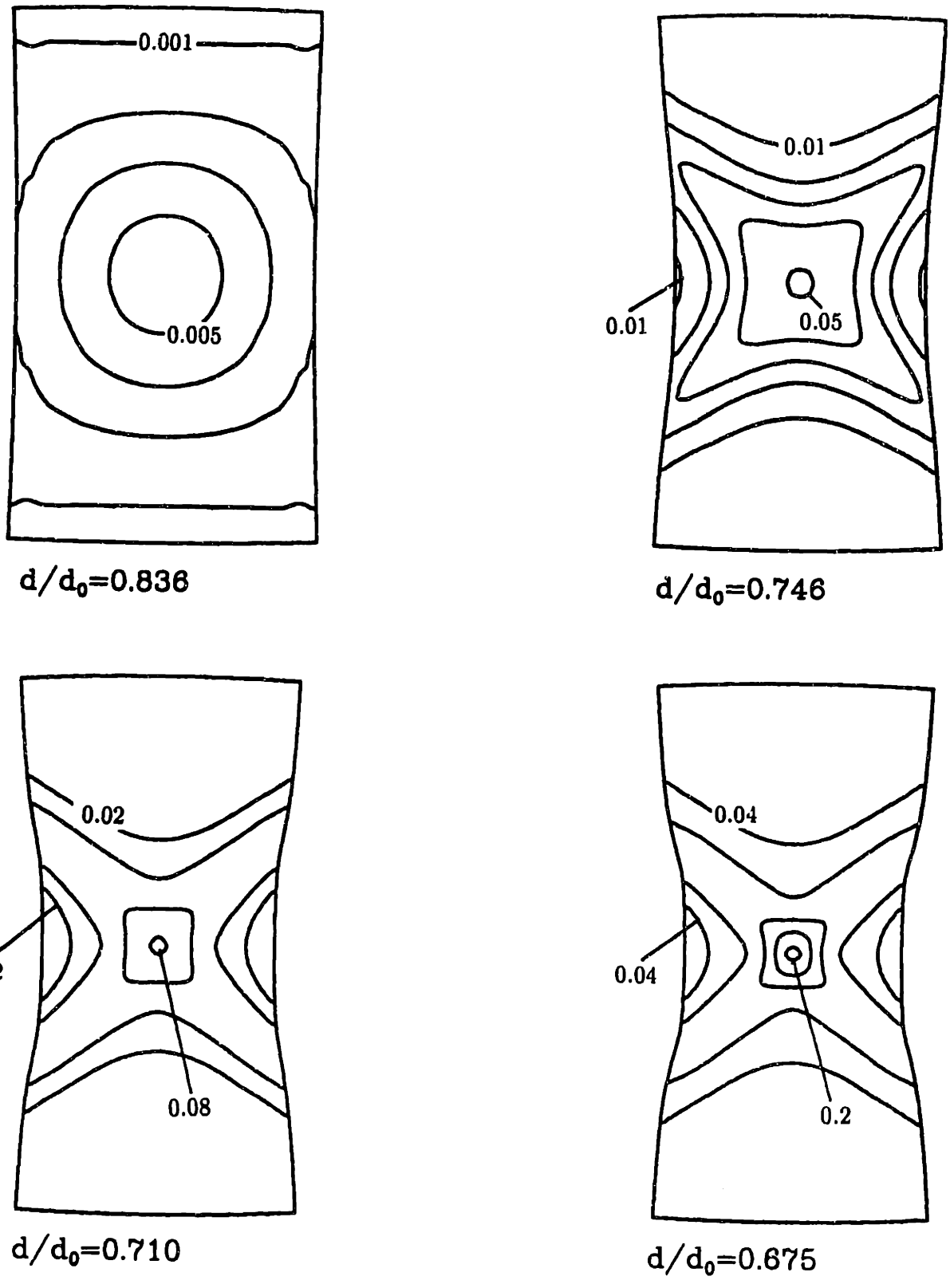

Figure 5.4 Contours of void volume fraction, ρ^*, at the four indicated mid-plane transverse displacement levels, for the *nontransforming* case.

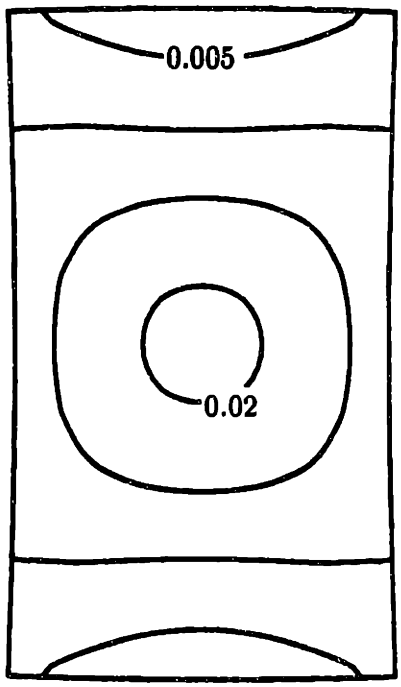

d/d_0=0.836

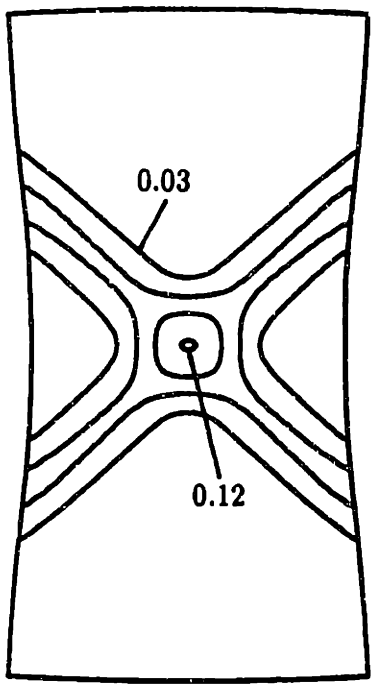

d/d_0=0.746

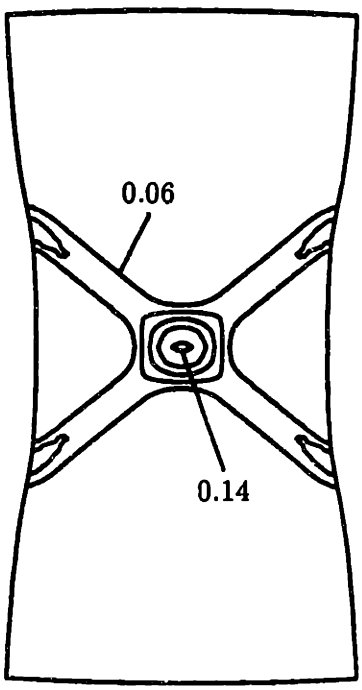

d/d_0=0.710

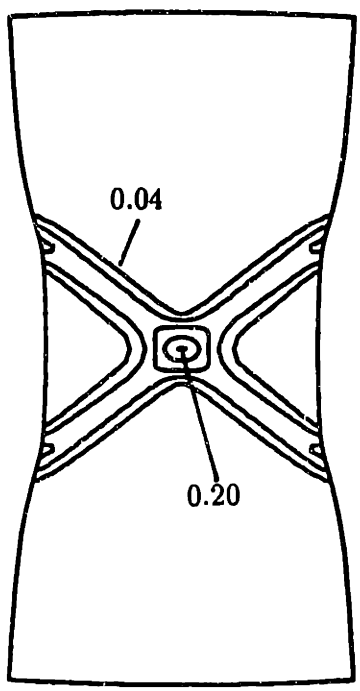

d/d_0=0.675

Figure 5.5 Contours of equivalent plastic shear strain rate, $\dot{\bar{\gamma}}$, at the four indicated mid-plane transverse displacement levels, for the *nontransforming* case. The reference strain rate, in consistent units, is $\dot{\gamma}_0 = 0.007$.

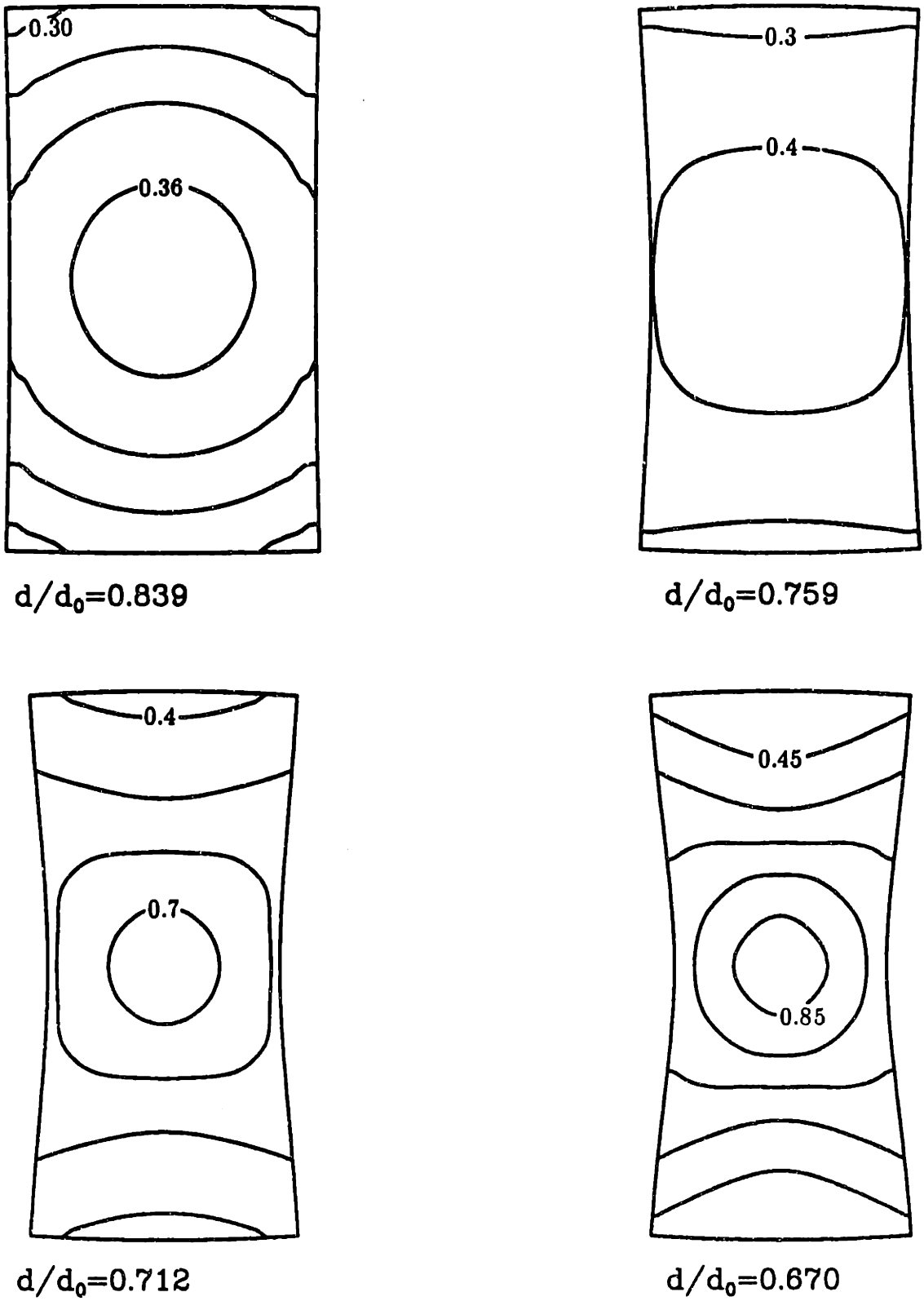

Figure 5.6 Contours of equivalent plastic shear strain, $\overline{\gamma}^p$, at the four indicated mid-plane transverse displacement levels, for the *transforming* case ($T = 448K$).

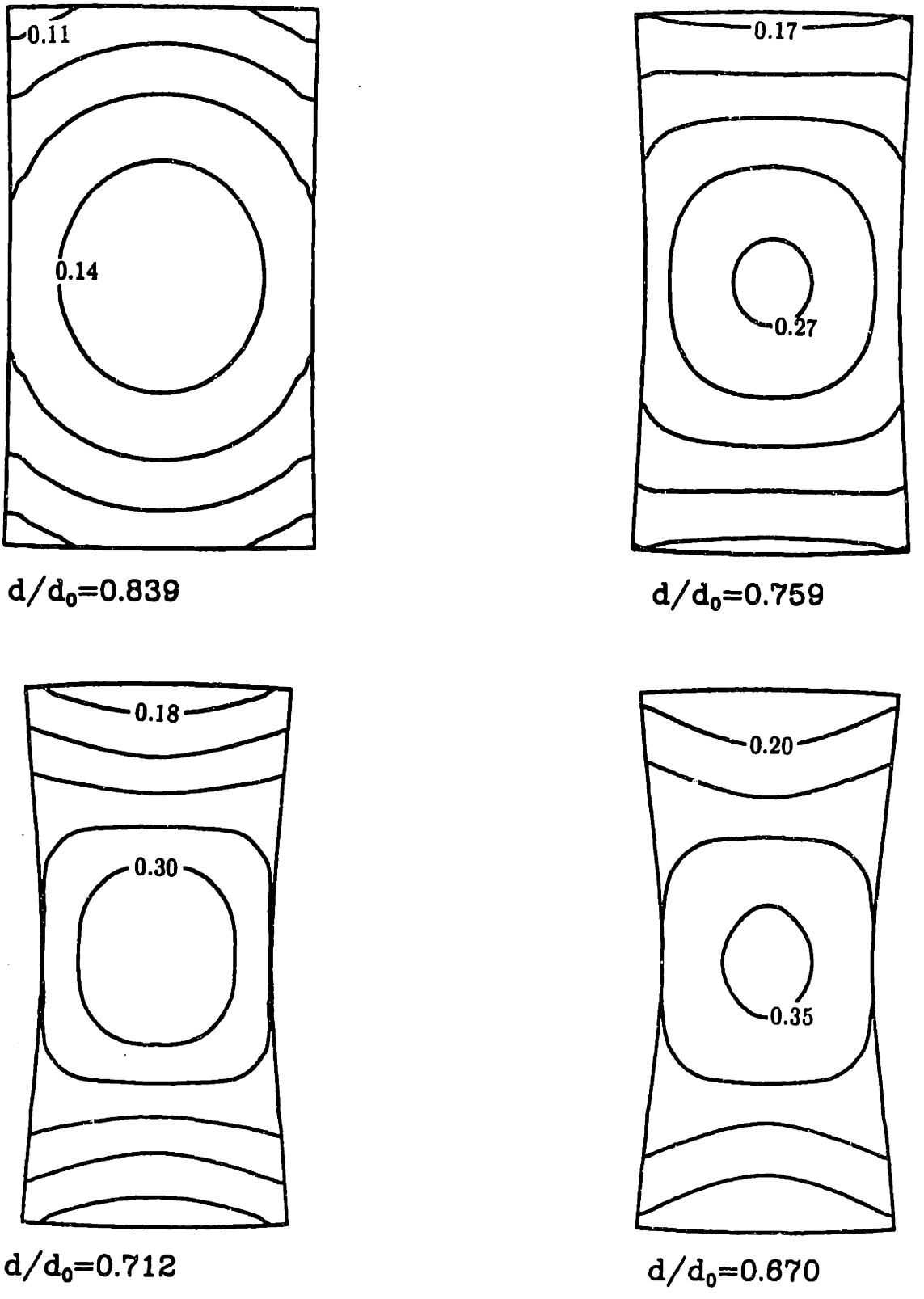

Figure 5.7 Contours of martensite volume fraction, f, at the four indicated mid-plane transverse displacement levels, for the *transforming* case ($T = 448K$).

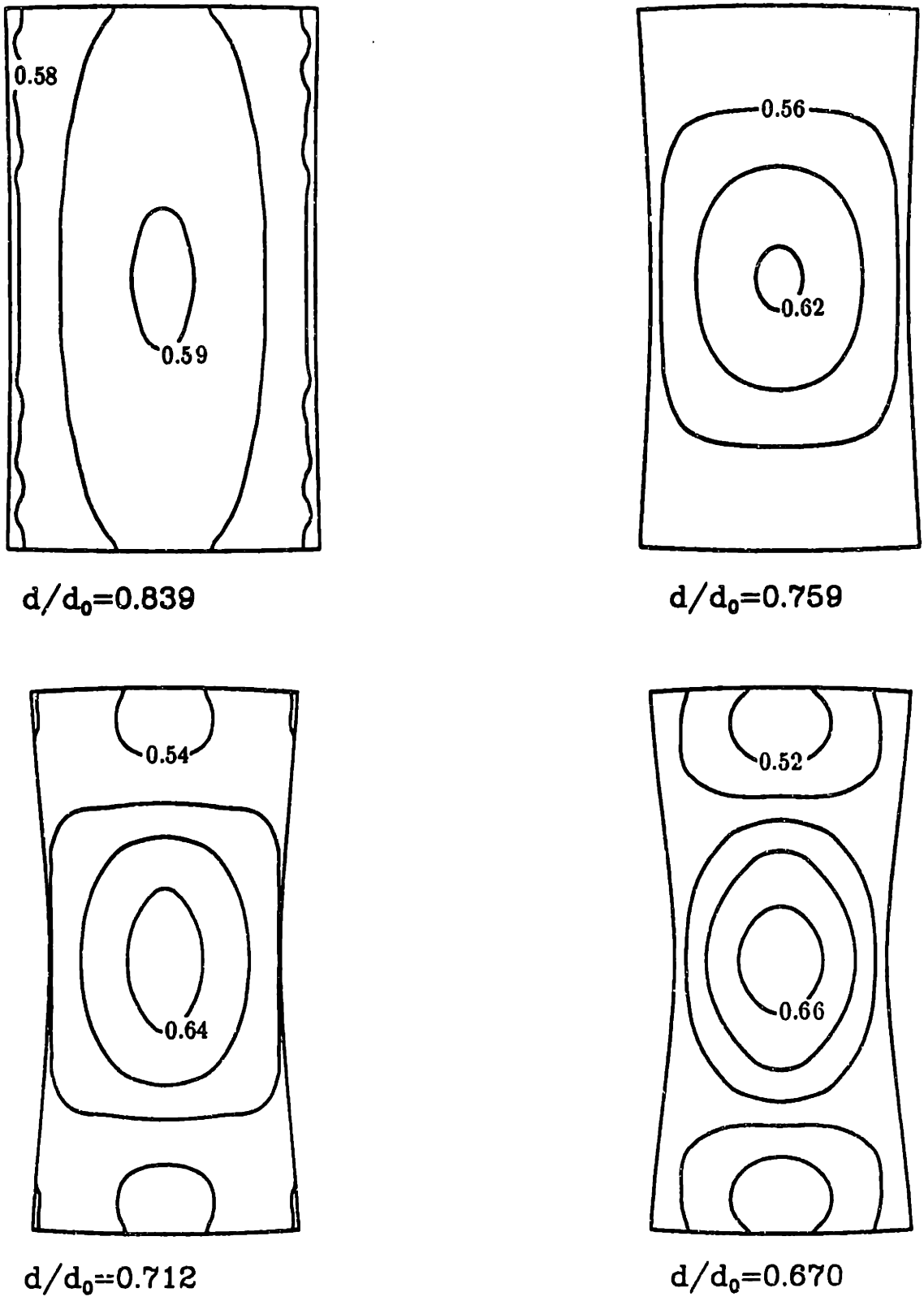

Figure 5.8 Contours of triaxiality, Σ, at the four indicated mid-plane transverse displacement levels, for the *transforming* case ($T = 448K$).

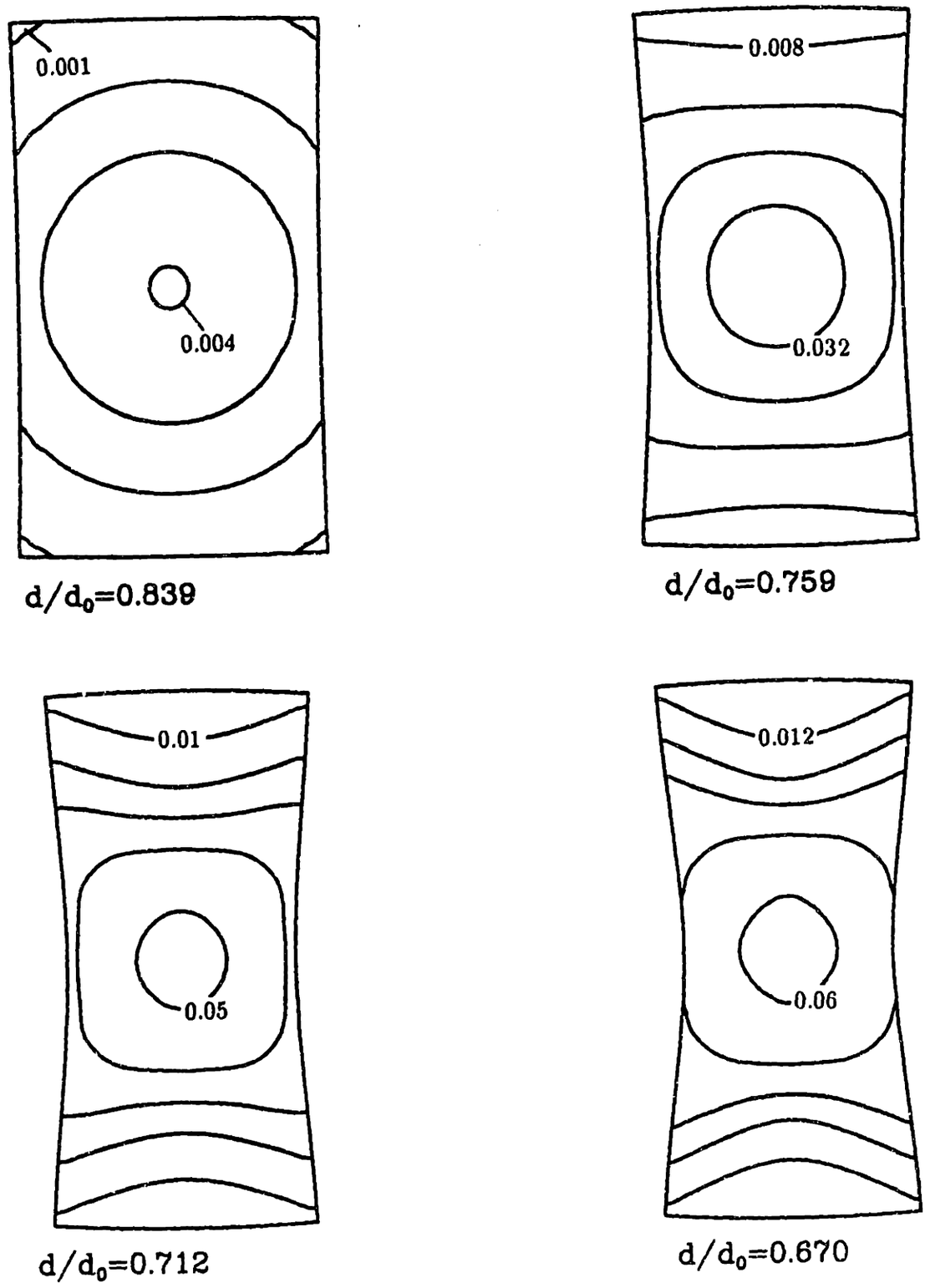

Figure 5.9 Contours of void volume fraction, ρ^*, at the four indicated mid-plane transverse displacement levels, for the *transforming* case ($T = 448K$).

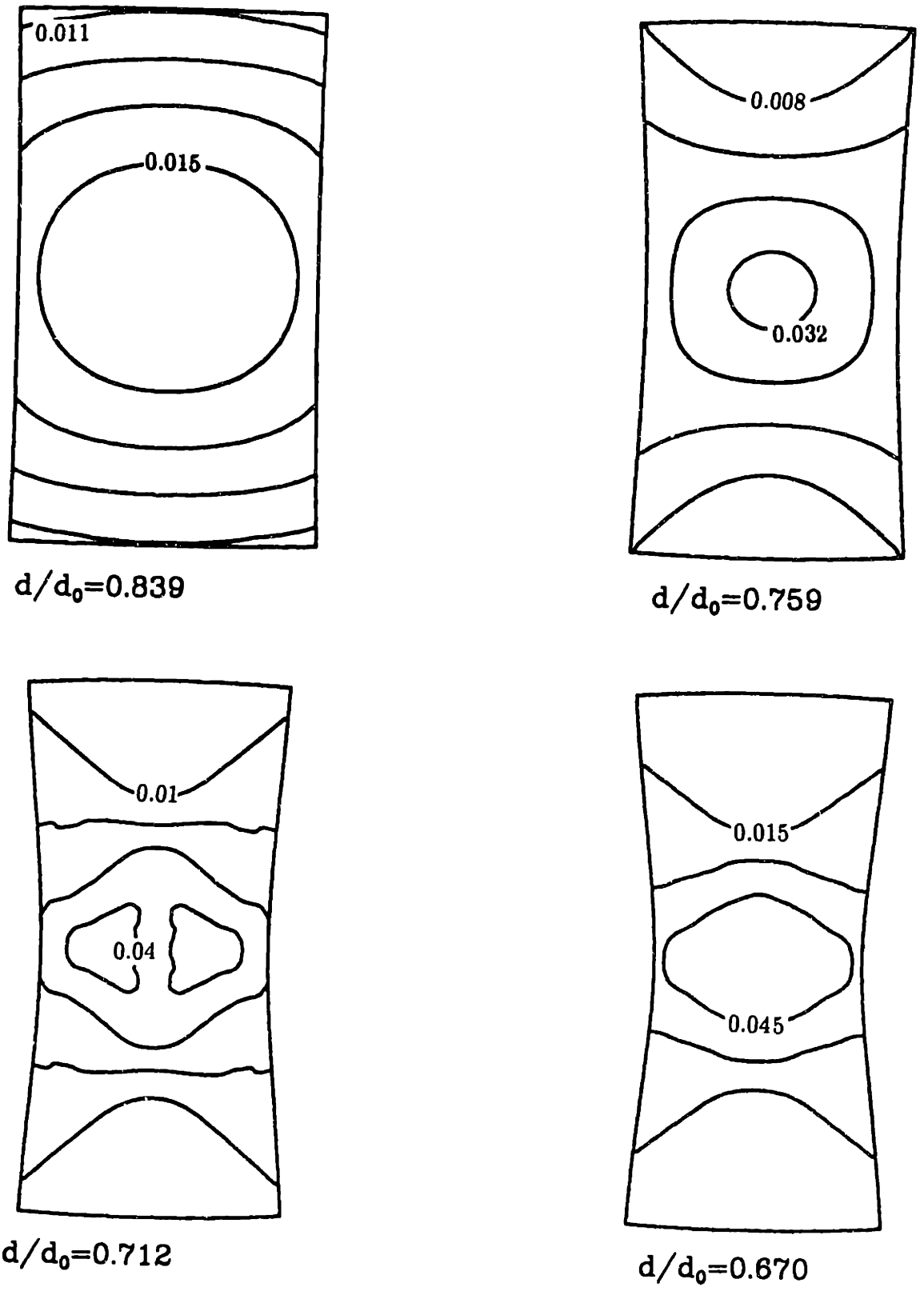

Figure 5.10 Contours of equivalent plastic shear strain rate, $\dot{\bar{\gamma}}^p$, at the four indicated mid-plane transverse displacement levels, for the *transforming* case ($T = 448K$). The reference strain rate, in consistent units, is $\dot{\gamma}_0 = 0.007$.

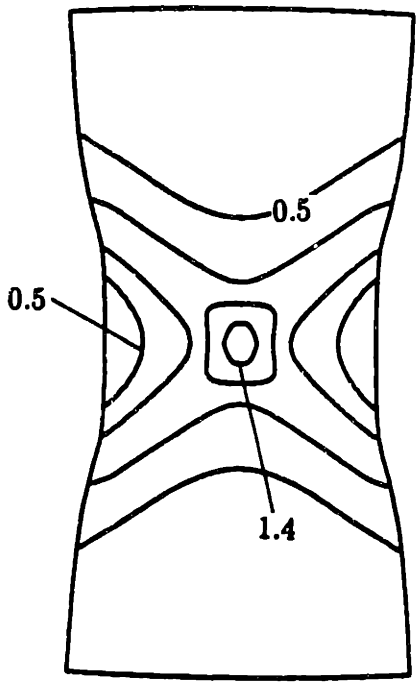

$\overline{\gamma}$, nontransforming case

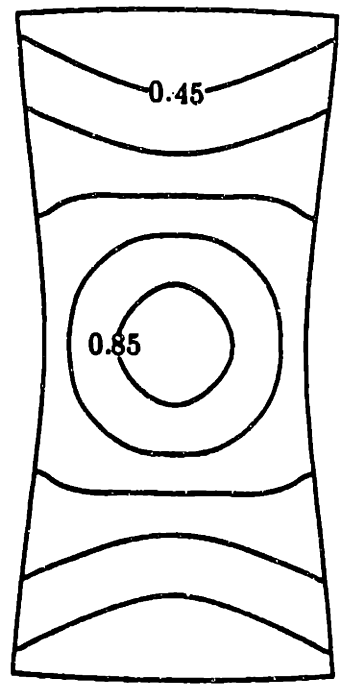

$\overline{\gamma}$, transforming case

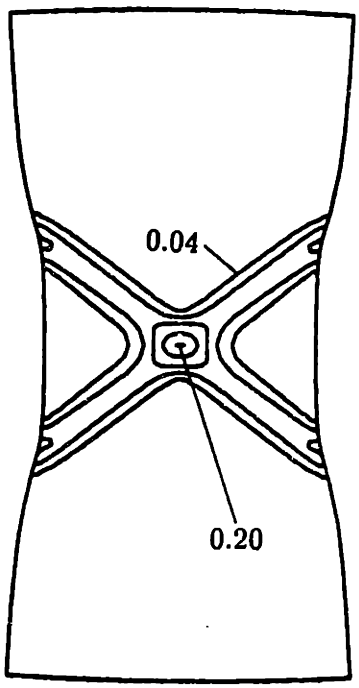

$\dot{\overline{\gamma}}$, nontransforming case

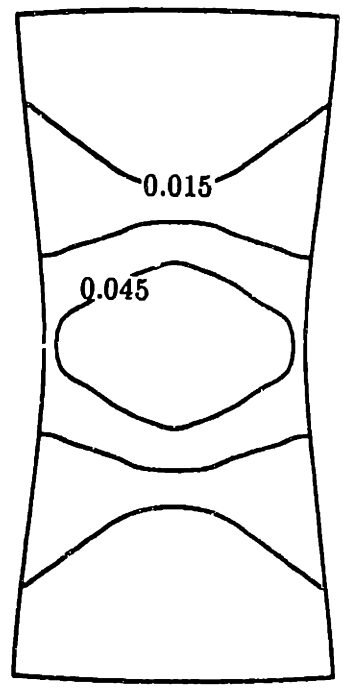

$\dot{\overline{\gamma}}$, transforming case

Figure 5.11 Comparison of equivalent plastic shear strain, $\overline{\gamma}^p$, (above) and equivalent plastic shear strain rate, $\dot{\overline{\gamma}}$ (below) for the nontransforming (left) and transforming ($T = 448K$) cases at equal mid-plane transverse strain levels ($\epsilon_d = ln(d/d_0) = 0.50$).

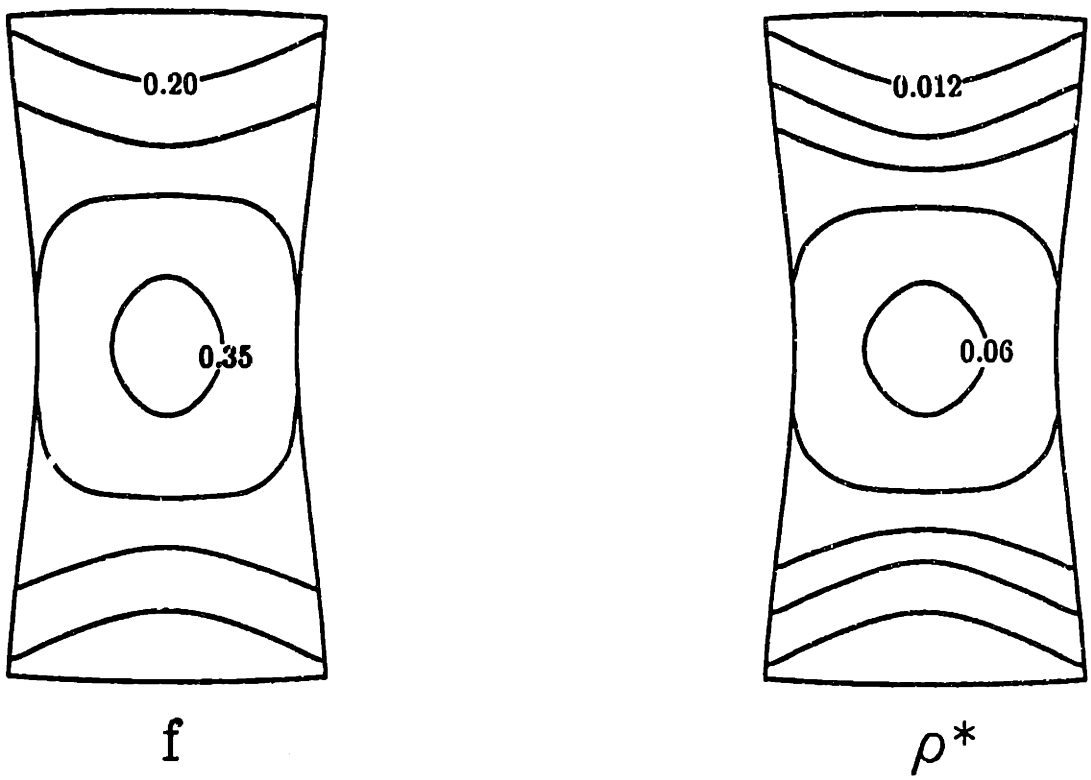

Figure 5.12 Comparison of contours of martensite volume fraction, f (left), and void volume fraction, ρ^* (right), for the transforming ($T = 448K$) case at mid-plane transverse displacement level ($\epsilon_d = ln(d/d_0) = 0.50$).

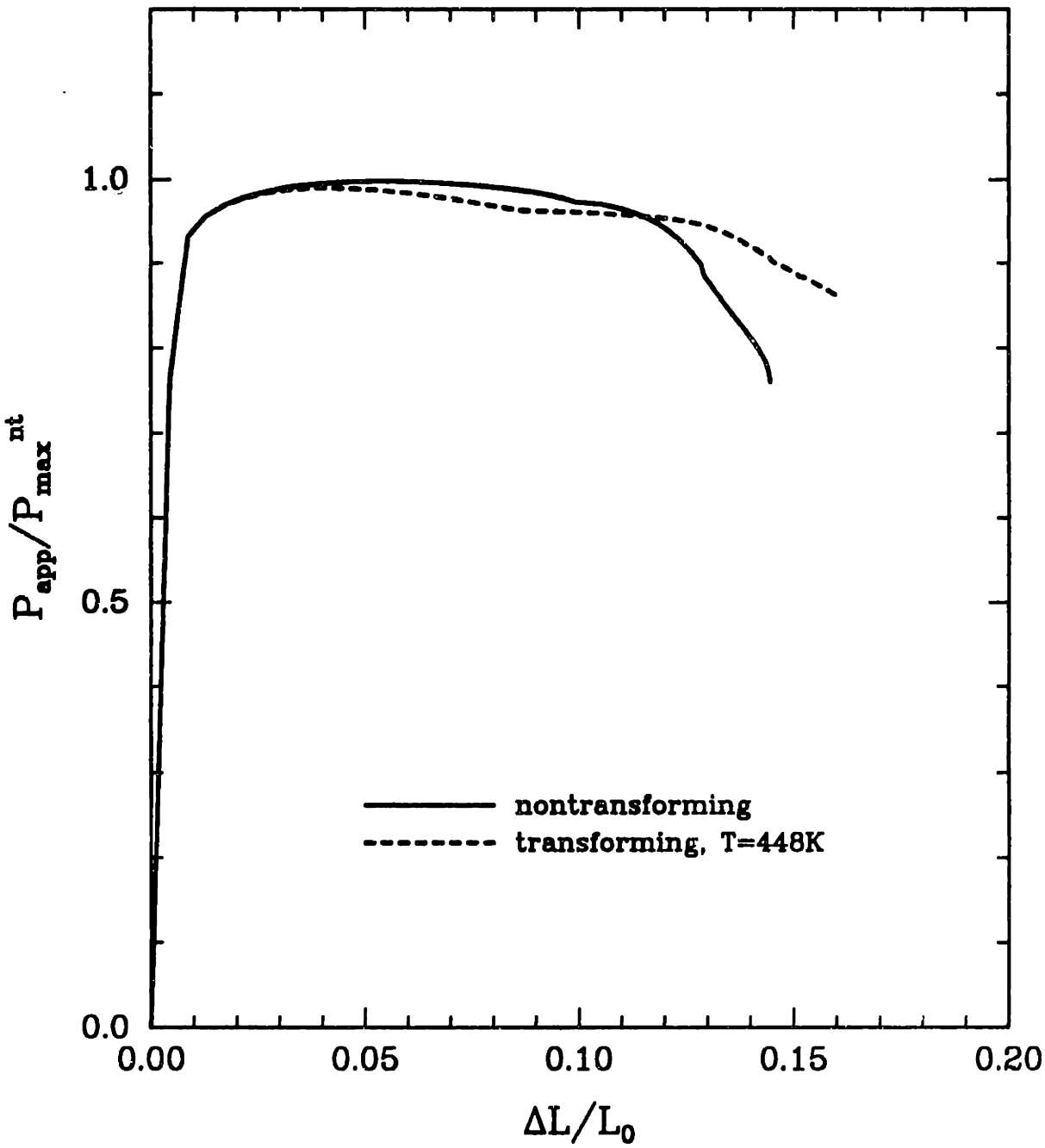

Figure 5.13 Comparison of load-displacement histories for the nontransforming and transforming ($T = 448K$) cases, plane-strain tension problem. Here P_{app} is the applied load and P_{max}^{nt} is the maximum load for the nontransforming case.

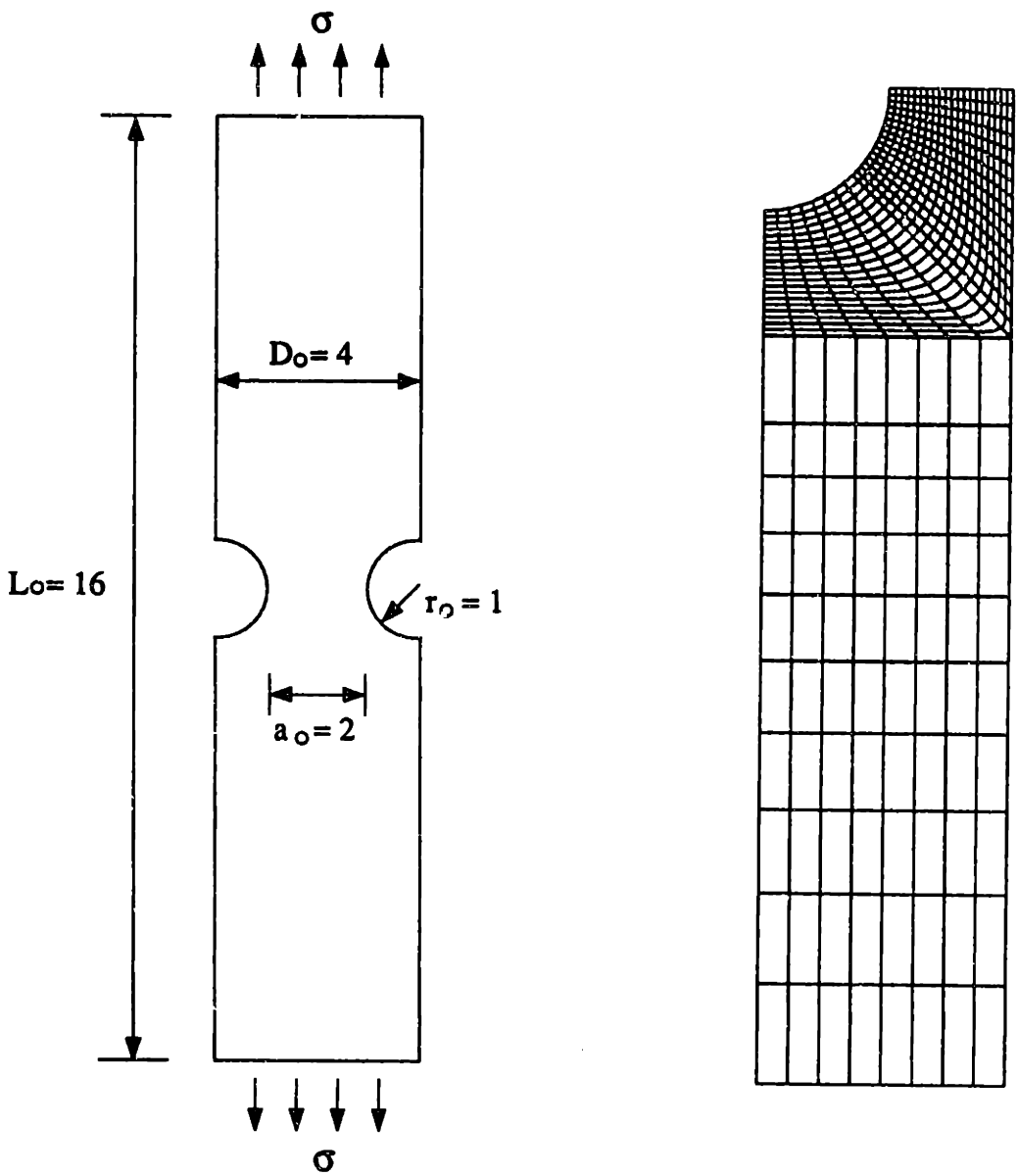

Figure 5.14 Description of the mildly-notched plane-strain extension problem: (a) the model notched-tensile specimen analyzed; (b) the finite element model, with symmetry and loading conditions indicated.

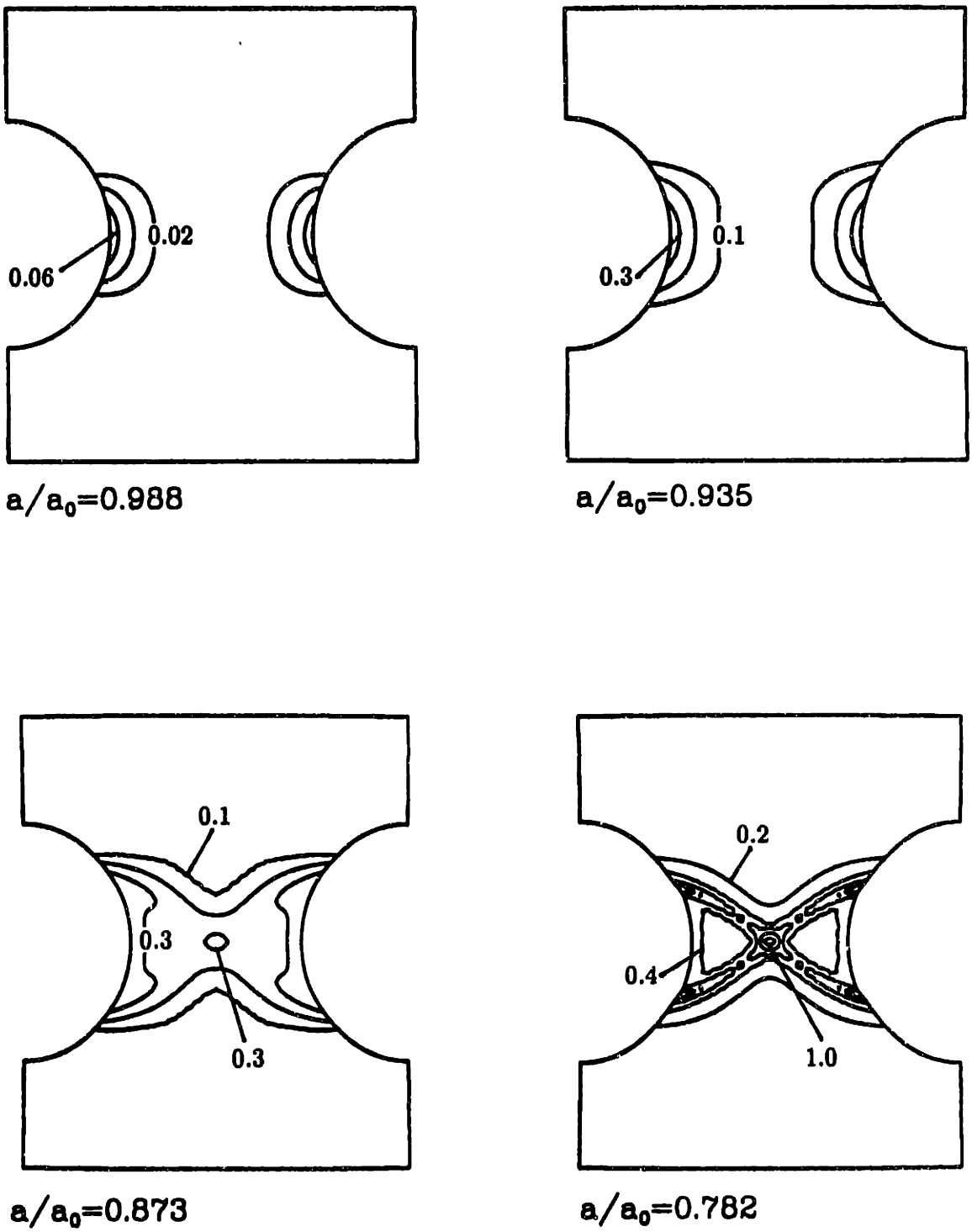

Figure 5.15 Contours of equivalent plastic shear strain, $\bar{\gamma}^p$, plotted on the deformed mesh at the four indicated mid-plane transverse displacement levels (a/a_0), for the *nontransforming* case. Only the notched region of the mesh (which, again, has been mirrored about the mid-plane and the longitudinal axis) is shown in these plots.

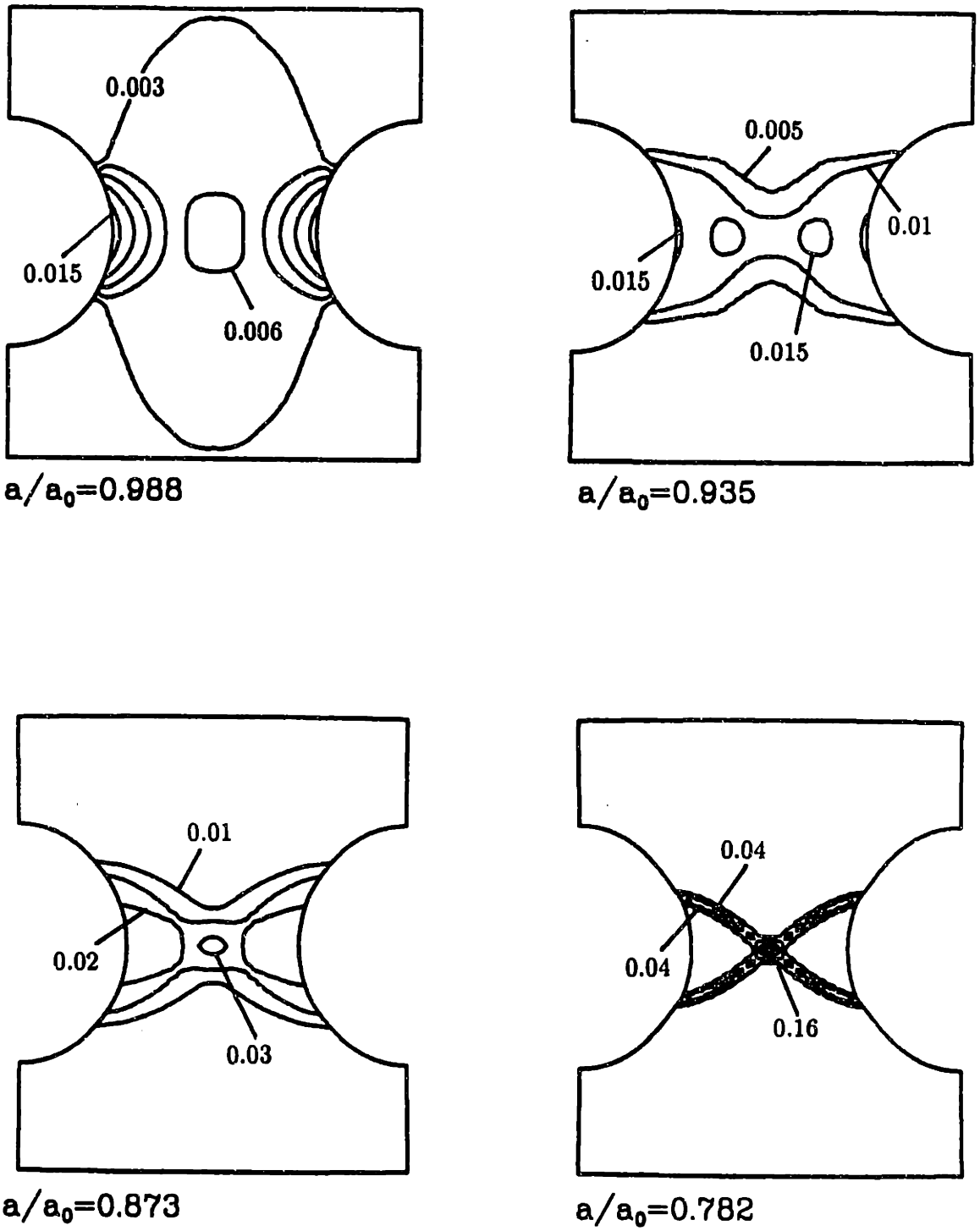

Figure 5.16 Contours of equivalent plastic shear strain rate, $\dot{\bar{\gamma}}^p$, at the four indicated mid-plane transverse displacement levels for the *nontransforming* case. The reference strain rate, in consistent units, is $\dot{\gamma}_0 = 0.007$.

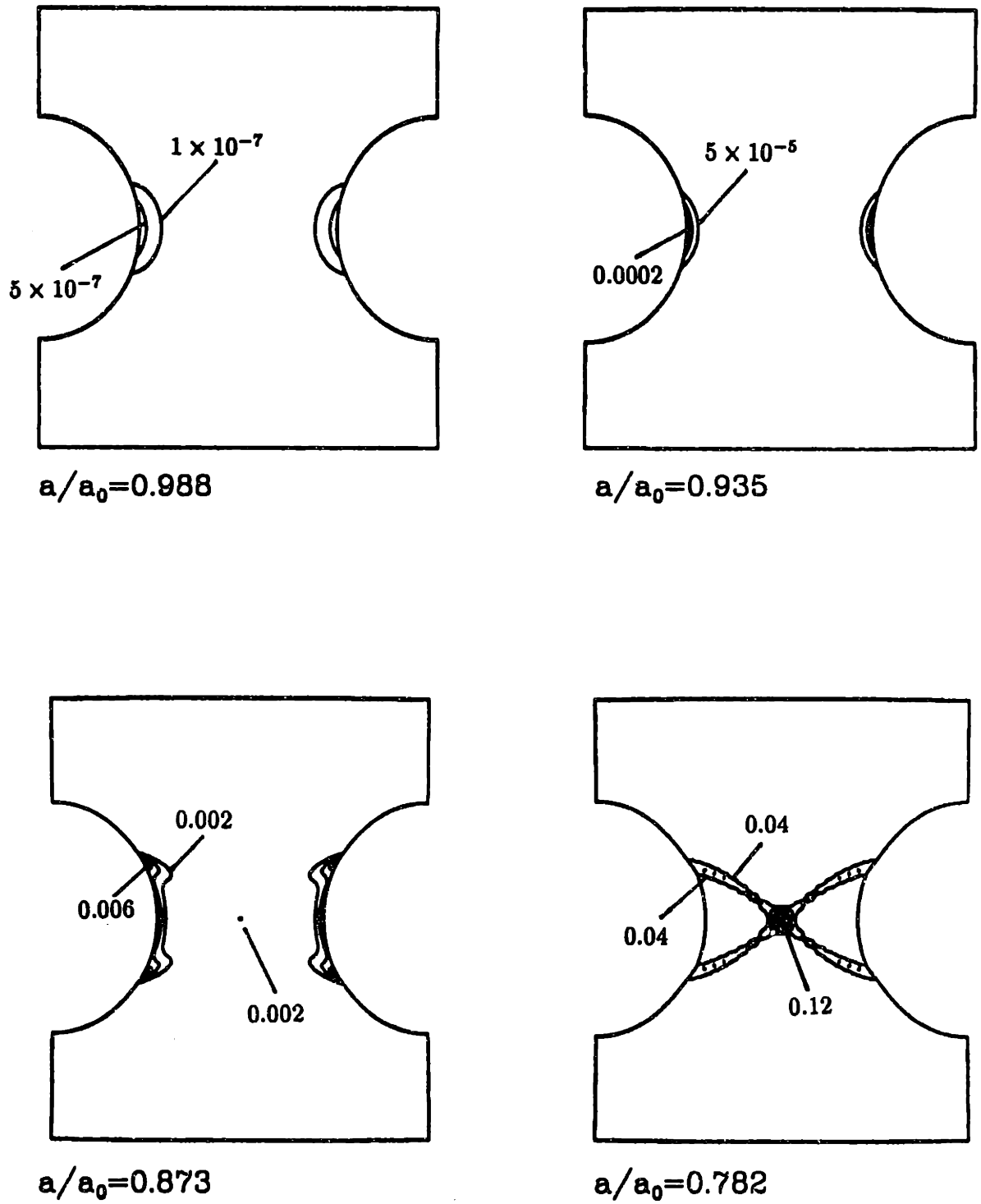

Figure 5.17 Contours of void volume fraction, ρ^*, at the four indicated mid-plane transverse displacement levels, for the *nontransforming* case.

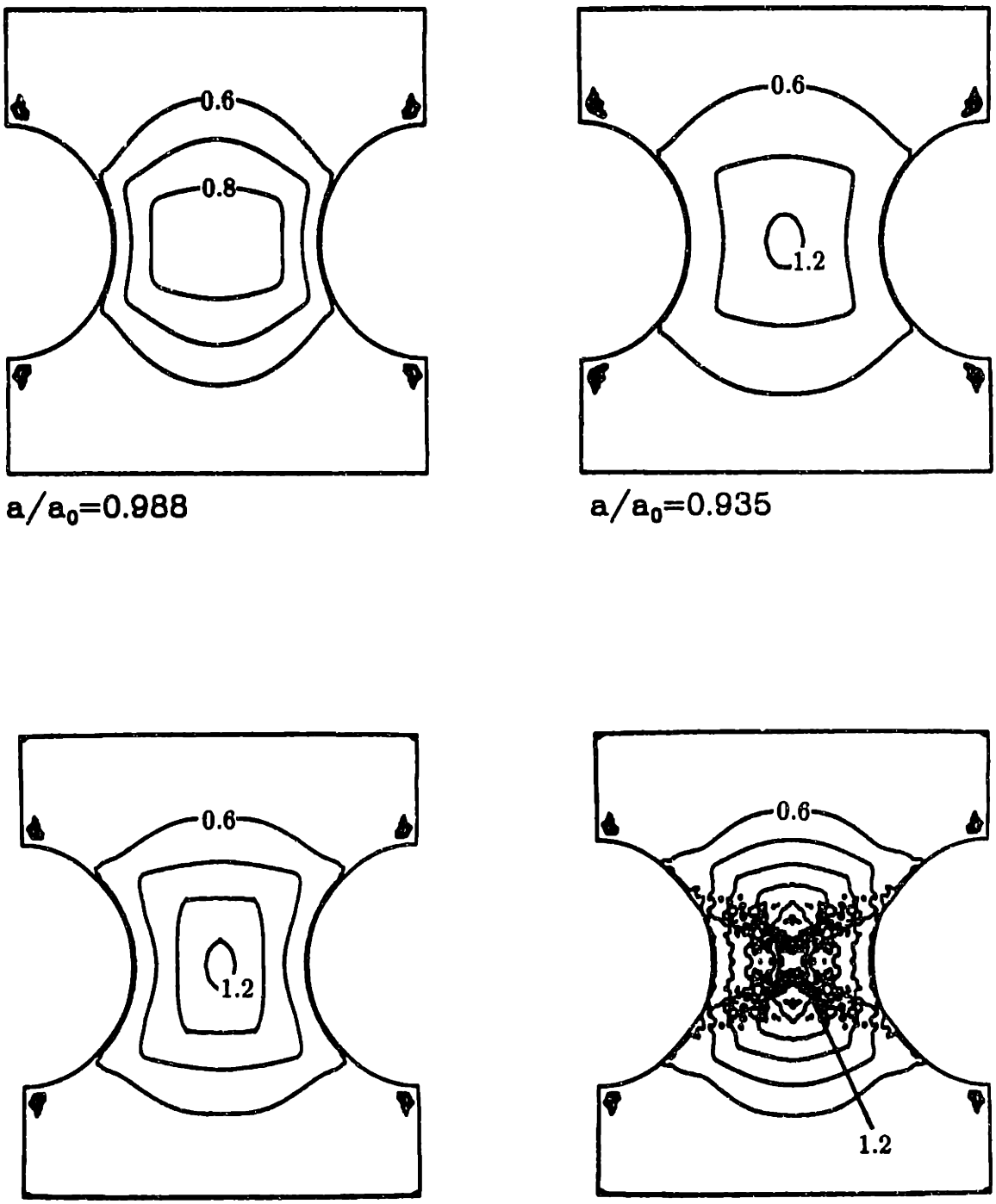

Figure 5.18 Contours of triaxiality, Σ, at the four indicated mid-plane transverse displacement levels, for the *nontransforming* case.

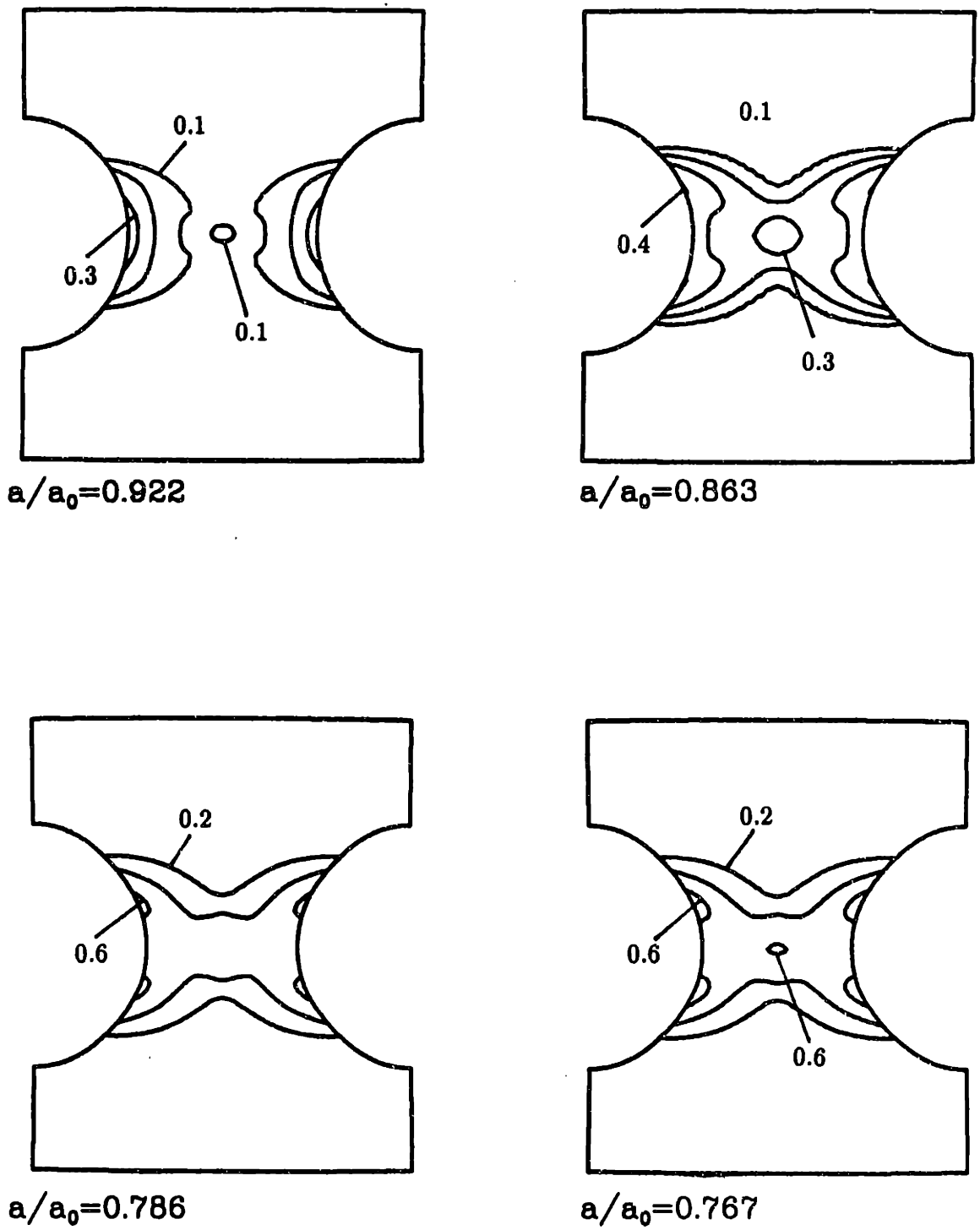

Figure 5.19 Contours of equivalent plastic shear strain, $\overline{\gamma}^p$, at the four indicated mid-plane transverse displacement levels, for the *transforming* case ($T = 473K$).

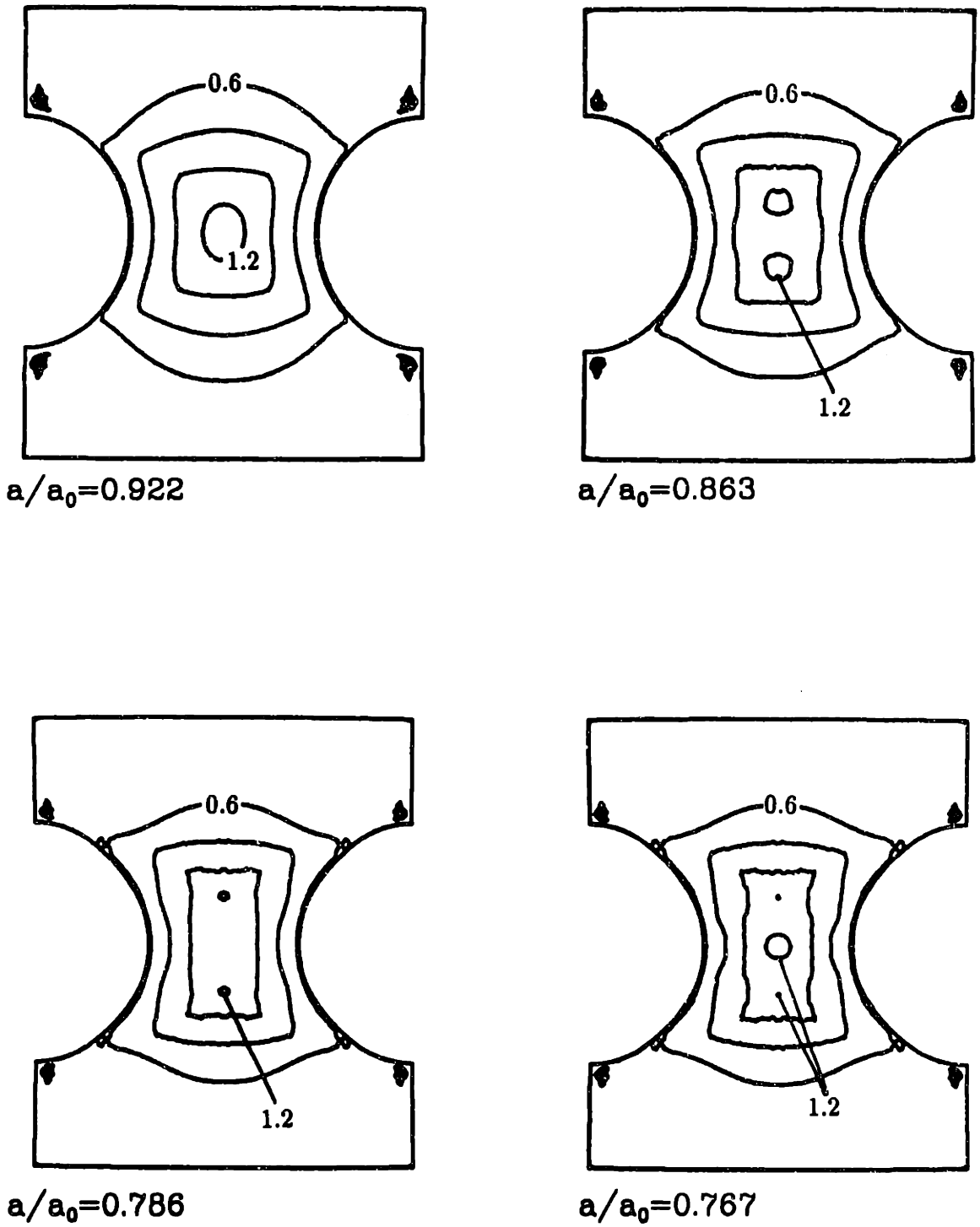

Figure 5.20 Contours of triaxiality, Σ, at the four indicated mid-plane transverse displacement levels, for the *transforming* case ($T = 473K$).

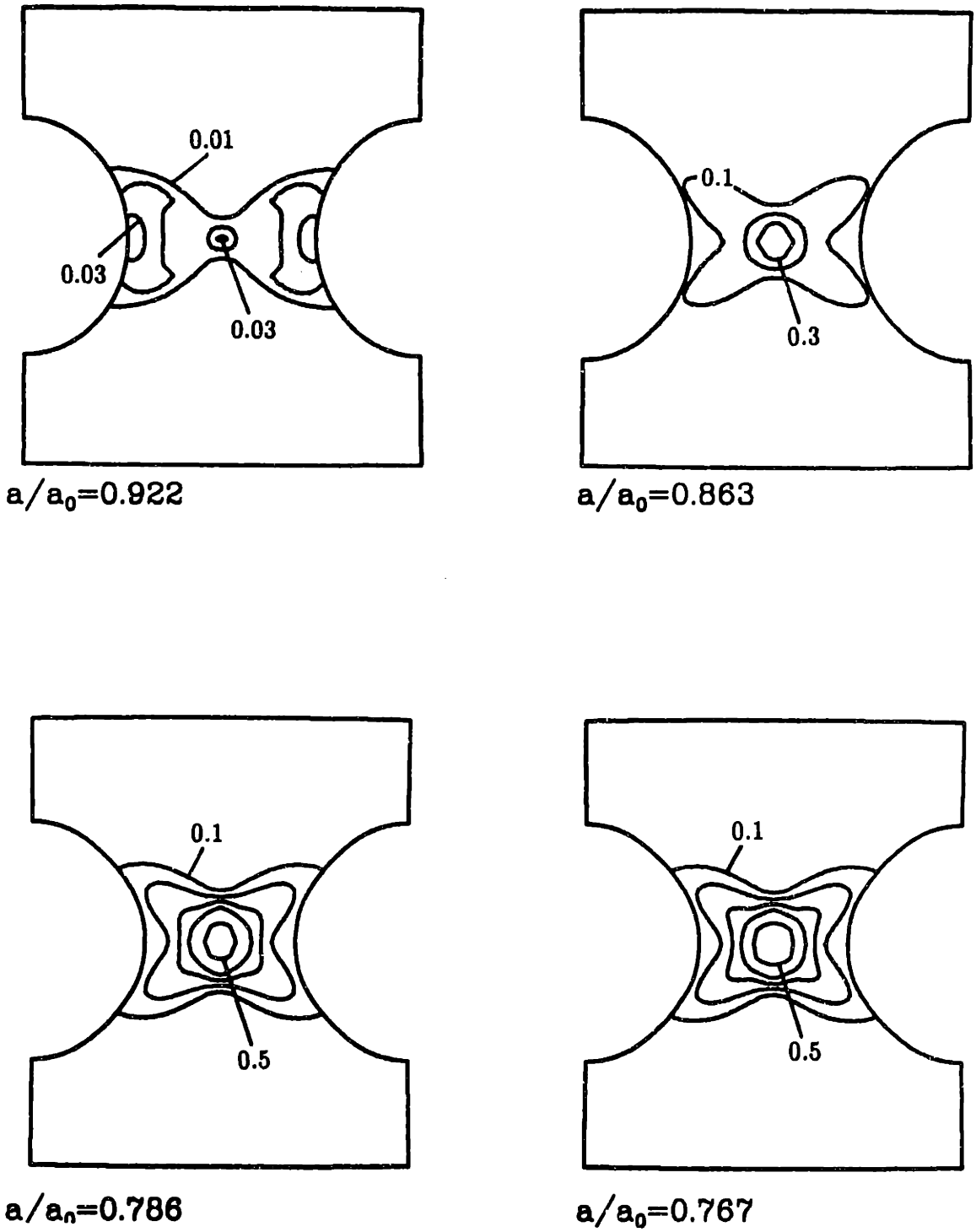

Figure 5.21 Contours of martensite volume fraction, f, at the four indicated mid-plane transverse displacement levels, for the *transforming* case ($T = 473K$).

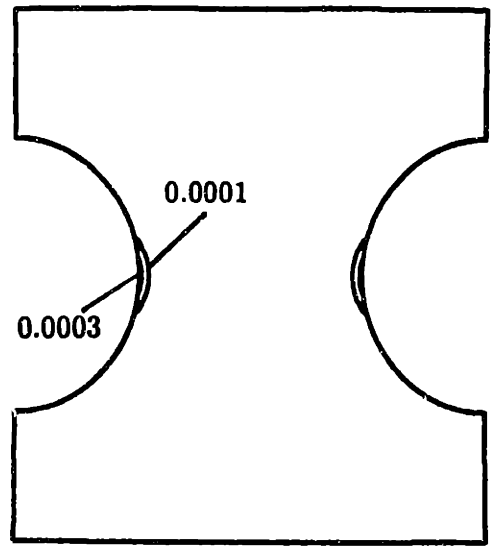

a/a_0=0.922

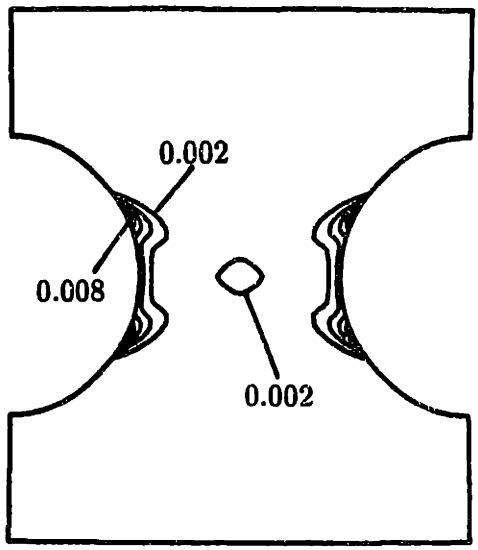

a/a_0=0.863

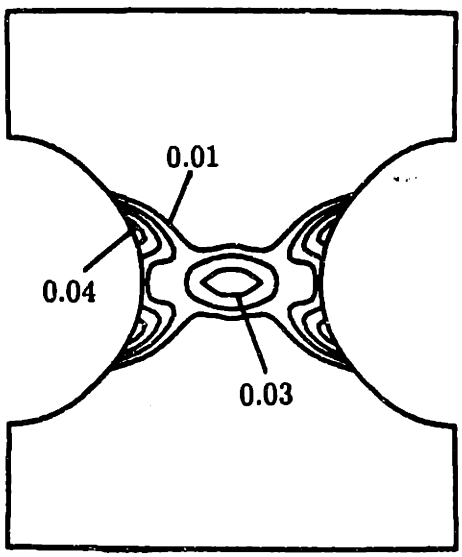

a/a_0=0.786

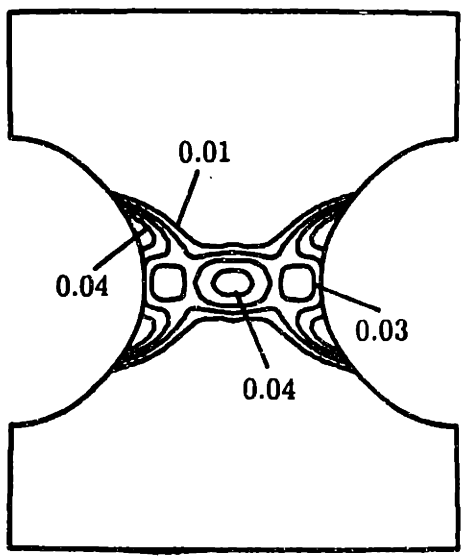

a/a_0=0.767

Figure 5.22 Contours of void volume fraction, ρ^*, at the four indicated mid-plane transverse displacement levels, for the *transforming* case ($T = 473K$).

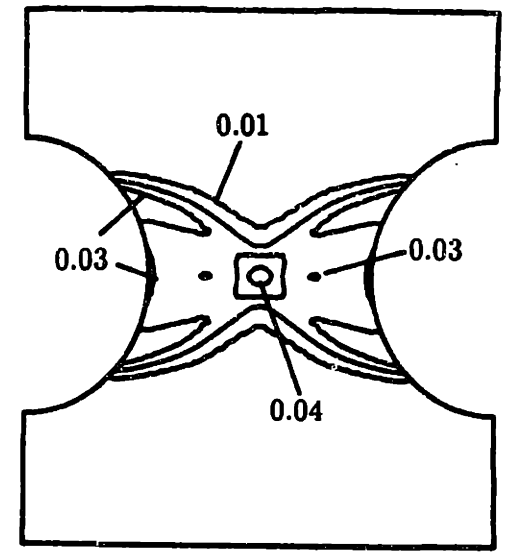

a/a_0=0.922

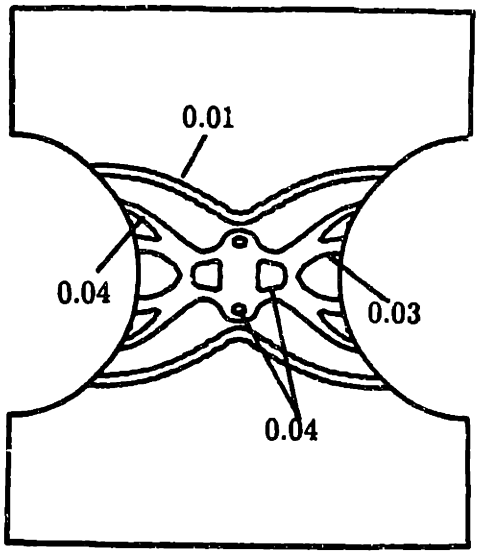

a/a_0=0.863

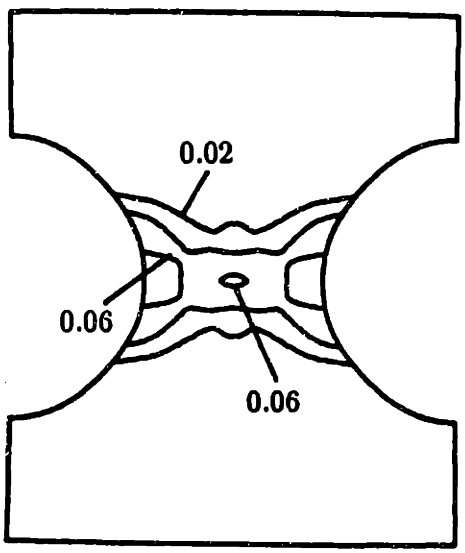

a/a_0=0.786

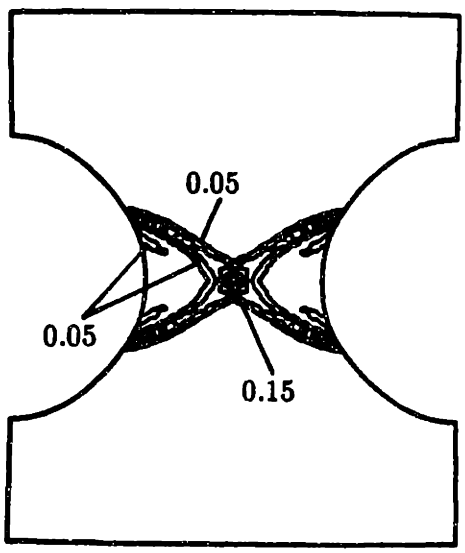

a/a_0=0.767

Figure 5.23 Contours of equivalent plastic shear strain rate, $\dot{\bar{\gamma}}^p$, at the four indicated mid-plane transverse displacement levels, for the *transforming* case ($T = 473K$). The reference strain rate, in consistent units, is $\dot{\gamma}_0 = 0.007$.

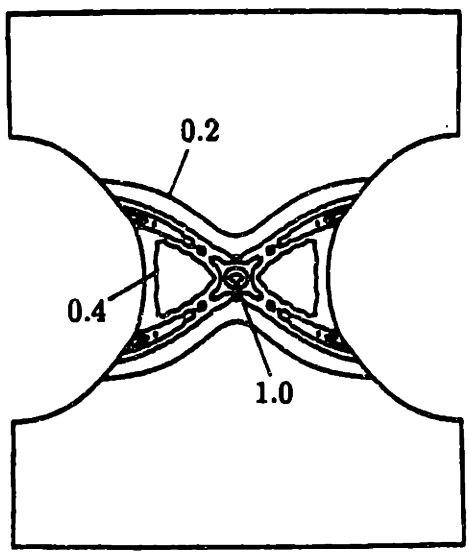

$\overline{\gamma}^p$, nontransforming case

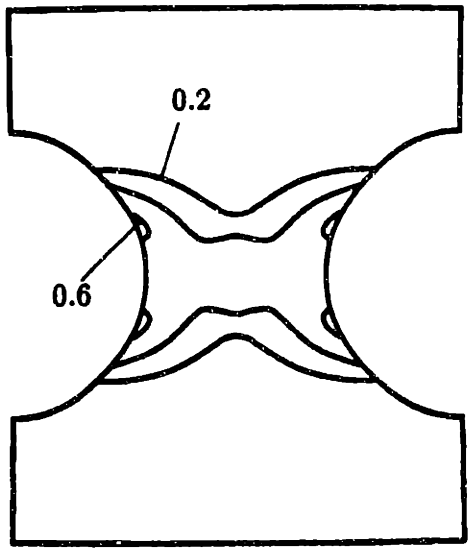

$\overline{\gamma}^p$, transforming case

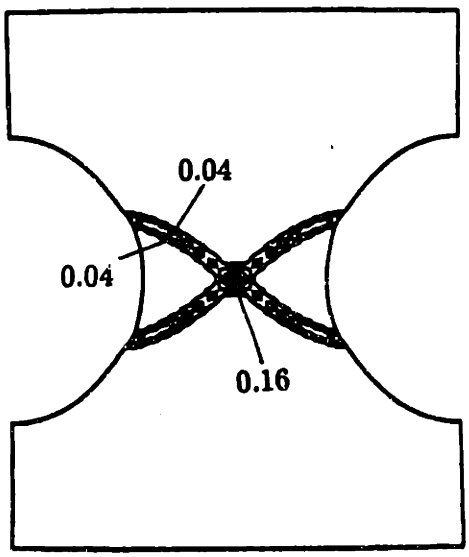

$\dot{\overline{\gamma}}^p$, nontransforming case

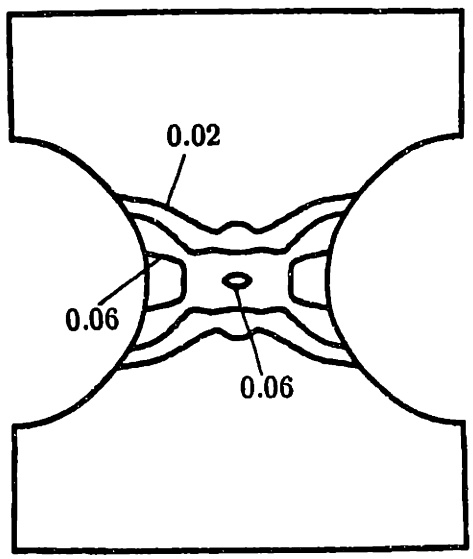

$\dot{\overline{\gamma}}^p$, transforming case

Figure 5.24 Comparison of equivalent plastic shear strain, $\overline{\gamma}^p$, (above) and equivalent plastic shear strain rate, $\dot{\overline{\gamma}}^p$ (below) for the nontransforming (left) and transforming ($T = 473K$) cases at equal mid-plane transverse displacement levels ($a/a_0 = 0.782$).

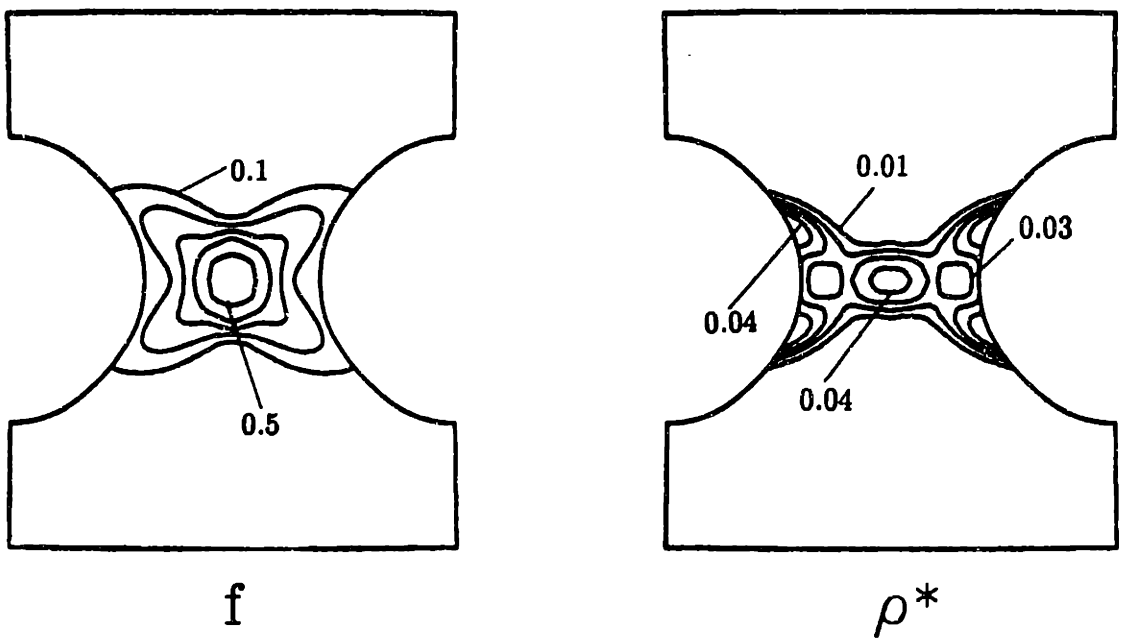

Figure 5.25 Comparison of contours of martensite volume fraction, f (left), and void volume fraction, ρ^* (right), for the transforming ($T = 473K$) case at mid-plane transverse displacement level ($a/a_0 = 0.782$).

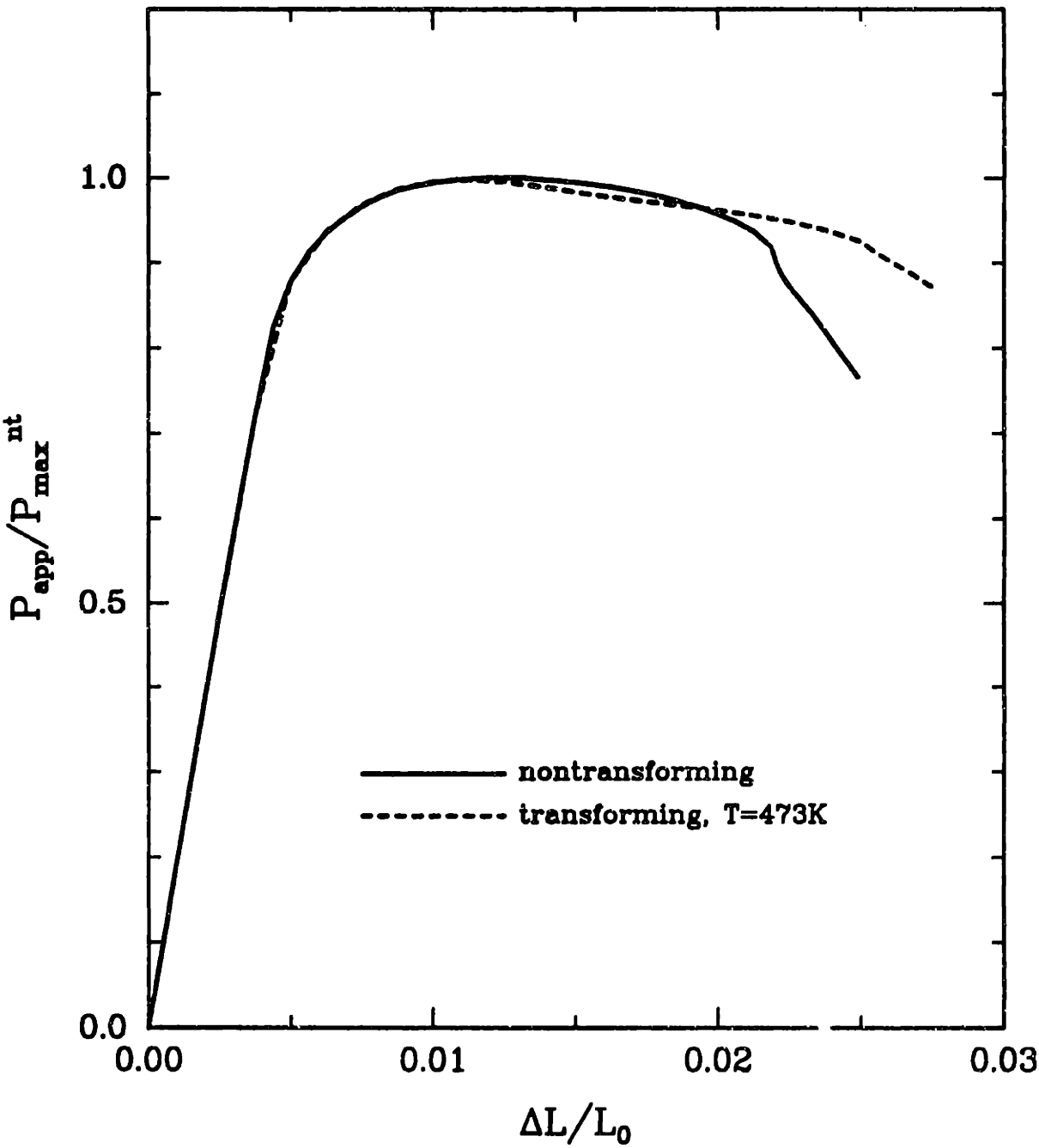

Figure 5.26 Comparison of load-displacement histories for the nontransforming and transforming ($T = 473K$) cases, mildly-notched extension problem. Here P_{app} is the applied load and P_{max}^{nt} is the maximum load for the nontransforming case.

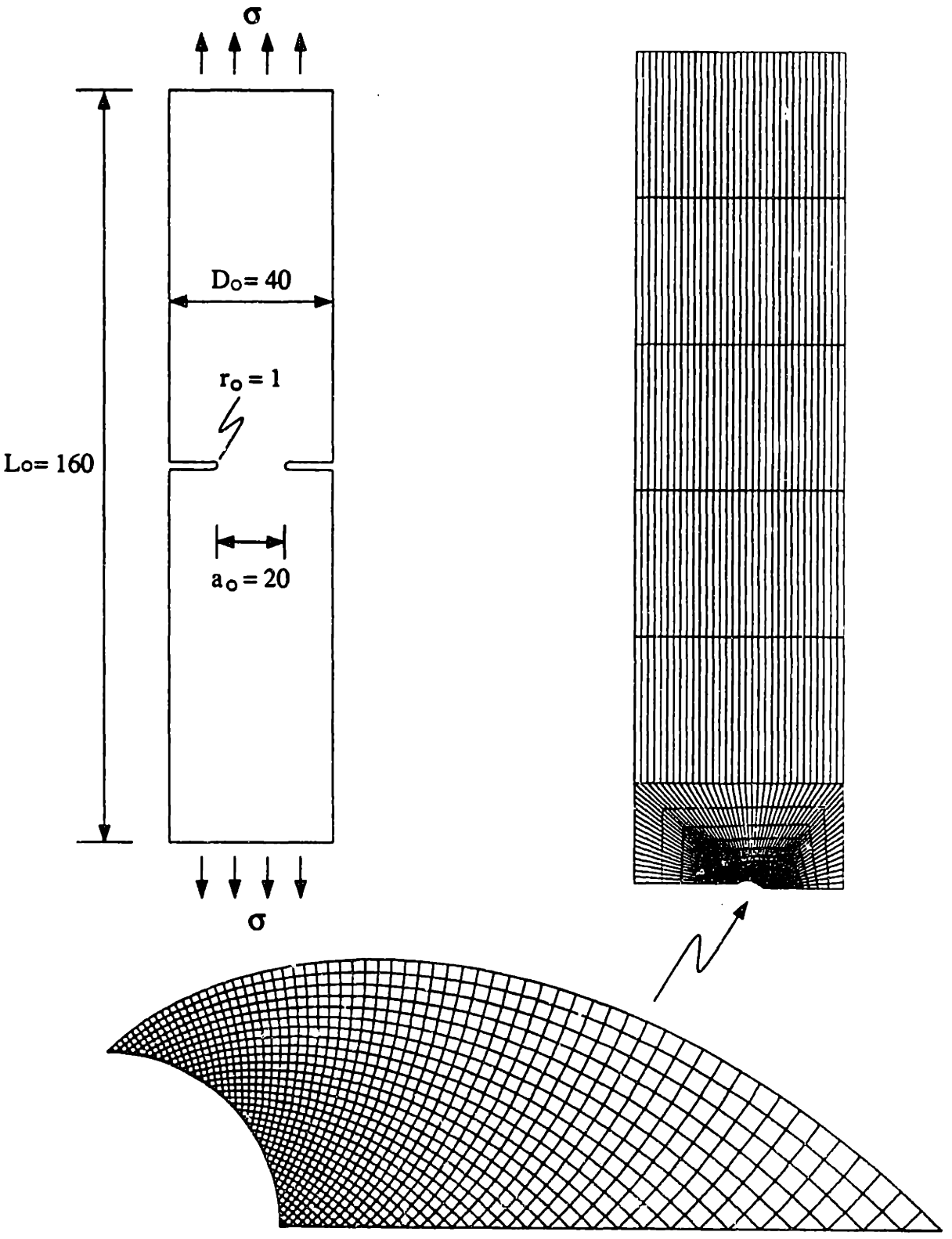

Figure 5.27 Description of the sharply-notched plane-strain extension problem: (a) the model notched-tensile specimen analyzed; (c) the far-field portion of the finite element mesh, with symmetry and loading conditions indicated; (c) the near-tip region of the finite element mesh, which takes the shape of a slip-line field for a semi-circular notch, and fits into the far-field part of the mesh as indicated.

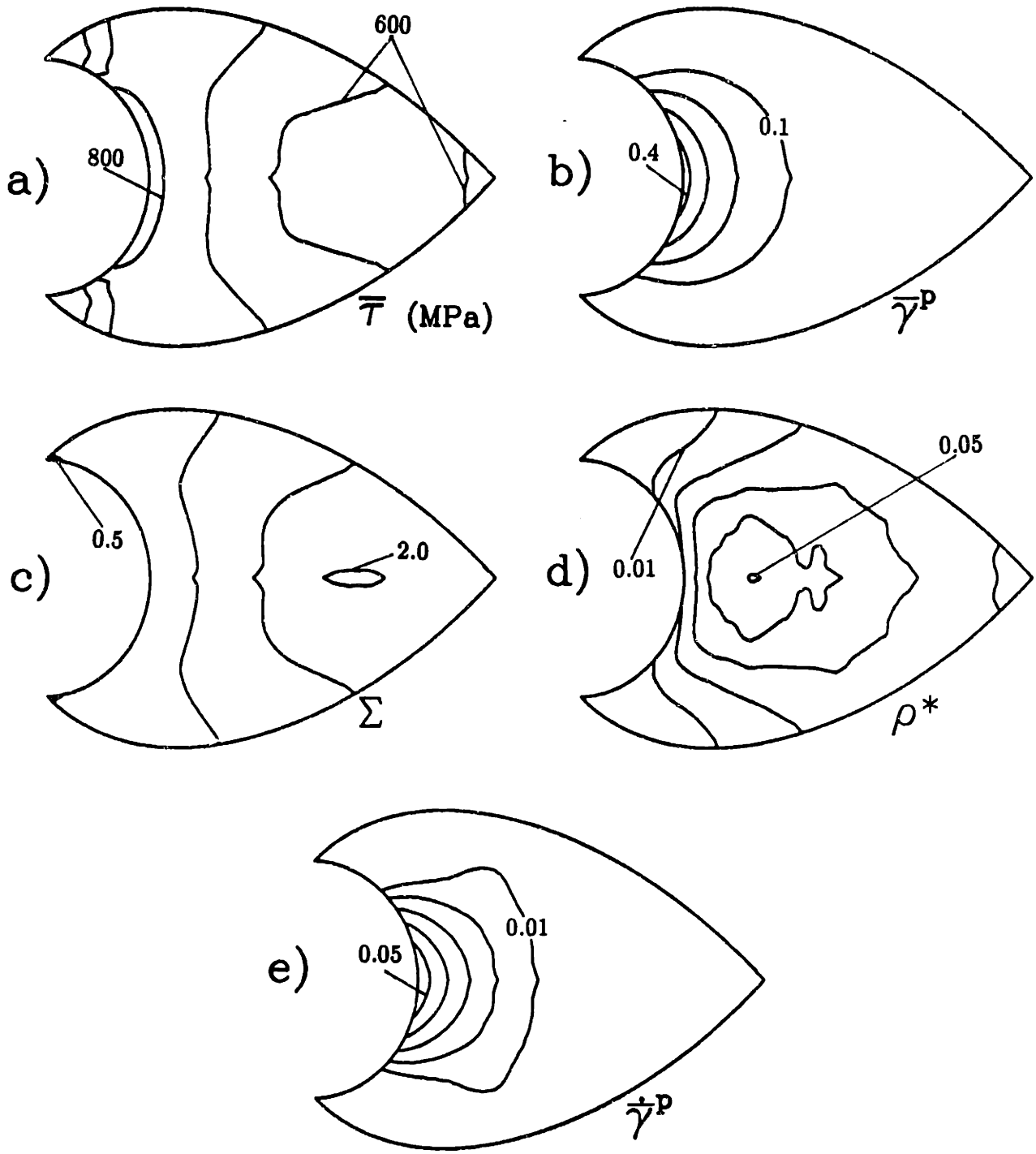

Figure 5.28 Contours of scalar fields for the *nontransforming* case, plotted on the deformed mesh at a deformation level characterized by a blunted opening displacement $b/b_0 = 1.065$. Only the near-tip portion of the mesh (see Fig. 5.27c), mirrored about the mid-plane axis, is shown in these plots. (a) equivalent shear stress, $\overline{\tau}$; (b) equivalent plastic shear strain, $\overline{\gamma}^p$; (c) triaxiality, Σ; (d) void volume fraction, ρ^*, and (e) equivalent plastic shear strain rate, $\dot{\overline{\gamma}}^p$ (reference strain rate, in consistent units, is $\dot{\gamma}_0 = 0.007$).

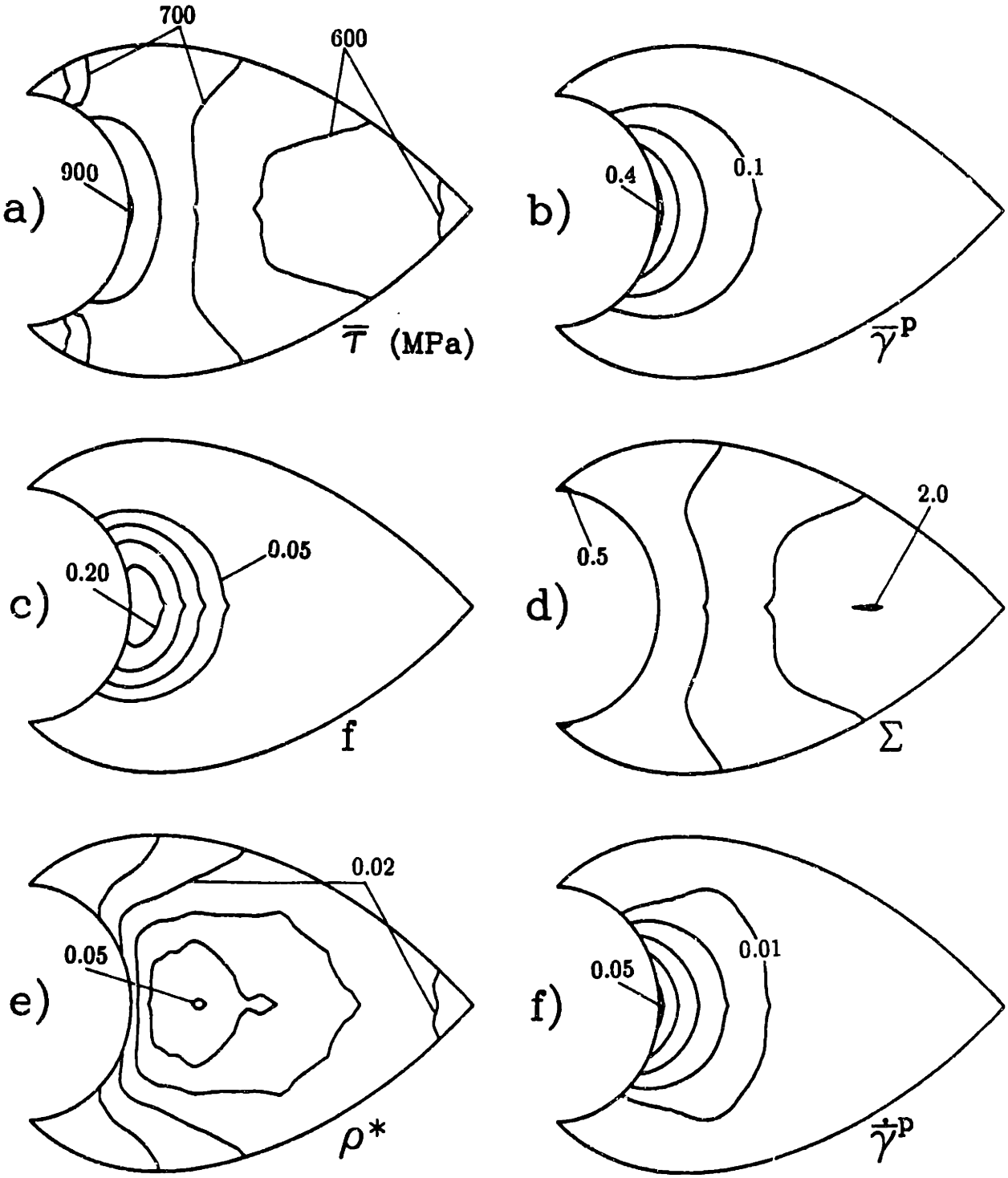

Figure 5.29 Contours of scalar fields for the *transforming* case ($T = 448K$), for $b/b_0 = 1.065$. (a) equivalent shear stress, $\bar{\tau}$; (b) equivalent plastic shear strain, $\bar{\gamma}^p$; (c) martensite volume fraction, f (d) triaxiality, Σ; (d) void volume fraction, ρ^*, and (e) equivalent plastic shear strain rate, $\dot{\bar{\gamma}}^p$ (reference strain rate, in consistent units, is $\dot{\gamma}_0 = 0.007$).

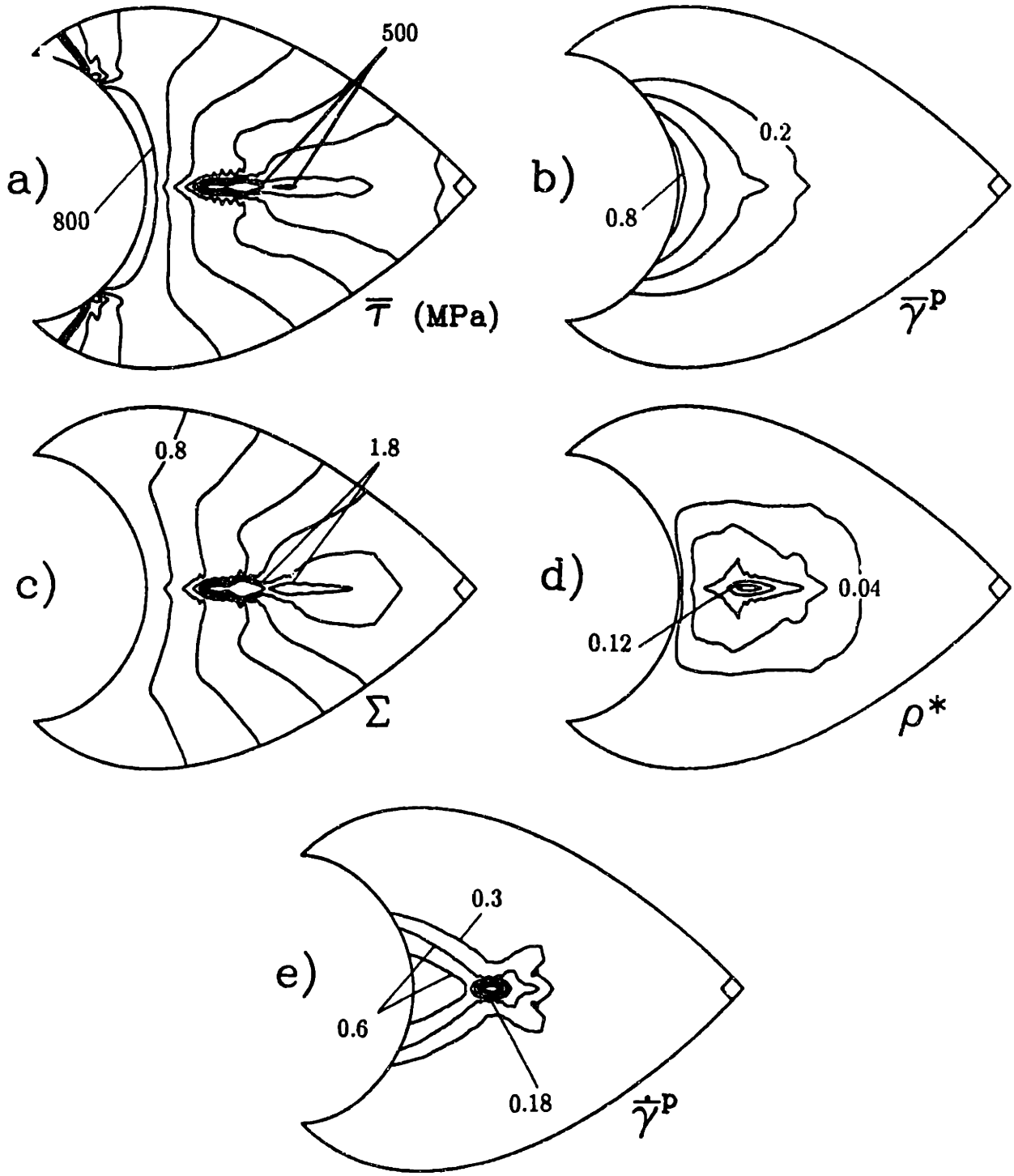

Figure 5.30 Contours of scalar fields for the *nontransforming* case, for $b/b_0 = 1.24$. (a) equivalent shear stress, $\overline{\tau}$; (b) equivalent plastic shear strain, $\overline{\gamma}^p$; (c) triaxiality, Σ; (d) void volume fraction, ρ^*, and (e) equivalent plastic shear strain rate, $\dot{\overline{\gamma}}^p$ (reference strain rate, in consistent units, is $\dot{\gamma}_0 = 0.007$).

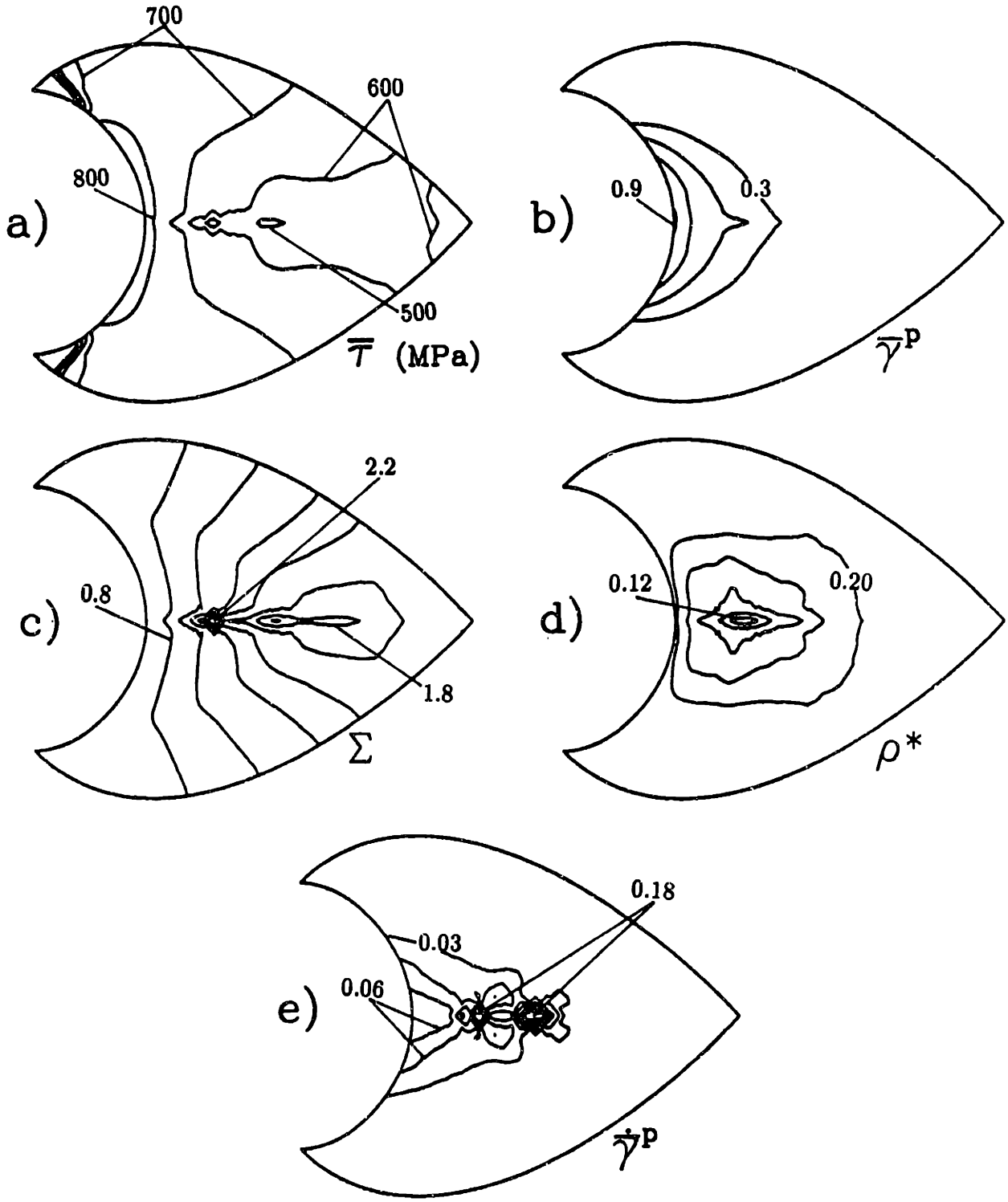

Figure 5.31 Contours of scalar fields for the *nontransforming* case, for $b/b_0 = 1.245$. (a) equivalent shear stress, $\overline{\tau}$; (b) equivalent plastic shear strain, $\overline{\gamma}^p$; (c) triaxiality, Σ; (d) void volume fraction, ρ^*, and (e) equivalent plastic shear strain rate, $\dot{\overline{\gamma}}^p$ (reference strain rate, in consistent units, is $\dot{\gamma}_0 = 0.007$).

Figure 5.32 Experimental observation of crack propagation in a slow bend test of a Charpy V-notch specimen of A4340 [151].

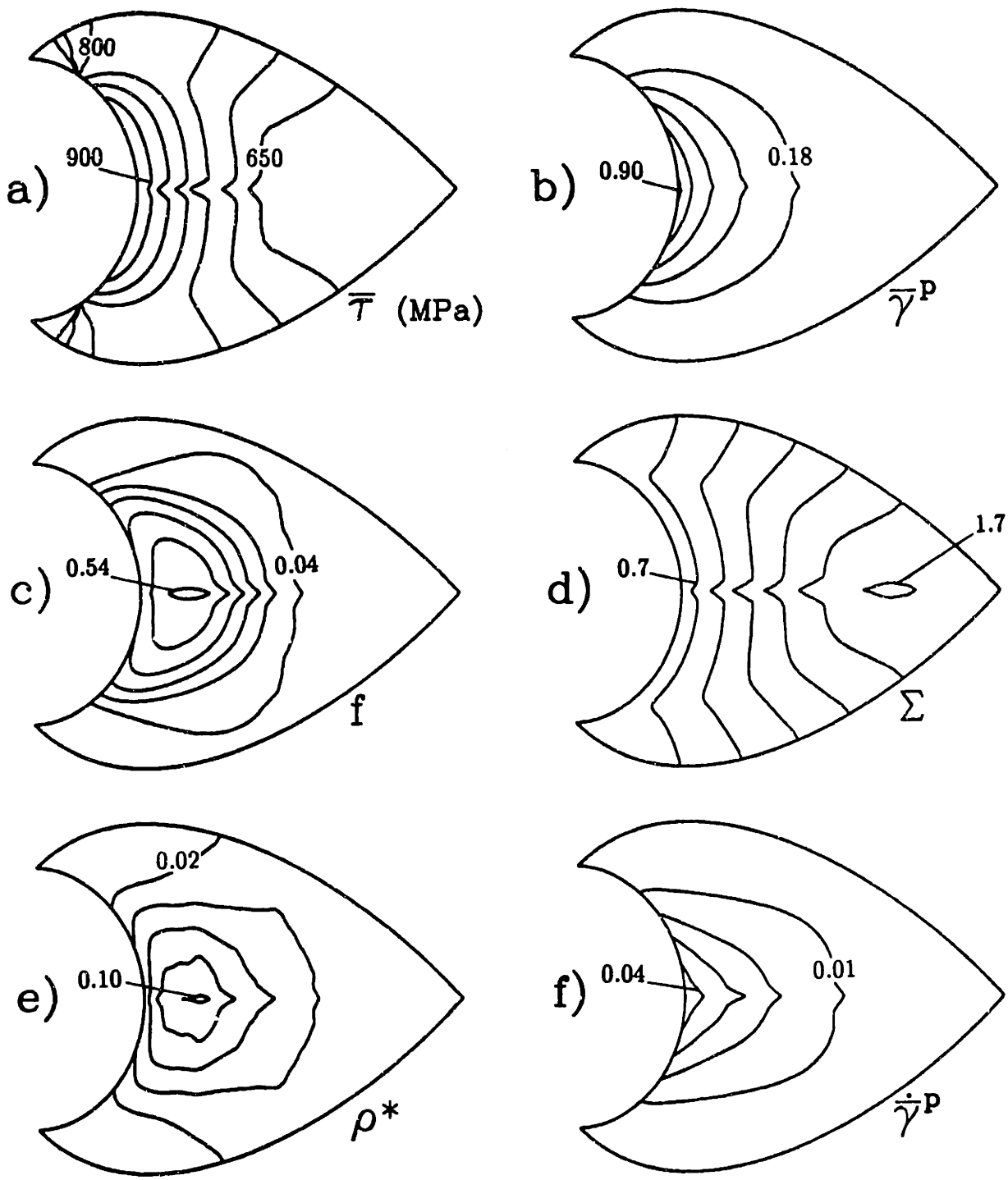

Figure 5.33 Contours of scalar fields for the *transforming* case ($T = 448K$), for $b/b_0 = 1.38$. (a) equivalent shear stress, $\overline{\tau}$; (b) equivalent plastic shear strain, $\overline{\gamma}^p$; (c) martensite volume fraction, f (d) triaxiality, Σ; (d) void volume fraction, ρ^*, and (e) equivalent plastic shear strain rate, $\dot{\overline{\gamma}}^p$ (reference strain rate, in consistent units, is $\dot{\gamma}_0 = 0.007$).

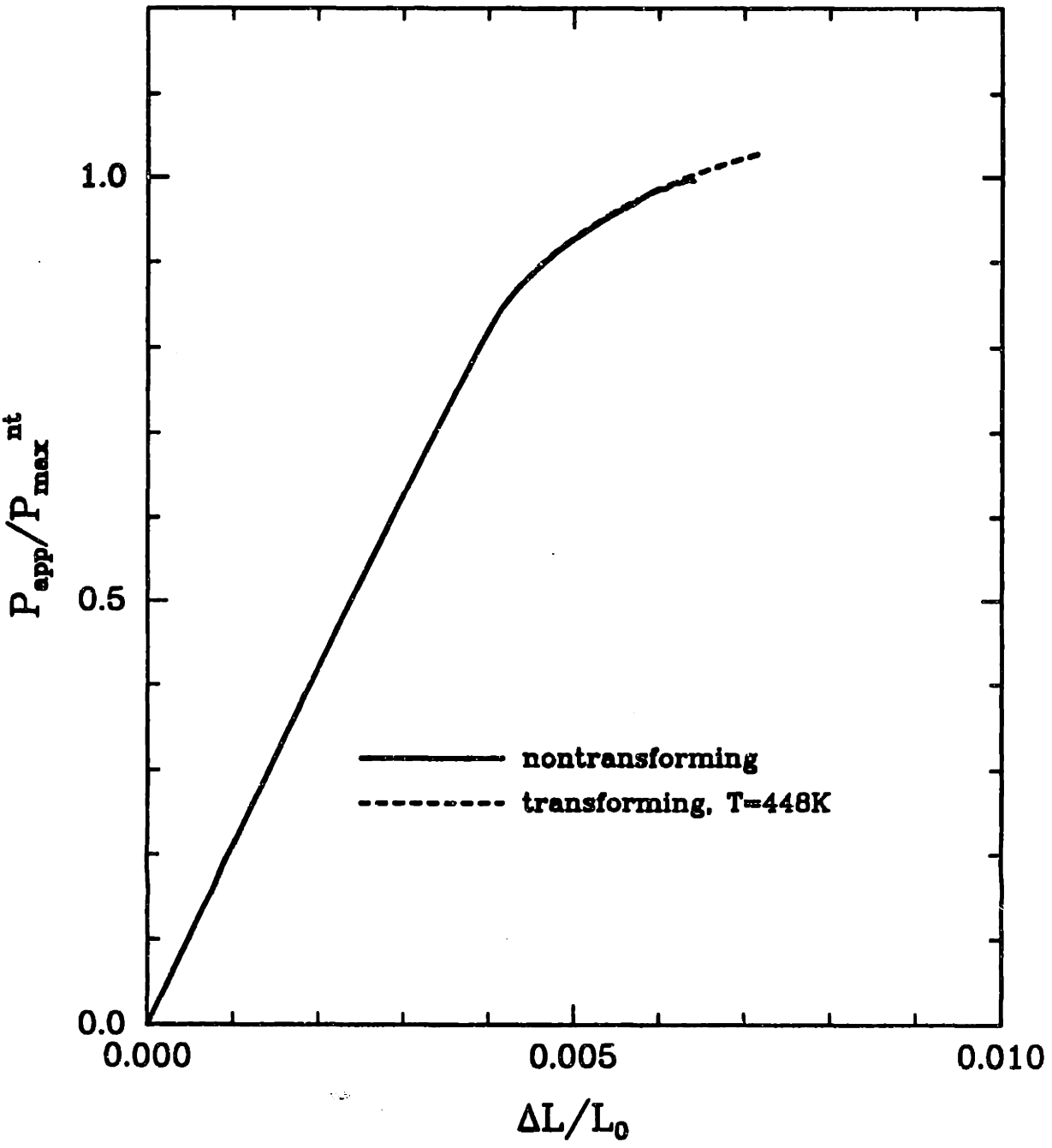

Figure 5.34 Comparison of load-displacement histories for the nontransforming and transforming ($T = 448K$) cases, sharply-notched extension problem. Here P_{app} is the applied load and P_{max}^{nt} is the maximum load for the nontransforming case.

Chapter 6

Summary and Conclusions

6.1 Introduction

The research that we have presented in this thesis has addressed two major issues concerning the mechanical behavior of metastable austenitic steels that exhibit transformation plasticity in the strain-induced temperature regime. The first part of the research, presented in chapter 3, focused on the development of a constitutive model which is able to reliably predict the behavior of these materials under various conditions, as well as on the numerical implementation of this model in conjunction with a finite element analysis program and a fitting of model material parameters to available experimental data. In the second part of the research, presented in chapters 4 and 5, we used this model for the numerical analysis of a series of boundary value problems designed to identify the mechanical sources of transformation toughening.

6.2 Constitutive Development

With regard to modeling the stress-strain behavior of these transforming materials, we found that incorporation of the stress-state sensitivity of the transformation kinetics into our constitutive model is essential for providing an accurate description of material behavior for a representative set of stress states. The results presented in chapters 4 and 5 show that the triaxiality-dependence of the strain-induced marten-

sitic transformation is a feature which plays a fundamental role in transformation toughening.

A substantial portion of the constitutive modeling effort focused on the implementation of an improved method for partitioning the strain between the constituent phases of the composite, accounting for the transformation strain as well, so as to produce self-consistent estimates of composite behavior.

Although the physical interpretation of the self-consistent method that we presented is still open to debate, it nonetheless leads to model predictions that are in reasonable agreement with experimental data and, of equal importance, it results in a constitutive integration scheme that is relatively robust, given its complexity. The general nature of the model makes it suitable not only for studying the special class of transforming materials upon which we have focused our research, but also for other isotropic multi-phase materials. As an example, with the recent oil crisis, there is an ever-increasing demand for lightweight materials to be used in the production of automobile body panels; one of the materials under study for this purpose is a *triple-phase* steel containing a retained metastable austenite phase. Because of its stiffness, such a material can result in thin body panels that, remarkably, are lighter than those made of plastic. The model presented in chapter 3 can be easily modified to simulate the behavior of these triple phase steels so that, through quantitative analysis, critical questions regarding the forming limits of these materials, as well as other related problems, can be addressed.

One issue that still must be resolved is the *degree* of the stress-state sensitivity of transformation kinetics. As we noted in chapter 3, the form that we have chosen for the driving force parameter, g, in which stress-state sensitivity enters through a linear function of triaxiality (see eq. 3.28), is an issue that requires closer scrutiny. Analysis of experimental data taken from tests where the triaxiality field is mildly varying, such as the plane strain notched-tension test that we simulated in section 5.3,

represents an excellent means for verifying the suggested triaxiality-dependence. The experimentally measured patterns of martensite formation at the macroscopic length scale provided by this geometry can be *directly* compared with model predictions. Of course, comparisons of this kind will only be worthwhile once fundamentally sound agreement between model predictions and experimental data has been attained for *fixed* triaxiality configurations, namely tension and compression tests. Each of the series of experiments conducted to date has been aimed at gaining a better understanding of a particular aspect of material behavior. As such, none of these data sets is complete to the extent that it provides data for *both* transformation kinetics *and* stress-strain behavior under various states of stress and over a wide range of temperatures. A complete data set of this sort would be invaluable from a modeling point of view. For example, with a complete data set in hand, the tensile test simulation (section 4.2) could then be used to fit tensile data in an iterative fashion: the experimental estimates of stress-strain data (*i.e.* through, say, load-displacement data coupled with a Bridgman analysis) could be compared with model predictions of stress-strain data obtained in the same manner; model parameters could then be iteratively adjusted until these two predictions are equal. An averaging of pointwise model stress-strain histories would then provide an estimate of pointwise material properties which does not suffer from the inherent limitations of a Bridgman analysis. Of course, complete data sets are not easily obtained for high toughness transforming materials, because their uniaxial properties are not necessarily remarkable (recall the tension test data of Young [7] at the higher temperatures, Fig. 3.10). In addition, the tensile properties of the martensite are also difficult to estimate, because of its brittle behavior.

A second topic related to constitutive modeling that may require further investigation is the correlation between transformation volume change and the stress-state sensitivity of transformation kinetics. Our results indicate that the extent of transformation volume change does not have a *direct* bearing on model predictions for the

state of stress and strain in the composite, yet the data of Young [7] show a strong correlation between toughening and transformation volume change. We argue that the effects of transformation volume change are indirectly accounted for in the model through the magnitude of the coefficient multiplying the triaxiality term of the probability argument (g_2) in (3.28) and the noted correspondence between volume change and stress-state sensitivity. The positive correlation between transformation volume change and toughness suggested by the data of Young and the further correlation between transformation volume change and the stress-state sensitivity of transformation kinetics needs to be better quantified.

The interaction of continuum models for void nucleation and growth with strain-induced transformation plasticity is another issue that could be further explored. The methods that we have presented in this thesis for incorporating void nucleation and growth into the model do not, for example, account for the interaction of transformation dilatation with the void nucleation and growth process. Given the already complex nature of the constitutive model, it might be difficult to account for this interaction in a precise manner without sacrificing the numerical soundness of the constitutive integration procedure. It would be interesting, however, to incorporate such changes and assess the extent to which transformation dilatation affects model predictions.

Finally, a next logical step in expanding the modeling effort might be to incorporate temperature as a state variable. This would allow for studies where, for example, the possibly deleterious effects of adiabatic heating accompanying high strain-rates could be assessed. Of course, this would substantially increase the complexity of the model and consequently, the computation time.

6.3 Analysis of Transformation Toughening

We can now address the fundamental issue of transformation toughening, which primarily motivated this research. Based upon the calculations presented in chapters 4 and 5, we conclude that, in essence, the sources of transformation toughening in these materials can be traced to the observation that the mechanical features which promote void nucleation and growth, namely high strain and triaxiality, are precisely the same features that promote nucleation of martensite. Our calculations indicate that the beneficial consequences of this localized formation of martensite are twofold: (1) retardation of void nucleation through early transformation-softening, as evidenced by the reduction of normal stresses at the interface of void nucleating particles (section 4.3); (2) counteraction of the the strain-softening effects of void nucleation and growth through transformation-hardening.

With respect to the latter of these two sources, the calculations presented in chapter 5, in which the effects of void nucleation and growth were accounted for, indicate strong qualitative tendencies towards resistance to plastic flow localization for each of the boundary value problems that we considered. Although the limited number of problems and cases studied do not allow us to draw quantitative conclusions regarding the relative increase in toughness with transformation, these qualitative results are indisputable, and are consistent with both the dramatic increases in toughness and the observed failure modes. With the constitutive model in hand and with these results in mind, continued research must focus on quantifying these trends through parametric studies aimed at assessing the relative importance of critical material parameters and direct comparison with experimental data through model simulation of toughness experiments. The success of such efforts is strongly dependent on the availability of fracture toughness data for a material whose properties are well quantified.

The results of the problems presented in chapter 4 further support the notion that

transformation stabilizes plastic flow, albeit less directly. The tensile necking problem, because of its triaxiality gradients, serves as an excellent test for the constitutive model and best illustrates the macroscopic consequences of the transformation in blunting the neck and, in some cases, eventually causing neck propagation.

The particle problem illustrates the first of the above-mentioned sources of transformation toughening, namely, that transformation softening leads to a reduction of interfacial normal stresses over a wide range of far-field strain levels. Of course, as indicated in section 4.3, as transformation hardening eventually prevails, the interfacial stresses increase to values larger than those predicted for the nontransforming material. However, considering the high triaxialities that are associated with crack tip fields, it is quite likely that the void nucleation regime would coincide with the early phase of transformation softening, before the stresses increase through transformation hardening.

Two interesting problems might lend helpful insight in further evaluation of this source of toughness. In the first, a triaxial field that increases with time could be imposed. Such a problem more closely models the actual stress history that a particle near to the crack tip might encounter, and would likely reveal some beneficial features of the transformation that the constant triaxiality problems of section 4.3 might have missed, because, as we saw in the tensile necking problem, an increasing triaxiality history would delay the effects of transformation softening to higher strain levels.

A second problem of interest would consider what happens just after the void has nucleated. After the particle and matrix have first decohered, an interfacial crack forms that must "unzip" in order for the nucleation process to be complete. Because of the tremendous local transformation hardening accompanying the large interfacial strains, the state of the transforming material will be quite different from that of the nontransforming material. It is possible that the same features that lead to crack resistance at larger length scales might also lead to a stronger resistance against growth

of this interfacial crack. Because of the very small size scale involved, a solution of this problem would surely bring the applicability of the continuum approach near to its inherent limits. Nonetheless, a model and analysis of the decohesion process might prove to be revealing.

At this point, we feel reasonably confident that our analysis has indeed identified the fundamental sources of the transformation toughening in metastable austenitic steels. In addition to improving the models presented here and quantifying model predictions in an effort to contribute to the development of better alloys, future studies can now also be directed at gaining an understanding of how these remarkable materials can be best used in practical engineering applications. More specifically, with the aid of the modeling tools that are now available, it should now be possible to *design* new steels whose properties are tailored for particular applications.

REFERENCES

1. Stavehaug, F.,"Transformation Toughening of γ'-Strengthened Metastable Austenitic Steels," Ph.D. Thesis, Department of Materials Science and Engineering, MIT, Cambridge, MA, 1990.

2. Olson, G.B. and Cohen, M., in *Mechanical Properties and Phase Transformation in Engineering Materials*, Antolovich, Ritchie, Gerberich, eds., TMS-AIME, 1986, p. 367.

3. Adler, P.H. and Olson, G.B., *Acta Metall.*, **34**, 1986, p. 2053.

4. Budiansky, B., Hutchinson, J.W., Lambropoulos, J.C., *Intl. J. Solids and Structures*, **19**, 1983, p. 337.

5. Perkins, J., ed., *Shape Memory Alloys*, TMS-AIME, Warrendale, PA, 1984.

6. Leal, R.H., "Transformation Toughening of Metastable Austenitic Steels," Ph.D. Thesis, MIT, Cambridge, MA, 1984.

7. Young, C.-C., "Transformation Toughening of Phosphocarbide-Strengthened Austenitic Steels," Ph.D. Thesis, MIT, Cambridge, MA, 1988.

8. Matthews, W. T. "Plane Strain Fracture Toughness (K_{Ic}) data Handbook for Metals," Army Materials and Mechanics Research Center, Report No. AMMRC MS 73-6, 1973.

9. Puttick, K.E., *Phil. Mag.*, **4**, 1959, p. 964.

10. Rogers, H.C., *Trans. TMS-AIME*, **218**, 1960, p.498.

11. Crussard, C., in *Fracture*, Averbach, *et al.*, eds., Wiley, New York 1959, p. 524.

12. Olson, G.B., in *Innovations in Ultrahigh-Strength Steel Technology*, Olson, M. Azrin and Wright, eds., Proc. 34^{th} Sagamore Army Materials Research Conference, 1990, p. 3.

13. Stringfellow, R.G., "Mechanics of Transformation Plasticity in Metastable Austenitic Steels," Master's Thesis, MIT, Cambridge, MA, 1988.

14. Olson, G.B. and Azrin, M., *Metall. Trans.*, **9A**, 1978, p. 713.

15. McClintock, F.A., *J. Appl. Mech*, **35**, 1968, p. 362.

16. Rice, J.R. and Tracey, D.M., *J. Mech. Phys. Solids*, **17**, 1969, p. 201.

17. Hancock, J.W. and MacKenzie, A.C., *J. Mech. Phys. Solids*, **24**, 1976, p. 147.

18. MacKenzie, A.C., Hancock, J.W. and Brown, D.K., *Eng. Fract. Mech.*, **9**, 1977, p. 167.

19. Hancock, J.W. and Brown, D.K., *J. Mech. Phys. Solids*, **31**, 1983, p. 1.

20. Olson, G.B. and Cohen, M., *Metall. Trans.*, **6A**, 1975, p. 791.

21. Narutani, T., Olson, G.B. and Cohen, M., *J. de Physique*, **43**, 1982, p. C4–429.

22. Needleman, A. and Tvergaard V., *J. Mech. Phys. Solids*, **35**, 1987, p. 151.

23. Needleman, A. and Rice, J.R., in *Mechanics of Sheet Metal Forming*, Koistinen and Wang, eds., Plenum Publ. Co., New York, 1978, p. 237.

24. Gurson, A.L. "Plastic Flow and Fracture Behavior of Ductile Materials Incorporating Void Nucleation, Growth and Interaction," Ph.D Thesis, Brown University, Providence, RI, 1975.

25. Gurson, A.L., *J. Eng. Mat. Tech.*, **99**, 1977, p. 2.

26. Cohen, M., Olson, G.B. and Clapp, P.C., *Proc. Intl. Conf. Mart. Transf. ICOMAT-79*, MIT, Cambridge, MA, May, 1979, p. 1.

27. Meyers, M.A. and Chawla, K.K., "Mechanical Metallurgy: Principles and Applications," Prentice Hall, Englewood Cliffs, NJ., 1984, p. 474.

28. Machlin, E.S. and Cohen, M., *Trans. AIME*, **191**, 1951, p. 1019.

29. Patel, J.R. and Cohen, M., *Acta Metall.*, **1**, 1953, p. 531.

30. Olson, G.B. and Cohen, M., *J. Less-Common Metall.*, **28**, 1972, p. 107.

31. Bolling, G.F. and Richman, R.H., *Acta Metall.*, **18**, 1970, p. 673.

32. Olson, G.B., in *Deformation, Processing, and Structure*, Krauss, ed., American Society of Metals, Metals Park, Ohio, 1983, p. 391.

33. Maxwell, P.C., Goldberg, A. and Shyne, J.C., *Metall. Trans.*, **5**, 1974, p. 1305.

34. Snell, E.O., Shyne, J.C. and Goldberg, A., *Metall.*, **10**, 1977, p. 299.

35. Venables, J.A., *Phil. Mag.*, **7**, 1962, p. 35.

36. Lagneborg, R., *Acta Metall.*, **12**, 1964, p. 823.

37. Mangonon, P.L., Jr. and Thomas, G., *Metall. Trans.*, **1**, 1970, p. 1577.

38. Suzuki, T., Kojima, H., Suzuki, K., Hashimoto, T. and Ichihara, M., *Acta Metall.*, **25**, 1977, p. 1151.

39. Murr, L.E., Staudhammer, K.P. and Hecker, S.S., *Metall. Trans.*, **13A**, 1982, p. 627.

40. Kulin, S.A., Cohen, M. and Averbach, B.L., *J. Metals*, **4**, 1952, p. 661.

41. Olson, G.B., Tsuzaki, K. and Cohen M., *Mat. Res. Soc. Symp. Proc*, **57** 1987, p. 129.

42. Porter, L.F. and Rosenthal, P.G., *Acta Metall.*, **7**, 1959, p. 504.

43. Clinard, F.W. and Sherby, O.D., *Acta Metall.*, **12**, 1964, p. 911.

44. Greenwood, G.W. and Johnson. R.H., *Proc. Roy. Soc. London*, **A283**, 1965, p. 403.

45. Magee, C.L. and Paxton, H.W., *Trans AIME*, **242**, 1968, p. 1741.

46. Kot, R.A. and Weiss, H.W., *Met Trans.*, **1**, 1970, p. 2685.

47. Brown, R.L., Rack, H.J. and Cohen, M., *Mat. Sci. Eng.*, **21**, 1975, p. 25.

48. Olson, G.B. and Hartman, H., *Proc. Intl. Conf. Mart. Transf. ICOMAT-82*, Leuven, Belgium, *J. de Physique*, **43**, 1982, p. C4-855.

49. Kurdjamov, G., Sachs, G., *Z. Phys.*, **64**, 1930, p. 325.

50. Schetky, L.M., *Sci. Am.*, **232**, 1974, p. 24.

51. Olson, G.B. and Cohen, M., *Metall. Trans.*, **13A**, 1982, p. 1907.

52. Kestenbach, H.-J. and Meyers, M.A., *Metall. Trans.*, **5**, 1974, p. 593.

53. Angel, T., *J. Iron Steel Inst.*, **177**, 1954, p. 165.

54. Garvie, R.C., Hannick, R.H. and Pascoe, R.T., *Nature*, **253**, 1975, p. 703.

55. Evans, A.G. and Heuer, A.H., *J. Amer. Cer. Soc.*, **63**, 1980, p. 241.

56. McMeeking, R,M. and Evans, A.G., *J. Amer. Cer. Soc.*, **65**, 1982, p. 242.

57. Zackay, V.F., Parker, E.R., Fahr, D. and Busch, R., *Trans. ASM*, **60**, 1967, p. 252.

58. Gerberich, W.W., Hemmings, P.L., Zackay, V.F. and Parker, E.R., *Fracture*, Chapman and Hall, Ltd., London, 1969, p. 288.

59. Antolovich, S.D. and Singh, B., *Metall. Trans.*, **2**, 1971, p. 2135.

60. Jahn, M.T., Fan, C.M. and Wan, C.M., *J. Mat. Sci.*, **20**, 1985, p. 2757.

61. Hecker, S.S., Stout, M.G., Staudhammer, K.P. and Smith, J.L., *Metall. Trans.*, **13A**, 1982, p. 619.

62. Niinomi, M., Kobayashi, T., Inagaki, I. and Thompson, A.W., *Metall. Trans.*, **21A**, 1990, p. 1733.

63. Argon, A.S., Im. J. and Safoglu, R., *Metall. Trans.*, **6A**, 1975, p. 825.

64. Gilman, J.J., in *Fracture*, Averbach, Felbeck, Hahn and Thomas, eds., Wiley, New York, 1959, p. 193.

65. Argon, A.S. *J. Eng. Mat. and Tech.*, **98**, 1976, p. 60.

66. Goods, S.H. and Brown, L.M., *Acta Metall.*, 1979, **27**, p. 1.

67. Le Roy, G., Embury, J.D., Edwards, G. and Ashby, M.F., *Acta Metall.*, **29**, 1981, p. 1509.

68. Cox, T.B. and Low, J.R., *Metall. Trans.*, **5**, 1974, p. 1457.

69. Argon, A.S. and Im, J., in *Structure and Property Control Through Rapid Quenching of Liquid Metals*, Final Technical Report ARPA Contract No. DACH17-70-C-0283, MIT, Cambridge, MA, 1973.

70. Ashby, M.F. and Jones, D.R.H., *Engineering Materials: An Introduction to Their Properties and Applications*, Pergamon Press, Oxford, 1980, p. 131.

71. Van den Avyle, J. A., "Correlation of Fractography, Microstructure and Fracture Toughness Behavior of High Strength Alloys," Doctoral Thesis, Department of Materials Science and Engineering, MIT, Cambridge, MA, 1975.

72. Backofen, W.A., *Deformation Processing*, Addison Wesley, Reading MA, 1972, p. 199.

73. Hutchinson, J.W. and Neale, K.W., *J. Mech. Phys. Solids*, **31**, 1983, p. 405.

74. Wojewodzki, A.M.S., "The Plastic Flow and Fracture of Dual-phase Steels," Ph.D. Thesis, Dept. of Mat. Sci and Eng., MIT, Cambridge, MA, 1982.

75. Gurtin, M.E., *An Introduction to Continuum Mechanics*, Academic Press, New York, 1981.

76. Haezebrouck, D., private communication, 1989.

77. Grujicic, M., Olson, G.B. and Owen, W.S., *Metall. Trans.*, **16A**, 1985, p. 1713.

78. Kula, E.B. and Azrin, M., in *Advances in Deformation Processing*, Burke and Weiss, eds., Plenum Press, NY, 1978, p. 245.

79. Anand, L., *Intl. J. Plast*, **1**, 1985, p. 213.

80. Hutchinson, J.W. and Tvergaard, V. *ASTM STP-1020*, 1989, p. 61.

81. Taylor, G.I., *J. Inst. Metals*, **62**, 1938, p. 67.

82. Hershey, A.V., *J. Appl. Mech.*, **21**, 1954, p. 236.

83. Kröner, E., *Acta Metall.*, **9**, 1961, p. 155.

84. Eshelby, J.D., *Proc. R. Soc.*, **A241**, 1957, p. 376.

85. Budiansky, B. and Wu, T.T., *Proc.* 4^{th} *U.S. National Congress of Applied Mechanics*, ASME, New York, 1962, p. 1175.

86. Hill, R., *J. Mech. Phys. Solids*, **13**, 1965, p. 213.

87. Hutchinson, J.W., *Proc. R. Soc.*, **A319**, 1970, p. 247.

88. Hutchinson, J.W., *Metall. Trans.*, **8A**, 1976, p. 1465.

89. Berveiller, M. and Zaoui, A., *J. Mech. Phys. Solids*, **26**, 1979, p. 325.

90. Berveiller, M. and Zaoui, A., *Res. Mech. Let.*, **1**, 1981, p. 119.

91. Berveiller, M. and Zaoui, A., *Proc. 4th Intl. Symposium on Metals and Material Science*, Riso, 1983, p. 153.

92. Mori, T. and Tanaka, K., *Acta Metall.*, **21**, 1973, p. 571.

93. Hashin, Z. and Shtrikman, S., *J. Mech. Phys. Solids*, **11**, 1963, p. 127.

94. Tandon, G.P. and Weng, G.J., *J. Appl. Mech.*, **55**, 1988, p. 126.

95. Talbot, D.R.S. and Willis, J.R., *IMA J. Appl. Math.*, *39*, 1987, p. 215.

96. Ponte Casteñeda, P. and Willis, J.R., *Proc. R. Soc.*, **A416**, 1988, p. 217.

97. Duva, J.M., *J. Eng. Mat. Tech.*, **196**, 1984, p. 317.

98. Duva, J.M., *Mech. Mat.*, **5**, 1986, p. 137.

99. Duva, J.M. and Hutchinson, J.W., *Mech. Mat.*, **3**, 1984, p. 41.

100. Molinari, A., Canova, G.R., and Ahzi, S., *Acta Metall.*, **35**, 1987, p. 2983.

101. Chen, I.W. and Argon, A.S., *Acta Metall.*, **27**, 1979, p. 785.

102. Kocks, U.F., Argon, A.S. and Ashby, M.F., *Progress in Materials Science*, **19**, Pergamon Press, Oxford, 1975, p. 275.

103. ABAQUS user's manual, version 4.7, Hibbitt, Karlsson and Sorensen, Inc., Providence, RI, 1988.

104. Krieg, R.D. and Krieg, D.B., *J. Press. Vess. Tech.*, **99**, 1977, p. 510.

105. Tomota, Y., Kuroki, K., Mori, T., Tamura, I., *Mat. Sci. Eng.*, **24**, 1976, p. 85.

106. Grujicic, M., Erturk, T. and Owen, W.S., *Mat. Sci. Eng.*, **82**, 1986, p. 151.

107. Gilormini, P. and Germain, Y., *Intl. J. Solids Structures*, **23**, 1987, p. 413.

108. Olson, G.B., private communication, 1990.

109. Needleman, A. and Tvergaard V., *J. Mech. Phys. Solids*, **32**, 1984, p. 161.

110. Tvergaard, V., *Intl. J. Solids Structures*, **18**, 1982, p. 659.

111. Becker, R., Needleman, A., Richmond, O. and Tvergaard, V., *J. Mech. Phys. Solids*, **36**, 1988, p. 317.

112. Narasimhan, R., Rosakis, A.J. and Moran, B., California Institute of Technology Graduate Aeronautical Laboratories, Report No. SM 89-5, 1990.

113. Zavaliangos, A. and Anand, L., "Thermal Aspects of Shear Localization in Microporous Viscoplastic Solids,", submitted to *Intl. J. Num. Meth. Eng.*, 1990.

114. Tvergaard, V., *Intl. J. Fract.*, **17**, 1981, p. 389.

115. Brown, L.M. and Embury, J.D., in *The Microstructure and Design of Alloys, Proc.* 3^{rd} *Intl. Conf. on Strength of Metals and Alloys*, Cambridge, England, 1973.

116. Andersson, H., *J. Mech. Phys. Solids*, **25**, 1977, p. 217.

117. Berg, C.A., in *Inelastic Behavior of Solids*, M.F. Kanninen, W.F. Adler, A.R. Rosenfield and R.I. Jaffee, eds., McGraw-Hill, 1970, p. 171.

118. Chu, C.C. and Needleman, A., *J. Eng. Mat. Tech.*, **102**, 1980, p. 249.

119. Budiansky, B., *J. Comp. Mat.*, **4**, 1970, p. 286.

120. Bridgman, P.W., *Rev. Mod. Phys.*, **17**, 1945, p. 3.

121. Bridgman, P.W., *Studies in Large Plastic Flow and Fracture*, Harvard Press, Cambridge, MA, 1952, p. 9.

122. Davidenkov, N.N. and Spiridonova, N.I., *Proc. ASTM*, **46**, 1946, p. 1147.

123. ABAQUS theory manual, version 4.7, Hibbitt, Karlsson and Sorensen, Inc., Providence, RI, 1988.

124. Crisfield, M.A., *Comp. and Struc.*, **13**, 1981, p. 55.

125. Ramm, E., "Strategies for Tracing the Nonlinear Response Near Limit Points," *Nonlinear Finite Element Analysis in Structural Mechanics*, Wunderlich, Stein, and Bathe, eds., Springer-Verlag, Berlin, 1981.

126. Powell, G. and Simons, J., *Comp. Meth. in Appl. Mech. and Eng.*, **12**, 1981, p. 1455.

127. Goodier, J.N., *Trans. ASME, Appl. Mech.*, **55**, 1933, p. 39.

128. Thomson, R.D. and Hancock, J.W., *Intl. J. Fract.*, **24**, 1984, p. 209.

129. Needleman, A., *J. Mech. Phys. Solids*, **34**, 1986, p. 525.

130. Wilner, B. *J. Mech. Phys. Solids*, **36**, 1988, p. 141.

131. Tvergaard, V., *J. Mech. Phys. Solids*, **35**, 1987, p. 43.

132. Laszlo, F. and Nolle, H., *J. Mech. Phys. Solids*, **7**, 1959, p. 193.

133. Argon, A.S., Im, J. and Needleman, A., *Metall. Trans.*, **6A**, April, 1975, p. 815.

134. McClintock, F.A., in *Fracture, III*, Liebowitz, ed., Academic Press, New York, 1971, p. 47.

135. Rawal, S.P. and Gurland, J., *Proc. of the 2nd International Conference on Mechanical Behavior of Materials*, Federation of Materials Societies, 1976, p. 1154.

136. McMeeking, R.M., *J. Mech. Phys. Solids*," **25**, 1977, p. 357.

137. McMeeking, R.M. and Parks, D.M., in *Elastic-Plastic Fracture, ASTM STP-668*, Landes, Begley and Clarke, eds., ASTM, Philadelphia., 1979, p. 175.

138. Rice, J.R., *J. Appl. Mech.*, **35**, 1968, p. 379.

139. Griffith, A.A., *Phil. Trans. Roy. Soc. Lond.*, **A221**, 1920, p. 163.

140. Rice, J.R. and Rosengren, G.F., *J. Mech. Phys. Solids*, **16**, 1968, p. 1.

141. Hutchinson, J.W., *J. Mech. Phys. Solids*, **16**, 1968, p. 13.

142. Begley, J.A. and Landes, J.D., in *Fracture Toughness, ASTM STP-514*, American Society of Testing Materials, Phil., 1972, p. 1.

143. Rice, J.R. and Tracey, D.M., *Proc. ONR Symposium*, Fenves, Perrone, Robinson and Schnobrich, eds., Academic Press, New York, 1973, p. 585.

144. Tracey, D.M., *J. Eng. Mat.*, **98**, 1976, p. 146.

145. Rice, J.R. and Johnson, M.A., in *Inelastic Behavior of Solids*, Kanninen, Alder, Rosenfield and Jaffee, eds., McGraw-Hill, New York, 1970, p. 641.

146. Saka, W., Shoji, T. and Takahashi, H., *J. Mech. Phys. Solids*, **30**, 1982, p. 209.

147. Jagota, A., Hui, C.Y. and Dawson, P.R., *Intl. J. Fract.*, **33**, 1987, p. 111.

148. Williams, M.L., *J. Appl. Mech.*, **24**, 1957, p. 109.

149. Muskhelishvili, N.I., *Some Basic Problems of the Mathematical Theory of Elasticity, Torsion and Bending*, Fourth Edition, Moscow, 1954, translated from Russian by Radok, J.R.M., Noordhoff, P., Ltd., The Netherlands, 1963.

150. Tvergaard, V., *J. Mech. Phys. Solids*, **30**, 1982, p. 399.

151. Du, Z.-Z. and Hancock, J.W., "The Effect of Non-Singular Stresses on Crack Tip Constraint," unpublished manuscript, 1990.

152. Zia-Ebrahimi, F., Matlock, D. K. and Krauss, G., *Scripta Metall.*, **16**, 1982, p. 987.

153. Hughes, T.J.R. and Winget, J., *Intl. J. Num. Meth. Eng.*, **15**, 1980, p. 1862.

Appendix A

Numerical Implementation of the Constitutive Model

The constitutive model outlined in Chapter 3 has been incorporated into the finite element code ABAQUS [103] via a user material law subroutine. The subroutine is provided with the current level of the Kirchhoff stress, $\mathbf{T}$, and any user-defined state variables. The strain increment $\Delta\,\boldsymbol{\epsilon}$ is also provided as an estimate of the kinematic solution for the increment. The subroutine updates the stress tensor and state variables based upon this estimate.

After the integration of the material state is successfully completed, the material Jacobian, which represents the change in the increment in Kirchhoff stress with respect to a virtual change in the increment in strain, must be computed. This quantity is needed by ABAQUS in its global Newton scheme to achieve an accurate assessment of the kinematics. In order to obtain a high rate of convergence, the Jacobian should be consistent with the integration operator. This appendix will discuss the numerical integration of the material state and the computation of the Jacobian. A listing of the corresponding FORTRAN subroutine, UMAT, is given at the end of this appendix.

A.1 Numerical Integration of State

Before discussing the method by which the state equations are integrated in the UMAT subroutine, it should first be noted that since this analysis considers large deformations, the effects of finite rotations must be considered. The stress tensor, as passed into the UMAT, has already been rotated using an algorithm developed by Hughes and Winget [153]. The details of this method are not discussed in this appendix.

Let the stress tensor passed into the subroutine be $\mathbf{T_0}$. The updated stress is then given by:

$$\mathbf{T} = \mathbf{T_0} + \Delta\mathbf{T} \,. \tag{A.1}$$

The increment in stress $\Delta\mathbf{T}$ is defined to be the integral of the Jaumann stress rate tensor $\overset{\triangledown}{\mathbf{T}}$, given by:

$$\Delta\mathbf{T} = \int_t^{t+\Delta t} \overset{\triangledown}{\mathbf{T}} dt \,. \tag{A.2}$$

Using the generalized trapezoidal rule, $\Delta\mathbf{T}$ can be approximated as

$$\Delta\mathbf{T} = \phi\overset{\triangledown}{\mathbf{T}}\Delta t + (1-\phi)\overset{\triangledown}{\mathbf{T}}_0\Delta t \,. \tag{A.3}$$

We set $\phi = 1$, providing an Euler backwards difference method for which

$$\Delta\mathbf{T} = \overset{\triangledown}{\mathbf{T}}\Delta t \,. \tag{A.4}$$

The stress evolution equation was given in eq. (3.38) as:

$$\overset{\triangledown}{\mathbf{T}} = \mathcal{L}^e\left[\mathbf{D} - \mathbf{D}^p\right] \,. \tag{A.5}$$

Substituting equation (A.4) and (A.5) into (A.1) yields:

$$\mathbf{T} = \mathbf{T}_0 + \Delta t\mathcal{L}^e\left[\mathbf{D} - \mathbf{D}^p\right] \,. \tag{A.6}$$

Since $\Delta\boldsymbol{\epsilon} \doteq \mathbf{D}\Delta t$, then

$$\mathbf{T} = \mathbf{T}_0 + \mathcal{L}^e\left[\Delta\boldsymbol{\epsilon}\right] - \Delta t\mathcal{L}^e\left[\mathbf{D}^p\right] \,. \tag{A.7}$$

Within the UMAT subroutine, the first two terms on the right side of this equation can be regarded as known, as they are passed into the subroutine. The third term is given through (3.42*b*) and (3.46) as

$$\mathbf{D}^p = \frac{1}{\sqrt{2}}\dot{\bar{\gamma}}^p \mathbf{N} + \frac{1}{3}\Delta_V \dot{f}\mathbf{1} \,. \tag{A.8}$$

Adopting the method of radial-return (Krieg and Krieg [104]) that is commonly used in *rate-independent* plasticity, we assume that the updated deviatoric stress is in the same tensorial direction as the elastic predictor, $\mathbf{S}^*$, where

$$\mathbf{S}^* = (\mathbf{T}_0 + 2G\Delta\boldsymbol{\epsilon})' \,. \tag{A.9}$$

The deviatoric flow direction tensor, $\mathbf{N}$, is thus given as

$$\mathbf{N} = \frac{1}{\sqrt{2}}\left(\frac{\mathbf{S}^*}{\bar{\tau}^*}\right) \,, \tag{A.10}$$

where

$$\bar{\tau}^* = \sqrt{\frac{1}{2}\mathbf{S}^* \cdot \mathbf{S}^*} \tag{A.11}$$

represents the elastic predictor of the equivalent shear stress.

Substituting (A.8) into (A.7) and utilizing the definition of $\mathcal{L}^e$ (3.40), we find that

$$\mathbf{T} = \mathbf{T}_0 + \mathcal{L}^e\left[\Delta\boldsymbol{\epsilon}\right] - \Delta t\left[2G(\mathcal{I} - \frac{1}{3}\mathbf{1}\otimes\mathbf{1}) + K\mathbf{1}\otimes\mathbf{1}\right]\left(\frac{1}{\sqrt{2}}\dot{\bar{\gamma}}^p\mathbf{N} + \frac{1}{3}\Delta_V\dot{f}\mathbf{1}\right) \,. \tag{A.12}$$

Since $\mathbf{N}\cdot\mathbf{1} = \mathbf{0}$, (A.12) can be simplified as follows:

$$\mathbf{T} = \mathbf{T}_0 + 2G\Delta\boldsymbol{\epsilon}' - Ktr\left(\Delta\boldsymbol{\epsilon}\right) - \sqrt{2}G\dot{\bar{\gamma}}^p\Delta t\mathbf{N} - K\Delta_V\dot{f}\Delta t \,. \tag{A.13}$$

Taking advantage of the assumed material isotropy, we separate this equation into its deviatoric and hydrostatic parts, obtaining an equivalent set of equations:

$$\mathbf{S} = \mathbf{S}^* - 2G\dot{\bar{\gamma}}^p\Delta t\mathbf{N} \,; \tag{A.14}$$

$$p = p_0 - Ktr\left(\Delta\boldsymbol{\epsilon}\right) + K\Delta_V\dot{f}\Delta t \,. \tag{A.15}$$

Taking the inner product of both sides of (A.14) with $\sqrt{2}\mathbf{N}$ yields the following scalar equation:

$$\overline{\tau} = \overline{\tau}^* - G\dot{\overline{\gamma}}^p \Delta t \,. \tag{A.16}$$

If we define p^* as the elastic predictor of the pressure stress,

$$p^* = p_0 + K tr\,(\Delta\epsilon) \,, \tag{A.17}$$

then (A.15) is likewise reduced to

$$p = p^* + K\Delta_V \dot{f}\Delta t \,, \tag{A.18}$$

To complete the integration procedure, we must update the internal variables s_a, s_m and f:

$$s_a = s_{a,0} + \dot{s}_a \Delta t \,, \tag{A.19}$$

$$s_m = s_{m,0} + \dot{s}_m \Delta t \,, \tag{A.20}$$

$$f = f_0 + \dot{f}\Delta t \,, \tag{A.21}$$

where $s_{a,0}$, $s_{m,0}$, and f_0 are values of s_a, s_m and f at the beginning of the increment, respectively. Thus, the integration of state over the given strain increment requires the solution of the set of five equations (A.16, A.18 - A.21).

A.2 Solution Procedure

To facilitate the solution of this relatively convoluted series of equations, we use an iterative procedure with a bi-level structure to determine the integrated quantities $\overline{\tau}$, p, s_a, s_m and f. The set of equations (A.16, A.18 - A.21) is solved at the *outer* level of iteration. At the *inner* level, the set of three equations (3.67, 3.74) is iteratively solved in order to predict the incremental quantities $\dot{\overline{\gamma}}^p$, $\dot{s}_a$, $\dot{s}_m$ and $\dot{f}$. With the viscoelastic formalism that we have chosen, stress and strain rate are directly related through (3.61). Because of the high rate sensitivity exponents ($M \geq 100$) that are

used to model the near rate-independent materials considered here, we obtained a more robust numerical procedure by inverting the stress evolution equation (A.16) so that $\dot{\bar{\gamma}}^p$ becomes the dependent variable:

$$\dot{\bar{\gamma}}^p = \frac{\bar{\tau}^* - \bar{\tau}}{G\Delta t}. \tag{A.22}$$

At each time step, i.e., each time the subroutine is called, an estimate of the desired quantities $\dot{\bar{\gamma}}^p$, p, s_a, s_m and f is first made based upon their values at the beginning of the increment, and the calculated value of the elastic predictor, $\bar{\tau}^*$. Using these values, control is passed directly to the inner level, with $\dot{\bar{\gamma}}^p$, p, s_a, s_m and f *fixed.* At the inner level, we solve the following set of equations, equivalent to (3.66, 3.73), for the unknowns χ_a, χ_m and $\bar{s}$:

$$\Phi_1 = f\chi_m + (1-f)\chi_a + A\chi_f - 1 = 0\,, \tag{A.23}$$

$$\Phi_2 = \chi_a - \frac{5}{3} + \frac{2}{3}\frac{s_a}{\bar{s}}\chi_a^{\frac{1}{M}} = 0\,, \tag{A.24}$$

$$\Phi_3 = \chi_m - \frac{5}{3} + \frac{2}{3}\frac{s_m}{\bar{s}}\chi_m^{\frac{1}{M}} = 0\,. \tag{A.25}$$

A Newton Method is used to solve this nonlinear set of equations. The procedure is as follows:

Let $\underline{X}_{int}$ represent the vector of unknowns:

$$\underline{X}_{int} = (\chi_a, \chi_m, \bar{s})\ . \tag{A.26}$$

1. Make a reasonable guess for $\underline{X}_{int}$:

$$\underline{X}_{int}^{guess} = \underline{X}_{int}^1 = \left(\chi_a^1, \chi_m^1, \bar{s}^1\right)\ . \tag{A.27}$$

This guess will usually be equal to the value of these quantities when the inner level was previously exited.

2. Let $\underline{\hat{Z}}_{int}$ be the vector of equations:

$$\underline{\hat{Z}}_{int} = (\Phi_1, \Phi_2, \Phi_3)\ . \tag{A.28}$$

Evaluate $\hat{\boldsymbol{Z}}_{int}(\boldsymbol{X}_{int}^k)$, where $\boldsymbol{X}_{int}^k$ is the value of $\boldsymbol{X}_{int}$ at the k^{th} iteration.

3. Verify whether $\|\hat{\boldsymbol{Z}}_{int,i}\| \leq TOL_i$, where TOL_i is a set of tolerances, one for each equation.

if yes $\longrightarrow$ $\chi_a = \chi_a^k$, $\chi_a = \chi_a^k$, $\bar{s} = \bar{s}^k$

if no $\longrightarrow$ correct $\boldsymbol{X}_{int}$ as follows:

4. Solve Newton's equation:

$$\hat{\boldsymbol{Z}}_{int}^k + \left(\frac{\Delta\hat{\boldsymbol{Z}}}{\Delta\boldsymbol{X}}\right)_{int}^k \cdot \Delta\boldsymbol{X}_{int}^{k+1} = 0 \,, \tag{A.29}$$

5. Correct the vector of unknowns:

$$\boldsymbol{X}_{int}^{k+1} = \boldsymbol{X}_{int}^k + \Delta\boldsymbol{X}_{int}^{k+1} \,. \tag{A.30}$$

5. Return to step 2 with an updated $\boldsymbol{X}_{int} = \boldsymbol{X}_{int}^{k+1}$.

In the above procedure, a good estimate of $\boldsymbol{X}_{int}^1$ is important for rapid convergence of the Newton algorithm.

Using the values for χ_a, χ_m, and $\bar{s}$ which have been determined using the fixed estimates of $\dot{\bar{\gamma}}^p$, p, s_a, s_m and f, we then can calculate estimates for $\dot{\bar{\tau}}$ and $\dot{p}$ according to (3.80, 3.81). Other quantities of interest are evaluated as follows:

$$\dot{\gamma}_a = \chi_a \dot{\bar{\gamma}}^p \,, \tag{A.31}$$

$$\dot{\gamma}_m = \chi_m \dot{\bar{\gamma}}^p \,, \tag{A.32}$$

$$\dot{\Sigma} = \Sigma\left(\frac{\dot{p}}{p} - \frac{\dot{\bar{\tau}}}{\bar{\tau}}\right) \,, \tag{A.33}$$

$$\dot{f} = A_f \dot{\gamma}_a + B_f \dot{\Sigma} \tag{A.34}$$

$$\dot{s}_a = h_a \dot{\gamma}_a \,, \tag{A.35}$$

$$\dot{s}_m = \frac{f - df}{f}(h_m \dot{\gamma}_m) + \frac{df}{f\Delta t}(s_{tm} - s_{m,0}) \,, \tag{A.36}$$

where

$$s_{tm} = s_m^* (\gamma_m^* + \gamma_a)^{n_m} \,. \tag{A.37}$$

Note that (A.37) and (A.38) model the running average of prior-formed martensite and the inherited structure of newly-formed martensite, which, as discussed in section 3.4.5, behaves as if it had been exposed to the austenite strain (γ_a).

Control is then returned to the outer level, where the following set of equations, which are a restatement of (A.18 - A.22), is solved:

$$\Psi_1 = \dot{\bar{\gamma}}^p - \frac{\bar{\tau}^* - \bar{\tau}}{G\Delta t} = 0 , \tag{A.38}$$

$$\Psi_2 = p - p^* + K\Delta_V \dot{f}\Delta t = 0 , \tag{A.39}$$

$$\Psi_3 = s_a - s_{a,0} - \dot{s}_a\Delta t = 0 , \tag{A.40}$$

$$\Psi_4 = s_m - s_{m,0} - \dot{s}_m\Delta t = 0 , \tag{A.41}$$

$$\Psi_5 = f - f_0 - \dot{f}\Delta t = 0 . \tag{A.42}$$

The Newton procedure outlined in (A.29 - A.33) is used at this level as well. Here, we define $\underline{X}_{out} = (\dot{\bar{\gamma}}^p, p, s_a, s_m, f)$ and $\underline{\hat{Z}}_{out} = (\Psi_1, \Psi_2, \Psi_3, \Psi_4, \Psi_5)$. We first evaluate (A.38–A.42). If any of the $\|\underline{\hat{Z}}_{out,i}\|$ exceed TOL_i, a new estimate for $\underline{X}^k_{out,i} = (\dot{\bar{\gamma}}^{p,k}, p^k, s^k_a, s^k_m, f^k)$ is calculated using the 5×5 matrix of derivatives $(\Delta\underline{\hat{Z}}/\Delta\underline{X})_{out}$. We will not explicitly write out each of the 25 terms in this appendix. They are given in the DERIVATIVES routine of UMAT. We note, however, that the calculation of this matrix is greatly simplified by using terms that have already been calculated for the inner level derivative matrix, $(\Delta\underline{\hat{Z}}/\Delta\underline{X})_{in}$. The inner level is then entered again with the corrected set of unknowns $\underline{X}^{k+1}_{out}$. After k iterations, we ultimately want

$$\|\underline{\hat{Z}}_{out}\| = \| \left(\Psi^k_1, \Psi^k_2, \Psi^k_3, \Psi^k_4, \Psi^k_5\right) \| \leq TOL_i . \tag{A.43}$$

Numerical problems can be encountered in solving this convoluted set of equations. The foremost of these problems involves the prediction of $\dot{\bar{\gamma}}^p$. If the first guess for $\underline{X}_{out}$ is not an accurate one, it is possible that a subsequent prediction for $\dot{\bar{\gamma}}^p$ will be negative, rendering the solution of the equations by standard Newton techniques practically impossible. This situation can, for example, be encountered when ABAQUS's prediction for $\Delta\epsilon$ is much different than its previous one, which often happens when solving boundary value problems that have steep gradients in stress and strain fields. To accommodate these difficulties, the Newton procedure is modi-

fied when this situation is encountered. More specifically, the updating of the vector X_{out} is underrelaxed.

A.3 Incorporation of Void Nucleation and Growth

The softening due to void nucleation and growth (section 3.7) has been incorporated into the numerical procedure in a straightforward manner. In order to minimize the impact on our already complex model, we account for the effects of void volume fraction based upon the value of ρ^* at the beginning of the increment. Within our bi-level structure, we use the self-consistent model at the inner level to calculate the matrix equivalent shear stress $\overline{\tau}_M$ as a function of the matrix shear strain rate $\dot{\overline{\gamma}}^p_M$. At the outer level, we use (3.91) and (3.97) to predict $\overline{\tau}$ and $\dot{\overline{\gamma}}^p$ as functions of $\overline{\tau}_M$ and the values of ρ^*, Z_1 and Z_2 at the beginning of the increment. We then update ρ^*, Z_1 and Z_2 based upon end-of-increment values of $\overline{\gamma}^p$, $\overline{\tau}$, *etc.* Additionally, beginning-of-increment values for G and K are calculated as functions of ρ^* and matrix parameters G_M and K_M (see 3.103, 3.104) and used throughout the procedure.

A.4 Calculation of the Jacobian

When the outer loop conditions are finally satisfied, the solution is known and the stress tensor can be updated. The Jacobian matrix must then calculated. The Jacobian, $\mathcal{J}$, is the fourth order tensor obtained by finding the change in the increment in Kirchhoff stress, $\mathbf{T}$, with respect to a virtual change in the increment in strain:

$$\mathcal{J} = \frac{d\Delta\mathbf{T}}{d\Delta\boldsymbol{\epsilon}} \,. \tag{A.44}$$

The calculations which lead to the final form of the Jacobian are straightforward, but somewhat lengthy, and for brevity will not be given here. Detailed calculations are given in Zavaliangos and Anand [114]. The final form of Jacobian is as follows:

$$\mathcal{J} = C_1\mathcal{I} + C_2\mathbf{1}\otimes\mathbf{1} + C_3\mathbf{N}\otimes\mathbf{N} + C_4\mathbf{N}\otimes\mathbf{1} + C_5\mathbf{1}\otimes\mathbf{N} \,, \tag{A.45}$$

The C_i are given by:

$$C_1 = 2\tilde{G}\,, \tag{A.46}$$

$$C_2 = Kd_{22} - \frac{1}{3}C_1\,, \tag{A.47}$$

$$C_3 = 2gd_{11} - C_1\,, \tag{A.48}$$

$$C_4 = -2Gd_{21}\,, \tag{A.49}$$

$$C_5 = -Kd_{12}\,, \tag{A.50}$$

where

$$\tilde{G} = G\frac{\overline{\tau}}{\overline{\tau}^*}. \tag{A.51}$$

and

$$d_{11} = \frac{\Delta\overline{\tau}}{\Delta\overline{\tau}^*}\,, \tag{A.52}$$

$$d_{12} = \frac{\Delta\overline{\tau}}{\Delta p^*}\,, \tag{A.53}$$

$$d_{21} = \frac{\Delta p}{\Delta\overline{\tau}^*}\,, \tag{A.54}$$

$$d_{22} = \frac{\Delta p}{\Delta p^*}\,. \tag{A.55}$$

Using the form (A.46) for the Jacobian, the unknowns d_{ij} can be obtained directly from the inverse of the derivative matrix $(\Delta\hat{\underline{Z}}/\Delta\underline{X})^{-1}_{out}$ calculated for the Newton-Raphson solution of the outer level set of equations (A.38 – A.42): For example, it can easily be shown that

$$d_{11} = \frac{\Delta\overline{\tau}}{\Delta\overline{\tau}^*} = 1 - \left(\frac{\Delta\hat{Z}_1}{\Delta X_1}\right)^{-1}_{out}\,. \tag{A.56}$$

All the d_{ij} are defined at the end of the SINT routine of UMAT.

A.5 UMAT Subroutine Listing

The FORTRAN code listed on the following pages performs the operations outlined in this appendix. It is written for use with ABAQUS version 4.7 but it can readily be

modified for use with other versions. The program contains includes several checks on the convergence of the numerical procedure. If numerical problems are encountered, the subroutine PAUSES, and the routine CHECKINP writes the current state of the program along with program input to the ABAQUS data file. This data can be used in conjunction with the DRIVER program (see Appendix B) to isolate the source of the error.

```
C**********************************************************************
C**********************************************************************
C
C                       SUBROUTINE UMAT
C
C  This UMAT uses the self-consistent method to integrate the
C  stress in a metastable austenite which undergoes a
C  strain-induced transformation to martensite and also
C  exhibits porosity.
C
C**********************************************************************
C**********************************************************************

      SUBROUTINE UMAT(STRESS,STATEV,DDSDDE,
     + SSE,SPD,SCD,
     + RPL,DDSDDT,DRPLDE,DRPLDT,
     + STRAN,DSTRAN,TIME,DTIME1,TEMP,DTEMP,PREDEF,DPRED,CMNAME,
     + NDI1,NSHR1,NTENS1,NSTATV,PROPS,NPROPS,COORDS,DROT)
      INCLUDE 'finalcom12'
      CHARACTER*8 CMNAME
      DIMENSION STRESS(4),STATEV(19),
     + DDSDDE(4,4),AUGRN(4),
     + DDSDDT(4),DRPLDE(4),
     + STRAN(4),DSTRAN(4),PREDEF(1),DPRED(1),
     + PROPS(27),COORDS(3),DROT(3,3)

C**********************************************************************
C
C     initialize variables
C
C**********************************************************************

      DATA GAMMA,GAMMAO,DELGAM,F,FO,TAUSTAR,PSTAR,BETA,PRESS,PROB,
     + PROBO,EPVI,EPVIO,TAUO,S1,S2,PPHI,DG,X,ESF,C1,C2,C3,C4,C5,
     + G10,G20,FVSTRO,FVSTR,FVGO,FVG,FV,CEI1,CEI2,SB/
     + 35*0.0D0/

      DATA FVCRIT,FVFRACT,FVULT/
     + 0.15D0,0.25D0,0.666667D0/

C**********************************************************************
C
C     initialize constants
C
C**********************************************************************

      DATA ZERO,THIRD,HALF,ONE,TWO,THREE,PI,FIVE,TEN,FIFTEEN,SQRT2,
     + SQRT3,DSQRT2,DSQRT3,ONEPT5/
     + 0.0D0,0.33333333333333333D0,0.5D0,1.0D0,2.0D0,3.0D0,
     + 3.1415926535897900,5.0D0,10.0D0,15.0D0,1.41421356D0,
     + 1.7320081457D0,0.707106781470D0,0.57735026900,1.5D0/

C**********************************************************************
C
C     set tolerances
C
C**********************************************************************

      DATA TOL1,TOL2,TOL3,TOL4,TOLPHI0,TOLPHI1,TOLPHI2,TOLPHI3,
     + SMPHI1,SMPHI2,SMPHI3,FTOL,TOL10,TOL20,TOL30,TOL40,TOL50,TOL/
     + 1.0D-4,1.0D-4,1.0D-4,1.0D-3,1.0D-5,1.0D-8,1.0D-06,1.0D-5,
     + 1.0D-11,1.0D-09,1.0D-09,1.0D-6,1.0D-7,1.0D-6,1.0D-6,1.0D-6,
     + 1.0D-7,1.0D-20/

C**********************************************************************
C
C     initialize arrays
C
C**********************************************************************

      DO 99 I = 1,19
99    STATEVO(I) = STATEV(I)
      DO 199 I = 1,4
199   DSTRAO(I) = DSTRAN(I)
      DO 299 I = 1,4
299   STRESSO(I) = STRESS(I)


C**********************************************************************
C
C     initialize material parameters
C
C**********************************************************************

      KAPPAMAT    = PROPS(1)
      MUMAT       = PROPS(2)
      ESF         = PROPS(3)
      EM1         = PROPS(4)
      EM2         = PROPS(5)
      S1R         = PROPS(6)
```

```
      S2R         =  PROPS(7)
      G1R         =  PROPS(8)
      G2R         =  PROPS(9)
      ALPHA       =  PROPS(10)
      DELV        =  PROPS(11)
      XB          =  PROPS(12)
      XI          =  PROPS(13)
      BETAO       =  PROPS(14)
      T           =  PROPS(15)
      IO          =  PROPS(16)
      I1          =  PROPS(17)
      I2          =  PROPS(18)
      EN          =  PROPS(19)
      GDO         =  PROPS(20)
      AO1         =  PROPS(21)
      AO2         =  PROPS(22)
      ANUCL       =  PROPS(23)
      GDMEAN      =  PROPS(24)
      GDSTD       =  PROPS(25)
      SNMEAN      =  PROPS(26)
      SNSTD       =  PROPS(27)

      DT = DTIME1
      IF (KITGEN.EQ.1) THEN
        DT = DT/100.0D0
      ENDIF

      PMULT       =  ONE/(SI*DSQRT(TWO*PI))
      ENF1        =  ENF - ONE
      ENF2        =  ENF - TWO
      EN11        =  EN1 - ONE
      EN21        =  EN2 - ONE
      ENM1        =  EN - ONE
      ENI         =  ONE/EN
      ENI1        =  ENI - ONE
      NTENS = NTENS1
      NDI   = NDI1
      NSHR  = NSHR1
      NDIP11      =  NDI + 1

C*****************************************************************
C
C     initialize state variables
C
C*****************************************************************

IF (STATEV(2).LE.ZERO) THEN
  STATEV(1)   =  ZERO
  STATEV(2)   =  ZERO
  STATEV(3)   =  ZERO
  STATEV(4)   =  ZERO
  STATEV(5)   =  ZERO
  STATEV(6)   =  THIRD
  STATEV(7)   =  ZERO
  STATEV(8)   =  ZERO
  STATEV(9)   =  ZERO
  STATEV(10)  =  ZERO
  STATEV(11)  =  ZERO
  STATEV(12)  =  ZERO
  STATEV(13)  =  ZERO
  STATEV(14)  =  ZERO
  STATEV(15)  =  ZERO
  STATEV(16)  =  ZERO
  STATEV(17)  =  ZERO
  STATEV(18)  =  ZERO
  STATEV(19)  =  ZERO
END IF

FO          =  STATEVO(1)
TAUO        =  STATEVO(2)
GAMMAO      =  STATEVO(3)
G1O         =  STATEVO(4)
G2O         =  STATEVO(5)
SIGMA       =  STATEVO(6)
ENVIO       =  STATEVO(7)
PROBO       =  STATEVO(8)
S1O         =  STATEVO(9)
S2O         =  STATEVO(10)
FVO         =  STATEVO(11)
FVSTRO      =  STATEVO(12)
FVGO        =  STATEVO(13)
FDOTO       =  STATEVO(14)
GAMDOTO     =  STATEVO(15)
COEFF1O     =  STATEVO(16)
COEFF2O     =  STATEVO(17)
TAUHATO     =  STATEVO(18)
SIGDOTO     =  STATEVO(19)

AO  = AO1 + AO2*(TAUO/S1R)
```

```
      CALL ELASTICITY

C*****************************************************************************
C
C     integrate stress
C
C*****************************************************************************

      DO 20 I = 1,4
        STRESS(I)  = ZERO
20    CONTINUE

      CALL SINT(NTENS1,NDIP11,NDI1,DSTRAN,STRESS,STATEV,ANORM)

C*****************************************************************************
C
C     update jacobian
C
C*****************************************************************************

      IF (INUMEROPT.LE.ZERO.AND.KITGEN.NE.1) THEN
        PERTURB    = 1.0D8
           CALL JACOBSUM(NTENS1,NDI1,NDIP11,PERTURB,STATEV,STRESS,
     +       DSTRAN,DDSDDE,ANORM)
      ELSE
           CALL JACOBANAL(NTENS1,NDI1,NDIP11,DDSDDE,ANORM)
      ENDIF

C*****************************************************************************
C
C     output state variables
C
C*****************************************************************************

      STATEV(1)   = F
      STATEV(2)   = TAU
      STATEV(3)   = GAMMA
      STATEV(4)   = G1
      STATEV(5)   = G2
      IF (TAU.GT.ZERO) THEN
      STATEV(6)   = -DSQRT3*PRESS/TAU
      ELSE
      STATEV(6)   = THIRD
      ENDIF
      STATEV(7)   = ENVI
      STATEV(8)   = PROB
      STATEV(9)   = S1
      STATEV(10)  = S2
      STATEV(11)  = FV
      STATEV(12)  = FVSTR
      STATEV(13)  = FVG
      STATEV(14)  = FDOT
      STATEV(15)  = GAMDOT
      STATEV(16)  = COEFF1
      STATEV(17)  = COEFF2
      STATEV(18)  = TAUHAT
      STATEV(19)  = SIGDOT

      RETURN
      END


C*****************************************************************************
C*****************************************************************************
C
C                        SUBROUTINE SINT
C
C     In this subroutine, the stress tensor is integrated.
C
C*****************************************************************************
C*****************************************************************************

      SUBROUTINE SINT(NTENS1,NDIP11,NDI1,DSTRAN,STRESS,STATEV,ANORM)
      INCLUDE 'finalcom12'
      DIMENSION DSTRAN(4),STATEV(19),STRESS(4),TOTDEV(4),ANORM(4),
     +  DSTRANDEV(4),B3(3,3)
      DATA H,HP,H,HP/4*3/

      TAUSTAR = ZERO
      PSTAR   = ZERO

C*****************************************************************************
C
C     if zero strain increment, return elastic jacobian
C
C*****************************************************************************

      IF (ABS(DSTRAN(1)).LT.TOL.AND.ABS(DSTRAN(2)).LT.TOL.AND.
     +   ABS(DSTRAN(3)).LT.TOL.AND.ABS(DSTRAN(4)).LT.TOL) THEN
        C1 = TWO*MU
```

```
        C2 = KAPPA - C1*THIRD
        C3 = ZERO
        C4 = ZERO
        C5 = ZERO
        DO 5 I = 1,4
5       ANORM(I) = ZERO
        RETURN
      ENDIF

C*****************************************************************************
C
C     calculate deviatoric terms, equivalent terms
C
C*****************************************************************************

      CALL SINV(DSTRAN,SINV1,SINV2)
      CALL SINV(STRESSO,SINV1,SINV2)
      PRESSO = -SINV1

      DO 30 J = 1,NDI
        DSTRANDEV(J) = DSTRAN(J) - SINV1
        STRESS(J) = STRESSO(J) - SINV1
30    CONTINUE
      DO 40 J = NDIP11,NTENS
        DSTRANDEV(J) = DSTRAN(J)
        STRESS(J) = STRESSO(J)
40    CONTINUE
      DO 50 J = 1,NDI
        TOTDEV(J) = STRESS(J) + TWO*MU*DSTRANDEV(J)
        TAUSTAR = TAUSTAR + TOTDEV(J)*TOTDEV(J)
50    CONTINUE
      DO 60 J = NDIP11,NTENS
        TOTDEV(J) = STRESS(J) + MU*DSTRANDEV(J)
        TAUSTAR = TAUSTAR + TWO*TOTDEV(J)*TOTDEV(J)
60    CONTINUE
      TAUSTAR = DSQRT(TAUSTAR)

C*****************************************************************************
C
C     at this point, TAUSTAR is actually equal to old STOT, so ANORM
C     will be a true normal ==> stress(i) = [TAU/sqrt(2) ] *ANORM(i)
C
C*****************************************************************************

      DO 110 J = 1,NTENS
        ANORM(J) = TOTDEV(J)/TAUSTAR
110   CONTINUE
      TAUSTAR = TAUSTAR*DSQRT2
      GDTOT   = (TAUSTAR-TAUO)/(MU*DT)
      Y = S1R*(G1R**EN1)
      PSTAR = PRESSO - KAPPA*SINV1/THIRD
      PRESS = PSTAR

C*****************************************************************************
C
C     integration procedure
C
C
C     if FIRST STEP -- determine constants for elastic Jacobian
C     routine, initialize state variables and RETURN.
C
C     or ...
C
C     if TAUSTAR/S1O is too small and void volume fraction is
C     small, causing GAMDOT to be too small, then assume step
C     is elastic
C
C*****************************************************************************

      IF (S1O.NE.ZERO) THEN
        RATIO = TAUSTAR/S1O
      ELSE
        RATIO = HALF
      ENDIF

      IF (TAUO.EQ.ZERO) THEN
        C1 = TWO*MU
        C2 = KAPPA - C1*THIRD
        C3 = ZERO
        C4 = ZERO
        C5 = ZERO
        DO 120 J = 1,4
          ANORM(J) = ZERO
120     CONTINUE
        ENVI = ZERO
        PROB = ZERO
        GAMMA = ZERO
        GAMDOT = ZERO
        F = ZERO
        FVSTR = ZERO
```

```
      FVG = ZERO
      FV  = ZERO
      DF = ZERO
      FDOT = ZERO
      S1 = S1R*(G1R**EN1)
      S2 = S2R*(G2R**EN2)
      G1 = ZERO
      G2 = ZERO
      TAU = TAUSTAR
      PRESS = PSTAR

    DO 130 J = 1,NTENS
130 STRESS(J) = TOTDEV(J)
    DO 140 J = 1,NDI
140 STRESS(J) = STRESS(J) - PRESS
      RETURN
    ENDIF

    IF ((RATIO.LT.HALF.AND.FVO.LT.0.10).OR.
   +  (RATIO.LT.0.700D0.AND.TAUSTAR.GT.TAUO.AND.FVO.LT.0.10)) THEN
      C1 = TWO*MU
      C2 = KAPPA - C1*THIRD
      C3 = ZERO
      C4 = ZERO
      C5 = ZERO
      DO 121 J = 1,4
        ANORM(J) = ZERO
121   CONTINUE
      ENVI = ENVIO
      PROB = PROBO
      GAMMA = GAMMAO
      GAMDOT = ZERO
      F = FO
      FVSTR = FVSTRO
      FVG = FVGO
      FV = FVO
      DF = ZERO
      FDOT = ZERO
      S1 = S10
      S2 = S20
      G1 = G10
      G2 = G20
      TAU = TAUSTAR
      PRESS = PSTAR
      DO 131 J = 1,NTENS
131   STRESS(J) = TOTDEV(J)
      DO 141 J = 1,NDI
141   STRESS(J) = STRESS(J) - PRESS
      RETURN
    ENDIF

C**********************************************************************
C
C     determine one-dimensional estimate of TAU, GAMDOT, F, S1, S2
C
C**********************************************************************

    NTAU = 0

    NTAU = NTAU + 1
    IF (NTAU.GT.100) THEN
    CALL CHECKISP
    PAUSE 'NTAU TOO BIG'
    ENDIF

    H10 = S10*EN1/( (S10/S1R)**(ONE/EN1) )
    IF (FVO.GT.0.95D0*FVFRACT) H10 = ZERO
    SBAR  = S20*FO + (S10*GAMDOT*DT*H10)*(ONE - FO)
    AA = DLOG(GDO*MU*DT) - EN*DLOG(SBAR)
    XP = ONE/EN
    XP1 = (ONE/EN) - ONE
    TAU = TAUO + 0.95D0*(TAUSTAR-TAUO)
    IF (TAUSTAR.LT.TAUO) THEN
      TAU = TAUSTAR - 0.001D0*(TAUO - TAUSTAR)
    ENDIF
810 TAU1 = TAU

    PHI1 = XP*DLOG(TAUSTAR - TAU) - XP*AA
    PHI1 = DEXP(PHI1)
    PHIO = TAU - PHI1
    IF(ABS(PHIO).LT.TOLPHIO.OR.(TAUSTAR-TAU).LT.TOLPHIO) GOTO 820
      DELPHI1 = XP1*DLOG(TAUSTAR- TAU) - XP1*AA-AA + DLOG(XP)
      DELPHI1 = DEXP(DELPHI1)
      DELPHIO = ONE + DELPHI1
      DELTAU = - PHIO/DELPHIO
      TAU = TAU + DELTAU
      IF (TAU.GT.TAUSTAR) TAU = TAU1 + 0.99*(TAUSTAR- TAU1)
      GOTO 810
820 GAMDOT = (ONE/MU/DT)*(TAUSTAR-TAU)
```

```
      IF (F0.GT.0.1D0.AND.GDTOT.GT.ZERO.AND.GAMDOTO.GT.ZERO)
     +  GAMDOT = GAMDOTO
      SBAR  = S20*F0 + (S10+GAMDOT*DT*H10)*(ONE - F0)
      GAMDOT1 = GD0*((TAU/(SBAR))**EM)
      IF (GAMDOT1.LT.GAMDOT) GAMDOT = GAMDOT1

C*********************************************************************
C
C     adjust guesses for effects of void porosity
C
C*********************************************************************

      IF (TAUHATO .EQ.ZERO) TAUHATO = S10
      ARG=-ONEPT5*Q2*PRESSO/TAUHATO/SQRT3
      RFACTOR1= ONE+Q1*Q1*FVSTRO*FVSTRO-TWO*Q1*FVSTRO*DCOSH(ARG)
      RFACTOR = DSQRT(DABS(RFACTOR1))
      IF (RFACTOR.LT.0.10D0.OR.RFACTOR.LT.ZERO) THEN
      RFACTOR = 0.10D0
      ENDIF
      IF (RFACTOR.EQ.0.10D0.AND.TAUSTAR.GT.TAUO) THEN
        TAU = TAUHATO*RFACTOR
      IF (TAUSTAR.GT.TAU) THEN
        GAMDOT =  (ONE/MU/DT)*(TAUSTAR-TAU)
      ELSE
        GAMDOT =  (ONE/MU/DT)*(TAUSTAR-TAUO)
      ENDIF
      ENDIF

C*********************************************************************
C
C     estimate f. If f is too small, adjust guess for TAU
C
C*********************************************************************

      DELGAM = GAMDOT*DT
      GD1 = GAMDOT
      GAMMA = GAMMAO + DELGAM
      G1 = G10 + DELGAM
      S1 = S10 + H10*DELGAM
      S2 = S20
      SAVE = TAU
      TAU = TAUO
      PRESS = PRESSO
      CALL FEVOLVE
      PRESS = PSTAR

      IF (TAU.GT.Y) THEN
        IF (FHAT.LT.FTOL) THEN
          TAU = S1*( (GAMDOT/GD0)**EMI)
        ELSE
          TAU = TAUO + H10*DELGAM
        ENDIF
      ENDIF

C*********************************************************************
C
C     solution of evolution equations
C
C     if f or gamdot is small, use simplified 2-parameter solution.
C     otherwise use full newton procedure.
C
C*********************************************************************

      IF (FHAT.LT.FTOL.AND.F0.LT.FTOL) THEN
        NTEST = 0
      ELSE IF (GAMDOT.LT.1.0D-10.OR.GAMDOT.LT.(GAMDOTO*1.0D-4)) THEN
        NTEST = 0
      ELSE
        NTEST = 1
      ENDIF

      IF (NTEST.EQ.0) THEN

      NSMALL = 0

      IF (TAUSTAR.LT.S10.AND.FVO.LT.ABUCL) THEN
      DO 774 I = 1,10
      IF ((TAUSTAR - MU*DT*GAMDOT).LT.ZERO) GAMDOT = ZERO
774   GAMDOT = (((TAUSTAR - MU*DT*GAMDOT)/S10)**EM)*GDO
      ENDIF

      A3(1,1) = ZERO
777   TAUHAT = S1*((GAMDOT/GDO)**EMI)
      DELGAM = GAMDOT*DT
      GAMMA  = GAMMAO + DELGAM
      GD1 = GAMDOT
      GD2 = ZERO
      G1 = G10 + GD1*DT
      G2 = ZERO
```

```
      B1 = S1*EN1/( (S1/S1R)**(ONE/EN1) )
      IF (FVO.GT.0.95D0*FVFRACT) B1 = ZERO
      DS1 = B1*DT*GD1
      DS2 = ZERO
      FDOT = ZERO
      F = FO

C     solve for tau and calculate derivatives

      TAU = TAUMAT

      CALL GURSON1

C     solve newton equations

      PHI1  = COEFF10*GAMDOT - (TAUSTAR-TAU)/(MU*DT)
      PHI2  = PRESS - PSTAR + KAPPA*COEFF20*GAMDOT*DT
      PHI3  = S1 - DS1 - S10

      IF (DABS(PHI1).LT.SMPHI1.AND.DABS(PHI2).LT.SMPHI2.
     +  AND.DABS(PHI3).LT.SMPHI3.AND.A3(1,1).NE.ZERO) THEN
        GOTO 703
      ENDIF

      NSMALL = NSMALL + 1
      IF (NSMALL.GT.100) THEN
        CALL CHECKINP
        PAUSE 'NSMALL TO BIG'
      ENDIF

      DTAUMATDGDB = S1/(EM*GDO)*((GAMDOT/GDO)**(EMI1))
      DS1DGDB  = B1
      DTAUMATDS1  = ((GAMDOT/GDO)**(EMI))
      DB1DS1   = EN1/( (S1/S1R)**(ONE/EN1) )
     +  - S1/( (S1/S1R)**(ONE/EN1 + ONE)*S1R )
      IF (FVO.GT.0.95D0*FVFRACT) DB1S1 = ZERO
      DS1DS1   = DB1DS1*GD1
      DARGDTAUMAT = ONEPT5*Q2/SQRT3*(PRESS/TAUMAT/TAUMAT)
      DRFDTAUMAT  = -(ONE/RFACTOR)*Q1*FVSTRO*DSINH(ARG)*DARGDTAUMAT
      DTAUDTAUMAT = RFACTOR + TAUMAT*DRFDTAUMAT
      DTAUDGDB=DTAUMATDGDB*DTAUDTAUMAT
      DTAUDP =  -(TAUMAT/TWO/RFACTOR)*PHIP
      DTAUDS1 = DTAUMATDS1*DTAUDTAUMAT

      A3(1,1) = COEFF10 + DTAUDGDB/(MU*DT)
      A3(1,2) = DTAUDP/(MU*DT)
      A3(1,3) = DTAUDS1/(MU*DT)
      A3(2,1) = KAPPA*DT*COEFF20
      A3(2,2) = ONE
      A3(2,3) = ZERO
      A3(3,1) = -DS1DGDB*DT
      A3(3,2) = ZERO
      A3(3,3) = ONE - DS1DS1*DT

C     take inverse

      CALL GAUSSJ (A3,N,NP,B3,M,MP)

      DELGAMDOT = -A3(1,1)*PHI1 - A3(1,2)*PHI2 - A3(1,3)*PHI3
      DELP      = -A3(2,1)*PHI1 - A3(2,2)*PHI2 - A3(2,3)*PHI3
      DELS1     = -A3(3,1)*PHI1 - A3(2,2)*PHI2 - A3(3,3)*PHI3

      GAMDOT = GAMDOT + DELGAMDOT
      PRESS = PRESS + DELP
      S1 = S1 + DELS1
      IF (GAMDOT.LT.ZERO) GAMDOT = GDO

      GOTO 777

703   CONTINUE

C     update f

      CALL FEVOLVE

C     update void nucleation parameters

      CALL GURSON2
      IF (DABS(FVSTR).GT.ONE) THEN
      CALL CHECKINP
      ENDIF
      CALL GURSON3
      IF (FV.GE.0.95*FVFRACT) THEN
        COEFF1 = COEFF10
        COEFF2 = COEFF20
      ENDIF

C     calculate jacobian coefficients

      A1(1,1) = ONE - A3(1,1)*COEFF10
```

```
      DGDBDTAUSTAR = ONE/(MU*DT*COEFF10)*(ONE - A1(1,1))
      A1(2,1) = -COEFF20*KAPPA*DT*DGDBDTAUSTAR
      A1(1,2) = ZERO
      A1(2,2) = A3(2,2)

      ELSE

C*****************************************************************
C
C     full Newton procedure
C
C*****************************************************************

      NEWTON = 0
      NSAVE =0
      NCOUNT = 0
      F = FO

      IF (FO.LT.1.0D-2) THEN
         TAU = TAUO
         PRESS = PRESSO
         CALL FEVOLVE
         F = FNAT
         DF = F - FO
         PRESS = PSTAR
         GOTO 467
      ENDIF

C     update estimate of f

      DS10 = H10*DELGAM*G10/GAMMAO
      S1   = S10 + DS10
      SF = S2R*((G2R + G1)**EM2)
      DS20 = H20*DELGAM*G20/GAMMAO

676   CALL FEVOLVE

      NCOUNT = NCOUNT + 1
      F = FNAT
      DF = F - FO
      S2  = (F - DF)/F*(S20 + DS200) + (DF/F)*SF
      DS20 = S2 - S20
      IF (NCOUNT.LT.3) GOTO 676

C     store initial guesses

467   SB = F*S2 + (ONE-F)*S1
      GAMDOTG = GAMDOT
      FG = F
      S1G = S1
      S2G = S2

      IF ((AO*(F-FO)/GAMDOT/DT).GT.0.2D0) THEN
      AO = 0.2D0*GAMDOT*DT/(F-FO)
      ELSE
      AO  = A01 + A02*(TAUO/S1R)
      ENDIF
667   CALL SELFC

      NEWTON = NEWTON + 1
      IF (NEWTON.GT.100) THEN
      CALL CHECKINP
      PAUSE 'NEWTON TOO BIG'
      ENDIF

      GD1 = GAMDOT*CHI1
      GD2 = GAMDOT*CHI2
      GAMMA = GAMMAO + GAMDOT*DT
      G1 = G10 + GD1*DT
      G2 = G20 + GD2*DT

      CALL HARDNESS

      TAUNAT = SB*((GAMDOT/GDO)**EMI)
      TAU = TAUNAT
      CALL GURSON1

      CALL FEVOLVE

      PRESS = PSTAR + KAPPA*DT*(DELV*FDOT - COEFF20*GAMDOT)

      PHI1 = COEFF10*GAMDOT - (TAUSTAR - TAU)/(MU*DT)
      PHI2  = PRESS - PSTAR + KAPPA*COEFF20*GAMDOT*DT
      PHI3 = S1 - DS1 - S10
      PHI4 = S2 - DS2 - S20
      PHI5 = F  - FO - FDOT*DT

      TOL1 = GAMDOT/100000.D0
      TOL2 = PRESS/100000.D0
      TOL3 = S1/100000.D0
```

```
      TOL4 = S2/100000.DO
      TOL5 = F/100000.DO
      IF (TOL1.LT.TOL10) TOL1 = TOL10
      IF (TOL2.LT.TOL20) TOL2 = TOL20
      IF (TOL3.LT.TOL30) TOL3 = TOL30
      IF (TOL4.LT.TOL40) TOL4 = TOL40
      IF (TOL5.LT.TOL50) TOL5 = TOL50

      IF (DABS(PHI1).LT.TOL1.AND.DABS(PHI2).LT.TOL2
     +  .AND.DABS(PHI3).LT.TOL3.AND.DABS(PHI4).LT.TOL4
     +  .AND.DABS(PHI5).LT.TOL5) THEN
        CALL ACALC
        GOTO 666
      END IF

C*****************************************************************************
C
C     calculate Newton-Raphson derivative matrix
C
C*****************************************************************************

      CALL ACALC

      DELGDB = -(A1(1,1)*PHI1+A1(1,2)*PHI2+A1(1,3)*PHI3+A1(1,4)*PHI4
     +  + A1(1,5)*PHI5)
      DELP   = -(A1(2,1)*PHI1+A1(2,2)*PHI2+A1(2,3)*PHI3+A1(2,4)*PHI4
     +  + A1(2,5)*PHI5)
      DELS1  = -(A1(3,1)*PHI1+A1(3,2)*PHI2+A1(3,3)*PHI3+A1(3,4)*PHI4
     +  + A1(3,5)*PHI5)
      DELS2  = -(A1(4,1)*PHI1+A1(4,2)*PHI2+A1(4,3)*PHI3+A1(4,4)*PHI4
     +  + A1(4,5)*PHI5)
      DELF   = -(A1(5,1)*PHI1+A1(5,2)*PHI2+A1(5,3)*PHI3+A1(5,4)*PHI4
     +  + A1(5,5)*PHI5)

C     adjust corrections to gamdot if necessary

      GDSAVE = GAMDOT
      GAMDOT = GAMDOT + DELGDB
      PRESS = PRESS + DELP
      S1    = S1    + DELS1
      S2    = S2    + DELS2
      F     = F     + DELF
      DF    = F     - F0
      DELTA = DELGDB

      IF (GAMDOT.LT.ZERO.AND.GDTOT.GT.ZERO.AND.NSAVE.EQ.0) THEN
       GAMDOT = GAMDOT0
       PRESS = PRESS0
       S1 = S10 + GAMDOT/GAMDOT0*(S1G - S10)
       S2 = S20 + GAMDOT/GAMDOT0*(S2G - S20)
       F  = F0  + GAMDOT/GAMDOT0*(FG  - F0)
       NSAVE = 1
      ELSE IF (GAMDOT.LT.ZERO) THEN
909     GAMDOT = GDSAVE + 0.3*DELTA
        DELTA = 0.8*DELTA
        IF (GAMDOT.LT.ZERO) GOTO 909
      ELSE IF ((GAMDOT*TEN).LT.GDSAVE) THEN
        GAMDOT = GDSAVE + 0.6*DELTA
      ELSE IF ((GAMDOT*FIVE).LT.GDSAVE) THEN
        GAMDOT = GDSAVE + 0.8*DELTA
      ELSE IF ((GAMDOT*THREE).LT.GDSAVE) THEN
        GAMDOT = GDSAVE + 0.9*DELTA
      ENDIF

      A0  = A01 + A02*(TAU0/S1R)

      GOTO 667
666   CONTINUE

      GAMMA = GAMMA0 + GAMDOT*DT

C     update void nucleation parameters

      CALL GURSON2
      IF (DABS(FVSTR).GT.ONE) THEN
      CALL CHECKIBP
      ENDIF
      CALL GURSON3
      IF (FV.GE.0.95*FVFRACT) THEN
        COEFF1 = COEFF10
        COEFF2 = COEFF20
      ENDIF

C     calculate jacobian calculation parameters

      DPDF = KAPPA*DELV*DT
      DFDPSTAR = ZERO

      A1(1,1) =  ONE - A1(1,1)*COEFF10
      DGDBDTAUSTAR = ONE/(ETA*DT*COEFF10)*(ONE - A1(1,1))
```

```
      A1(2,1) = -COEFF20*KAPPA*DT*DGDBDTAUSTAR + A1(4,1)*DPDF/(MU*DT)
      A1(1,2) = DFDPSTAR*DTAUDF
      A1(2,2) = A1(2,2)

      ENDIF

C*****************************************************************
C
C     update stress and state variables
C
C*****************************************************************

C     update the deviatoric stress

300   DO 310 J = 1,NTENS
        STRESS(J) = TAU*ABORM(J)/DSQRT2
310   CONTINUE


C     add dilatational stress components

      DO 320 J = 1,NDI
        STRESS(J) = STRESS(J) - PRESS
320   CONTINUE

C*****************************************************************
C
C     calculate jacobian constants
C
C*****************************************************************

      ETA = TAU/TAUSTAR
      MUTILDA = MU*ETA

      C1 = TWO*MUTILDA
      C2 = KAPPA*A1(2,2) - TWO*THIRD*MUTILDA
      C3 = -TWO*MU*(ETA - A1(1,1))
      C4 = -TWO*MU*A1(2,1)/SQRT2
      C5 = -KAPPA*A1(1,2)

C     symmetrize jacobian

      C4 = HALF*(C4+C5)
      C5 = C4

      RETURN
      END


C*****************************************************************
C*****************************************************************
C
C                     SUBROUTINE HARDNESS
C
C     In this subroutine, functions which are needed to determine the
C     unknown viscosities are determined.
C
C*****************************************************************
C*****************************************************************

      SUBROUTINE HARDNESS
      INCLUDE 'finalcom12'

C     calculate hardening rate

      H1 = S1*EN1/( (S1/S1R)**(ONE/EN1) )
      H2 = S2*EN2/( (S2/S2R)**(ONE/EN2) )
      IF (FVO.GT.0.95D0*FVFRACT) THEN
        H1 = ZERO
        H2 = ZERO
      ENDIF

C     determine austenite hardness

      DS1 = H1*DT*GD1

C     determine average martensite hardness

      DS2_PRIME = H2*GD2*DT
      SF = S2R*((G2R + G1)**EN2)
      S2_NEW = (FO/F)*(S2O + DS2_PRIME) + (DF/F)*SF
      DS2 = S2_NEW - S2O

      RETURN
      END
```

```
C*********************************************************************
C*********************************************************************
C
C                       SUBROUTINE FEVOLVE
C
C     In this subroutine, the volume fraction of martensite evolved
C     is calculated.
C
C*********************************************************************
C*********************************************************************

      SUBROUTINE FEVOLVE
      INCLUDE 'UMAT_COMMONS'

      ENVIMULT = (ENF*BETAO*ALPHA*DEXP(-ALPHA*G1)*
     +  ((ONE-DEXP(-ALPHA*G1))**ENF1))

      ENVI = ENVIO + ENVIMULT*GD1*DT

      SIGMA  = -DSQRT3*PRESS/TAU
      SIGMAO = -DSQRT3*PRESSO/TAUO
      TAUDOT = (TAU - TAUO)/DT
      PDOT   = (PRESS - PRESSO)/DT
      IF (PRESS.NE.ZERO) THEN
      SIGDOT = SIGMA*(PDOT/PRESS - TAUDOT/TAU)
      ELSE
      SIGDOT = ZERO
      ENDIF

C     calculate probability function

      X = XO - X1*T + X2*SIGMAO
      CALL PROBCALC
      DELPROB = PROB - PROBO
      IF (SIGDOTO.NE.ZERO) THEN
        PROBMULT = DELPROB/(SIGDOTO*DT)
      ELSE
        PROBMULT = ZERO
      ENDIF

      IF (DELPROB.LT.ZERO) THEN
        HSF = ZERO
      ELSE
        HSF = ONE
      ENDIF

      AFO = ENVIMULT*PROBO
      BFO = ENVIO*PROBMULT*HSF
      BF  = (ONE-F)*ENVIO*PROBMULT*HSF
      BF1 = -BF*SIGMA/TAU
      IF (PRESS.NE.ZERO) THEN
        BF2 = DF*SIGMA/PRESS
      ELSE
        BF2 = ZERO
      ENDIF

      FDOT = (ONE - FO)*(AFO*GD1 + BFO*SIGDOTO)/(ONE
     +  + DT*(AFO*GD1 + BFO*SIGDOTO))

      IF (FO.EQ.ZERO) THEN
        FO = ONE - DEXP(-ENVIO*PROBO)
      ENDIF

      FHAT = FO + FDOT*DT

      RETURN
      END


C*********************************************************************
C*********************************************************************
C
C                       SUBROUTINE PROBCALC
C
C     In this subroutine, the probability function is evaluated.
C
C*********************************************************************
C*********************************************************************

      SUBROUTINE PROBCALC
      INCLUDE 'UMAT_COMMONS'
      DIMENSION Z(10),PHIZ(10),PTOTAL(10),P2Z(10)

      PPHI = (X - XB)/SX
      DG = DEXP(-HALF*PPHI*PPHI)
      IF (PPHI.LT.ZERO) THEN
        JFLAG = 1
        FI = -PPHI
      ELSE
        JFLAG = 0
```

```
        FI = PPHI
      ENDIF
      IF (FI.GT.FIVE) THEN
       PROB = ONE
       GOTO 333
      ENDIF

C*****************************************************************************
C
C     probability look up table
C
C*****************************************************************************

      IF (FI.LT.0.2D0) THEN
        PROBADD = 0.5000D0
        ZZERO = ZERO
      ELSE IF (FI.LT.0.4D0) THEN
        PROBADD = 0.5793D0
        ZZERO = 0.2D0
      ELSE IF (FI.LT.0.6D0) THEN
        PROBADD = 0.6554D0
        ZZERO = 0.4D0
      ELSE IF (FI.LT.0.8D0) THEN
        PROBADD = 0.7257D0
        ZZERO = 0.6D0
      ELSE IF (FI.LT.ONE) THEN
        PROBADD = 0.7881D0
        ZZERO = 0.8D0
      ELSE IF (FI.LT.1.3D0) THEN
        PROBADD = 0.8413D0
        ZZERO = ONE
      ELSE IF (FI.LT.1.6D0) THEN
        PROBADD = 0.9032D0
        ZZERO = 1.3D0
      ELSE IF (FI.LT.TWO) THEN
        PROBADD = 0.9452D0
        ZZERO = 1.6D0
      ELSE IF (FI.LT.2.5D0) THEN
        PROBADD = 0.97725D0
        ZZERO = TWO
      ELSE IF (FI.LT.3.0D0) THEN
        PROBADD = 0.99379D0
        ZZERO = 2.5D0
      ELSE
        PROBADD = 0.99865D0
        ZZERO = 3.0D0
      END IF

C*****************************************************************************
C
C     calculate marginal probability
C
C*****************************************************************************

      PROB=PROBADD
      DELT=0.10D0*(FI-ZZERO)
      DO 400 I = 1,10
        Z(I) = (I-1)*DELT + ZZERO
        PHIZ(I) = ONE/(DSQRT(TWO*PI))*DEXP(-HALF*Z(I)*Z(I))
        P2Z(I) = -PHIZ(I)*Z(I)
        PTOTAL(I) = PHIZ(I)*DELT + HALF*P2Z(I)*DELT*DELT
        PROB = PROB + PTOTAL(I)
400   CONTINUE


333   IF (JFLAG.EQ.1) THEN
        PROB = ONE - PROB
      ENDIF

      RETURN
      END


C*****************************************************************************
C*****************************************************************************
C
C                       SUBROUTINE JACOBANAL
C
C     In this subroutine, the Jacobian is determined analytically.
C
C*****************************************************************************
C*****************************************************************************

      SUBROUTINE JACOBANAL(NTENS1,NDI1,NDIP11,DDSDDE,ANORM)
      INCLUDE 'UMAT_COMMONS'
      DIMENSION DDSDDE(4,4),ANORM(4)

      DO 509 J1 = 1,NTENS
      DO 509 J2 = 1,NTENS
509   DDSDDE(J1,J2) = ZERO
```

```
500   DO 510 J1 = 1,NTENS
        DO 510 J2 = 1,NTENS
          DDSDDE(J1,J2) = C3*ANORM(J1)*ANORM(J2)
510   CONTINUE
      DO 520 J1 = 1,NDI
        DO 520 J2 = 1,NTENS
          DDSDDE(J1,J2) = DDSDDE(J1,J2) + C4*ANORM(J2)
          DDSDDE(J2,J1) = DDSDDE(J2,J1) + C5*ANORM(J2)
520   CONTINUE
      DO 530 J1 = 1,NDI
        DDSDDE(J1,J1) = DDSDDE(J1,J1) + C1
        DO 530 J2 = 1,NDI
          DDSDDE(J1,J2) = DDSDDE(J1,J2) + C2
530   CONTINUE
      DO 540 J1 = NDIP11,NTENS
        DDSDDE(J1,J1) = DDSDDE(J1,J1) + HALF*C1
540   CONTINUE


      RETURN
      END


C*********************************************************************
C*********************************************************************
C
C                     SUBROUTINE JACOBNUM
C
C     In this subroutine, the Jacobian is determined numerically. This
C     routine is used for test purposes only.
C
C*********************************************************************
C*********************************************************************

      SUBROUTINE JACOBNUM(NTENS1,NDI1,NDIP11,PERTURB,STATEV,
     +  STRESS,DSTRAN,DDSDDE,ANORM)
      INCLUDE 'UMAT_COMMONS'
      DIMENSION STRESS(4),STRESSI(4),DSTRAN(4),STATEV(19),DDSDDE1(4,4),
     +  DDSDDE(4,4),ANORM(4),DDSDDE2(4,4)

      EQUIV = ZERO
      DO 600 I=1,4
        EQUIV = EQUIV + DSTRAN(I)*DSTRAN(I)
600   CONTINUE
      EQUIV = DSQRT(EQUIV + DSTRAN(4)*DSTRAN(4))
      DIFFD = EQUIV/PERTURB
      IF (DIFFD.LE.1.0D-10) DIFFD=1.0D-10
      DO 610 J = 1,4
        DSTRAN(J) = DSTRAN(J) - DIFFD
        NFLAG = 0
        CALL SINT(NTENS1,NDIP11,NDI1,DSTRAN,STRESSI,
     +    STATEV,ANORM)
        DSTRAN(J) = DSTRAN(J) + DIFFD
        DO 610 I = 1,4
          DDSDDE1(I,J) = (STRESS(I) - STRESSI(I))/DIFFD
610   CONTINUE
      DO 611 J = 1,4
        DSTRAN(J) = DSTRAN(J) + DIFFD
        NFLAG = 0
        CALL SINT(NTENS1,NDIP11,NDI1,DSTRAN,STRESSI,
     +    STATEV,ANORM)
        DSTRAN(J) = DSTRAN(J) - DIFFD
        DO 611 I = 1,4
          DDSDDE2(I,J) = -(STRESS(I) - STRESSI(I))/DIFFD
611   CONTINUE
        DO 612 I = 1,4
        DO 612 J = 1,4
          DDSDDE(I,J) = (DDSDDE1(I,J) + DDSDDE2(I,J) ) /TWO
612   CONTINUE
      RETURN
      END


C*********************************************************************
C
C                     SUBROUTINE SELF
C
C     In this subroutine, the composite stress is predicted using a
C     self-consistent method.
C
C*********************************************************************
C*********************************************************************

      SUBROUTINE SELFC
      INCLUDE 'UMAT_COMMONS'

      NCALC=0

      IF (CHI1.EQ.ZERO) THEN
        CHI1 = G10/GAMMA0
```

```
        CHI2 = G20/GAMMA0
        IF (CHI2.EQ.ZERO) CHI2 = 0.2D0
      ENDIF

C     calculate PHI1, PHI2, PHI3

700   CALL PHICALC

      IF (DABS(PHI1).LT.TOLPHI1.AND.DABS(PHI2).LT.TOLPHI2
     +  .AND.DABS(PHI3).LT.TOLPHI3) THEN
        GOTO 800
      END IF

C     calculate Derivatives for Newton Scheme

      CALL SCACALC

C     update X1, X2, SB

      DELCHI1 = -(A3(1,1)*PHI1 + A3(1,2)*PHI2 + A3(1,3)*PHI3)
      DELCHI2 = -(A3(2,1)*PHI1 + A3(2,2)*PHI2 + A3(2,3)*PHI3)
      DELSB   = -(A3(3,1)*PHI1 + A3(3,2)*PHI2 + A3(3,3)*PHI3)

      CHI1 = CHI1 + DELCHI1
      CHI2 = CHI2 + DELCHI2
      SB   = SB   + DELSB

      GOTO 700

800   CONTINUE

      RETURN
      END


C*********************************************************************
C*********************************************************************
C
C                       SUBROUTINE PHICALC
C
C     In this subroutine, the Newton equations are evaluated.
C
C*********************************************************************
C*********************************************************************

      SUBROUTINE PHICALC
      INCLUDE 'UMAT_COMMONS'

      NCALC = NCALC + 1

      IF (NCALC.GT.100) then
      CALL CHECKINP
      PAUSE 'NCALC TOO BIG'
      ENDIF

      IF (CHI2.LT.ZERO) THEN
        CHI2 = CHI2SAVE/1000.0
      ENDIF

      PHI1 = F*CHI2 + (ONE - F)*CHI1 - ONE + A0*(F-F0)/GAMDOT/DT

      PHI2 = CHI1 + TWO*THIRD*(S1/SB)*(CHI1**EMI) - FIVE*THIRD

      PHI3 = CHI2 + TWO*THIRD*(S2/SB)*(CHI2**EMI) - FIVE*THIRD

      CHI2SAVE = CHI2

      RETURN
      END


C*********************************************************************
C*********************************************************************
C
C                       SUBROUTINE SCACALC
C
C     In this subroutine, the A-matrix terms (for the self-consistent
C     analysis) are calculated.
C
C*********************************************************************
C*********************************************************************

      SUBROUTINE SCACALC
      INCLUDE 'UMAT_COMMONS'
      DIMENSION B3(3,3)
      DATA N,NP,M,MP/4*3/

      A11 = ONE - F
      A12 = F
      A13 = ZERO
```

```
      A21 = ONE + TWO*THIRD*EMI*(S1/SB)*(CHI1**EMI1)
      A22 = ZERO
      A23 = -TWO*THIRD*(S1/(SB*SB))*(CHI1**EMI)
      A31 = ZERO
      A32 = ONE + TWO*THIRD*EMI*(S2/SB)*(CHI2**EMI1)
      A33 = -TWO*THIRD*(S2/(SB*SB))*(CHI2**EMI)

      A3(1,1) = A11
      A3(1,2) = A12
      A3(1,3) = A13
      A3(2,1) = A21
      A3(2,2) = A22
      A3(2,3) = A23
      A3(3,1) = A31
      A3(3,2) = A32
      A3(3,3) = A33

      CALL GAUSSJ (A3,N,NP,B3,N,MP)

      RETURN
      END


C*********************************************************************
C*********************************************************************
C
C                     SUBROUTINE ACALC
C
C     In this subroutine, the A-matrix is calculated.
C
C*********************************************************************
C*********************************************************************

      SUBROUTINE ACALC
      INCLUDE 'UMAT_COMMONS'
      DIMENSION A1(5,5)
      DATA N,NP,M,MP/4*5/

      CALL DERIVATIVES

      A1(1,1) = COEFF10 + DTAUDGDB/(MU*DT)
      A1(2,1) = COEFF20*KAPPA*DT
      A1(3,1) = -DS1DGDB
      A1(4,1) = -DS2DGDB
      A1(5,1) = -DFDGDB*DT

      A1(1,2) = DTAUDP/(MU*DT)
      A1(2,2) = ONE
      A1(3,2) = ZERO
      A1(4,2) = ZERO
      A1(5,2) = ZERO

      A1(1,3) = DTAUDS1/(MU*DT)
      A1(2,3) = ZERO
      A1(3,3) = ONE - DS1DS1
      A1(4,3) = -DS2DS1
      A1(5,3) = -DFDS1*DT

      A1(1,4) = DTAUDS2/(MU*DT)
      A1(2,4) = ZERO
      A1(3,4) = -DS1DS2
      A1(4,4) = ONE - DS2DS2
      A1(5,4) = -DFDS2*DT

      A1(1,5) = DTAUDF/(MU*DT)
      A1(2,5) = ZERO
      A1(3,5) = -DS1DF
      A1(4,5) = -DS2DF
      A1(5,5) = ONE - DFDF*DT

C     calculate matrix inverse

      CALL GAUSSJ (A1,N,NP,B1,N,MP)

      RETURN
      END


C*********************************************************************
C*********************************************************************
C
C                     SUBROUTINE DERIVATIVES
C
C     In this subroutine, the derivatives needed for calculation of the
C     Newton scheme A-matrix and DFD1 are evaluated.
C
C*********************************************************************
C*********************************************************************

      SUBROUTINE DERIVATIVES
```

```
      INCLUDE 'UMAT_COMMONS'

C     calculate derivatives from self-consistent scheme

      DFI1DF    = CHI2 - CHI1 + AO/GAMDOT/DT
      DFI1DGDB  = -AO*(F-FO)/(GAMDOT*GAMDOT)/DT
      DFI2DS1   = TWO*THIRD/SB*(CHI1**EMI)
      DFI3DS2   = TWO*THIRD/SB*(CHI2**EMI)

      DSBDS1    = -DFI2DS1 /(A12*A21*A33/(A11*A32) + A23        )
      DSBDS2    = -DFI3DS2 /(A11*A32*A23/(A12*A21) + A33        )
      DSBDF     =  DFI1DF  /(A33*A12    / A32      + A23*A11/A21)
      DSBDGDB   =  DFI1DGDB/(A33*A12    / A32      + A23*A11/A21)

      DX1DS1    = -DFI2DS1 /(A32*A11*A23/(A33*A12) + A21        )
      DX1DS2    =  DFI3DS2 /(A21*A33/     A23      + A11*A32/A12)
      DX1DF     = -DFI1DF  /(A12*A33*A21/(A32*A23) + A11        )
      DX1DGDB   = -DFI1DGDB/(A12*A33*A21/(A32*A23) + A11        )

      DX2DS1    =  DFI2DS1 /(A32*A23    / A33      + A12*A21/A11)
      DX2DS2    = -DFI3DS2 /(A21*A12*A33/(A23*A11) + A32        )
      DX2DF     = -DFI1DF  /(A11*A23*A32/(A21*A33) + A12        )
      DX2DGDB   = -DFI1DGDB/(A11*A23*A32/(A21*A33) + A12        )

C*********************************************************************
C
C     calculate derivatives for newton scheme
C
C*********************************************************************


C     1st equation

      DTAUMATDSB   = ((GAMDOT/GDO)**EMI)
      DTAUMATDGDB  = SB/(EM*GDO)*((GAMDOT/GDO)**(EMI1))
     +             + DTAUMATDSB*DSBDGDB
      DTAUMATDS1   = DTAUMATDSB*DSBDS1
      DTAUMATDS2   = DTAUMATDSB*DSBDS2
      DTAUMATDF    = DTAUMATDSB*DSBDF
      DARGDTAUMAT  = ONEPT5*Q2/SQRT3*(PRESS/TAUMAT/TAUMAT)
      DRFDTAUMAT   = -(ONE/RFACTOR)*Q1*FVSTRO*DSINH(ARG)*DARGDTAUMAT
      DTAUDTAUMAT  = RFACTOR + TAUMAT*DRFDTAUMAT
      DPDGDB       = COEFF20*DT*KAPPA
      DARGDGDB     = -ONEPT5*Q2/SQRT3*( (ONE/TAUMAT)*DPDGDB
     +             - (PRESS/TAUMAT/TAUMAT)*DTAUMATDGDB )
      DRFDGDB      = -(ONE/RFACTOR)*Q1*FVSTRO*DSINH(ARG)*DARGDGDB
      DTAUDP       = -(TAUMAT/TWO/RFACTOR)*PHIP
      DARGDP       = -ONEPT5*Q2/SQRT3*( (ONE/TAUMAT) )
      DRFDP        = -(ONE/RFACTOR)*Q1*FVSTRO*DSINH(ARG)*DARGDP
      DTAUDGDB     = DTAUMATDGDB*DTAUDTAUMAT + DTAUDP*DPDGDB
      DTAUDS1      = DTAUMATDS1*DTAUDTAUMAT
      DTAUDS2      = DTAUMATDS2*DTAUDTAUMAT
      DTAUDF       = DTAUMATDF*DTAUDTAUMAT

C     2nd, part of 3rd equations

      DH1DS1 = EM1/( (S1/S1R)**(ONE/EM1) )
     +  - S1/( (S1/S1R)**(ONE/EM1 + ONE)*S1R )
      DH2DS2 = EM2/( (S2/S2R)**(ONE/EM2) )
     +  - S2/( (S2/S2R)**(ONE/EM2 + ONE)*S2R )
      IF (FVO.GT.0.95D0*FVFRACT) THEN
        DH1DS1 = ZERO
        DH2DS2 = ZERO
      ENDIF

      DGD1DGDB = CHI1 + GAMDOT*DX1DGDB
      DGD2DGDB = CHI2 + GAMDOT*DX2DGDB

      DGD1DS1  = GAMDOT*DX1DS1
      DGD2DS1  = GAMDOT*DX2DS1
      DGD1DS2  = GAMDOT*DX1DS2
      DGD2DS2  = GAMDOT*DX2DS2
      DGD1DF   = GAMDOT*DX1DF
      DGD2DF   = GAMDOT*DX2DF

      DS1DGDB = DT*H1*DGD1DGDB
      DS1DS1  = DT*H1*DGD1DS1 + DH1DS1*GD1*DT
      DS1DS2  = DT*H1*DGD1DS2
      DS1DF   = DT*H1*DGD1DF

      DS2DGDB = DT*H2*DGD2DGDB
      DS2DS1  = DT*H2*DGD2DS1
      DS2DS2  = DT*H2*DGD2DS2 + DH2DS2*GD2*DT
      DS2DF   = DT*H2*DGD2DF

C     if tau is adjusted before taudot is taken, then second deriv
C     must be included

      DENVIDGD1     = -ALPHA*DT*ENVIMULT
     + + DEXP(-ALPHA*G1)*ALPHA*DT*ENF1*(ENF*BETAO*ALPHA*DEXP(-ALPHA*G1)
```

```
     + * ((ONE-DEXP(-ALPHA*G1))**EMF2))
      DAFODGD1       = PROBO*DEVIDGD1
      DFDGD1 = (ONE - FO)*(DAFODGD1*GD1 + AFO)/(ONE
     +  + DT*(AFO*GD1 + BFO*SIGDOTO))
     +  - (ONE - FO)*(DAFODGD1*GD1 + AFO)*DT*(AFO*GD1
     +  + BFO*SIGDOTO)/((ONE + DT*(AFO*GD1 + BFO*SIGDOTO))**2)

      DFDGDB         = DFDGD1*DGD1DGDB + DFDTAU*DTAUDGDB
      DFDS1          = DFDGD1*DGD1DS1
      DFDS2          = DFDGD1*DGD1DS2
      DFDF           = DFDGD1*DGD1DF

C     4th  equation

      DSFDGDB = EM2*S2R*((G2R + G1)**EM21)*DGD1DGDB*DT
      DSFDS1  = EM2*S2R*((G2R + G1)**EM21)*DGD1DS1*DT
      DSFDS2  = EM2*S2R*((G2R + G1)**EM21)*DGD1DS2*DT
      DSFDF   = EM2*S2R*((G2R + G1)**EM21)*DGD1DF*DT

C     remainder of 3rd equation

      DS2DGDB = (FO/F)*DS2DGDB + (DF/F)*DSFDGDB
      DS2DS1  = (FO/F)*DS2DS1  + (DF/F)*DSFDS1
      DS2DS2  = (FO/F)*DS2DS2  + (DF/F)*DSFDS2
      DS2DF   = (FO/F)*DS2DF   + (DF/F)*DSFDF
     +  - (ONE/(F**2)) * (FO*H2*GD2*DT + FO*S20 + DF*SF) + (ONE/F) * SF

      RETURN
      END


C**********************************************************************
C**********************************************************************
C
C                       SUBROUTINE CHECKINP
C
C     In this subroutine, the initial state variables, stresses,
C     and strains are written to the ABAQUS .dat file.
C
C**********************************************************************
C**********************************************************************

      SUBROUTINE CHECKINP
      INCLUDE 'UMAT_COMMONS'

      DO 100 I = 1,9
100     WRITE(6,442) I,STATEVO(I)
442     FORMAT('      STATEV(',I1,') = ',D16.8)
      DO 101 I = 10,19
101     WRITE(6,443) I,STATEVO(I)
443     FORMAT('      STATEV(',I2,') = ',D16.8)
      DO 102 I = 1,4
102     WRITE(6,444) I,STRESSO(I)
444     FORMAT('      STRESS(',I1,') = ',D16.8)
      DO 103 I = 1,4
103     WRITE(6,445) I,DSTRANO(I)
445     FORMAT('      DSTRAN(',I1,') = ',D16.8)

      DO 10  I = 1,1000
10    WRITE(6,*) ' error ',I
      RETURN
      END


C**********************************************************************
C**********************************************************************
C
C                       SUBROUTINE GAUSSJ
C
C     In this subroutine, taken from NUMERICAL RECIPES, matrix
C     inverses are calculated.
C
C**********************************************************************
C**********************************************************************

      SUBROUTINE GAUSSJ(A,N,NP,B,M,MP)
      INCLUDE 'UMAT_COMMONS'
      PARAMETER (NMAX=50)
      DIMENSION A(NP,NP),B(NP,MP),IPIV(NMAX),INDXR(NMAX),INDXC(NMAX)

      DO 9 I = 1,N
      DO 9 J = 1,N
      IF (I.EQ.J) THEN
      B(I,J) = ONE
      ELSE
      B(I,J) = ZERO
      ENDIF
9     CONTINUE
      DO 11 J=1,N
        IPIV(J)=0
```

```
11    CONTINUE
      DO 22 I=1,N
        BIG=0.
        DO 13 J=1,N
          IF(IPIV(J).NE.1)THEN
            DO 12 K=1,N
              IF (IPIV(K).EQ.0) THEN
                IF (ABS(A(J,K)).GE.BIG)THEN
                  BIG=ABS(A(J,K))
                  IROW=J
                  ICOL=K
                ENDIF
              ELSE IF (IPIV(K).GT.1) THEN
                CALL CHECKINP
                PAUSE 'SINGULAR MATRIX 1'
              ENDIF
12          CONTINUE
          ENDIF
13      CONTINUE
        IPIV(ICOL)=IPIV(ICOL)+1
        IF (IROW.NE.ICOL) THEN
          DO 14 L=1,N
            DUM=A(IROW,L)
            A(IROW,L)=A(ICOL,L)
            A(ICOL,L)=DUM
14        CONTINUE
          DO 15 L=1,M
            DUM=B(IROW,L)
            B(IROW,L)=B(ICOL,L)
            B(ICOL,L)=DUM
15        CONTINUE
        ENDIF
        INDXR(I)=IROW
        INDXC(I)=ICOL
        IF (A(ICOL,ICOL).EQ.0.) THEN
          CALL CHECKINP
          PAUSE 'SINGULAR MATRIX2'
        ENDIF
        PIVINV=1./A(ICOL,ICOL)
        A(ICOL,ICOL)=1.
        DO 16 L=1,N
          A(ICOL,L)=A(ICOL,L)*PIVINV
16      CONTINUE
        DO 17 L=1,M
          B(ICOL,L)=B(ICOL,L)*PIVINV
17      CONTINUE
        DO 21 LL=1,N
          IF(LL.NE.ICOL)THEN
            DUM=A(LL,ICOL)
            A(LL,ICOL)=0.
            DO 18 L=1,N
              A(LL,L)=A(LL,L)-A(ICOL,L)*DUM
18          CONTINUE
            DO 19 L=1,M
              B(LL,L)=B(LL,L)-B(ICOL,L)*DUM
19          CONTINUE
          ENDIF
21      CONTINUE
22    CONTINUE
      DO 24 L=N,1,-1
        IF(INDXR(L).NE.INDXC(L))THEN
          DO 23 K=1,N
            DUM=A(K,INDXR(L))
            A(K,INDXR(L))=A(K,INDXC(L))
            A(K,INDXC(L))=DUM
23        CONTINUE
        ENDIF
24    CONTINUE
      RETURN
      END


C*********************************************************************
C*********************************************************************
C
C                     SUBROUTINE GURSON1
C
C     In this subroutine, tau is calculated based upon taumat and fvstr.
C     Also, derivatives of the plastic potential Phi are calculated.
C
C*********************************************************************
C*********************************************************************

      SUBROUTINE GURSON1
      INCLUDE 'UMAT_COMMONS'
      DATA Q1,Q2,Q3/1.5D0,1.0D0,2.0D0/

      IF ((FVSTRO.EQ.ZERO).OR.(Q1.EQ.ZERO)) THEN
           PHITAU  =  TWO*TAU/TAUMAT/TAUMAT
           PHIP = ZERO
```

```
            COEFF10 = ONE
            COEFF20 = ZERO
            IF (TAUMAT.EQ.ZERO) TAUMAT = S10
            ARG = -ONEPT5*Q2*PRESS/TAUMAT/SQRT3
            RFACTOR = ONE
            RETURN
         END IF

C        solve for tau

         IF (TAUMAT0.EQ.ZERO) TAUMAT = S10
         ARG=-ONEPT5*Q2*PRESS/TAUMAT/SQRT3
         RFACTOR1= ONE+Q1*Q1*FVSTRO*FVSTRO-TWO*Q1*FVSTRO*DCOSH(ARG)
         RFACTOR = DSQRT(DABS(RFACTOR1))
         IF (RFACTOR.LT.0.10D0.OR.RFACTOR.LT.ZERO) THEN
         RFACTOR = 0.10D0
         ENDIF
         TAU = TAUMAT*RFACTOR

C        compute phitau, phip, phif, phitaumat

         PHITAU =  TWO*TAU/TAUMAT/TAUMAT
         PHIP   =  -THREE*Q1*DSINH(ARG)*Q2*FVSTRO/TAUMAT/SQRT3

         RETURN
         END


C*************************************************************************
C*************************************************************************
C
C                        SUBROUTINE GURSON2
C
C     In this subroutine, fvdot is calculated.
C
C*************************************************************************
C*************************************************************************

         SUBROUTINE GURSON2
         INCLUDE 'UMAT_COMMONS'

         SIGNORM = SQRT3*TAUMAT  - PRESS
         TAUMATDOT = (TAUMAT - TAUMAT0)/DT
         PDOT   = (PRESS - PRESS0)/DT
         FVGDOT = -(ONE - FV0)*COEFF20*GAMDOT
         FVG = FVG0 + FVGDOT*DT
         FVDOT = ANUCL/(DSQRT(TWO*PI)*GDSTD)
        +  *EXP(-HALF*((GAMMA - GDMEAN)/GDSTD)**2)*GAMDOT
        +    +   BNUCL/(DSQRT(TWO*PI)*SNSTD)
        +  *EXP(-HALF*((SIGNORM - SNMEAN)/SNSTD)**2)
        +  *(SQRT3*TAUMATDOT - PDOT)
        +  + FVGDOT

         FV = FV0 + FVDOT*DT

         IF (FV.GT.0.95D0*FVFRACT) THEN
           FV = 0.95D0*FVFRACT
         ENDIF

         IF (FV.GT.FVCRIT) THEN
           FVSTR = FVCRIT + (FVULT-FVCRIT)/(FVFRACT-FVCRIT)*(FV-FVCRIT)
         ELSE
           FVSTR = FV
         ENDIF

         RETURN
         END


C*************************************************************************
C*************************************************************************
C
C                        SUBROUTINE GURSON3
C
C     In this subroutine, the coefficients Z1 and Z2 are calculated.
C
C*************************************************************************
C*************************************************************************

         SUBROUTINE GURSON3
         INCLUDE 'UMAT_COMMONS'

         DNOM = TAU*PHITAU + PRESS*PHIP
         IF (DNOM.LE.1.D-12) DNOM = 1.D-12
         COEFF1 = (ONE-FVSTR)*TAUMAT*PHITAU/DNOM
         COEFF2 = (ONE-FVSTR)*TAUMAT*PHIP/DNOM

         RETURN
         END
```

```
C*********************************************************************
C*********************************************************************
C
C                       SUBROUTINE ELASTICITY
C
C     In this subroutine, the elastic constants are calculated based
C     upon the value of fvstr and the matrix elastic constants
C
C*********************************************************************
C*********************************************************************

      SUBROUTINE ELASTICITY
      INCLUDE 'UMAT_COMMONS'

      ETOL = .01D0
      KAPPA = KAPPAMAT
      MU = MUMAT
10    TESTMU = MU
      TESTKAPPA = KAPPA
      VNU = (THREE*KAPPA - TWO*MUMAT)/(THREE*TWO*KAPPA + TWO*MUMAT)
      AA = THIRD*((ONE + VNU)/(ONE - VNU))
      BB = (TWO/FIFTEEN)*((FOUR - FIVE*VNU)/(ONE - VNU))

      AFACTOR = (ONE - FVSTRO)/( ONE - FVSTRO/(ONE - AA) ) - ONE + AA
      BFACTOR = (ONE - FVSTRO)/( ONE - FVSTRO/(ONE - BB) ) - ONE + BB

      KAPPA = AA*KAPPAMAT/AFACTOR
      MU    = BB*MUMAT/BFACTOR
      IF(DABS(MU-TESTMU).LT.ETOL.AND.DABS(KAPPA-TESTKAPPA).LT.ETOL)THEN
        GOTO 20
      ENDIF

      GOTO 10

20    CONTINUE

      RETURN
      END
```

```
C*********************************************************************
C*********************************************************************
C
C                          UMAT_COMMONS
C
C     Common Blocks, etc.
C
C*********************************************************************
C*********************************************************************

      IMPLICIT REAL*8 (A-H,O-Z)

      DIMENSION STRESSO(4),STATEVO(19),DSTRANO(4)

      REAL*8 KAPPA,MU,MUTILDA,MUMAT,KAPPAMAT

      COMMON / INARRAYS / STRESSO,STATEVO,DSTRANO

      COMMON / MYCONSTS / ZERO,THIRD,HALF,ONE,TWO,THREE,PI,FIVE,TEN,
     +  FIFTEEN,SQRT2,SQRT3,DSQRT2,DSQRT3,ONEPT5

      COMMON / UMATCONSTS / KAPPA,MU,TWOMU,EM1,EM2,EM11,
     +  EM21,ALPBAR,ALPHA,DELV,S1R,S2R,G1R,G2R,EMF,EMF1,EMF2,
     +  XB,SX,X0,X1,X2,PMULT,EMVIMULT,MUTILDA,T,AF,BF,BF1,BF2,
     +  SIGDOTO,SIGDOT,AFO,BFO,MUMAT,KAPPAMAT

      COMMON / VARIABLES / GAMMA,GAMMAO,F,FO,TAUSTAR,PSTAR,BETAO,
     +  PRESS,PRESSO,TAU,TAUO,PROB,PROBO,EMVI,EMVIO,PPHI,DG,X,HSF,
     +  C1,C2,C3,C4,C5,FHAT,DELMVI,Y,EMVALPO,EMVTOT,GDTOT,DT,FDOT,
     +  GAMMAP,GAMMAPO,PROBMULT,SIGMA,PDOT

      COMMON / GURSON / RFACTOR,PHITAU,PHIP,ARG,Q1,Q2,FV,FVO,
     +  COEFF1,COEFF10,COEFF2,COEFF20,TAUMAT,ANUCL,GDMEAN,GDSTD,
     +  BNUCL,SNMEAN,SNSTD,FVG,FVGO,TAUMATO,FVCRIT,FVFRACT,FVULT,
     +  FVSTR,FVSTRO

      COMMON / XINTEG / NFULL,NCALC,NTAU,NEWTON,NITER,NITER1,NSMALL,
     +  NSINTU,NLOOP,NJAC

      COMMON / SCCONSTS / EM,EM1,EMI,EMI1,GD1,GD2,GD0,A0,A01,A02

      COMMON / SCVARIABLES / GAMDOT,S1,S10,DS1,DS2,S2,S20,DELGAM,
     +  CHI1,CHI2,SB,GAMDOTO,H1,H2,DF,DFO,G1,G10,G2,G20,SF,
```

```
+  PHI1,PHI2,PHI3

 COMMON / TOLERANCES / TOL1,TOL2,TOL3,TOL4,TOL5,TOLPHIO,
+  TOLPHI1,TOLPHI2,TOLPHI3,SMPHI1,SMPHI2,SMPHI3,FTOL,
+  TOL10,TOL20,TOL30,TOL40,TOL50

 COMMON / PARTIALS / DTAUDGDB,DTAUDF,DTAUDS1,DTAUDS2,
+  DS1DGDB,DS2DGDB,DGDBDS1,DS1DS1,DS2DS1,DFDS1,DGDBDS2,DS1DS2,
+  DS2DS2,DFDS2,DGDBDF,DS1DF,DS2DF,DFDGDB,DFDF,DTAUDP,
+  DADGDB,DADS1,DADS2,DADF,DFDOTDGDB,DFDOTDS1,DFDOTDS2,DFDOTDF

 COMMON / MATRICES / A1(5,5),A2(2,2),A3(3,3)

 COMMON / ATERMS / A11,A12,A13,A14,A21,A22,A23,A24,
+  A31,A32,A33,A34,A41,A42,A43,A44

 COMMON/CEL/LELOP,JETP,JETP1,KEL,KINTK,KINTL,KINTSL,KSPT,MEMCRD,
1 JINTYP,JEXTYP,JEXTY2,
2 JLIB,MAM24,MDOF,MCRD,MNODE,MNODU,MTEMS,MDI,MSHR,MPR,
3 MINTK,MINTM,MINTSL,MINTLL,MMP,MDS,MSHL,MBM,MELZM,MINTTS,
4 MEINT,MDOFEL,JUMSYM,MEGEOM,LMODEK,MMODEP,LBASIS,MMODET,MTEMST,
5 MTDOFM,
6 LLUMPM,MOFFT,MMODI,JELHYP,MDGRAD,LELLIN,LELUMS,MELSTV,IETAT1,
7 IETAT2,
8 MXDIM,JCMVCT,JSHAP,JEGRP,MELSPR(6),
9 MSPT,MMOD2,MMOD3,MMOD4,MTDOFE,KSPTT,MINR,MEMB,JUMSEL,MDIP1,
1 MEGEOP,LEMREV,KLPT

 COMMON/COUNT/KINC,MINC,KITER,MITER,FATIME,ATIME,DATIME,
1 CTIME,DCTIME,DTIME,DDTIME,HTIME,DHTIME,DDTPRE,DATPRE,HTIM1,
2 DHTIM2,EXFAC,KSTEP,KCUTS,MCUTS,NUMBER,LSHAF1,LCUTBK,DTNEWS,
3 KITGEM,KMDINC,TTIME,DTMIN,DTMAX,MITEIG,LTIMEO,STIME,DSTIME
4,TPREV,TNEW,TOLD,TEND,MITRK,KITRK,KTOTIT,KSOLIT,KSOLM,KTINC,
5 KACUT,MITLSA,FREQR,FREQC,DELFRQ(2),KITLS,MITLS,DTNEW,DTOLD,
6 ODTOLD
```

Appendix B

Constitutive Subroutine Test Program

The driver program listed on the following page is able to simulate integration of the constitutive model for some hypothetical kinematical history, or it can be used in conjunction with an actual ABAQUS run to identify bugs in the subroutine which manifest themselves only for certain sets of input data. The integration procedure fails for such cases, and it becomes necessary to provide the driver program with the precise values of the data input into the UMAT during the actual ABAQUS run. This is accomplished through the CHECKINP routine of the UMAT, which prints out the value of all the parameters passed into the subroutine. These values can then be inserted into the driver program. The UMAT can then be debugged using the dbx or dbxtool procedures which are available on the Sun workstations or the Alliant machine (dbx only).

Testing the accuracy of the Jacobians was accomplished by comparing the predicted analytical Jacobian with a numerical estimation of the Jacobian obtained through finite difference techniques. For example, a numerical prediction of the Jacobian passed back to ABAQUS is obtained by implementing the numerical Jacobian calculation routine JACOBNUM (a part of the UMAT subroutine), instead of the standard analytical Jacobian calculation routine JACOBANAL.

```
      PROGRAM UMATDRIV

C     this program drives umat.f

      IMPLICIT REAL*8 (A-H,O-Z)

      DIMENSION STRESS(4),STATEV(19),
     +   DDSDDE(4,4),
     +   DDSDDT(4),DRPLDE(4),
     +   STRAN(4),DSTRAN(4),PREDEF(1),DPRED(1),PROPS(27),
     +   COORDS(3),DROT(3,3)
      CHARACTER*8 CMNAME
      DATA PROPS/ 1.75D5,8.077D4,4.0D0,0.060D0,0.120D0,
     +  903.7D0,1307.0D0,0.013D0,0.019D0,4.33,0.00D0,3230.0D0,
     +  292.0D0,4.42D0,100.00D0,3400.0D0,4.7D0,4.93D2,100.D0,
     +  0.0070D0,0.02,0.02,1.0,0.04,0.20,,0.0D0,0.0D0/

      NTENS1= 4
      NDI1= 3
      NSHR1= 1
      NPROPS = 27
      NSTATV = 18
      DTIME1 = 1.0D0
      STATEV(1) = 0.0D0
      STATEV(2) = 0.0D0
      STATEV(3) = 0.0D0
      STATEV(4) = 0.0D0
      STATEV(5) = 0.0D0
      STATEV(6) = THIRD
      STATEV(7) = 0.0D0
      STATEV(8) = 0.0D0
      STATEV(9) = 0.0D0
      STATEV(10) = 0.0D0
      STATEV(11) = 0.0D0
      STATEV(12) = 0.0D0
      STATEV(13) = 0.0D0
      STATEV(14) = 1000.0D0
      STATEV(16) = 0.0D0
      STATEV(17) = 0.0D0
      STRESS(1) = 0.0D0
      STRESS(2) = 0.0D0
      STRESS(3) = 0.0D0
      STRESS(4) = 0.0D0
      DO 50 I = 1,100
      DSTRAN(1)=-2.25E-04 * 6.0D0
      DSTRAN(2)=2.50E-04 * 6.0D0
      DSTRAN(3)=0.0
      DSTRAN(4)=0.5E-3
      DTIME1 = 1.0
      SSE = 0.0D0
      SPD = 0.0D0
      SCD = 0.0D0
      RPL = 0.0D0
      CALL UMAT(STRESS,STATEV,DDSDDE,
     + SSE,SPD,SCD,
     + RPL,DDSDDT,DRPLDE,DRPLDT,
     + STRAN,DSTRAN,TIME,DTIME1,TEMP,DTEMP,PREDEF,DPRED,CMNAME,
     + NDI1,NSHR1,NTENS1,NSTATV,PROPS,NPROPS,COORDS,DROT)

C     IF (MOD(I,10).EQ.0) THEN
      WRITE(12,*) ' '
      WRITE(12,*) ' '
      WRITE(12,*) '****  INCREMENT  ',I,'  ****'
      WRITE(12,*) ' '
      WRITE(12,*) ' '
      WRITE(12,*) ' '
      DO 11 J = 1,NTENS1
      WRITE(12,*) (DDSDDE(J,K), K = 1,NTENS1)
   11 CONTINUE
      WRITE(12,*) ' '
      WRITE(12,*) 'STRESS COMPONENTS'
      WRITE(12,*) ' '
      WRITE(12,4) (STRESS(K), K = 1,NTENS1)
      WRITE(12,*) ' '
      WRITE(12,*) 'STATE VARIABLES '
      WRITE(12,*) ' '
      WRITE(12,4) (STATEV(K), K = 1,4)
      WRITE(12,4) (STATEV(K), K = 5,8)
      WRITE(12,4) (STATEV(K), K = 9,12)
      WRITE(12,4) (STATEV(K), K = 13,16)
      WRITE(12,4) (STATEV(K), K = 17,19)
C     ENDIF
   50 CONTINUE
  100 FORMAT(4(2X,F12.3))
  200 FORMAT(8(2X,F12.3))
    4 FORMAT(4(2X,D12.6))
    5 FORMAT(2X,D12.6)
      STOP
      END
      SUBROUTINE SIEV(STRESS,SIEV1,SIEV2)
```

```
      IMPLICIT REAL*8(A-H,O-Z)
      DIMENSION STRESS(4)
      ZERO = 0.0D0
      SINV1 = ZERO
      DO 10 J = 1,3
   10 SINV1 = SINV1 + STRESS(J)
      SINV1 = SINV1/3.0D0
      SINV2 = ZERO
      RETURN
      END
```

Appendix C

Derivation of Equations (3.92) and (3.94)

In this appendix we provide a few details concerning the derivation of the ratio of differences in stress and strain-rate for the two-phase material (3.92). We then derive the approximate integrated form (3.94).

We begin by repeating equations (3.90a) and (3.90b):

$$\frac{\tau_2 - \tau_1}{\overline{\tau}} = \frac{5\mu_2}{3\overline{\mu} + 2\mu_2} - \frac{5\mu_1}{3\overline{\mu} + 2\mu_1} \; ; \tag{C.1}$$

$$\frac{\dot{\gamma}_1 - \dot{\gamma}_2}{\dot{\overline{\gamma}}} = \frac{5\overline{\mu}}{3\overline{\mu} + 2\mu_1} - \frac{5\overline{\mu}}{3\overline{\mu} + 2\mu_2}. \tag{C.2}$$

Dividing (C.1) by (C.2), combining fractions, and canceling the arbitrary factor $(3\overline{\mu} + 2\mu_2)(3\overline{\mu} + 2\mu_1)$, we find that

$$\frac{\dfrac{\tau_2 - \tau_1}{\overline{\tau}}}{\dfrac{\dot{\gamma}_1 - \dot{\gamma}_2}{\dot{\overline{\gamma}}}} = \frac{(3\overline{\mu} + 2\mu_1)\,\mu_2 - (3\overline{\mu} + 2\mu_2)\,\mu_1}{(3\overline{\mu} + 2\mu_2)\,\overline{\mu} - (3\overline{\mu} + 2\mu_1)\,\overline{\mu}} \; ; \tag{C.3}$$

Simplifying, this becomes

$$\frac{\dfrac{\tau_2 - \tau_1}{\overline{\tau}}}{\dfrac{\dot{\gamma}_1 - \dot{\gamma}_2}{\dot{\overline{\gamma}}}} = \frac{3\,(\mu_2 - \mu_1)}{2\,(\mu_2 - \mu_1)} = \frac{3}{2} \; . \tag{C.4}$$

To derive the integrated form (3.94), we first note the the following approximation:

$$\gamma = \int_0^t \dot{\gamma} dt \approx \sum_{i=1}^{N} \dot{\gamma} \Delta t \; . \tag{C.5}$$

With this approximation, we can write the normalized difference in *strains* between the two phases as

$$\frac{\gamma_1 - \gamma_2}{\overline{\gamma}^p} = \frac{\sum_0^t \dot{\gamma}_1 \Delta t - \sum_0^t \dot{\gamma}_2 \Delta t}{\sum_0^t \dot{\overline{\gamma}} \Delta t} . \tag{C.6}$$

Substituting for $\dot{\gamma}_1$ and $\dot{\gamma}_2$ using the Eshelby-type relations (3.59a),

$$\frac{\gamma_1 - \gamma_2}{\overline{\gamma}^p} = \frac{\sum_0^t \frac{5\overline{\mu}}{3\overline{\mu}+2\mu_1} \dot{\overline{\gamma}} \Delta t - \sum_0^t \frac{5\overline{\mu}}{3\overline{\mu}+2\mu_2} \dot{\overline{\gamma}} \Delta t}{\sum_0^t \dot{\overline{\gamma}} \Delta t} . \tag{C.7}$$

When $n_1 = n_2$, the Eshelby ratios do not change to any appreciable degree during the strain history, so they can be brought outside the summation:

$$\frac{\gamma_1 - \gamma_2}{\overline{\gamma}^p} \approx \frac{\frac{5\overline{\mu}}{3\overline{\mu}+2\mu_1} \sum_0^t \dot{\overline{\gamma}} \Delta t - \frac{5\overline{\mu}}{3\overline{\mu}+2\mu_2} \sum_0^t \dot{\overline{\gamma}} \Delta t}{\sum_0^t \dot{\overline{\gamma}} \Delta t} . \tag{C.8}$$

On canceling the arbitrary term $\sum_0^t \dot{\overline{\gamma}} \Delta t$,

$$\frac{\gamma_1 - \gamma_2}{\overline{\gamma}^p} \approx \frac{5\overline{\mu}}{3\overline{\mu} + 2\mu_1} - \frac{5\overline{\mu}}{3\overline{\mu} + 2\mu_2} . \tag{C.9}$$

Multiplying numerator and denominator by $\dot{\overline{\gamma}}$:

$$\frac{\gamma_1 - \gamma_2}{\overline{\gamma}^p} \approx \frac{1}{\dot{\overline{\gamma}}} \left(\frac{5\overline{\mu}}{3\overline{\mu} + 2\mu_1} \dot{\overline{\gamma}} - \frac{5\overline{\mu}}{3\overline{\mu} + 2\mu_2} \dot{\overline{\gamma}} \right) . \tag{C.10}$$

Finally, making use of the (3.59a) again, we find that

$$\frac{\gamma_1 - \gamma_2}{\overline{\gamma}^p} \approx \frac{\dot{\gamma}_1 - \dot{\gamma}_2}{\dot{\overline{\gamma}}} . \tag{C.11}$$

Appendix D

Application of Pressure Loads for Constant Triaxiality Boundary Conditions

In order to apply a constant triaxiality at the remote boundary of the cell problem (section 4.3), we used the DLOAD subroutine listed on the following page.

```
      SUBROUTINE DLOAD(F,KSTEP,KINC,TIME,NOEL,NPT,COORDS,JLTYP)
      IMPLICIT REAL*8 (A-H,O-Z)
      DELTA = 0.20D0
      GAMMAO = 0.013D0
      S10 = 903.7D0
      EN = .06D0
      EY = 0.00574D0
      YOUNG = 210000.0D0
      EPSLN = DLOG(1.0D0 + DELTA*TIME/100.0D0)
      GAMMA = DSQRT(3.0D0)*EPSLN
      S = S10*(GAMMA + GAMMAO)**EN
      TAU = S
      SIGMA = DSQRT(3.0D0)*TAU
      IF (EPSLN.LT.EY) THEN
      F = -0.80D0*EPSLN*YOUNG
      ELSE
      F = -0.80D0*SIGMA
      ENDIF
      IF (NPT.EQ.1.AND.NOEL.EQ.1) THEN
      WRITE (6,*) 'time = ',TIME
      write(6,*) 'epsln,f = ',epsln,f
      ENDIF
      RETURN
      END
```

Appendix E

Calculation of Mode I Asymptotic Crack-Tip Field Displacement Boundary Conditions

In order to model the fields near a plane-strain crack in an infinite body undergoing mode I (tensile opening) loading, it is necessary to develop relationships which determine the displacement boundary conditions which can be applied along the outer edge of the mesh, as illustrated in Fig. 4.25. Prescribing these displacements essentially imposes the asymptotic crack-tip stress and strain fields within this boundary, such that only the stress intensity factor, K_I, influences the crack tip behavior. In structuring the problem in this manner, this region can be considered to be well within the influence of any characteristic length parameters (e.g., crack length, a, specimen width, b), other than K_I.

This appendix outlines some of the details of the problem of a semi-infinite crack in an infinite body under plane-strain conditions subject to mode I (tensile opening) far-field loading. Details of the lengthy derivation of the general asymptotic stress fields, which involve use of equilibrium, mid-plane symmetry and plane-strain stress-strain relationships are not presented here. It can be shown, however, through solution of an appropriate harmonic equation derived from the compatibility condition, that the

stress field surrounding the crack tip is given by:

$$\sigma_{\theta\theta} = \sum_{\lambda} r^{\lambda} \left\{ A_{\lambda} \cos \lambda\theta + B_{\lambda} \cos\left(\lambda + 2\right)\theta \right\} \left(\lambda + 2\right)\left(\lambda + 1\right), \tag{E.1}$$

$$\begin{aligned} \sigma_{rr} &= \sum_{\lambda} r^{\lambda} \left\{ \left[\left(\lambda + 2\right) - \lambda^2 \right] A_{\lambda} \cos \lambda\theta \right. \\ &+ \left. \left[\left(\lambda + 2\right) - \left(\lambda + 2\right)^2 \right] B_{\lambda} \cos\left(\lambda + 2\right)\theta \right\}, \end{aligned} \tag{E.2}$$

$$\sigma_{r\theta} = \sum_{\lambda} r^{\lambda} \left(\lambda + 1\right) \left\{ \lambda A_{\lambda} \sin \lambda\theta + \left(\lambda + 2\right) B_{\lambda} \sin\left(\lambda + 2\right)\theta \right\}, \tag{E.3}$$

where r is the radial distance from the crack tip, θ is the angle measured from the mid-plane of the crack, and λ represents suitable real powers derived from a series expansion of an analytic solution to the harmonic equation. For a more complete derivation of these fields, see Williams [148]. Traction free boundary conditions along the surface of the crack; i.e., at $\theta = \pm\pi$, require that:

$$\sigma_{\theta\theta} \mid_{\theta=\pm\pi} = 0 \implies \left[A_{\lambda} + B_{\lambda}\right] \cos \lambda\pi = 0, \tag{E.4}$$

$$\sigma_{r\theta} \mid_{\theta=\pm\pi} = 0 \implies \left[\lambda A_{\lambda} + \left(\lambda + 2\right) B_{\lambda}\right] \sin \lambda\pi = 0 \tag{E.5}$$

for each λ-power in the expansion. This requirement can be met in one of two ways. The first solution demands that:

$$\sin \lambda\pi = 0 \implies \lambda = \cdots, -2, -1, 0, 1, \cdots, \tag{E.6}$$

in which case:

$$A_{\lambda} + B_{\lambda} = 0. \tag{E.7}$$

In the second possible scenario,

$$\cos \lambda\pi = 0 \implies \lambda = \cdots, -\frac{1}{2}, \frac{1}{2}, \frac{3}{2}, \cdots, \tag{E.8}$$

in which case:

$$\lambda A_{\lambda} + \left(\lambda + 2\right) B_{\lambda} = 0. \tag{E.9}$$

Using the plane-strain elastic stress-strain relationships, the strain field can be expressed as:

$$\begin{aligned}
\epsilon_{\theta\theta} &= \sum_{\lambda} \frac{1+\nu}{E} r^{\lambda} \left[\left\{ (\lambda+1)(\lambda+2)(1-\nu) - \nu \left[\lambda + 2 - \lambda^2 \right] \right\} A_{\lambda} \cos \lambda\theta \right. \\
&- \left. \left[\left\{ \nu(\lambda+1)(\lambda+2) + \nu \left[(\lambda+2) - (\lambda+2)^2 \right] \right\} \cos(\lambda+2)\theta \right], \qquad \text{(E.10)} \\
\epsilon_{rr} &= \sum_{\lambda} \frac{1+\nu}{E} r^{\lambda} \left[\left\{ (\lambda+1)(\lambda+2)(1-\nu) - \nu \left[\lambda + 2 - \lambda^2 \right] \right\} A_{\lambda} \cos \lambda\theta \right. \\
&- \left. \left\{ \nu(\lambda+1)(\lambda+2) + \nu \left[(\lambda+2) - (\lambda+2)^2 \right] \right\} \cos(\lambda+2)\theta \right], \qquad \text{(E.11)} \\
\gamma_{r\theta} &= \sum_{\lambda} \frac{1+\nu}{E} r^{\lambda} \left[\left\{ (\lambda+1)(\lambda+2)(1-\nu) - \nu \left[\lambda + 2 - \lambda^2 \right] \right\} A_{\lambda} \cos \lambda\theta \right. \\
&- \left. \left\{ \nu(\lambda+1)(\lambda+2) + \nu \left[(\lambda+2) - (\lambda+2)^2 \right] \right\} \cos(\lambda+2)\theta \right]. \qquad \text{(E.12)}
\end{aligned}$$

From strain-displacement relationships,

$$u_r(r,\theta) = \int_0^r \epsilon_{rr} dr + F(\theta). \qquad \text{(E.13)}$$

The constant of integration $F(\theta)$ represents a rigid body motion of the crack tip, which can be set equal to zero, essentially pinning the crack at $r = 0$. Thus:

$$\begin{aligned}
u_r &= \sum_{\lambda} \frac{1+\nu}{E} \frac{r^{\lambda+1}}{\lambda+1} \left[\left\{ \left[(\lambda+2) - \lambda^2 \right] (1-\nu) - \nu(\lambda+2)(\lambda+1) \right\} A_{\lambda} \cos \lambda\theta \right. \\
&+ \left. \left\{ \left[(\lambda+2) - (\lambda+2)^2 \right] (1-\nu) - \nu(\lambda+2)(\lambda+1) \right\} B_{\lambda} \cos(\lambda+2)\theta \right]. \qquad \text{(E.14)}
\end{aligned}$$

Similarly,

$$u_{\theta}(r,\theta) = \int_0^{\theta} \left[r\epsilon_{rr} - u_r \right] d\theta + F(r), \qquad \text{(E.15)}$$

and $F(r)$ can also be set to zero. Therefore, u_{θ} is given by:

$$\begin{aligned}
u_{\theta} &= \sum_{\theta} \frac{1+\nu}{E} r^{\lambda+1} \left[\lambda^{-1} \left\{ (\lambda+1)(\lambda+2-4\nu) - (2-\lambda-4\nu) \right\} A_{\lambda} \sin \lambda\theta \right. \\
&+ \left. (\lambda+2) B_{\lambda} \sin(\lambda+2)\theta \right]. \qquad \text{(E.16)}
\end{aligned}$$

The strain energy contained within a circular region of radius R_0 centered at the crack tip is given by:

$$W_{R_0} = \int_{-\pi}^{\pi} d\theta \int_0^{R_0} r dr \mathcal{W}(r,\theta), \qquad \text{(E.17)}$$

where $\mathcal{W}$ represents elastic strain energy density. It can be shown that $\mathcal{W}$ is proportional to $r^{2\lambda}$, so that in order that this expression does not diverge as $r \to 0$, it is required that $\lambda > -1$. With these restrictions, the $\lambda = -1/2$ term is the only singular term in the expansion of the stress field, while the $\lambda = 0$ term corresponds to a locally constant stress field, and thus in order to satisfy the traction free boundary conditions must represent a uniform loading parallel to the crack. The values of λ greater than zero vanish for the stress field as $R \to 0$, leaving the following expressions for the near-tip stress fields:

$$\sigma_{\theta\theta} = \frac{K_I}{(2\pi r)^{1/2}} \left\{ \frac{3}{4}\cos\frac{\theta}{2} + \frac{1}{4}\cos\frac{3\theta}{2} \right\}, \tag{E.18}$$

$$\sigma_{r\theta} = \frac{K_I}{(2\pi r)^{1/2}} \left\{ \frac{1}{4}\sin\frac{\theta}{2} + \frac{1}{4}\sin\frac{3\theta}{2} \right\}, \tag{E.19}$$

$$\sigma_{rr} = \frac{K_I}{(2\pi r)^{1/2}} \left\{ \frac{1}{4}\cos\frac{\theta}{2} - \frac{1}{4}\cos\frac{3\theta}{2} \right\}. \tag{E.20}$$

where the stress intensity factor, K_I, is defined such that:

$$A_{-1/2} = 3B_{-1/2} = \frac{K_I}{(2\pi r)^{1/2}}. \tag{E.21}$$

The displacement fields are then given by:

$$u_r = \frac{K_I(1+\nu)}{(2\pi r)^{1/2}} \left\{ \left(\frac{5}{2} - 4\nu\right)\cos\frac{\theta}{2} - \frac{1}{2}\cos\frac{3\theta}{2} \right\}, \tag{E.22}$$

$$u_\theta = \frac{K_I(1+\nu)}{(2\pi r)^{1/2}} \left\{ \left(4\nu - \frac{7}{2}\right)\sin\frac{\theta}{2} + \frac{1}{2}\sin\frac{3\theta}{2} \right\}. \tag{E.23}$$

In a Cartesian basis, these relationships are given by:

$$u_x = \frac{K_I(1+\nu)}{(2\pi r)^{1/2}} \left\{ (3 - 4\nu - \cos\theta)\cos\frac{\theta}{2} \right\}, \tag{E.24}$$

$$u_x = \frac{K_I(1+\nu)}{(2\pi r)^{1/2}} \left\{ (3 - 4\nu - \cos\theta)\sin\frac{\theta}{2} \right\}. \tag{E.25}$$

The local stress and displacement fields, therefore, scale linearly with the loading parameter, K_I.

The asymptotic stress and displacement fields can therefore be imposed in a finite element analysis of the mode I plane-strain crack tip problem by specifying this displacement field at the appropriate boundary nodes. Since these relationships are based on elastic stress fields, this asymptotic stress field is valid only as long as the plastic zone is small compared to the radius upon which these boundary displacements are applied, so that the influence of plasticity is minimal by St. Venant's principle.

These relationships are introduced into ABAQUS via a user subroutine option called MPC, which is listed at the end of this section. For more details on the contents of the subroutine, refer to the ABAQUS User's Manual [103].

E.1 MPC Subroutine Listing

The FORTRAN listed below performs the operations outlined in this appendix. It is written in a general form so that up to four λ terms can be included in the series.

```
      SUBROUTINE MPC(UE,A,JDOF,M,JTYPE,X,U,NMPCE)
C*****************************************************************
C
C  This subroutine connects the elastic K field theoretical solution
C  to the FE grid at the outer boundary of the grid. It is written
C  to take into account up to four terms of the solution expansion.
C
C*****************************************************************
      IMPLICIT REAL*8 (A-H,O-Z)
      DIMENSION A(M), JDOF(M), X(6,M), U(6,M)
C*****************************************************************
C
C  Common block CONSTS appears here exactly as it exists in ABAQUS
C  version 4-5-159.  It will generally be different for other ABAQUS
C  versions.
C
C*****************************************************************
      COMMON/CONSTS/PI,SIN60,COS60,KCROS2(3),KCROS3(3),ZERO,LZERO,LONE,
     +  ONE,TWO,HALF,ABIG,ASMALL,BCBIG,LOCSHR(2,3),THIRD,PRECIS,BLANK
C*****************************************************************
C
C  Define constants.
C
C*****************************************************************
      E = 2.1D5
      V = 0.30D0
      EPRM = (ONE + V)/E
      SQPI = .3989422D0
      FOUR = TWO*TWO
      FOUR_V = FOUR*V
      ONEPT5 = 1.5D0
      TWOPT5 = 2.5D0
      THRPT5 = 3.5D0
      FORPT5 = 4.5D0
      EXP3 = -1.5D0
C*****************************************************************
C
C  Determine current position of node and find its R and THETA.
C
C*****************************************************************
      XT = X(1,1) + U(1,1)
      YT = X(2,1) + U(2,1)
      R = DSQRT(XT**2 + YT**2)
      IF (XT.EQ.ZERO) THEN
      THETA = PI/2
      GOTO 10
      END IF
      THETA = DATAN(YT/XT)
      IF (XT.LT.ZERO) THETA = THETA + PI
C*****************************************************************
C
C  Determine all necessary trigonometric functions.
C
C*****************************************************************
   10 SINTH = DSIN(THETA)
      COSTH = DCOS(THETA)
      SIN12 = DSIN(HALF*THETA)
      COS12 = DCOS(HALF*THETA)
      SIN32 = DSIN(ONEPT5*THETA)
      COS32 = DCOS(ONEPT5*THETA)
      SIN42 = DSIN(TWO*THETA)
      COS42 = DCOS(TWO*THETA)
      SIN52 = DSIN(TWOPT5*THETA)
      COS52 = DCOS(TWOPT5*THETA)
C*****************************************************************
C
C  Determine Fr(THETA,V) and Ftheta(THETA,V) for all 4 coefficients.
C
C*****************************************************************
      FR12 = EPRM*DSQRT(R)*((TWOPT5 - FOUR_V)*COS12 - HALF*COS32)
      FR32 = EPRM*DSQRT(1/R)*((THRPT5 - FOUR_V)*COS32 - ONEPT5*COS12)
      FR42 = EPRM*(1/R)*(FOUR - FOUR_V)*COS42
      FR52 = EPRM*(R**EXP3)*((FORPT5 - FOUR_V)*COS52 - TWOPT5*COS12)
      FT12 = EPRM*DSQRT(R)*(-(THRPT5 - FOUR_V)*SIN12 + HALF*SIN32)
      FT32 = EPRM*DSQRT(1/R)*(-(TWOPT5 - FOUR_V)*SIN32 + ONEPT5*SIN12)
      FT42 = EPRM*(1/R)*(-(TWO - FOUR_V)*SIN42)
      FT52 = EPRM*(R**EXP3)*(-(ONEPT5 - FOUR_V)*SIN52 - TWOPT5*SIN12)
C*****************************************************************
C
C  Determine K-field displacements at boundary.
C
C*****************************************************************
      UR = U(1,2)*SQPI*FR12 + U(2,3)*FR32 + U(1,4)*FR42 + U(2,5)*FR52
      UT = U(1,2)*SQPI*FT12 + U(2,3)*FT32 + U(1,4)*FT42 + U(2,5)*FT52
C*****************************************************************
C
C  Go to appropriate routine depending on J-type (dof-1 or dof-2)
C
C*****************************************************************
      GOTO (1,2) JTYPE
```

```
C**********************************************************************
C
C  Determine MPC equation to eliminate FE dof-1 in favor of K-field
C  displacements.
C
C**********************************************************************
    1 UE = UR*COSTH - UT*SINTH
C**********************************************************************
C
C  Determine derivatives of all displacement components (used in
C  ABAQUS)
C
C**********************************************************************
      A(1) = 1.
      A(2) = -FR12*SQPI*COSTH + FT12*SQPI*SINTH
      A(3) = -FR32*COSTH + FT32*SINTH
      A(4) = -FR42*COSTH + FT42*SINTH
      A(5) = -FR52*COSTH + FT52*SINTH
C**********************************************************************
C
C  Give dof's corresponding to the nodes given on the *MPC card as used
C  in this routine.
C
C**********************************************************************
      JDOF(1) = 1
      JDOF(2) = 1
      JDOF(3) = 2
      JDOF(4) = 1
      JDOF(5) = 2
      GOTO 300
C**********************************************************************
C
C  Determine MPC equation to eliminate FE dof-2 in favor of K-field
C  displacements.
C
C**********************************************************************
    2 UE = UR*SINTH + UT*COSTH
C**********************************************************************
C
C  Determine derivatives of all displacement components (used in
C  ABAQUS)
C
C**********************************************************************
      A(1) = 1.
      A(2) = -FT12*SQPI*COSTH - FR12*SQPI*SINTH
      A(3) = -FT32*COSTH - FR32*SINTH
      A(4) = -FT42*COSTH - FR42*SINTH
      A(5) = -FT52*COSTH - FR52*SINTH
C**********************************************************************
C
C  Give dof's corresponding to the nodes given on the *MPC card as used
C  in this routine.
C
C**********************************************************************
      JDOF(1) = 2
      JDOF(2) = 1
      JDOF(3) = 2
      JDOF(4) = 1
      JDOF(5) = 2
  300 RETURN
      END
```

Appendix F

Mildly-notched Mesh Generation Program

The program listed on the following page was used to generate the ABAQUS geometric input data for the mildly-notched bar shown in Fig. 5.14. This program is sufficiently general for generation of notched-bars of various sizes geometries.

```
      PROGRAM NOTCH
IMPLICIT REAL*8 (A-H,O-Z)
DIMENSION Z(10000),Y(10000),R(10000),Y2(10000),Z2(10000)
      DIMENSION Z1(10000),Y1(10000)
CHARACTER*60 NAME

PRINT*, ' ENTER FILE NAME IN QUOTES.....   '
READ *,NAME
PRINT *, ' NOTCH RADIUS .................   '
READ *, A
      PRINT *, ' LENGTH OF LIGAMENT.............   '
      READ *, B1
      PRINT *, ' RADIUS OF BAR.................   '
      READ *, B
PRINT *, ' NUMBER OF NODES ALONG THE HOLE.   '
READ *, NANT
PRINT *, ' NUMBER OF NODES ALONG RADII....   '
READ *, NRE
PRINT *, ' TOTAL LENGTH OF BAR   .........   '
READ *, C
PRINT *, ' NUMBER OF ELEMENTS ALONG FLANK   '
READ *, NNOT
PRINT *, ' BIAS OF SPACING ALONG NOTCH...   '
READ *, BIAS2

OPEN(12,STATUS='NEW',FILE=NAME)
WRITE(12,1100) C,B,B1,A

      NBELOW2 = 0
      NDELT1 = 100
      NDELT2 = 2*NDELT1
      NNOT1 = NNOT - 1

NAET=NANT-1
NAN=NANT/2+1
NAE=NAN-1
NRE=NRE-1

ANGO=DATAN(1.DO)
PI=4.DO*ANGO
A1=B1/NRE

      ISKIP = -1
      TWOA = A + B1
      IF (TWOA.GT.B) THEN
      THETAO = DASIN((TWOA - B)/A)
      ISKIP = INT(4.0*NAE*THETAO/PI)
      WRITE(6,*) 'THETAO, SKIP =',THETAO,'  ',ISKIP
PRINT *, ' NUMBER OF NODES TO SKIP (EVEN)   '
READ *, ISKIP
      ENDIF

      NAN1 = NAN
      NAE1 = NAE
      IF (TWOA.LT.B) THEN
PRINT *, ' NUMBER OF ELS BELOW NOTCH (EVEN)  '
READ *, NBELOW
      NBELOW2 = NBELOW*2
      NAN1 = NAN + NBELOW2
      NAE1 = NAE + NBELOW2
      ENDIF

DO I=1,NAN1
DO J=1,NRE
      DIST=A + A1*(J-1)

      IJUMP = 0
      IF (I.LE.NBELOW2) THEN
      IJUMP = 1
      NODE = NDELT1*(I-1) + J
      Z(NODE) = DIST
      Y(NODE) = (B - TWOA)*(1.0*(1.0*(I-1)/NBELOW2))**0.8
      R(NODE) = B - Y(NODE)
WRITE(12,1000)NODE,R(NODE),Z(NODE)
      ENDIF
      IF (IJUMP.EQ.1) GOTO 666

      ANGBIAS = 0.8DO
ANG=PI*.25DO*(1.0* (I-1-NBELOW2)/NAE )**ANGBIAS

P=2.*NRE/(NRE-J)
      DIST11 = A*DCOS(THETAO)
      DIST1 = DIST11 + (TWOA - DIST11)*(J-1)/NRE
RAD=DIST*(DCOS(ANG)**P+DSIN(ANG)**P)**(-1.DO/P)
NODE=NDELT1*(I-1)+J
Z(NODE)=RAD*DCOS(ANG)
Y(NODE)=RAD*DSIN(ANG)
      NOD=NODE
      FACTOR = (4.0*ANG/PI - DTAN(ANG) )*((A/B1)**2)
      IF (ANG.NE.0.0) THEN
```

```
        Y(NODE) = Z(NODE) * (DTAN(ANG) +
     +  (   ( (Z(NODE)/(A)) - 1.0 )**2   )*FACTOR)
        ENDIF
        R(NODE) = TWOA - Y(NODE)

        IF (ISKIP.GE.0) THEN
        IF (I.GT.ISKIP) THEN
        YO = TWOA - B
C       IF (J.EQ.1) WRITE(6,*) 'YO      ',YO
        ZO = YO
C       RAD2 = RAD - DSQRT(2.0D0)*YO
        THETA1 = DATAN((TWOA - B)/DIST1)
        THETA = THETA1 + (PI*.25D0 - THETA1)*(I-1-ISKIP)/(NAE - ISKIP)
RAD2=DIST*(DCOS(THETA)**P+DSIN(THETA)**P)**(-1.D0/P)
Z2(NODE)=RAD2*DCOS(THETA)
Y21=RAD2*DSIN(THETA)
        FACTOR2 = (  (1.0D0/Z2(NODE))*(ZO + ( Z2(NODE) - ZO )
     +    *(THETA - THETA1)/(0.25D0*PI - THETA1) ) ) - DTAN(THETA)
        FACTOR2 = FACTOR2*( (A/B1)**2)
        IF (ISKIP.GE.0.AND.I.EQ.1+ISKIP) THEN
        Y2(NODE) = YO
        ELSE
        Y2(NODE) = Z2(NODE) * (DTAN(THETA) +
     +  (   ( (Z2(NODE)/(A)) - 1.0D0)**2   )*FACTOR2)
        ENDIF
        R(NODE) = TWOA - Y2(NODE)
WRITE(12,1000)NOD,R(NODE),Z2(NODE)
        ENDIF
        ELSE
WRITE(12,1000)NOD,R(NODE),Z(NODE)
        ENDIF
666     CONTINUE
ENDDO

NODE=NRM+NDELT1*(I-1)
Z(NODE)=TWOA

        IJUMP = 0

        IF (I.LE.NBELOW2) THEN
        IJUMP = 1
        Y(NODE) = (B - TWOA)*(1.0*(1.0*(I-1)/NBELOW2))**0.8
        R(NODE) = B - Y(NODE)
WRITE(12,1000)NODE,R(NODE),Z(NODE)
        ENDIF

        IF (IJUMP.EQ.1) GOTO 667
Y(NODE)=TWOA*4.0D0*ANG/PI
        IF (ANG.NE.0.0) THEN
        Y(NODE) = Z(NODE) * (DTAN(ANG) +
     +  (   ( (Z(NODE)/(A)) - 1.0 )**2   )*FACTOR)
        ENDIF
        NOD=NODE
        FACTOR = ( 4.0*ANG/PI - DTAN(ANG) ) * ( (A/B1)**2)
        IF (ANG.NE.0.0) THEN
        Y(NODE) = Z(NODE) * (DTAN(ANG) +
     +  (   ( (Z(NODE)/(A)) - 1.0 )**2   )*FACTOR)
        ENDIF
        R(NODE) = TWOA - Y(NODE)

        IF (ISKIP.GE.0) THEN
        IF (I.GT.ISKIP) THEN
        Z2(NODE) = TWOA
        Y2(NODE) = YO + B*(I-1-ISKIP)/(NAE - ISKIP)
C       WRITE(6,* 'end Y,Y2 ',Y(NODE),Y2(NODE)
C       WRITE(6,* 'end Z,Z2 ',Z(NODE),Z2(NODE)
        R(NODE) = TWOA - Y2(NODE)
WRITE(12,1000)NOD,R(NODE),Z2(NODE)
        ENDIF
667     CONTINUE
        ELSE
WRITE(12,1000)NOD,R(NODE),Z(NODE)
        ENDIF
ENDDO


PRINT *, ' NUMBER OF NODES ALONG THE HOLE.    '
READ *, NANT

OPEN(12,STATUS='NEW',FILE=NAME)

        NBELOW2 = 0
        NDELT1 = 100
        NDELT2 = 2*NDELT1
        NNOT1 = NNOT - 1

NAET=NANT-1
NAN=NANT/2+1
NAE=NAN-1
NRE=NRM-1
```

```
ANGO=DATAN(1.DO)
PI=4.DO*ANGO
A1=B1/NRE

        ISKIP = -1
        TWOA = A + B1
        IF (TWOA.GT.B) THEN
        THETAO = DASIN((TWOA - B)/A)
        ISKIP = INT(4.0*NAE*THETAO/PI)
PRINT *, ' NUMBER OF NODES TO SKIP (EVEN)    '
READ *, ISKIP
        ENDIF

        NAN1 = NAN
        NAE1 = NAE
        IF (TWOA.LT.B) THEN
PRINT *, ' NUMBER OF ELS BELOW NOTCH (EVEN)  '
READ *, NBELOW
        NBELOW2 = NBELOW*2
        NAN1 = NAN + NBELOW2
        NAE1 = NAE + NBELOW2
        ENDIF

DO I=1,NAN1
DO J=1,NRE
        DIST=A + A1*(J-1)

        IJUMP = 0
        IF (I.LE.NBELOW2) THEN
        IJUMP = 1
        NODE = NDELT1*(I-1) + J
        Z(NODE) = DIST
        Y(NODE) = (B - TWOA)*(1.0*(1.0*(I-1)/NBELOW2))**0.8
        R(NODE) = B - Y(NODE)
        ENDIF
        IF (IJUMP.EQ.1) GOTO 766

        ANG=PI*.25DO*(1.0* (I-1-NBELOW2)/NAE )**ANGBIAS
P=2.*NRE/(NRE-J)
        DIST11 = A*DCOS(THETAO)
        DIST1 = DIST11 + (TWOA - DIST11)*(J-1)/NRE
RAD=DIST*(DCOS(ANG)**P+DSIN(ANG)**P)**(-1.DO/P)
NODE=NDELT1*(I-1)+J
Z(NODE)=RAD*DCOS(ANG)
Y(NODE)=RAD*DSIN(ANG)
        NOD=NODE
        FACTOR = (4.0*ANG/PI - DTAN(ANG) )*((A/B1)**2)
        IF (ANG.NE.0.0) THEN
        Y(NODE) = Z(NODE) * (DTAN(ANG) +
     +  (   ( (Z(NODE)/(A)) - 1.0 )**2   )*FACTOR)
        ENDIF
        R(NODE) = TWOA - Y(NODE)

        IF (ISKIP.GE.0) THEN
        IF (I.GT.ISKIP) THEN
        YO = TWOA - B
        ZO = YO
C       RAD2 = RAD - DSQRT(2.0DO)*YO
        THETA1 = DATAN((TWOA - B)/DIST1)
        THETA = THETA1 + (PI*.25DO - THETA1)*(I-1-ISKIP)/(NAE - ISKIP)
RAD2=DIST*(DCOS(THETA)**P+DSIN(THETA)**P)**(-1.DO/P)
Z2(NODE)=RAD2*DCOS(THETA)
Y21=RAD2*DSIN(THETA)
        FACTOR2 = (  (1.0DO/Z2(NODE))*(ZO + ( Z2(NODE) - ZO )
     +    *(THETA - THETA1)/(0.25DO*PI - THETA1) ) ) - DTAN(THETA)
        FACTOR2 = FACTOR2*( (A/B1)**2)
        IF (ISKIP.GE.0.AND.I.EQ.1+ISKIP) THEN
        Y2(NODE) = YO
        ELSE
        Y2(NODE) = Z2(NODE) * (DTAN(THETA) +
     +  (   ( (Z2(NODE)/(A)) - 1.0DO)**2   )*FACTOR2)
        ENDIF
        R(NODE) = TWOA - Y2(NODE)
        ENDIF
        ELSE
        ENDIF
766     CONTINUE
ENDDO

NODE=NRN+NDELT1*(I-1)
Z(NODE)=TWOA

        IJUMP = 0

        IF (I.LE.NBELOW2) THEN
        IJUMP = 1
        Y(NODE) = (B - TWOA)*(1.0*(1.0*(I-1)/NBELOW2))**0.8
        R(NODE) = B - Y(NODE)
        ENDIF
        IF (IJUMP.EQ.1) GOTO 767
```

```
Y(NODE)=TWOA+4.0D0+ANG/PI
        IF (ANG.NE.0.0) THEN
        Y(NODE) = Z(NODE) + (DTAN(ANG) +
     +  (    ( (Z(NODE)/(A)) - 1.0 )**2    )*FACTOR)
        ENDIF
        NOD=NODE
        FACTOR = ( 4.0*ANG/PI - DTAN(ANG) ) * ( (A/B1)**2)
        IF (ANG.NE.0.0) THEN
        Y(NODE) = Z(NODE) + (DTAN(ANG) +
     +  (    ( (Z(NODE)/(A)) - 1.0 )**2    )*FACTOR)
        ENDIF
        R(NODE) = TWOA - Y(NODE)

        IF (ISKIP.GE.0) THEN
        IF (I.GT.ISKIP) THEN
        Z2(NODE) = TWOA
        Y2(NODE) = YO + B*(I-1-ISKIP)/(NAE - ISKIP)
        R(NODE) = TWOA - Y2(NODE)
        ENDIF
767     CONTINUE
        ELSE
        ENDIF
ENDDO
        NAN21 = (NAN1+1)/2 + NBELOW

DO I=1,NAE
DO J=1,NRE
NODE=NDELT1*(I-1)+NDELT1*NAN21+J
MIR=NDELT1*NAN1-NDELT1*(I+1)+J
Z1(NODE)=Y(MIR)
Y1(NODE)=Z(MIR)
        NOD=NODE
        R(NODE) = TWOA - Y1(NODE)
WRITE(12,1000)NOD,R(NODE),Z1(NODE)
ENDDO
ENDDO

PRINT *, ' NUMBER OF NODES ALONG THE HOLE.    '
READ *, NANT

OPEN(12,STATUS='NEW',FILE=NAME)

        NBELOW2 = 0
        NDELT1 = 100
        NDELT2 = 2*NDELT1
        NNOT1 = NNOT - 1

NANT=NANT-1
NAN=NANT/2+1
NAE=NAN-1
NRE=NRN-1

ANGO=DATAN(1.D0)
PI=4.D0*ANGO
A1=B1/NRE

        ISKIP = -1
        TWOA = A + B1
        IF (TWOA.GT.B) THEN
        THETAO = DASIN((TWOA - B)/A)
        ISKIP = INT(4.0*NAE*THETAO/PI)
PRINT *, ' NUMBER OF NODES TO SKIP (EVEN)    '
READ *, ISKIP
        ENDIF

        NAN1 = NAN
        NAE1 = NAE
        IF (TWOA.LT.B) THEN
PRINT *, ' NUMBER OF ELS BELOW NOTCH (EVEN)   '
READ *, NBELOW
        NBELOW2 = NBELOW*2
        NAN1 = NAN + NBELOW2
        NAE1 = NAE + NBELOW2
        ENDIF

DO I=1,NAN1
DO J=1,NRE
        DIST=A + A1*(J-1)

        IJUMP = 0
        IF (I.LE.NBELOW2) THEN
        IJUMP = 1
        NODE = NDELT1*(I-1) + J
        Z(NODE) = DIST
        Y(NODE) = (B - TWOA)*(1.0*(1.0*(I-1)/NBELOW2))**0.8
        R(NODE) = B - Y(NODE)
        ENDIF
        IF (IJUMP.EQ.1) GOTO 866

        ANGBIAS = 0.65
```

```
        ANG=PI*.25D0*(1.0* (I-1-NBELOW2)/NAE )**ANGBIAS
P=2.*NRE/(NRM-J)
        DIST11 = A*DCOS(THETA0)
        DIST1 = DIST11 + (TWOA - DIST11)*(J-1)/NRE
RAD=DIST*(DCOS(ANG)**P+DSIN(ANG)**P)**(-1.D0/P)
NODE=NDELT1*(I-1)+J
Z(NODE)=RAD*DCOS(ANG)
Y(NODE)=RAD*DSIN(ANG)
        NOD=NODE
        FACTOR = (4.0*ANG/PI - DTAN(ANG) )*((A/B1)**2)
        IF (ANG.NE.0.0) THEN
        Y(NODE) = Z(NODE) * (DTAN(ANG) +
     +  (   ( (Z(NODE)/(A)) - 1.0 )**2   )*FACTOR)
        ENDIF
        R(NODE) = TWOA - Y(NODE)

        IF (ISKIP.GE.0) THEN
        IF (I.GT.ISKIP) THEN
        YO = TWOA - B
        ZO = YO
C       RAD2 = RAD - DSQRT(2.0D0)*YO
        THETA1 = DATAN((TWOA - B)/DIST1)
        THETA = THETA1 + (PI*.25D0 - THETA1)*(I-1-ISKIP)/(NAE - ISKIP)
RAD2=DIST*(DCOS(THETA)**P+DSIN(THETA)**P)**(-1.D0/P)
Z2(NODE)=RAD2*DCOS(THETA)
Y21=RAD2*DSIN(THETA)
        FACTOR2 = (  (1.0D0/Z2(NODE))*(ZO + ( Z2(NODE) - ZO )
     +    *(THETA - THETA1)/(0.25D0*PI - THETA1) ) ) - DTAN(THETA)
        FACTOR2 = FACTOR2*( (A/B1)**2)
        IF (ISKIP.GE.0.AND.I.EQ.1+ISKIP) THEN
        Y2(NODE) = YO
        ELSE
        Y2(NODE) = Z2(NODE) * (DTAN(THETA) +
     +  (   ( (Z2(NODE)/(A)) - 1.0D0)**2   )*FACTOR2)
        ENDIF
        R(NODE) = TWOA - Y2(NODE)
        WRITE(12,1000)NOD,R(NODE),Z2(NODE)
        ENDIF
        ELSE
        WRITE(12,1000)NOD,R(NODE),Z(NODE)
        ENDIF
866     CONTINUE
ENDDO

NODE=NRM+NDELT1*(I-1)
Z(NODE)=TWOA

        IJUMP = 0

        IF (I.LE.NBELOW2) THEN
        IJUMP = 1
        Y(NODE) = (B - TWOA)*(1.0*(1.0*(I-1)/NBELOW2))**0.8
        R(NODE) = B - Y(NODE)
        ENDIF
        IF (IJUMP.EQ.1) GOTO 867
Y(NODE)=TWOA*4.0D0*ANG/PI
        IF (ANG.NE.0.0) THEN
        Y(NODE) = Z(NODE) * (DTAN(ANG) +
     +  (   ( (Z(NODE)/(A)) - 1.0 )**2   )*FACTOR)
        ENDIF
        NOD=NODE
        FACTOR = ( 4.0*ANG/PI - DTAN(ANG) ) * ( (A/B1)**2)
        IF (ANG.NE.0.0) THEN
        Y(NODE) = Z(NODE) * (DTAN(ANG) +
     +  (   ( (Z(NODE)/(A)) - 1.0 )**2   )*FACTOR)
        ENDIF
        R(NODE) = TWOA - Y(NODE)

        IF (ISKIP.GE.0) THEN
        IF (I.GT.ISKIP) THEN
        Z2(NODE) = TWOA
        Y2(NODE) = YO + B*(I-1-ISKIP)/(NAE - ISKIP)
        R(NODE) = TWOA - Y2(NODE)
        WRITE(12,1000)NOD,R(NODE),Z2(NODE)
        ENDIF
867     CONTINUE
        ELSE
        WRITE(12,1000)NOD,R(NODE),Z(NODE)
        ENDIF
ENDDO

        NODE1=1
        NODE2=3
        NODE3=NDELT2 + 3
        NODE4=NDELT2 + 1
        NODE5=2
        NODE6=NDELT1 + 3
        NODE7=NDELT2 + 2
        NODE8=NDELT1 + 1
```

```
      IF (ISKIP.LT.0) ISKIP = 0
      NODE1 = NODE1 + ISKIP*NDELT1
      NODE2 = NODE2 + ISKIP*NDELT1
      NODE3 = NODE3 + ISKIP*NDELT1
      NODE4 = NODE4 + ISKIP*NDELT1
      NODE5 = NODE5 + ISKIP*NDELT1
      NODE6 = NODE6 + ISKIP*NDELT1
      NODE7 = NODE7 + ISKIP*NDELT1
      NODE8 = NODE8 + ISKIP*NDELT1

C     NOTCH CALCULATIONS

      DELTA2 = (C-B1)/NNOT
      DELTA1 = 0.5*DELTA2

      NOTCH1 = 6501
      NOTCH2 = NOTCH1 + NDELT1*(NAE1- ISKIP)
      NOTCH3 = NOTCH1 + 2*NNOT1
      NOTCH4 = NOTCH2 + 2*NNOT1
      NOTCH5 = NOTCH1 + 1
      NOTCH6 = NOTCH5 + NDELT1*(NAE1- ISKIP)
      NOTCH7 = NOTCH5 + 2*NNOT1
      NOTCH8 = NOTCH6 + 2*NNOT1
C     BIAS1 = DSQRT(B1/(C-B1))
C     BIAS2 = 1.0D0/BIAS1
      BIAS1 = 1.0D0/BIAS2
      BIAS = (0.5D0*BIAS1)**(1.0D0/NNOT1)
      R(NOTCH1) = B
      Z(NOTCH1) = TWOA + DELTA1*BIAS1
      R(NOTCH2) = 0.0D0
      Z(NOTCH2) = TWOA + DELTA1*BIAS1
      R(NOTCH3) = B
      Z(NOTCH3) = C - DELTA1*BIAS2/2.0D0
      R(NOTCH4) = 0.0D0
      Z(NOTCH4) = C - DELTA1*BIAS2/2.0D0
      R(NOTCH5) = B
      Z(NOTCH5) = TWOA + DELTA2*BIAS1
      R(NOTCH6) = 0.0
      Z(NOTCH6) = TWOA + DELTA2*BIAS1
      R(NOTCH7) = B
      Z(NOTCH7) = C
      R(NOTCH8) = 0.0
      Z(NGTCH8) = C

      WRITE(12,1000) NOTCH1,R(NOTCH1),Z(NOTCH1)
      WRITE(12,1000) NOTCH2,R(NOTCH2),Z(NOTCH2)
      WRITE(12,1000) NOTCH3,R(NOTCH3),Z(NOTCH3)
      WRITE(12,1000) NOTCH4,R(NOTCH4),Z(NOTCH4)
      WRITE(12,1000) NOTCH5,R(NOTCH5),Z(NOTCH5)
      WRITE(12,1000) NOTCH6,R(NOTCH6),Z(NOTCH6)
      WRITE(12,1000) NOTCH7,R(NOTCH7),Z(NOTCH7)
      WRITE(12,1000) NOTCH8,R(NOTCH8),Z(NOTCH8)

      WRITE(12,3002)
      WRITE(12,3006) NOTCH1,NOTCH2,NDELT2
      WRITE(12,3003)
      WRITE(12,3006) NOTCH3,NOTCH4,NDELT2
      WRITE(12,3004)
      WRITE(12,3006) NOTCH5,NOTCH6,NDELT1
      WRITE(12,3005)
      WRITE(12,3006) NOTCH7,NOTCH8,NDELT1

      BIAS = (0.5D0*BIAS1)**(1.0D0/NNOT1)
      WRITE(12,3007) BIAS
      WRITE(12,3008) NNOT1
      WRITE(12,3007) BIAS
      WRITE(12,3010) NNOT1


3002  FORMAT('*NGEN,NSET=BODY1')
3003  FORMAT('*NGEN,NSET=BODY2')
3004  FORMAT('*NGEN,NSET=BODY3')
3005  FORMAT('*NGEN,NSET=BODY4')
3006  FORMAT(3I5)
3007  FORMAT('*NFILL,BIAS=',F8.6)
3008  FORMAT('BODY1,BODY2,',I2,',2')
3010  FORMAT('BODY3,BODY4,',I2,',2')

      NELEM=1 + NDELT1*ISKIP
      NRE1=NRE/2
      NAET1=NAET/2 + NBELOW2
      NAET2=NAET1/2
      NAET3=NAET2 - ISKIP/2
      NAET2=NAET2 - NBELOW

      NELEM0 = NELEM  + NAET3*NDELT1
      NELEM1 = NRE1+1 + NDELT1*ISKIP
      NELEM2 = NRE1+2 + NDELT1*ISKIP
      WRITE(6,*) 'NELEM0, ETC ',NELEM0,NAET1,NAET2,NAET3,NBELOW
```

```
      WRITE(12,1700)NELEM,NODE1,NODE2,NODE3,NODE4,NODE5,NODE6,NODE7,
     +  NODE8
      NOD1 = NODE1 + NDELT2*NAET3
      NOD2 = NODE2 + NDELT2*NAET3
      NOD3 = NODE3 + NDELT2*NAET3
      NOD4 = NODE4 + NDELT2*NAET3
      NOD5 = NODE5 + NDELT2*NAET3
      NOD6 = NODE6 + NDELT2*NAET3
      NOD7 = NODE7 + NDELT2*NAET3
      NOD8 = NODE8 + NDELT2*NAET3
      WRITE(12,1700)NELEM0,NOD1,NOD2,NOD3,NOD4,NOD5,NOD6,NOD7,NOD8

      WRITE(12,7000)NELEM,NRE1,NAET3,NDELT2,NDELT1

      NAET21 = NAET2*2
      WRITE(12,7000)NELEM0,NRE1,NAET2,NDELT2,NDELT1

      NT11 = NRE + NDELT1*ISKIP
      NT12 = NOTCH1
      NT13 = NOTCH5
      NT14 = NOTCH5 + NDELT1
      NT15 = NOTCH5 + NDELT2
      NT16 = NOTCH1 + NDELT2
      NT17 = NT11 + NDELT2
      NT18 = NT11 + NDELT1
      WRITE(12,1700) NELEM1,NT11,NT13,NT15,NT17,NT12,NT14,NT16,NT18
      WRITE(12,7001) NELEM1,NAET3,NDELT2,NDELT1

      NT21 = NOTCH1 + 1
      NT22 = NOTCH1 + 2
      NT23 = NOTCH1 + 3
      NT24 = NT23   + NDELT1
      NT25 = NT23   + NDELT2
      NT26 = NT22   + NDELT2
      NT27 = NT21   + NDELT2
      NT28 = NT21   + NDELT1
      WRITE(12,1700) NELEM2,NT21,NT23,NT25,NT27,NT22,NT24,NT26,NT28
      WRITE(12,7002) NELEM2,NAET3,NDELT2,NDELT1,NNOT1

      NAE3 = NAE1 - NBELOW
      NID1 = 1 + NDELT2*NAE3
      NID2 = NID1 + NRE
      NAXIS1 = 1 + NAE1*NDELT1 + NRE
      NAXIS2 = NID2
      NAXIS3 = NOTCH2
      NAXIS4 = NOTCH8
      NEND1 = NOTCH7
      NEND2 = NOTCH8
      WRITE(12,5001) NID1,NID2
      WRITE(12,5002) NAXIS1,NAXIS2,NDELT1,NAXIS3,NAXIS4
      WRITE(12,5003) NEND1,NEND2,NDELT1
      WRITE(12,5004)

      WRITE(12,2100)

1000  FORMAT(I5,2E10.4)
1100  FORMAT('*HEADING'/
     2 '   NOTCH -- L =',F5.2,'  W =',F5.2,' l=',F5.2,'  r =',F5.2/
     3  '*NODE')
1700     FORMAT('*ELEMENT,TYPE=CAX8R  ',/,9I5)
5001     FORMAT('*NSET,NSET=MIDDLE,GENERATE',/,2I5,'    1')
5002     FORMAT('*NSET,NSET=AXIS,GENERATE',/,3I5,/,2I5,'    1')
5003     FORMAT('*NSET,NSET=END,GENERATE',/,3I5)
5004     FORMAT('*BOUNDARY',/,'MIDDLE,2',/,'AXIS,1')
7000     FORMAT('*ELGEN,ELSET=NOTCH',/,I5,I5,'    2    1',3I5)
7001     FORMAT('*ELGEN,ELSET=FLANK',/,4I5)
7002     FORMAT('*ELGEN,ELSET=FLAPK',/,5I5,'    2    1')
2100     FORMAT ('*MATERIAL',/,
     6  '*ELASTIC',/,
     7  ' 1.',/,
     8  '*PLOT',/,'*DETAIL,ELSET=NOTCH',/,
     9  '*DRAW'/'**DRAW,ELNUM'/'**DRAW,NODENUM')
STOP
END
```

Appendix G

Sharply-notched Mesh Generation Program

The program listed on the following page was used to generate the ABAQUS geometric input data for the sharply-notched bar showr. in Fig. 5.27 which features a near-tip mesh pattern that follows the slip-line field for this geometry. This program is capable of generating a limited variety of notched-bar gemetries.

```
      PROGRAM SLIPLINE
      DIMENSION F(0:100),FO(0:100),ABIAS(0:100)
      N = 65
      A = 0.00005
      C = 0.005
      D = 0.025
      PI = 3.1415926
      N1 = 20
      N3 = 5
      BIAS2 = 1.3
      BIAS1 = 1.05
      SUM = 0.0
      ADELT = (PI*A/(N-1))
      WRITE(12,*) '*HEADING'
      WRITE(12,*) ' '
      WRITE(12,*) '*NODE'
      DO 100 I = ((N-1)/2),0,-1
      DELTAO= PI/(1.0*(N-1))
      DELTA = I*DELTAO
      BETA = 0.5*PI - DELTA
      DO 100 J = I,N-I-1
      ARG = 0.5*(J-I)*PI/(1.0*(N-1))
C     ARG = 0.5*J*DELTAO
      THETA = BETA - ARG
      R = A*EXP(ARG)
      X = R*COS(THETA)
      Y = R*SIN(THETA)
      NODE = ((N-1)/2-I)*N + J + 1
      WRITE(12,1000) NODE,X,Y
100   CONTINUE
      WRITE(12,*) '*SECOND LAYER'
      DO 130 I = 1,N1
      SAVE = ADD
      ADD = I*ADELT*(BIAS1**(I-1))
      AA = A + ADD
      BETA = 0.5*PI
      XMAX = AA*EXP(0.5*PI)
      DO 130 J = 0,N-1
      ARG = 0.5*J*PI/(1.0*(N-1))
      THETA = BETA - ARG
      R = AA*EXP(ARG)
      X = R*COS(THETA)
      Y = R*SIN(THETA) - ADD*(1.0-X/XMAX)
      X = X - ADD
      NODE = NODE + 1
      WRITE(12,1000) NODE,X,Y
130   CONTINUE
      WRITE(12,*) '*THIRD LAYER'
      FO1 = (ADD-SAVE)*2.0
      DO 10 I = 1,100
      SUM = SUM + FO1*(BIAS2**I)
      IF (SUM.GT.(C-Y)) GOTO 20
10    CONTINUE
20    CONTINUE
      N2 = I

      ABIAS1 = 2.0**(1.0/(1.0*(N-1)))
      DO 40 J = 0,N-1
      F(J) = 0
      SUM = 0
      ABIASO = ABIAS1**(N-1-J)
      ABIAS(J) = ABIASO**(1.0/N2)
      DO 30 I = 1,N2
30    SUM = SUM + ((BIAS2*ABIAS(J))**I)
40    FO(J) = 1.0/SUM

      DO 110 I = 1,N2
      DO 110 J = 0,N-1
      ARG = 0.5*J*PI/(1.0*(N-1))
      THETA = BETA - ARG
      R = AA*EXP(ARG)
      XO = R*COS(THETA)
      YO = R*SIN(THETA) - ADD*(1.0-XO/XMAX)
      XO = XO - ADD
      IF (J.LT.((N-1)/4)) THEN
        X1 = -C
        Y1 = A + (C-A)*J*4/(1.0*(N-1))
      ELSE IF (J.GT.(3*(N-1)/4)) THEN
        X1 = C
        Y1 = C*(N-1-J)*4/(1.0*(N-1))
      ELSE
        X1 = -C + 4*C*(J-((N-1)/4))/(1.0*(N-1))
        Y1 = C
      ENDIF
      F(J)  = F(J)  + FO(J)*((ABIAS(J)*BIAS2)**I)
      X = F(J)*X1 + (1.0-F(J))*XO
      Y = F(J)*Y1 + (1.0-F(J))*YO
      NODE = NODE + 1
      WRITE(12,1000) NODE,X,Y
110   CONTINUE
```

```
      WRITE(12,*) '**FLANK NODES'
      DO 140 I = 1,N3
      DO 140 J = (N-1)/4,3*(N-1)/4
      X =-C + 4*C*(J-((N-1)/4))/(1.0*(N-1))
      Y = C + (D-C)*I/N3
      NODE = N*(N-1)/2 + (N2+N1)*N + J + I*N + 1
140   WRITE(12,1000) NODE,X,Y
      WRITE(12,*) '*ELEMENT,TYPE=CPE4,ELSET=INNER'
      DO 200 I = 1,(N-3)/2
      NEL    = 2 + (N-1)*I
      NODE1 = (N-1)/2 + (N-1)*I + 1
      NODE2 = NODE1 + 1
      NODE3 = NODE2 + N
      NODE4 = NODE1 + N
200   WRITE(12,2000) NEL,NODE1,NODE2,NODE3,NODE4
      WRITE(12,*) '*ELGEN,ELSET=INNER'
      DO 300 I = 1,(N-3)/2
      NEL = 2 + (N-1)*I
      NUMELS = 2*I
300   WRITE(12,3000) NEL,NUMELS
      WRITE(12,*) '*ELEMENT,TYPE=CPE4,ELSET=OUTER'
      NEL    = 1 + (N-1)*(N-1)/2
      NODE1 = N*(N-1)/2 + 1
      NODE2 = NODE1 + 1
      NODE3 = NODE2 + N
      NODE4 = NODE1 + N
      WRITE(12,2000) NEL,NODE1,NODE2,NODE3,NODE4
      WRITE(12,*) '*ELGEN,ELSET=OUTER'
      NEL = 1 + (N-1)*(N-1)/2
      NUMELS = N-1
      WRITE(12,4000) NEL,NUMELS,N2+N1,N,N-1
      WRITE(12,*) '*ELEMENT,TYPE=CPE3,ELSET=INNER'
      NEL = 1
      NODE1 = (N-1)/2 + 1
      NODE2 = NODE1 + N
      NODE3 =  NODE2 - 1
      WRITE(12,5000) NEL,NODE1,NODE2,NODE3
      NUMELS = (N-1)/2
      WRITE(12,*) '*ELGEN,ELSET=INNER'
      WRITE(12,5000) NEL,NUMELS,N-1,N-1
      WRITE(12,*) '*ELEMENT,TYPE=CPE3,ELSET=INNER'
      NEL = N-1
      NODE1 = (N-1)/2 + 1
      NODE2 = NODE1 + N + 1
      NODE3 = NODE2 - 1
      WRITE(12,5000) NEL,NODE1,NODE2,NODE3
      WRITE(12,*) '*ELGEN,ELSET=INNER'
      WRITE(12,5000) NEL,NUMELS,N+1,N-1
      WRITE(12,*) '*ELEMENT,TYPE=CPE4,ELSET=FLANK'
      NEL    = 1 + (N-1)*(N-1)/2 + (N-1)*(N2+N1)
      NODE1 = N*(N-1)/2 + (N2+N1)*N + (N-1)/4 + 1
      NODE2 = NODE1 + 1
      NODE3 = NODE2 + N
      NODE4 = NODE1 + N
      WRITE(12,2000) NEL,NODE1,NODE2,NODE3,NODE4
      WRITE(12,*) '*ELGEN,ELSET=FLANK'
      NEL = 1 + (N-1)*(N-1)/2 +(N-1)*(N2+N1)
      NUMELS = N3
      WRITE(12,4000) NEL,(N-1)/2,N3,N,(N-1)/2
      WRITE(12,*) 'NSET,NSET=CORNER'
      WRITE(12,6000) N*(N-1)/2+(N2+N1)*N+(N-1)/4+N3*N+1
      WRITE(12,*) 'NSET,NSET=AXIS,GENERATE'
      WRITE(12,7000) N,(N1+N2)*N,N
      WRITE(12,*) '*ELEMENT,TYPE=IRS21,ELSET=INTER1'
      DO 400 I = 1,(N-1)/4
400   WRITE(12,8000) NEL+N3*(N-1)/2+(I-1),
     +  (N1+N2+(N-1)/2+1)*N-(I-1),(N1+N2+(N-1)/2+1)*N-I
      WRITE(12,*) '*PLOT'
      WRITE(12,*) '*DETAIL,ELSET=INNER'
      WRITE(12,*) '*DRAW'
      WRITE(12,*) '*PLOT'
      WRITE(12,*) '*DETAIL,ELSET=OUTER'
      WRITE(12,*) '*DRAW'
      WRITE(12,*) '*PLOT'
      WRITE(12,*) '*DETAIL,ELSET=FLANK'
      WRITE(12,*) '*DRAW'


1000  FORMAT(I5,2F10.8)
2000  FORMAT(5I5)
3000  FORMAT(2I5,'    1    1')
4000  FORMAT(2I5,'    1    1',3I5)
5000  FORMAT(4I5)
6000  FORMAT(I5)
7000  FORMAT(3I5)
8000  FORMAT(3I5,' 5000')

      STOP
      END
```